ISBN 978-82-326-4818-4 (printed ver.)
ISBN 978-82-326-4819-1 (electronic ver.)
ISSN 1503-8181

NTNU
Norwegian University of
Science and Technology

Doctoral thesis

Weizhi Wang

Doctoral theses at NTNU, 2020:235

NTNU
Norwegian University of Science and Technology
Thesis for the Degree of
Philosophiae Doctor
Faculty of Engineering
Department of Civil and Environmental
Engineering

NTNU

Doctoral theses at NTNU, 2020:235

Weizhi Wang

Large-Scale Phase-Resolved Wave Modelling for the Norwegian Coast

NTNU
Norwegian University of
Science and Technology

Weizhi Wang

Large-Scale Phase-Resolved Wave Modelling for the Norwegian Coast

Thesis for the Degree of Philosophiae Doctor

Trondheim, September 2020

Norwegian University of Science and Technology
Faculty of Engineering
Department of Civil and Environmental Engineering

NTNU
Norwegian University of
Science and Technology

NTNU
Norwegian University of Science and Technology

Thesis for the Degree of Philosophiae Doctor

Faculty of Engineering
Department of Civil and Environmental Engineering

ISBN 978-82-326-4818-4 (printed ver.)
ISBN 978-82-326-4819-1 (electronic ver.)
ISSN 1503-8181

Doctoral theses at NTNU, 2020:235

Printed by NTNU Grafisk senter

Abstract

The coastal Highway Route E39 aims to build a continuous road connection along the west coast of Norway. Floating bridges are planned to replace the ferries at seven major fjords along the route. These innovative floating structures require comprehensive understanding of the wave fields in the fjords. Currently, the information on the wave fields can only be obtained from discrete field measurements. However, the measurements cannot represent the entire domain due to the limited number of wave gauges. Therefore, numerical wave modelling is needed in order to obtain an extensive understanding of the wave propagation and transformation in the entire domain of interest.

Phase-resolved wave models are able to represent most of the wave transformation phenomena and provide time domain information for further engineering analysis. However, the special coastal conditions in Norway limit the validity of many existing phase-resolved wave models. The deep water conditions and strong variation of the bathymetry created by the fjords go beyond the limits of many shallow water wave models. The irregular coastline challenges the grid generation and boundary treatments of many existing potential flow wave models. The large domain of interest in the fjords makes the usage of computational fluid dynamics (CFD) models impractical because of their high-demand of computational resources. Therefore, a new phase-resolved numerical wave model is required for an accurate and efficient simulation of large-scale wave propagation in the Norwegian fjords.

The first development for the new model is based on the improvement of depth-averaged shallow water modelling technique. A quadratic non-hydrostatic pressure profile is used to improve the ability of representing water waves in deeper water conditions. The numerical model is implemented in the open-source hydrodynamics framework REEF3D. The resulting wave model REEF3D::SFLOW inherits the high-order discretisation schemes and parallel computation algorithm from the framework. Comprehensive verification and validation of the model are performed through a series of test cases. The tests show speed-up factors in the scale of 10 to 100 in comparison to the CFD model REEF3D::CFD. This enables the model to be used for large-scale simulations over a longer duration. The model demonstrates accurate representations of wave propagation and transformation including wave breaking. However, significant wave phase differences are observed during the de-shoaling process in the test of wave propagation over a submerged obstacle. This is due to the emerging short waves in the de-shoaling process resulting in deepwater conditions.

The best performance of the model is found to be within a water depth to wavelength ratio up to 0.25. As a result, the model is not recommended for the wave modelling in the deepwater Norwegian fjords.

Further development of a fully nonlinear potential flow (FNPF) model is conducted. The resulting model REEF3D::FNPF solves the Laplace equation together with the boundary conditions on a σ-coordinate grid. The model also inherits the high-order discretisation schemes and parallel computation algorithm. In some simulations, the model is 800 times as fast as REEF3D::CFD for achieving the same accuracy. The model is also validated through a large variety of test cases. It is found that the accuracy of the model is not compromised by the water depth conditions, for example the free surface elevations during the de-shoaling process show a good agreement with the experimental measurements. The model is then used to investigate relevant phenomena regarding the floating bridges inside the fjords, including the evolution of rogue waves and the high-fidelity reproducing of three-hour irregular sea states with different severity of wave breaking.

In order to address the irregular coastline, a novel coastline algorithm is developed in REEF3D::FNPF. This algorithm provides a universal solution for the inclusion of coastlines and boundary treatments. The model is then used to simulate full-scale wave propagation in Mehamn harbour in northern Norway. The significant wave heights H_s inside the harbour after the strong wave diffraction around the peninsulas and breakwaters show a good agreement with experimental measurements. This confirms the effectiveness of the coastline algorithm and the ability of the model of representing strong wave diffraction. Further studies of the wave fields in Sulafjord and Barørnafjord using REEF3D::FNPF provide insights on the wave frequency transition inside the fjords. A maximum simulation time to real time factor of 10 is also found for the large-scale simulations with tens of millions of cells.

The two new models REEF3D::SFLOW and REEF3D::FNPF are compared with the original CFD model REEF3D::CFD through several test cases to highlight the differences among them as well as their special features and area of applications. REEF3D::FNPF is an ideal model for large-scale wave propagation over varying bathymetry. REEF3D::SFLOW is a fast model for wave modelling in shallow to intermediate water depth and a model to study swash zone dynamics and sediment transport. REEF3D::CFD is the only model within the framework that is able to represent the overturning wave breaker and an ideal model to study local wave impacts and wave interaction with structures.

In conclusion, REEF3D::FNPF is suggested as the phase-resolving numerical model for the wave analysis in the fjords for the E39 project. The model is seen to be computationally efficient, phase-resolved, accurate and flexible. Developed as part of the open-source numerical framework REEF3D, the model is freely available to users. Future works of model coupling, inclusion of wind and current effects are also summarised in the end.

Acknowledgments

I would like to thank my supervisor, Associate Professor Hans Bihs, for the opportunity to work with the exciting development of numerical wave models. The support, the engagement and the encouragement from him keeps my determination to solve the research task during the Ph.D. study. I would also like to thank my co-supervisor Dr. Arun Kamath for his patient guidance from day one and the continuous help on both technical topics and academic writing; and my co-supervisor Associate Professor Øivind A. Arntsen for his kind advices and the sharing of his insights on wave hydrodynamics and knowledge of experimental tests.

I express my thanks to my peer Ph.D. student Tobias Martin and visiting researcher Dr. Csaba Pákozdi as I have learned much from them on hydrodynamics, numerics, research methods as well as new ideas and solutions that have broadened my horizons. The discussions with both of them have been both educational and enjoyable. I also thank my previous colleagues Dr. Nadeem Ahmad and Dr. Ankit Aggarwal for their helps and advices on research and academic life.

The sharing of knowledge and experience and the engagement from my supervisors and peer researchers is one of the key elements to make the Ph.D. research fruitful. For that they have all my gratitude.

The research cannot be productive if there were not great colleagues and friends in the department who give supports and cares and create a family-like atmosphere. I express my thanks to all my colleagues and friends at the department, from different research groups and different floors. I would also like to thank the administrative team for all the help and for enriching the academic life.

I express my thanks to the Norwegian Road Administration for the challenging and exciting research topic under the E39 ferry-free fjord-crossing project and the funding to make the research possible. I would also like to thank the Norwegian Metacenter for Computational Sciences (NOTUR)-NTNU for the valuable computational resources.

I express my sincere thanks to all my friends and my family for all the laughters and fun in spite of the ups and downs in my work as well as theirs. I thank you all for the shared support and positivity that will get us through whatever the future brings.

Contents

Abstract **i**

Acknowledgments **iii**

List of publications **ix**

Declaration of authorship **xi**

Declaration of contribution to the appended papers xi

Nomenclature **xiii**

Symbols xiii

Abbreviations xiv

1 Introduction **1**

1.1 Background 1

1.2 Motivation and objectives 4

1.3 Scope and limitations 7

1.4 Organisation of the thesis 8

2 Background and State-of-the-Art **11**

2.1 Laboratory investigations 11

2.2 Phase-averaged wave modelling 12

2.2.1 Spectral wave models 12

2.3 Phase-resolved wave modelling 13

2.3.1 Mild-slope wave models 13

2.3.2 Shallow water equation based wave models 14
2.3.3 3D non-hydrostatic wave models 15
2.3.4 Potential flow wave models 16
2.3.5 Computational fluid dynamics wave models 18
2.3.6 Smooth-particle hydrodynamics wave models 19
2.3.7 Numerical wave model coupling 20
2.4 Wave analysis in the Norwegian fjords for the E39 project 20
2.5 Summary of numerical wave modelling 21

3 Present Numerical Models 25
3.1 REEF3D 25
3.2 REEF3D::CFD 26
3.2.1 Governing equations 26
3.2.2 Free surface representation 27
3.2.3 Numerical schemes 28
3.2.4 Wave generation and absorption 30
3.3 REEF3D::SFLOW 32
3.3.1 Governing equations 32
3.3.2 Numerical schemes 34
3.3.3 Wave generation and absorption 36
3.3.4 Breaking wave algorithm 36
3.3.5 Wetting-drying algorithm 36
3.4 REEF3D::FNPF 37
3.4.1 Governing equations 37
3.4.2 Numerical schemes 38
3.4.3 Vertical grid arrangement 40
3.4.4 Wave generation and absorption 42
3.4.5 Breaking wave algorithm 42
3.4.6 Coastline algorithm 43

4 Summary of Major Results **47**
4.1 REEF3D::SFLOW model description and applications 48
4.1.1 Paper 1: An improved depth-averaged non-hydrostatic shallow water model with quadratic pressure approximation 48
4.2 REEF3D::FNPF model description 52
4.2.1 Paper 2: REEF3D::FNPF - a flexible fully nonlinear potential flow solver 52
4.3 REEF3D::FNPF applications for deepwater conditions 54
4.3.1 Paper 3: Investigation of focusing wave properties in a numerical wave tank with a fully nonlinear potential flow model . . . 54
4.3.2 Paper 4: A fully nonlinear potential flow wave modelling procedure for full-scale simulations of sea states with various wave breaking scenarios 57
4.4 REEF3D::FNPF applications for Norwegian coastal conditions 60
4.4.1 Paper 5: A flexible fully nonlinear potential flow model for wave propagation over the complex topography of the Norwegian coast 60
4.4.2 Paper 6: Phase-resolved wave modelling in the Norwegian fjords for the ferry-free E39 project 63
4.5 REEF3D open-source hydrodynamics framework 66
4.5.1 Paper 7: A comparison of different wave modelling techniques in an open-source hydrodynamic framework 66

5 Conclusions and Outlooks **69**
5.1 Conclusions 69
5.2 Outlook 71

6 Appended Publications **87**
Paper 1 An improved depth-averaged non-hydrostatic shallow water model with quadratic pressure approximation 89
Paper 2 REEF3D::FNPF - a flexible fully nonlinear potential flow solver 123
Paper 3 Investigation of focusing wave properties in a numerical wave tank with a fully nonlinear potential flow model 141
Paper 4 A fully nonlinear potential flow wave modelling procedure for full-scale simulations of sea states with various wave breaking scenarios 181
Paper 5 A flexible fully nonlinear potential flow model for wave propagation over the complex topography of the Norwegian coast 213
Paper 6 Phase-resolved wave modelling in the Norwegian fjords for the ferry-free E39 project 261
Paper 7 A comparison of different wave modelling techniques in an open-source hydrodynamic framework 311

List of publications

List of international journal papers appended in the thesis

Paper 1 Wang W., Martin T., Kamath A. and Bihs H. 2020. **An improved depth-averaged non-hydrostatic shallow water model with quadratic pressure approximation**. *International Journal for Numerical Methods in Fluids*, 1-22.

Paper 2 Bihs H., Wang W., Pákozdi C. and Kamath A. 2020. **REEF3D::FNPF - a flexible fully nonlinear potential flow solver**. *Journal of Offshore Mechanics and Arctic Engineering* 142(4).

Paper 3 Wang W., Kamath A., Pákozdi C. and Bihs H. 2019. **Investigation of focusing wave properties in a numerical wave tank with a fully nonlinear potential flow model**. *Journal of Marine Science and Engineering* 7(10), 375.

Paper 4 Wang W., Pákozdi C, Kamath A. and Bihs H. **A fully nonlinear potential flow wave modelling procedure for full-scale simulations of sea states with various wave breaking scenarios**. Submitted to *Ocean Engineering* 2020.

Paper 5 Wang W., Pákozdi C., Kamath A., Fouques S. and Bihs H. **A flexible fully nonlinear potential flow model for wave propagation over the complex topography of the Norwegian coast**. Submitted to *Applied Ocean Research* 2020.

Paper 6 Wang W., Pákozdi C, Kamath A. and Bihs H. **Phase-resolved wave modelling in the Norwegian fjords for the ferry-free E39 project**. Submitted to *Journal of Ocean Engineering and Marine Energy* 2020.

Paper 7 Wang W., Kamath A., Pákozdi C. and Bihs H. **A comparison of different wave modelling techniques in an open-source hydrodynamic framework**. Submitted to *Journal of Marine Science and Engineering* 2020.

Related conference papers not included in the thesis

1. Wang W., Pákozdi C., Kamath A., Bihs H. (2019) **High performance phase-resolved wave modelling for irregular coastal topography**. *MekIT19 - 10th National Conference on Computational Mechanics*, Trondheim, Norway.

2. Pákozdi C., Wang W., Kamath A., Bihs H. (2019) **Definition of the vertical spacing of a sigma grid based on the constant truncation error**. *MekIT19 - 10th National Conference on Computational Mechanics*, Trondheim, Norway.

3. Wang W., Pákozdi C., Kamath A., Bihs H. (2019) **Large-scale wave modeling for hydrodynamic load calculations on bridges foundations in Norwegian fjords**. *Coastal Structures Conference 2019*, Hannover, Germany.

4. Pákozdi C., Wang W., Bihs H., Sebastien F. (2019) **Validation of a high-performance computing nonlinear potential theory based numerical wave tank for wave structure interaction**. *Coastal Structures Conference 2019*, Hannover, Germany.

5. Bihs H., Wang W., Martin T., Kamath A. (2019) **REEF3D::FNPF - a flexible fully nonlinear potential flow solver**. *38th International Conference on Offshore Mechanics and Arctic Engineering*, Glasgow, Scotland, UK.

6. Wang W., Kamath A., Bihs H. (2018) **CFD simulations of multi-directional irregular wave interaction with a large cylinder**. *37th International Conference on Offshore Mechanics and Arctic Engineering*, Madrid, Spain.

7. Wang W., Kamath A., Bihs H., Arntsen Ø.A. (2018) **Multi-directional irregular wave modelling with CFD**. *ICOE 2018 4th International Conference in Ocean Engineering*, Chennai, India.

8. Wang W., Kamath A., Bihs H., Arntsen Ø.A. (2017) **Large scale CFD modelling of wave propagation into Mehamn harbour**. *MARINE 2017 Computational Methods in Marine Engineering VII*, Nantes, France.

9. Wang W., Kamath A., Bihs H., Arntsen Ø.A. (2017) **Large scale CFD modelling of wave propagation in Sulafjord for the E39 project**. *MekIT17 - 9th National Conference on Computational Mechanics*, Trondheim, Norway.

Declaration of authorship

In the seven appended international journal papers, the author of the thesis is listed as the first author of six journal papers. The author was responsible for the writing of the manuscripts, performing numerical simulations and analysis as well as participating in the development of the numerical wave models. As the second author on Paper 2, the author was responsible for the numerical simulations and analysis and wrote the section of numerical results.

Sébastien Fouques, as a fourth author of Paper 5 provided with experimental measurements and participated in the proofreading.

Tobias Martin, as a second author of Paper 1 contributed methodologies in the verification of the model in section 3. He also aided with proof-reading of the manuscript.

Csaba Pákozdi, as a second author of Papers 4, 5 and 6 contribute the methodology in the determination of the numerical grid arrangement and provided with experimental measurements for some cases. As a third author in Papers 2, 3 and 7, he participated with the setup of some of the numerical simulations.

Arun Kamath, as co-supervisor, aided with the proofreading advised the first author on the discussion of the results in all appended papers. As a second author of Paper 7, he is responsible for the simulations in section 3.3 and the numerical description of section 2.1. As a second author of Paper 7, he also helped with the numerical setup.

Hans Bihs as main supervisor and creator of the open-source hydrodynamic framework REEF3D, developed the numerical solver REEF3D::CFD, REEF3D::SFLOW and REEF3D::FNPF. He helped with case study suggestion, proofreading and paper structure in all appended papers. As the first author of Paper 2, he was responsible for the numerical model description as well as involved in the writing of abstract, introduction and conclusion.

Declaration of contribution to the appended papers

Papers 1, 4, 3, 5, 6: The thesis author was responsible for all the numerical simulations, analysis of the results and the writing of the full manuscript. The thesis author was also involved in the development of the numerical models presented in the papers.

Paper 2: The thesis author was responsible for all the simulations and analysis of the results. The author also participated in the writing of the introduction and conclusion.
Paper 7: The thesis author was responsible for the execution of two simulations in sections 3.1 and 3.2 and was involved in the third simulation in section 3.3. The thesis author also responsible for writing in sections 2.3 and 2.3 as well as part of the introduction and conclusion. The thesis author was involved in the planning, testing and validation of the numerical models REEF3D::SFLOW and REEF3D::FNPF presented in sections 2.3 and 2.3.

Nomenclature

Symbols

A	incident wave amplitude
A_F	input focused wave amplitude
k_p	wave number corresponding to the peak period
ϵ_p	steepness of focused wave
C_s	phase velocity corresponding to low-frequency limit
d	still water depth
ζ	free surface elevation in the shallow water wave model
h	local water depth $h = d + \zeta$
dx	horizontal grid size
dt	time step size
f	incident wave frequency
g	acceleration due to gravity
H	incident wave height
h_p	water level in the centre of the cell
H_s	significant wave height
k	wave number
L	incident wavelength
L_p	wavelength with peak period
L_e	wavelength corresponding to high-frequency limit
P	hydrostatic pressure
P_T	total pressure including hydrostatic and dynamic parts
Q	Non-hydrostatic pressure (dynamic pressure)
q	depth-averaged non-hydrostatic pressure (dynamic pressure)
S	spectral power density
T	wave period
T_p	peak period
δx_F	delay of wave focusing in space
δt_F	delay of wave focusing in time

η	free surface elevation in the potential flow wave model
α	stretching factor in the vertical stretching function
α_s	phase velocity criterion threshold for shallow water breaking
β	steepness criterion threshold for deep water breaking
β_i	angular components for directional spreading
θ_i	wave phase term of each wave component in a irregular wave
ε_i	initial wave phase of each wave component in a irregular wave
Γ	relaxation function
ρ	density
ω	angular wave frequency
ω_s	low-frequency limit of a frequency band
ω_e	high-frequency limit of a frequency band
Φ	velocity potential in σcoordinate grid
η	free surface elevation
ν_t	turbulent viscosity
σ	sigma-coordinate grid

Abbreviations

BEM	Boundary Element Method
BiCGStab	Bi-Conjugate Stabilized
CFD	Computational Fluid Dynamics
CFL	Courant-Friedrichs-Lewy's
FNPF	Fully Nonlinear Potential Flow
GCIBM	Ghost Cell Immersed Boundary Method
VOF	Volume of Fluids
WENO	Weighted Essentially Non-scillatory
ENO	Essentially Non Oscillatory
LSM	Level-set Method
TLP	Tension Leg Platform
NTP	National Transport Plan
FDM	Finite Difference Method
HOS	High-order Spectrum
MPI	Message Passing Interface

EEM	Equal Energy Method
PEM	Peak Enhance Method
TVD	Total Variation Diminishing
NWT	Numerical Wave Tank
FFT	Fast Fourier transform
RANS	Reynolds-averaged Navier-Stokes
SPH	Smooth-particle Hydrodynamics
SEM	Spectral Element Method
MAC	Marker-And-Cell
PDE	Partial Differential Equation
CPU	Central Processing Unit
GPU	Graphic Processing Unit
WSI	Wave Structure Interaction
NH	Non-Hydrostatic
EMSE	Elliptic mild-slope equation
PA	Parabolic Approximation
DOF	Degree of Freedom

Chapter 1

Introduction

1.1 Background

As part of the National Transport Plan (NTP) for 2014-2023, the coastal highway route E39 is a major coastal infrastructure project in Norway. It aims to build a continuous road connection between Kristiansand and Trondheim across 5 counties and covering 1000 km along the west coast of Norway (Dunham (2016)). The route of the E39 coastal highway is illustrated in Fig. 1.1. The 5 counties along the route represent 40% of the total Norwegian population (Statistics Norway (2020)) and include the commercial shipping centre and second largest city Bergen, the research hub and third largest city Trondheim and the offshore industry base and fourth largest city Stavanger. Therefore, a road connection in this area will bring tremendous benefits to society as well as commerce, industry and research. Currently, there are seven major ferry-crossings along the road, as shown in Fig. 1.1. This makes traveling and transport discontinuous and leads to much of the travelling time being spent on waiting for the next ferry. The E39 project plans to replace the ferry connections with permanent bridge connections. It is estimated that these planned permanent connections will nearly halve the travel time along the complete route from Kristiansand to Trondheim from the current 21 hours to merely 13 hours (Dunham (2016)). This dramatically shortened traveling time will greatly boost the movement of the population as well as the transport and distribution of cargo and goods. The continuous ferry-free E39 route is thus expected to have significant social and economic impact on both the local regions as well as the entire nation.

The key engineering challenge of the E39 project is the fjord-crossings. In contrast to rivers, the fjords were formed when ancient glaciers glided into the ocean, carving deep trenches in its wake. As a result, the fjords are usually extremely wide and deep and have strong variations in water depth. The width of the seven fjords along the route E39 varies between 1.6 km to 5 km and the depth has a range from 400 m to 1300 m (Dunham (2016)). If a traditional suspension bridge is to be built for a 5 km span in the fjords, the bridge length is about twice that of the Golden Gate Bridge (2.7 km) in California, United States. It is a tremendous engineering challenge to

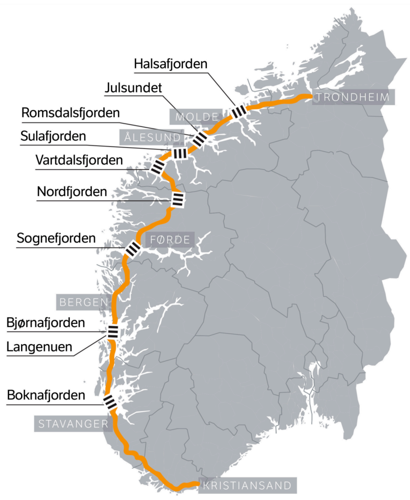

Figure 1.1: Overview of the E39 coastal highway route (Vegvesen (2019)). The seven major ferry-crossings to be replaced with permanent floating bridges are: Halsafjord, Jusundet, Sulafjord, Vartdalsfjord, Nordfjord, Sognefjord, Bjørnafjord-Langenuen. Subsea tunnels are planned for Romsdalfjord and Boknafjord in stead of floating structures (Dunham (2016)).

design and build a suspension bridge of such a long span. With the technology from the Norwegian offshore industry and engineering experience of construction and maintaining large moored floating platforms, alternative and innovative designs of floating structures have been proposed for the fjord-crossings. There are so far three main concepts of floating structures: a floating bridge with tension-leg platform (TLP) type supporting structures, a floating bridge with multiple supporting pontoons and a floating submerged tunnel-bridge. Those concepts are illustrated in Fig. 1.2.

The TLP floating bridge concept is inspired by the offshore industry. The deck of the bridge is supported and connected by a few platforms with a tension-leg mooring system that resembles the TLP platforms for offshore oil exploitation. Instead of using ground based bridge towers, the floating TLP platforms serve as bridge towers and carry the weight of the bridge. TLP platforms are usually used for deepwater operations and therefore the concept is well suited for the water conditions inside the fjords. The concept of the multi-pontoon bridge is based on existing bridges of the same type in Norway, such as the Bergsysund bridge in the county of Møre and Romsdal. Here, the weight of the bridge is distributed on a series of floating pontoons rather than on bridge towers. This concept can be used together with a tall bridge tower in a more shallow region to rise the height of the bridge in order for ships to pass. The submerged tunnel-bridge has a similar supporting structure as the multi-pontoon bridge. However, the road is located inside the submerged tunnel connected to the pontoons, as seen in Fig. 1.2c. Fig. 1.2c shows how vehicles drive through the enclosed structure beneath the water surface. The submerged design allows ships to pass over the tunnel-bridges and thus avoid collision.

One of the main design concerns of these novel floating structures are the envi-

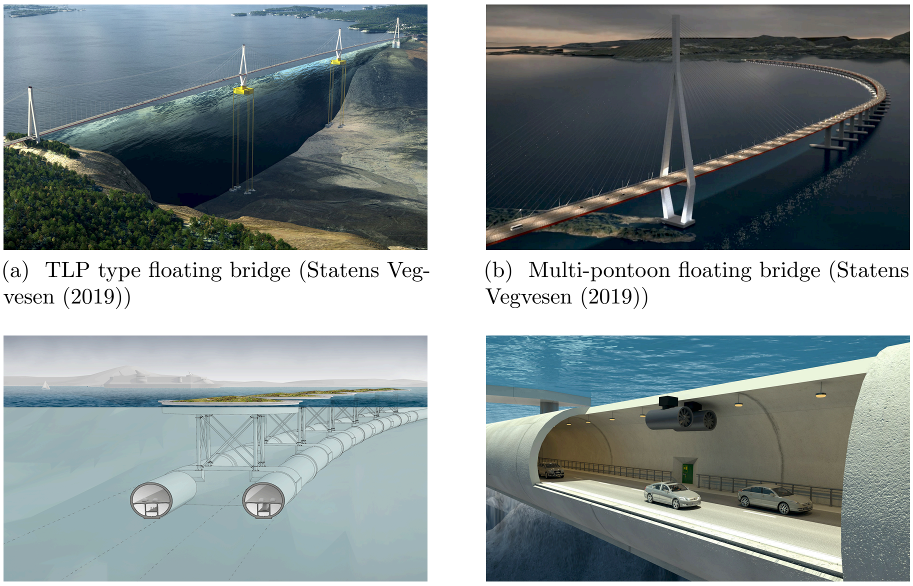

(a) TLP type floating bridge (Statens Vegvesen (2019))

(b) Multi-pontoon floating bridge (Statens Vegvesen (2019))

(c) Submerged tunnel-bridge (Statens Vegvesen (2019))

(d) Interior of a submerged tunnel-bridge (Eidem (2018))

Figure 1.2: Concepts of floating structures for the permanent connections at Norwegian fjords along the E39 coastal highway.

ronmental loads. Since these structures are usually moored to the bottom of the fjords instead of having a ground based foundation, their motions are much more influenced by wind, waves and current. In spite of the differences in the concepts, all floating bridges have floating supporting structures such as TLP platforms or pontoons at the free surface of the water. Therefore the influence of surface water waves is one of the key design considerations to ensure the structural integrality and limit the structure motion for the safety of passengers and vehicles.

The wave field is complicated inside the fjords. First, there is usually a mixture of both ocean swell from the offshore area and local wind generated waves (Cheng et al. (2019); DHI (2016)). These two wave systems tend to propagate in different directions with different dominating frequencies. The relative importance of the two wave systems also varies from fjord to fjord and changes over time in the same fjord. The varying and interacting wave systems make the wave fields more unpredictable. Second, the strong variation of the water depth inside the fjords and the irregular coastlines creates strongly non-linear wave transformations, including shoaling, refraction, diffraction, refraction and wave breaking. These wave transformations often take place simultaneously and the joint effects are hard to calculate with analytical formulations made for each individual phenomenon. As a result, the wave fields inside the fjords are not stationary in time and not homogeneous in space. The inhomogeneity can be significant even within the span of a bridge (Cheng et al. (2019); Dai et al. (2020)), resulting in different wave loads for each pontoon. The understanding of the complicated wave field is the first step in the design process.

1.2 Motivation and objectives

So far, the only reliable source for the wave field information are in-situ measurements that have been ongoing in the past years at several fjords. For example, both floating buoys and acoustic wave gauges have been used to measure wave height time series as well as directionality in Bjørnafjord from January 6, 2015 to April 30, 2019 (DHI (2016)). Measurements at four wave gauges at Sulafjord have also started gradually since 2016 (Fergstad et al. (2018)). However, the duration of the measurements is not yet adequate to obtain long-term wave statistics at the time of writing the thesis. It is also hard to obtain the comprehensive information of the waves in the entire domain of interest due to the limited number of wave gauges that can be deployed. In spite of these limitations, the field measurements provide valuable short-term wave information at several locations under various wave conditions. There have been extensive experimental investigations on coastal waves at many facilities around the world. An alternative to the physical experiments are numerical simulations. Many numerical wave models have been developed in the past decades due to the progress in numerical methods and computational hardware. Numerical wave models are usually less expensive as they do not require the time and material for the construction and execution of the physical tests. The cost of numerical wave models further reduces as many open-source wave models have been developed, such as the spectral wave model SWAN (Booij et al. (1999)), the non-hydrostatic wave model SWASH (Zijlema et al. (2011a)) and the hydrodynamics framework REEF3D (Bihs et al. (2016)). Meanwhile, the efficiency of numerical wave models has been further improved in recent years as high performance computation (HPC) facilities become increasingly available. Numerical models are also less restricted to physical limitations of facilities. Thus, it is possible to conduct full-scale investigations and perform several numerical simulations simultaneously. Due to these practical features, numerical models become increasingly important in coastal engineering. However, the numerical simulation of waves near the Norwegian coast faces several challenges because of the unique coastal topography in Norway.

The coastal area in Norway is special in comparison to most coasts along the North Sea. Usually, the coastal area has shallow water conditions with mild changes of bathymetry. For example, the bathymetry near Haringvliet, the Netherlands (Ris et al. (1999); Navionics) is shown in Fig. 1.3a. The water depth near the shore is typically below 10 m even 7 km away from the shoreline and the variation of the water depth contours is moderate. In contrast, the Norwegian coastal area mostly has deep water conditions and strong variations of bathymetry due to the fjords. As an example, the bathymetry of Sulafjord is shown in Fig. 1.3b. Here, the water depth quickly reaches 200 to 500 m inside the fjord within a short horizontal distance. The red circle in Fig. 1.3b shows an area where water depth increases to 200 m only 211 m away from the nearest shoreline, creating a near 45° underwater slope. In addition to the special bathymetry, the islands and archipelagos outside the fjords also increase the complexity of the coastlines. Moreover, the domain of interest at the Norwegian coast extends to several tens of kilometres in each horizontal direction due to the dimensions of the fjords. These Norwegian coastal conditions and the associated challenges in numerical modelling are briefly summarised as the following:

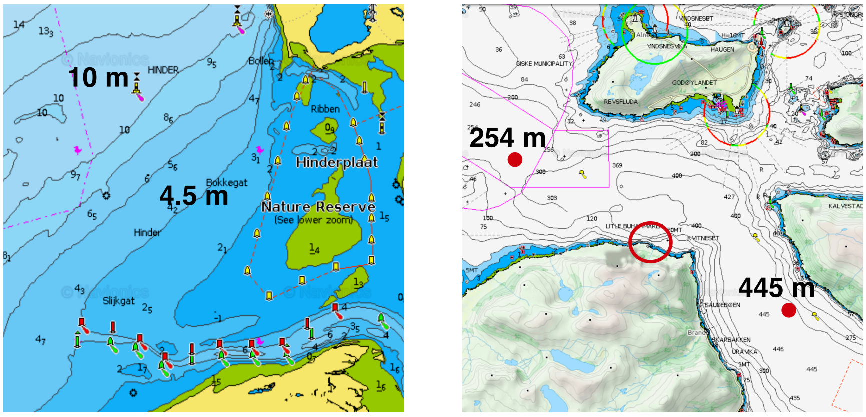

(a) (b)

Figure 1.3: Comparison of coastal topography between a typical northsea coast (Haringvliet, the Netherlands (Ris et al. (1999); Navionics)) and Norwegian fjord (Sulafjord (Navionics (2020)).

- **Deep water conditions**. The extraordinary water depths in the Norwegian fjords limit the application of many shallow-water equation based numerical wave models where shallow water assumptions are made and the flow properties in the vertical direction are considered as depth-averaged.
- **Significant bathymetry variations**. The strong variations of the under water topography limit the usage of wave models that are based on the assumption of small seabed slope variations, such as e.g. elliptic mild slope or spectral wave models..
- **Irregular coastlines**. With the presence of the complex geometry of the coastlines, it is challenging to generate a boundary-following horizontal grid and treat the boundary conditions efficiently.
- **Large domain of interest**. The large simulation domains require high computational efficiency of numerical models. As a result, the widely used computational fluid dynamics (CFD) models are seen to be impractical for the coastal wave modelling due to their high demand of computational resources.

Currently, most existing numerical wave modelling studies in the Norwegian fjords have been using spectral wave models with phase-averaging (Aarnes (2019); Fergstad et al. (2018)). In the phase-averaged approach, the wave field is often represented as the distribution of wave energy in terms of the significant wave height H_s. Such an approach cannot provide time-domain information and has limited capability of representing some of the strongly non-linear wave transformations such as diffraction ((Thomas and Dwarakish, 2015)). In contrast, a phase-resolved approach represents the wave phase information and free surface elevations. This enables the phase-resolving wave models to provide time series of wave properties and represent most of the highly non-linear wave transformation phenomena. As an example, a comparison of phase-averaged and phase-resolved results is shown in Fig. 1.4. In order to provide comprehensive wave information, a phase-resolved approach is preferred for Norwegian coastal wave modelling. However, there are few attempts of phase-resolved wave modelling of the Norwegian fjords. Wang et al. (2017) performed a phase-resolved CFD modelling of a Norwegian fjord for only a short period due to the time consumption of the CFD model for the large computational domain.

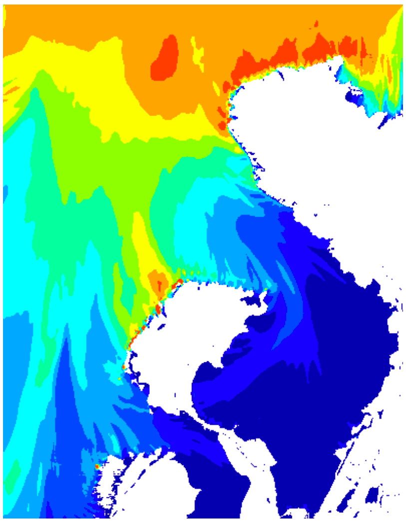

(a)

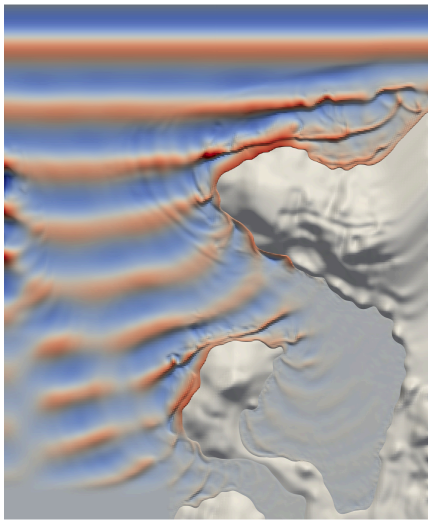

(b)

Figure 1.4: Illutstration of the difference between phase-averaged and phase-resolved simulation results from wave modelling at Mehamn harbour in Norway. (a) significant wave height distribution produced by SWAN (Booij et al. (1999)), (b) Wave surface eelevation produced by REEF3D::SFLOW (Wang et al. (2020)).

In summary, the Norwegian coastal conditions present several challenges for numerical wave modelling and there is a lack of an effective phase-resolving model to address these challenges. Therefore, the Ph.D. candidate is tasked with the development of such a numerical wave model for the Norwegian coast. Considering the engineering challenges as well as the social impact of the E39 project, the new model should fulfil the following criteria:

- **Efficient**. The model should be computationally efficient for large-scale simulations (tens of kilometres) over long durations (typically three-hours for short-term wave statistics (DNV-GL (2018)) with currently available computational resources and reasonable time consumption.

- **Phase-resolved**. The model is supposed to provide phase-resolved results to reveal the details of the wave field, represent all wave transformations and provide time domain information.

- **Accurate**. The model should be verified and validated to ensure that wave propagation and transformation are represented correctly.

- **Flexible**. The model is expected to simulate waves at all water depth conditions, different coastal bathymetry and various irregular coastlines. The model should also reproduce a wide range of wave inputs in the fjord.

- **Open-source**. The model will keep the source-code freely available to ensure technical transparency and to maximise the impact on the industry and society.

1.3 Scope and limitations

The study focuses on the development of a wave propagation model for the Norwegian coast that fulfils the criteria defined in section 1.2. As a wave propagation model, the model uses wave parameters as input to investigate the wave propagation and transformation in the fjords. The effects of wind and current on waves are not within the scope of the project. The mechanism of wave generation from wind fields is also not included.

The specific scope of the study is summarised as follows:

- Examine and evaluate the current phase-resolved numerical wave models and choose a strategy for wave modelling in the Norwegian fjords.

- Implement new numerical wave models in the numerical framework REEF3D (Bihs et al. (2016)).

- Improve the performance and include new utilities in the numerical models to meet the challenges presented by the Norwegian coastal wave conditions.

- Verify and validate the numerical models for their performance and accuracy with benchmark cases.

- Apply the numerical models to large-scale engineering scenarios and evaluate its readiness for industrial applications.

1.4 Organisation of the thesis

This thesis is submitted as a collection of seven international journal papers. The structure of the thesis is as follows:

- **Chapter 1**: description of the research topic presented by the E39 coastal highway project.
- **Chapter 2**: state-of-the-art development of coastal wave investigations and numerical wave modelling.
- **Chapter 3**: description of the numerical wave models that have been developed and used during the current research.
- **Chapter 4**: summary of major results from the Ph.D. research.
- **Chapter 5**: conclusion and the suggested future work for further development.
- **Chapter 6**: seven appended research articles produced during the Ph.D. period.

The appended research articles follow the work flow of the wave model development as well as the research progress to address the challenges presented by the Norwegian coast. The wave model development, research progress and the sequence and topics of each article are summarised in Fig. 1.5.

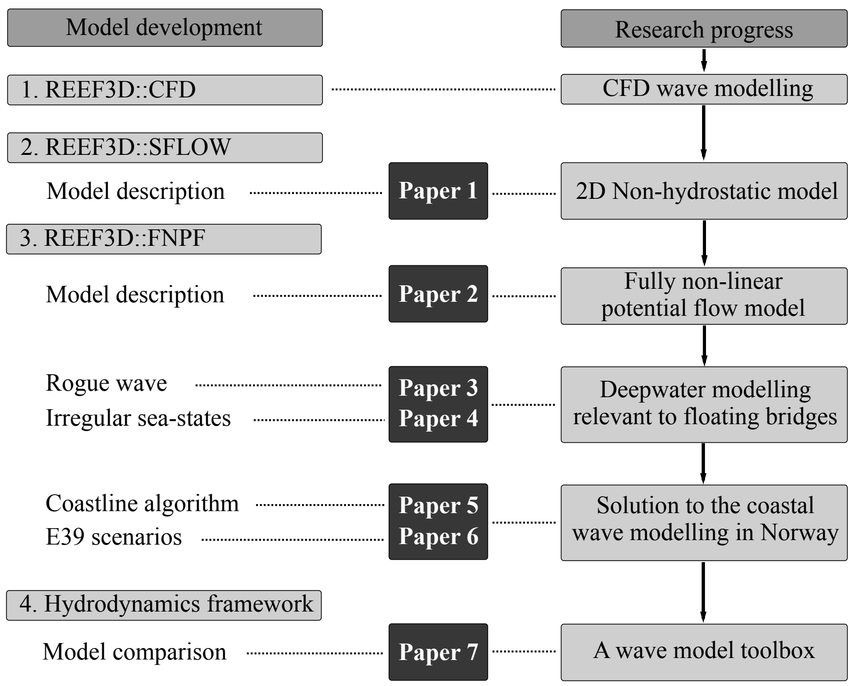

Figure 1.5: Structure of the thesis and correlation between the appended publications and numerical model development and research progress.

Chapter 2

Background and State-of-the-Art

The investigation of water surface waves has been carried out for a long time due to its significance for shipping, navigation, ocean engineering, offshore activities and coastal processes. Prior to the fast advances of computer technology, the investigations on surface waves were primarily carried out in physical laboratories. There were a series of significant developments of physical experiments in the 19th century. Some of the milestones are, for example, the development of hydraulic scaling criterion by Ferdinand Reech in 1852 (Rouse and Ince (1957)), the ship towing experiments conducted by William Froude in 1870's (Ivicsics (1980)) and the first moveable-bed model test performed by Louis Fargue in 1875 (Ivicsics (1980)). Many prominent coastal engineering experimental facilities have been established since late 19th century and during the 20th century. For example, the Franzius Institute was founded in Germany in 1914, the University of Iowa hydraulic laboratory was founded in the United States in 1918 and the Delft hydraulics laboratory was established in the Netherlands in 1927. The development of numerical wave models occurred much later in comparison. Some operational numerical wave models started to show their significance around 1990, for example, the spectral wave model WAM (The Wamdi Group (1988)) and Madsen's Boussinesq model (Madsen et al. (1991)). Since 1990, there have been a rapid development of numerical methods for representing surface waves as well as a significant advance in computational infrastructure. Today, there is a large variety of numerical wave models to simulate ocean waves digitally using modern computing infrastructures. In this chapter, some of the experimental activities for coastal waves in Norway, the various wave modelling techniques and the current wave field investigation in the Norwegian fjords are summarised.

2.1 Laboratory investigations

Experimental studies were the main method for the analysis of a certain wave field before the numerous numerical wave models were developed in the recent decades. Physical wave basins and wave flumes have been used world wide for a large variety of research on marine hydrodynamics, design of ships and offshore platforms and coastal development. In comparison to field measurements, the laboratory studies show a few advantages. For example, the small size of the model allows for easier data collection and the experimental environment offers much higher degree of control over the wave field. In Norway, there have been several notable experimental studies on coastal waves. For example, a customised wave basin was used by the SINTEF Coast and Habour Research Laboratory for optimising the breakwater design at Mehamn harbour in northern Norway (Vold and Lothe (2009)). Here, a replicate of the topography at the harbour was constructed in a model scale of 1:80, as shown in Fig. 2.1. The wave propagation and transformation into the harbour is well visualised and the time series of the surface elevations are collected at the nine wave gauges near the coastlines. There are also reports of physical experiments for the Norwegian fjords. For example, Lindstrøm et al. (2014) used a physical model with a scale of 1 : 500 to investigate the landslide generated waves in Storfjord. The model test examined the maximum run-up at the nearby settlements, Hellesylt and Geiranger. These experiments provide data sets of great value for the assessment of numerical wave models for similar phenomena. However, as pointed out by Hughes (1993), physical models are in general more expensive to operate than numerical models. Thus if a numerical model is validated against the experimental data and provides reliable results with engineering accuracy, then a numerical model is often the tool of choice.

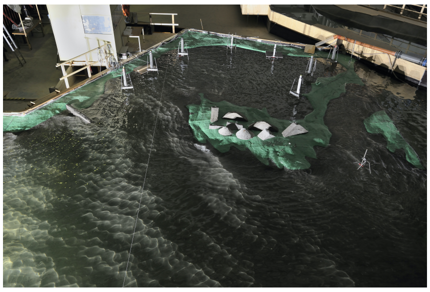

Figure 2.1: Laboratory setup for the breakwater optimisation at Mehamn harbour (Vold and Lothe (2009)). 9 wave gauges are deployed, 8 of them are arranged inside the harbour behind the breakwater to provide time domain measurements of the free surface elevations.

2.2 Phase-averaged wave modelling

2.2.1 Spectral wave models

Some of the most used wave models are spectral wave models. This type of model describes the wave field in terms of wave energy density, wave action density (defined as energy over frequency) and wave propagation directions. As a result, the governing equation is the spectral action balance equation that describes the evolution of the wave action density. Some of the notable spectral waves models are WAM (The Wamdi Group (1988)), WAVEWATCH III (Komen et al. (1994)), STWAVE (Massey et al. (2011)), MIKE 21 SW (DHI (2017b)) and SWAN ((Booij et al., 1999)). The spectral wave models are very computationally efficient and they are often used for large-scale wave modelling from the offshore area to the nearshore coastal waters. Though the phase-averaging approach of spectral wave models has limited capability of representing some of the nonlinear phenomena such as strong diffraction and reflection ((Thomas and Dwarakish, 2015; SWAN, 2016)), the simulation results provide valuable input wave conditions for other wave models that are more accurate in the near shore to surface zone area with the presence of complex coastlines. It is also straightforward to include the effects of wind and wave-wave interaction as source terms in these models. In some Norwegian fjords, the dominating waves are the local wind generated waves. In this case, the spectral models can be used for the study on wind wave generations. In general, the combined use of a spectral wave model and a phase-resolved wave model is beneficial for the balance between accuracy and computational efficiency.

2.3 Phase-resolved wave modelling

Phase-resolved wave models are able to present the wave phase information and free surface. The transient wave field can be visualised in the simulations as can be observed in nature and the time history of the flow information can be recorded. In comparison to the phase-averaged approach, phase-resolved models represent the nonlinear wave transformations such as diffraction around large obstacles with higher accuracy. Therefore, the phase-resolving approach is preferred near the complex coastal geometry of a fjord or a harbour. In the following sections, the various phase-resolved models are briefly introduced and discussed.

2.3.1 Mild-slope wave models

Within the framework of linear wave theory, an improvement to the ray theory was introduced and developed by Eckart (1952) and Berkhoff (1972, 1976) to combine the effects of both refraction and diffraction. This leads to the elliptic mild-slope equation (EMSE). From the EMSE, one can solve for the free surface elevations in terms of the horizontal coordinates. In order to specify boundary conditions along land boundaries, which are essential for solving the elliptic-type equation, the parabolic approximation (PA) is introduced based on the assumption that the percentage changes of depth within a typical wavelength are small compared to the wave slope (Demirbilek and Panchang (1998)). One of the notable EMSE model with the PA assumption is CGWAVE (Demirbilek and Panchang (1998)). The model is reported to be able to simulate wave refraction over a submerged dune as well as wave diffraction around breakwater in harbours. However, the model's validity is limited by the bottom slope. An accurate calculation is usually found with a bottom slope up to 1 : 3 (Demirbilek and Panchang (1998)). Therefore, such models are usually used for very long waves over slowly varying bottom, for example storm surge and wave-current interaction (Chen et al. (2005)).

2.3.2 Shallow water equation based wave models

Most coastal areas have shallow water conditions (typically defined as water depth to wave length ratio $d/\lambda \leqslant 0.05$) with moderate variations of bathymetry. For long waves in shallow waters, the wave dispersion relation is less important and the variation of particle motions in the vertical direction is insignificant (Mei et al. (2005)). Therefore, it is assumed that the flow information in the vertical direction is depth-averaged. Consequently, the computational domain is essentially two-dimensional (2D) and this greatly increases the computational speed. The depth-averaging of the mass and momentum conservation equations for an incompressible flow leads to the shallow water equations (SWE), from which the depth-averaged velocities and pressure can be solved. Two SWE based wave models, Boussinesq-type models and 2D non-hydrostatic models are discussed in this section.

Boussinesq wave models

The classical Boussinesq equations were developed by Peregrine (1967) as 2D depth-averaged shallow water equations in terms of depth-averaged velocity components for non-dispersive linear wave propagation. Abbott et al. (1984) introduced a third-order accurate finite difference scheme for modelling the Boussinesq equations in two dimensions. Since then, continuous efforts have been made to improve the Boussinesq models for a better representation of nonlinearity and the frequency dispersion in intermediate to deep water. Madsen et al. (1991) introduced a new form of Boussinesq equations that improved the dispersion relation and made it possible to simulate the wave propagation in deep water where the water depth to wavelength ratios is 0.6. Madsen and Sørensen (1992) further included the first derivatives of the sea bed and allowed for the simulations over varying bathymetry. Nwogu (1993) derived another form of the Boussinesq equations by using the velocity at an arbitrary distance from the still water level instead of the depth-averaged velocity, making the model applicable to a wider range of water depths. Further development by Wei et al. (1995) improved the dispersion relation for deeper water and enabled the model for strong non-linear interactions. This development was then incorporated into the wave model FUNWAVE (Kirby et al. (1998)). Madsen and Schäffer (1998) achieved very good dispersion accuracy up to dimensionless wave number $kd = 6$ with their high-order derivations. Similarly, a fourth-order polynomial is used in the model developed by Gobbi et al. (2000) and a faithful representation of linear dispersion is achieved up to $kd = 6$. These methods result in up to fifth-order spatial derivatives in an extremely complex equation system, which increases the risk of numerical instabilities. Madsen et al. (2002) applied multiple expansions at various vertical levels of the water column with high-order polynomial approximations and managed to represent the dispersion relation accurately up to $kd = 40$. This polynomial multiple expansion, on the other hand, also results in a large set of equations and more unknowns (Lynett and Liu (2004)). Taking a different approach, Lynett and Liu (2004) divided the vertical water column into a finite number of layers with quadratic polynomials and matched them at the interfaces.

This multi-layer approach shows good representation of linear dispersive properties up to $kd = 8$ with two layers. In addition, only 3rd-order spatial derivatives are needed even with three or four layers. This method is incorporated into the wave model COULWAVE (Lynett et al. (2008)). Some commercial software of this type can also be found, for example MIKE 21 BW (DHI (2017a)). These developments and achievements have improved the Boussinesq wave models greatly, enabling them to simulate more non-linear waves at deeper waters.

2D non-hydrostatic wave models

In the non-hydrostatic (NH) approach, the pressure is split into hydrostatic and non-hydrostatic components. The non-hydrostatic pressure is described implicitly in the momentum equations. As a result, the high-order spatial derivatives for the explicit expression of the non-hydrostatic pressure in a Boussinesq-type model is avoided. Stelling and Duinmeijer (2003a) introduced a Keller-Box scheme (Lam and Simpson (1976)) for the approximation of the vertical gradient of the non-hydrostatic pressure. This scheme is edge-based for the non-hydrostatic pressure instead of cell-centred. This way, even with only one vertical layer, the numerical model is able to represent frequency dispersion with a similar accuracy as the Boussinesq model from Peregrine (1967) (Stelling and Duinmeijer (2003a)). When multiple layers are used, the vertical information is much better represented, which leads to 3D non-hydrostatic models that will be discussed in section 2.3.3. Jeschke et al. (2017) presented an alternative approach for non-hydrostatic representation by introducing a quadratic pressure assumption. This way, the model can achieve at least a good equivalence to a second-order Boussinesq model ((Jeschke et al., 2017)). The effectiveness of such a method for simulating wave propagation over varying bathymetry is also proved by Wang et al. (2020). The quadratic approach for the non-hydrostatic pressure leads to one of the models developed during the current Ph.D. study, REEF3D::SFLOW, the details of which can be found in **Paper 1**.

2.3.3 3D non-hydrostatic wave models

In the 3D non-hydrostatic approach, the method of decomposing the pressure into hydrostatic and non-hydrostatic components is also applied. Stansby and Zhou (1998) and Zhou and Stansby (1999) used the non-hydrostatic approach to solve the 3D Non-hydrostatic Reynolds-averaged Navier-Stokes (RANS) equations with a surface and bottom following σ-coordinate grid in the vertical direction and a Cartesian grid in the horizontal directions. The non-hydrostatic pressure is solved from the Poisson equation with a conjugate gradient method. The model represents the free surface with a single-valued function. Here, the free surface is the upper boundary of the computational domain with appropriate dynamic boundary conditions on normal and tangential stresses at the top and bottom interfaces (Ma et al. (2012)). Though the single-valued approach does not allow for a geometric representation of an overturning wave breaker, this type of model can represent most details in the flow field, including the effects of viscosity and turbulence with less assumptions. Some notable models of this type are NHWAVE (Ma et al. (2012)) and MIKE 3 Flow Model FM (HD) (DHI (2017)). It is reported that such models are able to simulate deepwater waves as well as approximate wave breaking in the surface zone (Ma et al. (2012)).

Instead of using a σ-coordinate grid, Stelling and Duinmeijer (2003a) recommended a Keller-Box scheme (Lam and Simpson (1976)) for the representation of the vertical gradient of the non-hydrostatic pressure, as discussed in section 2.3.2. Based on the continuous development by Stelling and Duinmeijer (2003a), Zijlema and Stelling (2005) and Zijlema and Stelling (2008), Zijlema et al. (2011a) introduced the operational multi-layer non-hydrostatic wave model SWASH. Though the governing equations of SWASH are the non-hydrostatic depth-averaged shallow water equations, the approximation of the vertical gradient of the non-hydrostatic pressure enables the model to represent the flow information in a vertical water column with fewer vertical layers. This essentially gives the model a three-dimensional (3D) representation of the flow field and lets the model simulate waves at a large range of water depth. For example, the model exhibits accurate wave dispersion for up to kd$\approx$16 with only three non-equidistant vertical layers for linear progressive waves (Zijlema et al. (2011a)). With only two layers, the model is still able to represent wave proportion accurately for kd$\leq$3 (Zijlema et al. (2011a)). Wave propagation at deeper water condition can be better represented with more vertical layers. However, it is also noticed that the increase of vertical layers leads to a significant increase in computational costs (Monteban (2016)).

2.3.4 Potential flow wave models

Assuming that water is inviscid and that the water flow is irrotational, the incompressible water flow is considered as potential flow. Mathematically, the particle velocity vector can then be expressed as a gradient of the scalar velocity potential. With this assumption, the mass conservation equation in the Navier-Stokes equation becomes the Laplace equation. The Laplace equation is an elliptic type partial differential equation (PDE) and its solution is a boundary-value problem. Various methods have been designed to solve for the velocity potential from the Laplace equation and they are referred to as potential flow wave models.

Boundary element potential flow wave models

The early development to solve the boundary value problem is the Boundary Element Method (BEM). The use of BEM transforms the elliptic Laplace equations into a boundary integrated equation and significantly reduces the number of unknowns (Li and Fleming (1997)). Grilli et al. (1994) introduced a BEM model for wave shoaling over a slope. Since then, many efforts have been made to model highly non-linear waves. For example, Grilli and Horrillo (1997) demonstrated successful simulations of severe wave shoaling and approximation of wave breaking. After a continuous development, a fully non-linear model for three-dimensional wave propagation over arbitrary bottoms was presented and a severe breaking wave was investigated (Grilli et al. (2001)). In this study, the free surface is represented with a higher-order three-dimensional BEM and a mixed Eulerian-Lagrangian time updating and a 3D approximation of an overturning breaking wave is made((Grilli et al., 2001)). The BEM models are computationally efficient but mathematically demanding. The fully populated unsymmetrical matrix in a BEM model means that it is difficult to implement high-order numerical schemes and parallel computation techniques and thus there are only few attempts to use a BEM model for large-scale wave modelling (Li and Fleming (1997)).

Finite difference potential flow wave models

A solution for the Laplace equation together with the boundary conditions using a finite difference method (FDM) also exists. Li and Fleming (1997) presented a three dimensional fully nonlinear potential flow model with a finite difference method and a multi-grid solver. A σ-coordinate grid is used to place the boundary conditions at the free surface and the bottom precisely even with varying bathymetry (Li and Fleming (1997)). The model is able to simulate nonlinear wave phenomena over the complete range of water depths though it lacks the capability of representing breaking waves. Based on the method, Bingham and Zhang (2007) applied higher-order numerical schemes which further improved the model's ability for representing waves of increasing nonlinearity with increasing accuracy tolerance. In a further development, Engsig-Karup and Bingham (2009) introduced a general purpose flexible order 3D fully nonlinear potential flow (FNPF) model OceanWave3D. The model is capable of simulating different wave transformations over arbitrary bathymetry. In addition, a GPU (Graphic Processing Unit)-accelerated version of OceanWave3D was developed ((Engsig-Karup et al., 2012; Glimberg et al., 2013)), which further improved the computational efficiency of the model. An adaptive curvilinear grid is also introduced in the horizontal plane, which offers flexibility with regards to coastal geometry. However, a more general curvilinear boundary-fitted mesh in the horizontal directions is yet to be implemented for efficiency and flexibility (Engsig-Karup and Bingham (2009); Engsig-Karup et al. (2013)). In order to include the irregular boundaries along the coastlines more efficiently, a novel coastline algorithm is thus introduced to the FDM FNPF model REEF3D::FNPF, of which more details can be found in **Paper 5**.

High-order spectrum wave models

A different technique to solve for the velocity potential is the high-order spectral (HOS) method, where the Laplace equation is solved analytically, so that only the free surface boundary conditions needs to be time-integrated. In addition, the use of Fast Fourier Transform (FFT) further increases the computational efficiency dramatically.

The method was initially develop by West et al. (1987) and Dommermuth and Yue (1987). Following this methodology, several operational HOS models have been developed, such as the HOS-NWT and HOS-Ocean models ((Ducrozet et al., 2012; Bonnefoy et al., 2006a,b)). The models are highly effective for large-scale wave modelling with constant water depth. However, the inclusion of varying bathymetry is an intrinsic challenge for HOS models due to the inherent limitations from the Taylor expansions and that periodic boundary conditions are required in order to efficiently apply FFT ((Fructus et al., 2005)). In spite of the challenges, Gouin et al. (2016) presented an improved method that allow HOS models for wave propagation over varying water depth by considering two different orders of nonlinearity at the bottom and the surface (Guyenne and Nicholls (2008)). In other efforts, a finite difference model based on the HOS method, Whisper3D, was developed ((Raoult et al., 2016; Yates and Benoit, 2015)). Derived from the Laplace equation and boundary conditions, the Zakharov equations (Zakharov (1968)) are solved in Whisper3D and a Chebyshev polynomial is used to represent the vertical velocity potential. The model is also seen to show flexibility with irregular topography and the capability of modelling nonlinear steep waves and approximating breaking waves ((Raoult et al., 2016; Zhang et al., 2019; Simon et al., 2019)). At the current status, an algorithm that allows the inclusion of irregular boundaries in the horizontal plane is yet to be developed, which will make HOS models more applicable for coastal wave modelling.

Spectrum element wave models

The use of spectral element method (SEM) to model hydrodynamic problems is first developed by Patera (1984). Here, the Laplace equation and the boundary conditions are solved on nodal finite elements with Lagrange polynomials. This modelling technique combines some of the best properties of spectral methods and finite element methods and thus obtain high accuracy and flexibility in the spatial representation of domains (Engsig-Karup et al. (2016a)). As a result, the SEM models enable the use of unstructured grids of triangular or arbitrary shape while keeping high-order discretisation schemes (Engsig-Karup et al. (2016a)). One prominent example of the SEM type model is MarineSEM (Engsig-Karup et al. (2016b)), which has been introduced for simulations of dispersive and non-linear waves over varying bottoms as well as wave-structure interactions (Monteserin et al. (2018); Engsig-Karup and Eskilsson (2019)). The MarineSEM model shows great potential for the modelling of complex coastal waves. As stated by Engsig-Karup and Eskilsson (2019), the ongoing work is to extend the model for freely floating structures and to implement the method in C++ to allow for large-scale simulations using high performance computing.

2.3.5 Computational fluid dynamics wave models

The computational fluid dynamics (CFD) models solve the 3D incompressible Reynolds-Averaged Navier-Stokes (RANS) equations for particle velocities and pressure in the fluids. The interface between water and air is tracked or captured using different techniques. After the early development of the marker-and-cell method (MAC) (Harlow and Welch (1965)) method, the currently most commonly used techniques for the free surface are the volume-of-fluid (VOF) method (Hirt and Nichols (1981)) and level-set method (LSM) (Osher and Sethian (1988)). In the VOF method, the interface is captured by a discontinuous fraction function. The cells filled with water phase are assigned values of 1, the cells filled with air phase are assigned with the values 0 and the cells at the interface with mixed water and air are assigned with values in between 0 and 1. This way, the free-surface is not defined sharply, instead it is distributed over the height of a cell. Therefore, large number of cells per wave height are usually needed to capture the free surface sufficiently. Examples of existing VOF CFD models are waves2Foam(Jacobsen et al. (2012)) and IHFOAM (Higuera et al. (2013)) in the OpenFOAM (OpenFOAM (2019)) framework, ReFRESCO(Vaz et al. (2009)) and the commercial software ANSYS-Fluent (OpenFOAM (2019)) and Star CCM+ (Siemens (2019)). In contrast to the VOF method, LSM uses a continuous signed-distance function across the interface and thus requires less number of cells near the free surface for a given accuracy. As an example, REEF3D::CFD (Bihs et al. (2016)) is a CFD model with the LSM free surface capturing technique. Since viscosity and turbulence are inherently included in the governing equations, CFD models provide the most detailed information in the wave field with few assumptions and they are able to simulate complicated highly non-linear free surfaces such as overturning breaking waves (Alagan Chella et al. (2019)). However, this type of model often requires a large number of cells with small time steps for accuracy and thus they tend to be computationally demanding.

2.3.6 Smooth-particle hydrodynamics wave models

In stead of using a computational grid to solve for the flow information, mesh-free methods have also been used for wave modelling. Smooth-particle Hydrodynamics (SPH) (Gingold and Monaghan (1977)) is one of the most used technique to solve the Navier-Stokes equations in Lagrangian form for particle velocities and pressure using a mesh-free method. In the SPH method, the continuum property of the fluid is represented by locally smoothed quantities at discrete Lagrangian locations (Zhang et al. (2018)), and this gives SPH advantages of a straightforward modelling of free surface and complex and moving boundaries in comparison to the mesh-based methods (Altomare et al. (2017)). An open-source SPH model SPHysics (Crespo et al. (2007b,a)) has been developed and tested on various hydrodynamic studies on sloshing, wave breaking and air-entry Gomez-Gesteira et al. (2012b,a). Domnguez et al. (2013) introduced GPU-based computation and Crespo et al. (2015) officially presented the GPU-based parallel version DualSPHysics writer in C++ and CUDA. Altomare et al. (2017) further included various wave generation and absorption algorithms. However, SPH is computationally expensive, a large number of particles are often needed for many hydrodynamics studies (Dickenson (2009)).

2.3.7 Numerical wave model coupling

As discussed, there are various numerical wave modelling techniques, and each has its own advantages and disadvantages. Therefore, it is intuitive to apply a combined usage of different models and utilise the advantages of each model to achieve the best result. This is especially beneficial for studies where both the large-scale wave field and near-field phenomena are important. Several studies have been carried out for the numerical coupling between a computationally demanding, detail-revealing near-field model such as a CFD model or a SPH model with a computationally efficient wave propagation model such as a shallow water model or a potential flow model. There are two main types of coupling: 1) one-way coupling, where the flow information is transferred from one model to another but not vice versa; 2) two-way coupling, where the two wave models exchange flow informations, and thus the flow field from the two coupled models influence each other. Paulsen et al. (2014) used a one-way coupling technique to couple the FDM FNPF model OceanWave3D with the VOF CFD model using the waves2Foam library from OpenFOAM to investigate wave interaction with a surface-piercing circular cylinder. Kim et al. (2010) applied a two-way coupling method for a combined simulation of wave propagation using a BEM potential flow model and a VOF CFD model. Several couplings between other models can also be found, for example, the coupling between a HOS model and a CFD model (Gouin et al. (2018)), the coupling between the Boussinesq model FUNWAVE and the SPH model SPHysics (Narayanaswamy et al. (2010)) and the coupling between the SPH model DualSPHysics and the 3D non-hydrostatic model SWASH (Altomare et al. (2014)). However, various numerical models solve for different flow quantities, store the quantities on different grids and use different discretisation schemes. Therefore, there are no coupling algorithms for a universal application and the optimisation of the interface between models reply on case-based solutions.

2.4 Wave analysis in the Norwegian fjords for the E39 project

Currently, the information of the wave field inside the Norwegian fjords rely on the in-situ measurements. For example, extensive reports of wave measurements in Bjøranfjord and Sulafjord have been reported by DHI (2016) and Fergstad et al. (2018). Wind and wave measurements have also been gradually conducted at multiple fjord-crossing locations in the past years, including Vartdalsfjord, Breisundet, Halsafjord, etc. Some of the measurement data are also made public as can be accessed at `https://thredds.met.no/thredds/catalog/obs/buoy-svv-e39/catalog.html`. Several numerical analyses have also been conducted with the phase-averaged wave model SWAN. Aarnes (2019) performed a comprehensive analysis with SWAN in Bjornafjord. The authors divided the simulation domain so that the simulations do not include strong diffraction. Simulation results obtained from the computational domain before the diffraction are then used as input to the computational domain after the diffraction. This way, the numerical simulation achieved fairly good agreement with the in-situ measurements at most of the investigated locations. However, it is still reported that the SWAN simulation tends to underestimate the H_s inside the fjords. There are few efforts on phase-resolved wave modelling in the Norwegian fjords so far. Wang et al. (2017) used a CFD model to perform phase-resolved numerical simulation at Sulafjord and confirmed that the phase-averaged simulations tend to underestimate the significant wave height. However, the simulation is only for a short duration as the CFD model has high demand on computational resource and computation time. In this thesis, the phase-resolved wave modelling with REEF3D::FNPF in Bjøranfjord and Sulafjord are among the first attempts of such, and the details can be found in **Paper 6**.

2.5 Summary of numerical wave modelling

In summary, there are currently numerous numerical wave models that solve various governing equations for various quantities using various numerical schemes. As a result, these numerical models also have various strengths, validities and practicalities for different scenarios. In the context of coastal wave modelling in Norway, these numerical models also face different challenges. The applicabilities of the EMSE models and SWE based models in the Norwegian coast are limited by the deep water conditions. In spite of the developments that enable Boussinesq models to simulate waves at relatively deep water, it can still be challenging for some scenarios, for example high frequency wind generated waves in great water depth. The irregular coastlines create strong diffraction that may exceed the capacity of spectral wave models. It is also difficult for potential flow models to include the irregular boundaries in the horizontal plane effectively. For computationally demanding numerical models such as the CFD models and SPH models, the large domain of interest in the Norwegian fjords is the main challenge. The 3D non-hydrostatic models present themselves as effective and flexible candidates for coastal wave modelling. However their computational efficiency and compatibility with HPC are still to be explored. The SEM models also show potentials as coastal wave modelling candidates. However the SEM technique is still under development, more computationally efficient codes with new features are expected in the future. The challenges of the various numerical models due to the Norwegian coastal conditions are summarised in Fig. 2.2. These challenges also provide various research opportunities to improve existing approaches for the coastal wave modelling in Norway.

Finally, some of the most commonly used numerical wave models are categorised and summarised in Table. 2.1 as an overview.

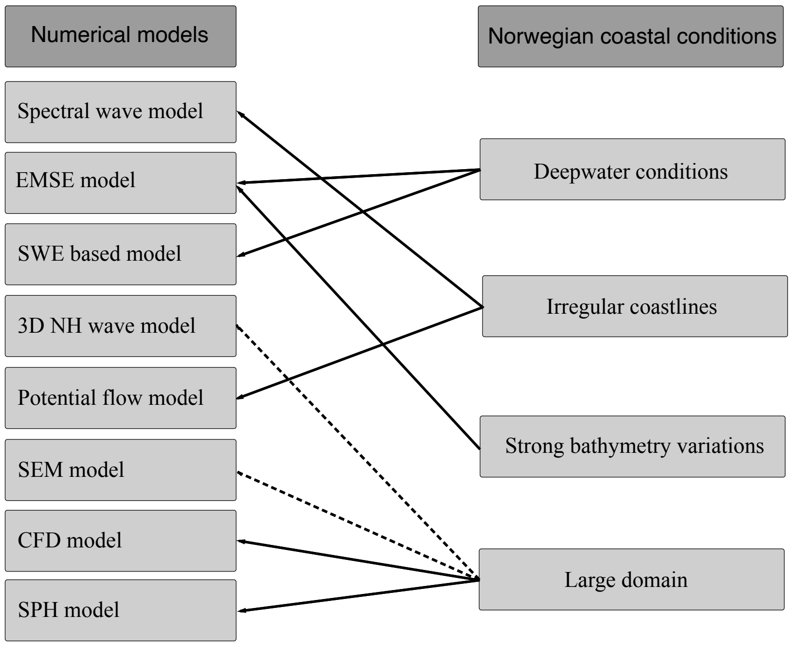

Figure 2.2: The wave modelling techniques and their respective challenges for the coastal wave modelling in Norway. The dashed lines indicate that these challenges may be solved with further developments.

Model	Spectral wave model	EMSE model	SWE based models		3D NH model	SPH models
Results	Phase-averaged	Phase-resolved	Phase-resolved		Phase-resolved	Phase-resolved
Dimension	2D	2D	2D		3D	3D
Technique	Wave action balance	EMSE	Boussinesq	NH	NH	SPH
Examples	SWAN WAM MIKE SW STWAVE	CGWAVE	MIKE BW FUNWAVE COULWAVE	REEF3D::SFLOW SWASH (one-layer)	SWASH NHWAVE MIKE 3 HD	SPHysics DualSPHysics
Model	Potential flow model				CFD model	
Results	Phase-resolved				Phase-resolved	
Dimension	3D				3D	
Technique	BEM	FDM	HOS	SEM	VOF	LSM
Examples	((Grilli et al., 2001))	OceanWave3D REEF3D::FNPF	HOS-NWT HOS-OCEAN Whisper3D	MarineSEM	OpenFOAM ANSYS-Fluent Star CCM+ ReFRESCO	REEF3D::CFD

Table 2.1: Overview of some recognized numerical wave models

Chapter 3

Present Numerical Models

3.1 REEF3D

In the current study, REEF3D is the main tool for the research and all numerical models are developed within this framework. REEF3D was developed as an open-source CFD code before the Ph.D. study. High-order spatial and temporal schemes are used for discretisation, the fully parallelized BiCGStab algorithm of the HYPRE library (van der Vorst (1992)) is used to provide the solution for pressure from the Poisson equation, a Message Passing Interface (MPI) and ghost cell based approach enables parallel computations with multi-core hardware. The source code of REEF3D is available at http://www.reef3d.com and is published under the GPL license, version 3. REEF3D is written in an object-oriented C++ structure which enables a modular design. This led to the development of several extensions of the main code for a large range of applications. For example, overturning breaking waves and their interactions with various structures were investigated using REEF3D by Alagan Chella et al. (2019) and Aggarwal et al. (2019), the morphological module in REEF3D was used to simulate the scouring process around piles (Ahmad et al. (2018)), the environmental module was adapted for vegetation and coastal protection (Arunakumar et al. (2019)), a six degree-of-freedom (DOF) floating algorithm was introduced in REEF3D by Bihs and Kamath (2017) and a mooring model based on finite elements (Martin et al. (2019)) was added which improves the capabilities of the model for the simulation of moored-floating structures in waves (Martin et al. (2018)).

With several new implementations during the Ph.D. period, REEF3D has evolved into an open-source hydrodynamics framework. Currently REEF3D is consisted of four models: the CFD model REEF3D::CFD that solves the Navier-Stokes equation (Bihs et al. (2016)), the shallow water equations model REEF3D::SFLOW (Wang et al. (2020)) that solves the depth-averaged shallow water equation with a quadratic non-hydrostatic pressure profile (introduced in **Paper 1**), the fully non-linear potential flow model REEF3D::FNPF (Bihs et al. (2020)) that solves the Laplace equation (introduced in **Paper 2**) and the three-dimensional non-hydrostatic Navier-Stokes solver REEF3D::NSEWAVE (Bihs et al. (2018)). The first three models are included in the thesis, the development of these models and the corresponding papers are summarised in Fig. 3.1. Among these three models, REEF3D::CFD is inherited from the original REEF3D code while REEF3D::SFLOW and REEF3D::FNPF are developed during the Ph.D. study in search for a solution for the wave modelling in the Norwegian fjords for the E39 project. In this section, the key numerical schemes and algorithms of these models are described.

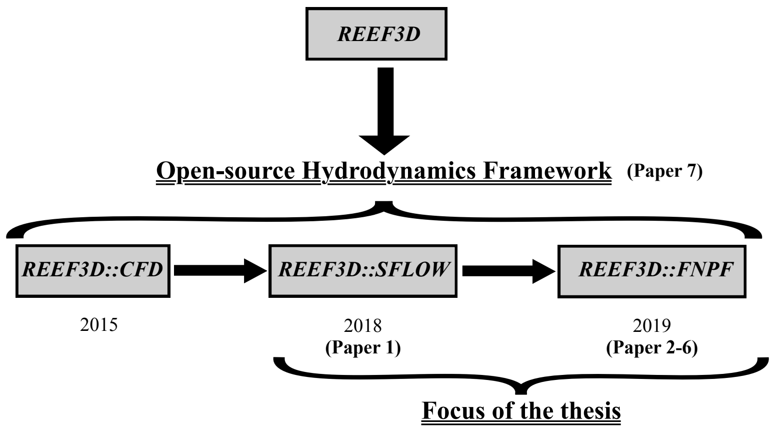

Figure 3.1: Numerical model development and the associated publications.

3.2 REEF3D::CFD

3.2.1 Governing equations

Mass and momentum are conserved for an incompressible fluid by solving the continuity and Reynolds-averaged Navier-Stokes (RANS) equations

$$\frac{\partial u_i}{\partial x_i} = 0, \tag{3.1}$$

$$\frac{\partial u_i}{\partial t} + u_j \frac{\partial u_i}{\partial x_j} = -\frac{1}{\rho}\frac{\partial p}{\partial x_i} + \frac{\partial}{\partial x_j}\left[(\nu + \nu_t)\left(\frac{\partial u_i}{\partial x_j} + \frac{\partial u_j}{\partial x_i}\right)\right] + g_i, \tag{3.2}$$

with u_i the velocity vector, ρ the fluid density, p the pressure, ν and ν_t the kinematic and turbulent viscosity, and g_i the gravity acceleration vector.

The Boussinesq hypothesis is used to calculate ν_t from the turbulent kinetic energy k and its specific rate of dissipation ω according to

$$\nu_t = \frac{k}{\omega}. \tag{3.3}$$

In REEF3D::CFD, the two-equations k-ω turbulence model (Wilcox (1988)) is applied to propagate the turbulence properties in space and time. Wall functions are taken into account to approximate the boundary layer flow. A limiter for ν_t is introduced to account for eventual overproduction of turbulence in highly strained flows outside the boundary layer (Durbin (2009)):

$$\nu_t = \min\left(\frac{k}{\omega}, \sqrt{\frac{2}{3}}\frac{k}{|\mathbf{S}|}\right) \tag{3.4}$$

Special attention is paid to the correct turbulence modelling near the free surface as the turbulent length scales in the water are reduced in its proximity. Standard two-phase RANS turbulence models do not account for this which can lead to increased ω and damped fluctuations normal to the surface as they are redistributed to the ones parallel to the interface. Additionally, standard RANS turbulence closure will incorrectly predict the maximum turbulence intensity at the free surface because the mean rate of strain $\mathbf{S}$ can be large especially in the vicinity of the interface between water and air (Kamath et al. (2019)). A more realistic representation of the free surface effect on the turbulence can be achieved through the replacement of the original equation for ω in the vicinity of the surface by the empirical formula (Naot and Rodi (1982); Kamath et al. (2019)):

$$\omega_s = \frac{c_\mu^{-0.25}}{\kappa} k^{0.5}\left(\frac{1}{y'} + \frac{1}{y^*}\right), \tag{3.5}$$

with $c_\mu = 0.07$ and $\kappa = 0.4$. The virtual origin of the turbulent length scale y' is empirically found to be 0.07 times the mean water depth (Hossain and Rodi (1980)). y^* is the distance from the nearest wall. Hence, a smooth transition from the free surface value to the wall boundary value of ω is ensured.

3.2.2 Free surface representation

The location of the free surface is represented implicitly by the zero level set of a smooth signed distance function ϕ which can be expressed with the Eikonal equation $|\nabla\phi| = 1$. The simple advection equation

$$\frac{\partial \phi}{\partial t} + u_j \frac{\partial \phi}{\partial x_j} = 0, \tag{3.6}$$

is applied for propagating the function in space and time. The level set function has to be reinitialized regularly in order to keep its signed distance property. The PDE-based reinitialization algorithm by Sussman et al. (1994) is executed after each time step. By solving

$$\frac{\partial \phi}{\partial \tau} + S(\phi)\left(\left|\frac{\partial \phi}{\partial x_j}\right| - 1\right) = 0, \tag{3.7}$$

with $\Delta\tau$ being an artificial time step, the original properties of ϕ can be retained. $S(\phi)$ is the smoothed sign function Peng et al. (1999).

The material properties of the two phases are determined for the whole domain in accordance with the continuum surface force model of Brackbill et al. (1992). The properties are defined at any location in the domain as

$$\rho_i = \rho_w H(\phi_i) + \rho_a(1 - H(\phi_i)), \tag{3.8}$$
$$\nu_i = \nu_w H(\phi_i) + \nu_a(1 - H(\phi_i)), \tag{3.9}$$

with w indicating water and a air properties. H is the smoothed Heaviside step function

$$H(\phi_i) = \begin{cases} 0 & if\ \phi_i < -\epsilon \\ \frac{1}{2}\left(1 + \frac{\phi}{\epsilon} + \frac{1}{\pi}\sin\left(\frac{\pi\phi_i}{\epsilon}\right)\right) & if\ |\phi_i| \leq \epsilon \\ 1 & if\ \phi_i > \epsilon, \end{cases} \tag{3.10}$$

Typically, the thickness of the smoothed out interface is chosen to be $\epsilon = 2.1\Delta x$ on both sides of the interface. The density is generally determined directly at the cell faces in order to avoid spurious oscillations at the interface (see Bihs et al. (2016) for details).

3.2.3 Numerical schemes

The numerical discretisation of the governing equations is achieved using finite difference methods on rectilinear grids. The coupling of pressure and velocity during the solution of (3.2) is ensured by employing a staggered grid. A fifth-order accurate weighted essentially non-oscillatory (WENO) scheme (Jiang and Shu (1996)) adapted to non-uniform cell sizes is applied for the convection terms. In (3.6), the convection term is discretised by the fifth-order accurate Hamilton-Jacobi WENO method of Jiang and Peng (2000). Diffusion terms are discretised using second-order accurate central finite differences.

The solution process follows the projection method for incompressible flows of Chorin (1968). In the predictor step, the conservation equation for momentum (3.2) is solved without considering the pressure gradients

$$\frac{u_i^{(*)} - u_i^{(n)}}{\Delta t} = -u_j \frac{\partial u_i}{\partial x_j} + \frac{\partial}{\partial x_j}\left(\nu \cdot \left(\frac{\partial u_i}{\partial x_j} + \frac{\partial u_j}{\partial x_i}\right)\right) + g_i. \tag{3.11}$$

Thus, an intermediate velocity field $u_i^{(*)}$ is obtained. Here, the time derivatives are solved by applying the third-order accurate Total Variation Diminishing (TVD) Runge-Kutta scheme (Shu and Osher (1988)). The same time discretisation is also used in (3.6) and (3.7). Turbulence time advancement is solved using implicit methods due to its source term driven character. The general time-stepping is controlled adaptively under consideration of the CFL condition (see Bihs et al. (2016)). Diffusion terms are treated implicitly to overcome their restrictions on this condition. The insertion of the predicted velocities into the continuity equation leads to the Poisson equation

$$\frac{\partial}{\partial x_i}\left(\frac{1}{\rho(\widehat{\phi}^{n+1})}\frac{\partial p^{(n+1)}}{\partial x_i}\right) = \frac{1}{\Delta t}\frac{\partial u_i^{(*)}}{\partial x_i}. \tag{3.12}$$

for the pressure of the new time step. It is solved by the fully parallelized BiCGStab algorithm of the HYPRE library (van der Vorst (1992)) with the geometric multigrid PFMG pre-conditioner (Ashby and Flagout (1996)) to enhance the performance. As the final step, the divergence-free velocity field of the new time step is obtained following

$$u_i^{(n+1)} = u_i^{(*)} - \frac{\Delta t}{\rho(\widehat{\phi}^{n+1})}\frac{\partial p^{(n+1)}}{\partial x_i}. \tag{3.13}$$

High-performance computations are enabled in REEF3D::CFD by applying the Message Passing Interface (MPI) and ghost cells as the parallelisation strategy. Three layers of ghost cells are added to each sub-domain as required by the fifth-order accurate WENO scheme. Similarly, the directional ghost cell immersed boundary method (GCIBM) of Berthelsen and Faltinsen (2008) is implemented to handle complex solid geometries. Here, the domain is virtually extended into the geometry, and the values at these ghost cells are found through extrapolation and under consideration of the wall boundary condition. Thus, the numerical discretisation of the fluid domain does not need to account for the boundary conditions explicitly. Instead, they are incorporated implicitly. Simple geometries such as boxes, cylinders or prisms can be generated directly through user input. Otherwise, STL files can be generated. Then a level set function, with the zero level set representing the solid boundary, is generated using a ray-tracing algorithm as presented in Yang and Stern (2013), see above. In the same way, natural bathymetries can be incorporated in a straight forward manner.

3.2.4 Wave generation and absorption

Typical inlet boundary conditions for free surface flow applications are of Dirichlet type. When generating waves at the inlet, the free surface is in constant motion and the flow direction is changing periodically. As a result, simple Dirichlet type wave generation does not necessarily deliver waves of the highest quality. In REEF3D, waves are generated with the relaxation method, which is presented in Mayer et al. (1998) and extended for CFD models in Jacobsen et al. (2012). Here, the wave generation takes place in a relaxation zone with a typical size of one wavelength.

The values for the velocities and the free surface are ramped up from the computational values to the values obtained from wave theory (Eq. (3.14)). The waves are generated without any disturbances occurring at the interface. In addition, reflected waves that travel back towards the inlet are absorbed with this method. At the outlet of a wave flume, the waves need to be dissipated in order to avoid reflections that can negatively impact the numerical results. This can also be achieved with the relaxation method. In the numerical beach relaxation zone, the computational values for the horizontal and vertical velocities are smoothly reduced to zero, the free surface to the still water level and the pressure is relaxed to the hydrostatic distribution for the still water level. Thus, the wave energy is effectively absorbed and reflections are prevented.

$$
\begin{aligned}
u(\widetilde{x})_{relaxed} &= \Gamma(\widetilde{x})u_{analytical} + (1-\Gamma(\widetilde{x}))u_{computational} \\
w(\widetilde{x})_{relaxed} &= \Gamma(\widetilde{x})w_{analytical} + (1-\Gamma(\widetilde{x}))w_{computational} \\
p(\widetilde{x})_{relaxed} &= \Gamma(\widetilde{x})p_{analytical} + (1-\Gamma(\widetilde{x}))p_{computational} \\
\phi(\widetilde{x})_{relaxed} &= \Gamma(\widetilde{x})\phi_{analytical} + (1-\Gamma(\widetilde{x}))\phi_{computational}
\end{aligned}
\tag{3.14}
$$

The relaxation function presented in Jacobsen et al. (2012) is used. The wave generation zone has the length of one wavelength, the numerical beach extends over two wavelengths.

$$
\Gamma(\widetilde{x}) = 1 - \frac{e^{(\widetilde{x}^{3.5})} - 1}{e-1} \; for \; \widetilde{x} \in [0;1]
\tag{3.15}
$$

The coordinate $\widetilde{x}$ is scaled to the length of the relaxation zone. Several wave theories are implemented in REEF3D: linear waves, $2nd$-order and $5th$-order Stokes waves, $1st$-order and $5th$-order cnoidal waves, $1st$-order and $5th$-order solitary waves and first and second-order irregular and focused waves. As an example, the equations used in the case of linear waves for general water depths, the horizontal and vertical velocities u and w and the level set function ϕ for the free surface location are prescribed over the water domain in the model as:

$$
\begin{aligned}
u(x,z,t)_{analytical} &= \frac{\pi H}{T}\frac{cosh\left[k\left(z+d\right)\right]}{sinh\left(kd\right)}cos\theta \\
w(x,z,t)_{analytical} &= \frac{\pi H}{T}\frac{sinh\left[k\left(z+d\right)\right]}{sinh\left(kd\right)}sin\theta \\
\phi(x,z,t)_{analytical} &= \frac{H}{2}cos\theta - z + d
\end{aligned}
\tag{3.16}
$$

The wave number k and the wave phase θ are defined as follows:

$$
\begin{aligned}
k &= \frac{2\pi}{L} \\
\theta &= kx - \omega t
\end{aligned}
\tag{3.17}
$$

where H is the wave height, L the wavelength, T the wave period, ω the angular wave frequency and z the vertical coordinate with the origin at the still water level d. In the wave generation zone, the pressure is not prescribed in the current numerical model, in order not to over define the boundary conditions. At the numerical beach, the pressure is always set to its hydrostatic values based on the still water level d, independent of the wave input.

In order to generate higher order waves, the equations for velocities and the free surface are calculated in the wave generation zone using the relevant wave theories such as the $2nd$-order Stokes wave theory Dean and Dalrymple (1991), the $5th$-order Stokes theory Fenton (1985), the $5th$-order cnoidal wave theory Fenton (1999) and $3rd$-order solitary wave theory Grimshaw (1971), to name a few. The classification of waves based on the wave height, wave period and water depth given by Le Méhauté Le Méhauté (1976) is used to determine the wave theory to generate the desired wave type. In this way, the relaxation method employs different wave theories to generate different waves based on the wave type selected by the user.

In addition, wavemaker motions of piston type and flap type (Dean and Dalrymple (1991)) can also be used for wave generation in REEF3D. A wave reconstruction method is also introduced, especially for irregular wave generation, as described by Aggarwal et al. (2018).

3.3 REEF3D::SFLOW

3.3.1 Governing equations

The mass and momentum conservation for an incompressible inviscid flow leads to the continuity and Euler equations in three dimensions:

$$\frac{\partial U}{\partial x} + \frac{\partial V}{\partial y} + \frac{\partial W}{\partial z} = 0, \tag{3.18}$$

$$\frac{\partial U}{\partial t} + U\frac{\partial U}{\partial x} + V\frac{\partial U}{\partial y} + W\frac{\partial U}{\partial z} = -\frac{1}{\rho}\frac{\partial P_T}{\partial x}, \tag{3.19}$$

$$\frac{\partial V}{\partial t} + U\frac{\partial V}{\partial x} + V\frac{\partial V}{\partial y} + W\frac{\partial V}{\partial z} = -\frac{1}{\rho}\frac{\partial P_T}{\partial y}, \tag{3.20}$$

$$\frac{\partial W}{\partial t} + U\frac{\partial W}{\partial x} + V\frac{\partial W}{\partial y} + W\frac{\partial W}{\partial z} = -\frac{1}{\rho}\frac{\partial P_T}{\partial z} - g. \tag{3.21}$$

where U, V and W are velocities in x, y and z directions, ρ is the constant density, P_T represents the total pressure and g is the gravitational acceleration. Additional source terms such as bottom friction and turbulent stresses are omitted here but are straightforward to include if needed.

The water depth $h = d + \zeta$ consists of two parts: the still water depth d and the free-surface elevation ζ, as displayed in Fig. 3.2. Defining the horizontal velocity vector as $\boldsymbol{U} = (U, V)$, the kinematic boundary conditions at the free-surface and the bottom are:

$$W|_{\zeta} = \frac{\partial \zeta}{\partial t} + \boldsymbol{U}|_{\zeta} \cdot \nabla\zeta, \tag{3.22}$$

$$W|_{-d} = -\boldsymbol{U}|_{-d} \cdot \nabla d. \tag{3.23}$$

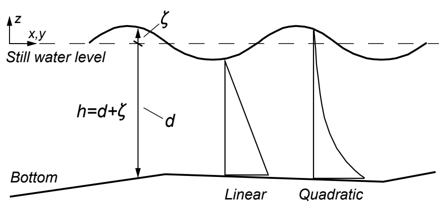

Figure 3.2: Basic definitions in the shallow water model: the water depth h, the still water depth d, the free-surface elevation ζ, the coordinates system and the schematics of the assumed linear pressure profile and quadratic pressure approximation

The shallow water assumption, i.e. the horizontal acceleration is much greater than the vertical acceleration, implies a hydrostatic pressure. In order to get a hydrodynamic pressure correction, the total pressure P_T is assumed to consist of a hydrostatic part P and a hydrodynamic part Q. The pressure and its boundary condition at the free-surface is given by:

$$P_T = P + Q = \rho g(\zeta - z) + Q, \tag{3.24}$$

$$P_T|_\zeta = P|_\zeta = Q|_\zeta = 0. \tag{3.25}$$

The velocities and the dynamic pressure are depth-averaged by integrating over the water depth:

$$\boldsymbol{u} = (u, v) = \frac{1}{h}\int_{-d}^{\zeta} \boldsymbol{U}\,\mathrm{d}\,z; \quad w = \frac{1}{h}\int_{-d}^{\zeta} W\,\mathrm{d}\,z; \quad q = \frac{1}{h}\int_{-d}^{\zeta} Q\,\mathrm{d}\,z \tag{3.26}$$

In contrast to previous models (Zijlema et al. (2011b)), where the dynamic pressure is solved at the bottom, the proposed model consists of only depth-averaged quantities. A relation between the depth-averaged pressure q and the pressure at the bottom $Q|_{-d}$ needs to be defined in order to close the system. If the linear pressure profile (Stelling and Duinmeijer (2003a); Zijlema et al. (2011b)) is assumed, the pressure at the bottom is simply twice the depth-averaged pressure, or:

$$Q|_{-d} = 2q. \tag{3.27}$$

Consequently, the governing equations with only depth-averaged variables are:

$$\frac{\partial \zeta}{\partial t} + \frac{\partial hu}{\partial x} + \frac{\partial hv}{\partial y} = 0, \tag{3.28}$$

$$\frac{\partial u}{\partial t} + u\frac{\partial u}{\partial x} + v\frac{\partial u}{\partial y} = -g\frac{\partial \zeta}{\partial x} - \frac{1}{\rho h}\left(\frac{\partial hq}{\partial x} - 2q\frac{\partial d}{\partial x}\right), \tag{3.29}$$

$$\frac{\partial v}{\partial t} + u\frac{\partial v}{\partial x} + v\frac{\partial v}{\partial y} = -g\frac{\partial \zeta}{\partial y} - \frac{1}{\rho h}\left(\frac{\partial hq}{\partial y} - 2q\frac{\partial d}{\partial y}\right), \tag{3.30}$$

$$\frac{\partial w}{\partial t} + u\frac{\partial w}{\partial x} + v\frac{\partial w}{\partial y} = -\frac{2q}{\rho h}. \tag{3.31}$$

Jeschke et al. (2017) replaces the linear assumption with a quadratic vertical pressure profile as shown in Eqn. (3.32).

$$Q|_{-d} = \frac{3}{2}q + \frac{1}{4}\rho h\Phi, \tag{3.32}$$

$$\Phi = -\nabla d \cdot (\partial_t \boldsymbol{u} + (\boldsymbol{u}\cdot\nabla)\boldsymbol{u}) - \boldsymbol{u}\cdot\nabla(\nabla d)\cdot\boldsymbol{u}. \tag{3.33}$$

Following the quadratic assumption, the governing equations with depth-averaged variables become:

$$\frac{\partial \zeta}{\partial t} + \frac{\partial hu}{\partial x} + \frac{\partial hv}{\partial y} = 0, \tag{3.34}$$

$$\frac{\partial u}{\partial t} + u\frac{\partial u}{\partial x} + v\frac{\partial u}{\partial y} = -g\frac{\partial \zeta}{\partial x} - \frac{1}{\rho h}\left(\frac{\partial hq}{\partial x} - \left(\frac{3}{2}q + \frac{1}{4}\rho h\Phi\right)\frac{\partial d}{\partial x}\right), \tag{3.35}$$

$$\frac{\partial v}{\partial t} + u\frac{\partial v}{\partial x} + v\frac{\partial v}{\partial y} = -g\frac{\partial \zeta}{\partial y} - \frac{1}{\rho h}\left(\frac{\partial hq}{\partial y} - \left(\frac{3}{2}q + \frac{1}{4}\rho h\Phi\right)\frac{\partial d}{\partial y}\right), \tag{3.36}$$

$$\frac{\partial w}{\partial t} + u\frac{\partial w}{\partial x} + v\frac{\partial w}{\partial y} = \frac{1}{\rho h}\left(\frac{3}{2}q + \frac{1}{4}\rho h\Phi\right). \tag{3.37}$$

3.3.2 Numerical schemes

The governing equations with the boundary conditions are solved on a structured staggered grid using a finite difference method (FDM). Chorin's projection method (Chorin (1968)) is applied for the solution of the velocities. The 5^{th}-order conservative finite difference Weighted-Essentially-Non-Oscillatory (WENO) scheme proposed by Jiang and Shu (1996) is used for the discretisation of convective terms for the velocities u,v and w. The Total-Variation-Diminishing (TVD) 3^{rd}-order Runge-Kutta explicit time scheme developed by Shu and Osher (1988) is employed for time discretisation. It involves the calculation of the spatial derivatives and the dynamics pressure three times per time step. The information containing the pressure is solved using the Poisson equation:

$$\frac{h_p}{\rho}\left(\frac{\partial^2 q}{\partial x^2}+\frac{\partial^2 q}{\partial y^2}\right)+\frac{2q}{\rho h_p}=\frac{1}{\partial x \partial t}\left(-h_p\left(\frac{\partial u}{\partial x}+\frac{\partial v}{\partial y}\right)-2w-u\frac{\partial d}{\partial x}-v\frac{\partial d}{\partial y}\right) \tag{3.38}$$

Here, the parameter h_p denotes the water level in the centre of the cell. In a staggered grid arrangement, this is where the dynamic pressure q, the vertical velocities w and the free surface location ζ are solved. The horizontal velocities are solved at the faces of the cells. The high-performance solver library HYPRE (hypre (2015)) is employed to solve the Poisson pressure equation using the PFMG-preconditioned BiCGStab algorithm (Ashby and Flagout (1996)). The dynamic pressure q is then used to correct the velocities in a correction step. Hence, the corrections of the velocities with the quadratic pressure approximation are

$$u^{n+1}=u^*+\Delta t\left(\frac{3}{2}\frac{q^{n+1}}{\rho h_p}\frac{\partial d}{\partial x}+\frac{1}{4}\Phi\frac{\partial d}{\partial x}\right), \tag{3.39}$$

$$v^{n+1}=v^*+\Delta t\left(\frac{3}{2}\frac{q^{n+1}}{\rho h_p}\frac{\partial d}{\partial y}+\frac{1}{4}\Phi\frac{\partial d}{\partial y}\right), \tag{3.40}$$

$$w^{n+1}=w^*+\Delta t\left(\frac{3}{2}\frac{q^{n+1}}{\rho h_p}+\frac{1}{4}\Phi\right). \tag{3.41}$$

where u^*, v^*, w^* are intermediate-step velocities with only hydrostatic pressure.

The term Φ on the right-hand side of Eqn. (3.35) to Eqn. (3.37) is treated with a procedure following the principles of the fractional step method of Le and Moin (1991). Assuming the dynamic pressure does not change significantly within one Runge-Kutta sub-step, the intermediate velocities u^*, v^*, w^* are corrected with the dynamic pressure gradients of the previous sub-step:

$$u^{**}=u^*-\frac{\partial q^{n,rk}}{\partial x}, \tag{3.42}$$

$$v^{**}=v^*-\frac{\partial q^{n,rk}}{\partial y}, \tag{3.43}$$

$$w^{**}=w^*-\frac{\partial q^{n,rk}}{\partial z}, \tag{3.44}$$

where $q^{n,rk}$ is the dynamic pressure from the previous Runge-Kutta sub-step. The spatial derivatives of Φ are updated with the corrected velocities u^{**}, v^{**} and w^{**} in equation Eqn. 3.33, which is then inserted into Eqn. (3.39) to Eqn. (3.41) to obtain the velocities at the new time step. The time derivative term inside Φ is then calculated with simple finite differences:

$$\partial_t \boldsymbol{u} = \frac{u^{**} - u^{n,rk}}{\alpha \Delta t}, \tag{3.45}$$

$$\partial_t \boldsymbol{v} = \frac{v^{**} - v^{n,rk}}{\alpha \Delta t}, \tag{3.46}$$

$$\partial_t \boldsymbol{w} = \frac{w^{**} - w^{n,rk}}{\alpha \Delta t}, \tag{3.47}$$

$$\tag{3.48}$$

where α is the increment factor of the corresponding Runge-Kutta sub-step and $u^{n,rk}, v^{n,rk}, w^{n,rk}$ are the velocities from the previous Runge-Kutta sub-step.

The location of the free-surface ζ is determined based on the divergence of the depth-integrated horizontal velocities as given in Eqn. (3.34). The free-surface is reconstructed using the 5^{th}-order WENO scheme (Jiang and Shu (1996)). The solutions of the stencils are weighted, i.e. a coefficient or weight is assigned to the solution of each stencil. The scheme assigns the largest weight to the smoothest solution and can therefore handle large-gradient free-surface changes caused by the varying bathymetry. As an example, the discretised form of Eqn. (3.34) in x-direction is presented in Eqn. (3.49).

$$\frac{\zeta_i^{n+1} - \zeta_i^n}{\triangle t} + \frac{\widehat{h}_{i+1/2}^n u_{i+1/2}^{n+1/2} - \widehat{h}_{i-1/2}^n u_{i-1/2}^{n+1/2}}{\triangle x} = 0, \tag{3.49}$$

where $\widehat{h}_{i+1/2}$ is the water level at the cell face $i + 1/2$. $\widehat{h}_{i+1/2}$ is reconstructed with the WENO procedure:

$$\widehat{h}_{i+1/2}^{\pm} = \omega_1^{\pm} \widehat{h}_{i+1/2}^{1\pm} + \omega_2^{\pm} \widehat{h}_{i+1/2}^{2\pm} + \omega_3^{\pm} \widehat{h}_{i+1/2}^{3\pm}. \tag{3.50}$$

The $\pm$ sign indicates the upwind direction. The nonlinear weights $\omega_n^{\pm}$ are calculated for each ENO stencil based on the smoothness indicators (Jiang and Shu (1996)). For the upwind direction in the positive i-direction, the three possible ENO stencils $\widehat{h}^1$, $\widehat{h}^2$ and $\widehat{h}^3$ are:

$$\widehat{h}_{i+1/2}^{1-} = \frac{1}{3} h_{i-2} - \frac{7}{6} h_{i-1} + \frac{11}{6} h_i, \tag{3.51}$$

$$\widehat{h}_{i+1/2}^{2-} = -\frac{1}{6} h_{i-1} + \frac{5}{6} h_i + \frac{1}{3} h_{i+1}, \tag{3.52}$$

$$\widehat{h}_{i+1/2}^{3-} = \frac{1}{3} h_i + \frac{5}{6} h_{i+1} - \frac{1}{6} h_{i+2}. \tag{3.53}$$

3.3.3 Wave generation and absorption

Wave generation and absorption are carried out with the relaxation method as described in Bihs et al. (2016) and section 3.2.4. Here, the depth-averaged horizontal velocities u, v, the surface elevation ζ and the pressure p are increased to the analytical values in the wave generation zone and reduced to zero or initial still wave values in the wave energy dissipation zone following the relaxation function. All types of wave theories as well as wavemaker inputs in REEF3D::CFD code are also applicable to the shallow water model as well.

3.3.4 Breaking wave algorithm

A breaking wave criterion is introduced (SWASH developers (2017)) to represent the wave breaking process. The wave breaking is initialised when the vertical velocity of the free-surface exceeds a fraction of the shallow water celerity:

$$\frac{\partial \zeta}{\partial t} > \alpha \sqrt{gh}. \tag{3.54}$$

At the same time, the dynamic pressure is neglected and remains so at the front of the breaker. For the persistence of the wave breaking, the coefficient β $(0 < \beta < \alpha)$ is introduced in Eqn. (3.84) instead of α to stop the wave breaking process. The computations become non-hydrostatic again when the vertical velocity of the free-surface falls out of the range of the criterium. $\alpha = 0.6$ and $\beta = 0.3$ are recommended as they work well with most of the waves (SWASH developers (2017)). By introducing the wave breaking criterion and removing the dynamic pressure during breaking, the momentum is well conserved, the energy dissipation is well represented and the asymmetry and skewness of non-linearity are respected (SWASH developers (2017)).

3.3.5 Wetting-drying algorithm

Wetting and drying are handled by setting the velocities in cells below a certain user-defined threshold of the water level to zero:

$$\begin{cases} u = 0, & if\ \widehat{h}_x < threshold, \\ v = 0, & if\ \widehat{h}_y < threshold. \end{cases} \tag{3.55}$$

The default threshold is set to be 0.00005 m, which is used throughout the presented work. The approach tracks the variation of the shoreline accurately and avoids numerical instabilities by ensuring non-negative water depth (Stelling and Duinmeijer (2003b); Zijlema and Stelling (2008)).

3.4 REEF3D::FNPF

3.4.1 Governing equations

The governing equation for the proposed fully nonlinear potential flow model is the Laplace equation:

$$\frac{\partial^2 \phi}{\partial x^2} + \frac{\partial^2 \phi}{\partial y^2} + \frac{\partial^2 \phi}{\partial z^2} = 0. \tag{3.56}$$

Boundary conditions are required in order to solve for the velocity potential ϕ from this elliptic equation, specifically at the free surface and at the bed. The fluid particles at the free surface should remain at the surface where the pressure in the fluid should be equal to the atmospheric pressure. These conditions must be fulfilled at all times and they form the kinematic and dynamic boundary conditions at the free surface respectively:

$$\frac{\partial \eta}{\partial t} = -\frac{\partial \eta}{\partial x}\frac{\partial \widetilde{\phi}}{\partial x} - \frac{\partial \eta}{\partial y}\frac{\partial \widetilde{\phi}}{\partial y} + \widetilde{w}\left(1 + \left(\frac{\partial \eta}{\partial x}\right)^2 + \left(\frac{\partial \eta}{\partial y}\right)^2\right), \tag{3.57}$$

$$\frac{\partial \widetilde{\phi}}{\partial t} = -\frac{1}{2}\left(\left(\frac{\partial \widetilde{\phi}}{\partial x}\right)^2 + \left(\frac{\partial \widetilde{\phi}}{\partial y}\right)^2 - \widetilde{w}^2\left(1 + \left(\frac{\partial \eta}{\partial x}\right)^2 + \left(\frac{\partial \eta}{\partial y}\right)^2\right)\right) - g\eta. \tag{3.58}$$

where η is the free surface elevation, $\widetilde{\phi} = \phi(\mathbf{x}, \eta, t)$ is the velocity potential at the free surface, $\mathbf{x} = (x, y)$ represents the location at the horizontal plane and $\widetilde{w}$ is the vertical velocity at the free surface.

At the bottom, the component of the velocity normal to the boundary must be zero at all times since the fluid particle cannot penetrate the solid boundary. This gives the bottom boundary condition:

$$\frac{\partial \phi}{\partial z} + \frac{\partial h}{\partial x}\frac{\partial \phi}{\partial x} + \frac{\partial h}{\partial y}\frac{\partial \phi}{\partial y} = 0, \quad z = -h. \tag{3.59}$$

where $h = h(\mathbf{x})$ is the water depth measured from the still water level to the seabed.

The Laplace equation, together with the boundary conditions are solved on a σ-coordinate system. The σ-coordinate system follows the water depth changes and offers flexibility for irregular boundaries. The transformation from a Cartesian grid to a σ-coordinate is expressed as follows:

$$\sigma = \frac{z + h(\mathbf{x})}{\eta(\mathbf{x}, t) + h(\mathbf{x})}. \tag{3.60}$$

The velocity potential after the σ-coordinate transformation is denoted as Φ. The boundary conditions and the governing equation in the σ-coordinate are then written in the following format:

$$\Phi = \widetilde{\phi} \qquad , \sigma = 1; \tag{3.61}$$

$$\begin{aligned} &\frac{\partial^2 \Phi}{\partial x^2} + \frac{\partial^2 \Phi}{\partial y^2} + \left(\frac{\partial^2 \sigma}{\partial x^2} + \frac{\partial^2 \sigma}{\partial y^2}\right)\frac{\partial \Phi}{\partial \sigma} + 2\left(\frac{\partial \sigma}{\partial x}\frac{\partial}{\partial x}\left(\frac{\partial \Phi}{\partial \sigma}\right) + \right. \\ &\left.\frac{\partial \sigma}{\partial y}\frac{\partial}{\partial y}\left(\frac{\partial \Phi}{\partial \sigma}\right)\right) + \left(\left(\frac{\partial \sigma}{\partial x}\right)^2 + \left(\frac{\partial \sigma}{\partial y}\right)^2 + \left(\frac{\partial \sigma}{\partial z}\right)^2\right)\frac{\partial^2 \Phi}{\partial \sigma^2} = 0 \quad , 0 \leq \sigma < 1; \end{aligned} \tag{3.62}$$

$$\left(\frac{\partial \sigma}{\partial z} + \frac{\partial h}{\partial x}\frac{\partial \sigma}{\partial x} + \frac{\partial h}{\partial y}\frac{\partial \sigma}{\partial y}\right)\frac{\partial \Phi}{\partial \sigma} + \frac{\partial h}{\partial x}\frac{\partial \Phi}{\partial x} + \frac{\partial h}{\partial y}\frac{\partial \Phi}{\partial y} = 0 \qquad , \sigma = 0. \tag{3.63}$$

Once the velocity potential Φ is obtained in the σ-domain, the velocities can be calculated as follows:

$$u(\mathbf{x}, z) = \frac{\partial \Phi(\mathbf{x}, z)}{\partial x} = \frac{\partial \Phi(\mathbf{x}, \sigma)}{\partial x} + \frac{\partial \sigma}{\partial x}\frac{\partial \Phi(\mathbf{x}, \sigma)}{\partial \sigma}, \tag{3.64}$$

$$v(\mathbf{x}, z) = \frac{\partial \Phi(\mathbf{x}, z)}{\partial y} = \frac{\partial \Phi(\mathbf{x}, \sigma)}{\partial y} + \frac{\partial \sigma}{\partial y}\frac{\partial \Phi(\mathbf{x}, \sigma)}{\partial \sigma}, \tag{3.65}$$

$$w(\mathbf{x}, z) = \frac{\partial \Phi(\mathbf{x}, z)}{\partial z} = \frac{\partial \sigma}{\partial z}\frac{\partial \Phi(\mathbf{x}, \sigma)}{\partial \sigma}. \tag{3.66}$$

3.4.2 Numerical schemes

The Laplace equation is discretized using second-order central differences and solved using a parallelized geometric multigrid preconditioned conjugated gradient solver provided by Hypre (van der Vorst (1992)).

The gradient terms of the free-surface boundary conditions are discretized with the $5th$-order Hamilton-Jacobi version of the weighted essentially non-oscillatory (WENO) scheme (Jiang and Shu (1996)). The WENO stencil consists of three local essentially non-oscillatory (ENO)-stencils based on the smoothness indicators IS (Jiang and Shu (1996)). A large IS means a non-smooth solution in a local stencil. The scheme is designed such that the local stencil with the highest smoothness (smallest IS) is assigned the largest weight ω_i and therefore contributes the most significantly. In this way, the scheme is able to handle large gradients up to shock with good accuracy. The WENO approximation for Φ is a convex combination of the three possible ENO approximations. For example, in the x-direction, the discretisation is formulated as the following:

$$\Phi_x^{\pm} = \omega_1^{\pm}\Phi_x^{1\pm} + \omega_2^{\pm}\Phi_x^{2\pm} + \omega_3^{\pm}\Phi_x^{3\pm}. \tag{3.67}$$

The three stencils are defined as:

$$\begin{aligned}
\Phi_x^{\pm} &= \frac{1}{3}q_1^{\pm} - \frac{7}{6}q_2^{\pm} + \frac{11}{6}q_3^{\pm}, \\
\Phi_x^{\pm} &= -\frac{1}{6}q_2^{\pm} + \frac{5}{6}q_3^{\pm} + \frac{1}{3}q_4^{\pm}, \\
\Phi_x^{\pm} &= \frac{1}{3}q_3^{\pm} + \frac{5}{6}q_4^{\pm} - \frac{1}{6}q_5^{\pm}.
\end{aligned} \tag{3.68}$$

with

$$\begin{aligned}
q_1^- &= \frac{\Phi_{i-2} - \Phi_{i-3}}{\Delta x}, q_2^- = \frac{\Phi_{i-1} - \Phi_{i-2}}{\Delta x}, q_3^- = \frac{\Phi_i - \Phi_{i-1}}{\Delta x}, \\
q_4^- &= \frac{\Phi_{i+1} - \Phi_i}{\Delta x}, q_5^- = \frac{\Phi_{i+2} - \Phi_{i+1}}{\Delta x}
\end{aligned} \tag{3.69}$$

and

$$\begin{aligned}
q_1^+ &= \frac{\Phi_{i+3} - \Phi_{i+2}}{\Delta x}, q_2^+ = \frac{\Phi_{i+2} - \Phi_{i+1}}{\Delta x}, q_3^+ = \frac{\Phi_{i+1} - \Phi_i}{\Delta x}, \\
q_4^+ &= \frac{\Phi_i - \Phi_{i-1}}{\Delta x}, q_5^+ = \frac{\Phi_{i-1} - \Phi_{i-2}}{\Delta x}
\end{aligned} \tag{3.70}$$

The weights are written as

$$\omega_1^{\pm} = \frac{\alpha_1^{\pm}}{\alpha_1^{\pm} + \alpha_2^{\pm} + \alpha_3^{\pm}}, \omega_2^{\pm} = \frac{\alpha_2^{\pm}}{\alpha_1^{\pm} + \alpha_2^{\pm} + \alpha_3^{\pm}}, \omega_3^{\pm} = \frac{\alpha_3^{\pm}}{\alpha_1^{\pm} + \alpha_2^{\pm} + \alpha_3^{\pm}} \tag{3.71}$$

and

$$\alpha_1^{\pm} = \frac{1}{10}\frac{1}{\left(\widetilde{e} + IS_1^{\pm}\right)^2}, \alpha_2^{\pm} = \frac{6}{10}\frac{1}{\left(\widetilde{e} + IS_2^{\pm}\right)^2}, \alpha_3^{\pm} = \frac{3}{10}\frac{1}{\left(\widetilde{e} + IS_3^{\pm}\right)^2} \tag{3.72}$$

with the regularisation parameter $\widetilde{e} = 10^{-6}$ and the following smoothness indicators:

$$\begin{aligned}
IS_1^{\pm} &= \frac{13}{12}\left(q_1 - 2q_2 + q_3\right)^2 + \frac{1}{4}\left(q_1 - 4q_2 + 3q_3\right)^2, \\
IS_2^{\pm} &= \frac{13}{12}\left(q_2 - 2q_3 + q_4\right)^2 + \frac{1}{4}\left(q_2 - q_4\right)^2, \\
IS_3^{\pm} &= \frac{13}{12}\left(q_3 - 2q_4 + q_5\right)^2 + \frac{1}{4}\left(3q_3 - 4q_4 + q_5\right)^2,
\end{aligned} \tag{3.73}$$

For time treatment, a $3rd$-order accurate total variation diminishing (TVD) Runge-Kutta scheme (Shu and Osher (1988)) is used. Adaptive time stepping is used by controlling a constant time factor as an equivalence to the Courant-Friedrichs-Lewy (CFL) condition:

$$\begin{aligned}
c_u &= \frac{dx}{\left|max(u_{max}, 1.0\sqrt{9.81 * h_{max}})\right|}, \\
c_v &= \frac{dx}{\left|max(v_{max}, 1.0\sqrt{9.81 * h_{max}})\right|}, \\
c_{tot} &= min(c_u, c_v), \\
dt &= c_{tot} CFL.
\end{aligned} \tag{3.74}$$

where u_{max}, v_{max} are the maximum particle velocities in x and y directions at the free surface, h_{max} is the maximum water depth.

The model is fully parallelised following the domain decomposition strategy where ghost cells are used to exchange information between adjacent domains. These ghost cells are updated with the values from the neighbouring processors via Message Passing Interface (MPI). The parallel computation enables the model to simulate large-scale scenarios.

3.4.3 Vertical grid arrangement

In the model, the vertical coordinates follow a stretching function so that the grid becomes denser close to the free surface:

$$\sigma_i = \frac{\sinh\left(-\alpha\right) - \sinh\left(\alpha\left(\frac{i}{N_z} - 1\right)\right)}{\sinh\left(-\alpha\right)}, \tag{3.75}$$

where α is the stretching factor and i and N_z stand for the index of the grid point and the total number of cells in the vertical direction.

Th vertical stretching further reduces the computational cost. A correct arrangement of the stretching is important to an accurate representation of the dispersion relation and phase information for deep water waves. In order to chose an appropriate vertical grid arrangement for a correct representation of the phase information, a constant-truncation error method is introduced.

As an example, a general description of a progressive Airy wave can be expressed as:

$$\eta(x, z, t) = A(z)B(z)\Gamma(t). \tag{3.76}$$

And function A(z) follows:

$$A(z) = Ce^{kz}. \tag{3.77}$$

Which is governed only by the wave number k, which can be defined by the linear dispersion relationship to the wave angular frequency:

$$\omega^2 = gk. \tag{3.78}$$

where g is the gravity acceleration.

A correct representation of the phase velocity depends on the correct representation of the wave number. This is especially true for deep water where the dispersion relation is very important. The new method is based on the assumption that a constant absolute truncation error at every vertical location can preserve the correct shape of the function $f(z)$ and yield the correct wave number. Function $f(z)$ is a Taylor expansion of free surface over the depth:

$$\begin{aligned} f(z) =& f(\eta) + \frac{df(\eta)}{dz}(z-\eta) + \frac{1}{2}\frac{d^2 f(\eta)}{dz^2}(z-\eta)^2 + \frac{1}{6}\frac{d^3 f(\eta)}{dz^3}(z-\eta)^3 \\ &+ \frac{1}{24}\frac{d^4 f(\eta)}{dz^4}(z-\eta)^4 + O((z-\eta)^5) \end{aligned} \tag{3.79}$$

If the absolute error is set to a constant E for every vertical location and the function$f(z)$ and its derivatives are known, one can find a maximum cell size $\Delta z(\eta) = z - \eta$ at every location (Pakozdi et al. (2019b)):

$$E(z, \eta) = f(z) - \left(f(\eta) + \frac{df(\eta)}{dz}(z-\eta) + \frac{1}{2}\frac{d^2 f(\eta)}{dz^2}(z-\eta)^2 \right) \tag{3.80}$$

$$0 = E - f(\eta + \Delta z) + \left(f(\eta) + \frac{df(\eta)}{dz}(z-\eta) + \frac{1}{2}\frac{d^2 f(\eta)}{dz^2}(z-\eta)^2 \right) \tag{3.81}$$

3.4.4 Wave generation and absorption

The relaxation method for wave generation and absorption as described in section 3.2.4 are also used in REEF3D::FNPF. Here, the free surface velocities potential $\widetilde{\phi}$ and the surface elevation η are increased to theoretical values in the wave generation zone and reduced to zero or initial still water values in the wave energy dissipation zone.

Waves can also be generated at the inlet using a Neumann boundary condition where the spatial derivatives of the velocity potential are defined. In this way, the velocity potential at the boundary is calculated using the desired analytical horizontal velocity:

$$\phi_{i-1} = -u(\boldsymbol{x}, z, t)\triangle x + \phi_i. \tag{3.82}$$

where $u(\boldsymbol{x}, z, t)$ is the analytical horizontal velocity.

All types of wave theories and wavemaker inputs available in REEF3D::CFD and REEF3D::SFLOW are applicable to the potential flow model as well.

3.4.5 Breaking wave algorithm

In the presented potential flow model, the free surface is represented by a single value, therefore it is not possible for the model to represent an over-turning breaker as in a CFD simulation (Bihs et al. (2016)). However, a correct detection of wave breaking events and energy dissipation can be achieved with an effective breaking wave algorithm. The proposed model aims to address both steepness-induced deep water wave breaking and depth-induced shallow water breaking.

The depth-induced shallow water wave breaking criterion is the same as deployed in REEF3D::SFLOW. A wave breaking is initialised when the vertical velocity of the free-surface exceeds a fraction of the shallow water celerity (SWASH developers (2017)):

$$\frac{\partial \eta}{\partial t} \geq \alpha_s \sqrt{gh}. \tag{3.83}$$

$\alpha_s = 0.6$ is recommended as it works well with most of the waves (SWASH developers (2017)).

Deepwater steepness-induced breaking is initialised with a steepness criterion:

$$\frac{\partial \eta}{\partial x_i} \geq \beta. \tag{3.84}$$

After a wave breaking is detected, two methods are available to represent the energy dissipation during the wave breaking process. The first method is a geometric filtering algorithm that smoothens the free surface for energy dissipation (Jensen et al. (1999)). Here, an explicit scheme is used and therefore there is no CFL constraint. Another method is to introduce a viscous damping term in the free surface boundary conditions locally around the breaking region (Baquet et al. (2017)). When wave breaking is detected, the free surface boundary conditions Eqn. 3.57 and Eqn. 3.58 then become:

$$\frac{\partial \eta}{\partial t} = -\frac{\partial \eta}{\partial x}\frac{\partial \widetilde{\phi}}{\partial x} - \frac{\partial \eta}{\partial y}\frac{\partial \widetilde{\phi}}{\partial y} + \widetilde{w}\left(1 + \left(\frac{\partial \eta}{\partial x}\right)^2 + \left(\frac{\partial \eta}{\partial y}\right)^2\right) + \nu_b\left(\frac{\partial^2 \eta}{\partial x^2} + \frac{\partial^2 \eta}{\partial y^2}\right), \quad (3.85)$$

$$\begin{aligned}\frac{\partial \widetilde{\phi}}{\partial t} =& -\frac{1}{2}\left(\left(\frac{\partial \widetilde{\phi}}{\partial x}\right)^2 + \left(\frac{\partial \widetilde{\phi}}{\partial y}\right)^2 - \widetilde{w}^2\left(1 + \left(\frac{\partial \eta}{\partial x}\right)^2 + \left(\frac{\partial \eta}{\partial y}\right)^2\right)\right) \\ & - g\eta + \nu_b\left(\frac{\partial^2 \widetilde{\phi}}{\partial x^2} + \frac{\partial^2 \widetilde{\phi}}{\partial y^2}\right).\end{aligned} \quad (3.86)$$

where ν_b is the artificial turbulence viscosity. ν_b is calibrated from the comparison of the potential flow model simulations with model test data and the CFD simulations. As a result, the value of ν_b is recommended to be 1.86 (Baquet et al. (2017)) for the offshore deep water conditions and 0.0055 for shallow water breaking in the proposed model. In the new free surface boundary conditions Eqn. 3.85 and Eqn. 3.86, the newly introduced diffusion term is treated with an implicit time scheme while the rest of the terms are treated with explicit time schemes. This way, there is no extra constraint on time step sizes.

The two wave breaking methods can also be used in combination for challenging wave breaking scenarios. In this manuscript, the combination of the two methods is used for shallow water breaking for a sufficient energy dissipation at very shallow areas and swash zones in the simulations of the large-scale engineering scenarios.

3.4.6 Coastline algorithm

Handling the complex coastline has been a challenge when applying a potential flow model in the coastal area. The first difficulty is an efficient grid generation around the complex boundaries. The curvilinear grid presented in OceanWave3D (Engsig-Karup and Bingham (2009)) provides one solution. However, the generation of a curvilinear grid is difficult and time consuming when complex coastlines are present. The second difficulty is possible numerical instability during the wave run-up process in the swash zone. The derivatives of velocity potential over the water depth in Eqn. 3.62 indicate a possible numerical instability when the water depth becomes infinitesimal. In order to address these two difficulties, an efficient and flexibility coastline algorithm is introduced.

First, the computational cells are identified as wet cells and dry cells following a relative-depth criterion. The local water depth h is defined as a sum of still water level d and the free surface elevation η:

$$h = \eta + d \tag{3.87}$$

η is the surface elevation, d is the still water level measured from the bottom. The relationship among h, d and η is illustrated in Fig. 3.3.

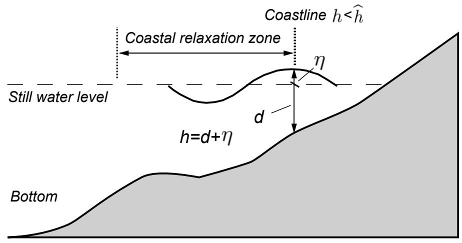

Figure 3.3: Illustration of the still water level h, local water depth d, free surface elevation η and coastline detection algorithm.

If the local water depth h is smaller than a threshold $\widehat{h}$, then the local cell is identified as a dry cell:

$$\begin{cases} u = 0, & if\ h < \widehat{h}, \\ v = 0, & if\ h < \widehat{h}. \end{cases} \tag{3.88}$$

When a cell is identified as a dry cell, the velocities in the cell is set to be zero. The default threshold is set to be 0.00005 m, however it can be customised based on the specific conditions.

After the wet and dry cells are identified, the wet cells are assigned with a value +1 and the dry cells are assigned with a value −1. With the signed initial values, the coastline is captured using a two-dimensional level-set function (Osher and Sethian (1988)):

$$\phi(\vec{x}, t) \begin{cases} > 0\ if\ \vec{x} \in wet\ cell \\ = 0\ if\ \vec{x} \in \Gamma \\ < 0\ if\ \vec{x} \in dry\ cell \end{cases} \tag{3.89}$$

Γ indicates the coastline, and the Eikonal equation $|\nabla \phi| = 1$ holds valid in the level-set function. The distance perpendicular to the coastline is also calculated based on the level-set method. From the initial values, the correct signed distance function is obtained by solving the following Partial Differential Equation (PDE) based reinitialisation function (Sussman et al. (1994)). This equation is solved until convergence and results in the correct signed distance away from the coastline in the whole computational domain. The excact coastline location is the zero-contour of the level set function.

$$\frac{\partial \phi}{\partial t} + S\left(\phi\right)\left(\left|\frac{\partial \phi}{\partial x_j}\right| - 1\right) = 0 \tag{3.90}$$

where $S(\phi)$ is the smoothed sign function (Peng et al. (1999)).

Using this level-set method, the computational grid remains a uniform structured grid in the horizontal plane even though complex topography is included in the computational domain. Therefore, the coastline is accurately captured without extra efforts and costs on the grid generation. This also gives the model great flexibility, as there is no need to generate a new set of grid every time there is a change in the topography. Thus, the model is able to simulate all kinds of topography with a straightforward, efficient and consistent grid generation.

Relaxation zones are applied along the the wet side of the coastline covering a given distance from the coastline. This way, the extreme run-ups are avoided and therefore numerical instabilities in the free surface boundary conditions at extreme shallow regions are eliminated. In addition, the reflection property of the coastline can be customised by adjusting the strength or size of the coastal relaxation zones.

Chapter 4

Summary of Major Results

The major results from the research are summarised as a collection of excerpts from the journal papers produced during the course of the Ph.D. study. The new numerical models developed during the study are introduced in **Paper 1** and **Paper 2**, where the numerical details of the models are described, verification and validation are performed and the numerical performances are evaluated. The performance of REEF3D::SFLOW is found to be limited by water depth conditions and thus REEF3D::FNPF is considered to be a more suitable solution for the task of deep water wave propagation. In **Paper 3**, REEF3D::FNPF is used to investigate rogue wave evolution for the extreme design condition of the floating bridges. It is found that an increasing nonlinearity delays the wave focusing point dramatically using the current wave focusing techniques. Several other parameters are also discussed, such as the wave directional spreading properties. In **Paper 4**, REEF3D::FNPF is used to study irregular wave propagation over three hours for the operational conditions of the floating bridges. A working procedure for reproducing a high-quality irregular wave field is introduced and the importance of wave crest distribution as an evaluation criterion is stressed. In **Paper 5**, a novel coastline algorithm is introduced to REEF3D::FNPF that makes the inclusion of complicated shorelines straightforward and versatile. The new algorithm solves the difficulty in shoreline treatment in the potential flow modelling approach and its effectiveness is validated from a series of test cases. It is concluded that REEF3D::FNPF with its coastline algorithm is the solution for wave modelling in the Norwegian condition. Therefore, full-scale wave simulations in Sulafjord and Bjørnafjord are performed in **Paper 6** with REEF3D::FNPF. The studies confirm the computational efficiency and several detailed findings on the wave fields are discussed. Finally, in **Paper 7**, the different wave models within the REEF3D framework are compared in an objective manner to evaluate their features and suggestions for their field of application are given. The workflow and the topics of the papers can be seen to in Fig. 1.5. The locations of the large-scale wave simulations at the Norwegian coast in **Paper 5** and **Paper 6** are summarised in Fig. 4.1, including the harbour at Mehamn, the fish farm site near Flatøya and Sulafjord and Bjørnafjord along the E39 coastal highway.

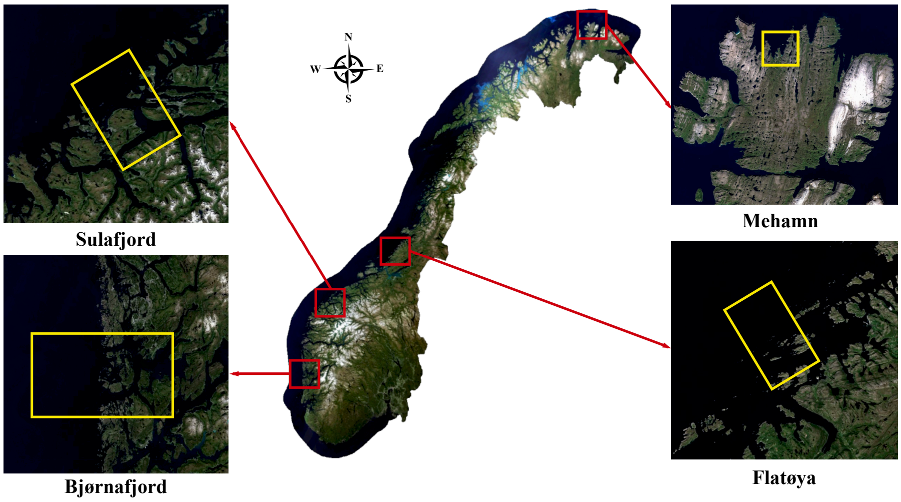

Figure 4.1: Locations of the engineering applications presented in the thesis.

4.1 REEF3D::SFLOW model description and applications

4.1.1 Paper 1: An improved depth-averaged non-hydrostatic shallow water model with quadratic pressure approximation

It is challenging for depth-averaged shallow water wave models to represent deepwater dispersion relation without sacrificing numerical performance. Jeschke et al. (2017) proposed a quadratic vertical pressure profile that enables the shallow water models to achieve at least a good equivalence to existing fully non-linear weakly dispersive Boussinesq models. This method presents itself as an attractive alternative for modelling shallow water waves, while potentially avoiding the numerical instabilities due to higher-order terms in a Boussinesq-type model and the increased computational costs from a larger number of vertical layers in a multi-layer non-hydrostatic model. Following the quadratic pressure profile assumption, REEF3D::SFLOW is developed as an improved numerical model that discretises the depth-related terms appropriately in the original equation set from Jeschke et al. (2017). The 5th-order WENO scheme (Jiang and Shu (1996)) is used for the convective terms and the Total-Variation-Diminishing (TVD) 3rd-order Runge-Kutta explicit time scheme developed by Shu and Osher (1988) is used for the temporal discretisation. Wetting and drying is handled by setting the velocities in cells below a certain user-defined threshold of the water level to zero (Stelling and Duinmeijer (2003b); Zijlema and Stelling (2008)). A breaking wave criterion is introduced (SWASH developers (2017)) to represent the wave breaking process. The wave breaking is initialised when the vertical velocity of the free-surface exceeds a fraction of the shallow water celerity. During the wave breaking, the dynamic pressure is neglected and remains so at the front of the breaker. Parallel computation is enabled by domain decomposition. The message passing interface (MPI) is then used for the communication at the sub-domain boundaries. The accuracy gain from the quadratic pressure approximation for non-constant bathymetry and overall numerical performance are the main results from the study.

- The model demonstrates great computational scalability.

The model's scaling capacity is investigated by conducting a series of simulations for 500 time step iterations with the number of processors being 16, 32, 64, 128, 256 and 512 on the supercomputer Vilje. The dimension of the computational domain is (10000 m $\times$ 1000 m $\times$ 10 m). The input wave is a 2nd-order Stokes wave of wave height $H = 5$ m and wavelength $L = 100$ m. A cell size of $dx = 1$ m is used, resulting in 10 million cells in total. It is empirically assumed that the scaling is linear within 16 processors, i.e. one physical node on the cluster. Therefore, the computation time with one processor is linearly extrapolated from the 16-processor simulation. The computational speed of the one-processor simulation is considered as the base reference. The simulation time on one processor divided by the simulation time on multiple processors is defined as a speed-up factor. The relation between the speed-up factor and the number of processors as well as the number of cells per processor are plotted in Fig. 4.2. It shows that the performance increases almost linearly with the number of processors within the chosen range.

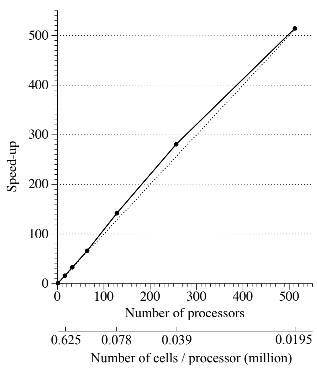

Figure 4.2: The performance of the parallel computation, shown as a relation between the speed-up factor in reference to the single-processor simulation for 500 iterations versus the number of processors and the number of cells per processor

- The model is able to represent energy loss during wave breaking correctly.

The numerical wave tank is initialised based on the experiments in (Ting and Kirby (1994, 1996)) to model a breaking wave scenario. The wave tank has a total length of 40 m. A wave generation zone of 9.8 m is located at the inlet of the tank; a wave energy dissipation zone of the same length is arranged at the outlet. An inclined bed with a slope of 1:35 is located 4 m away from the wave generation zone.

The obstacle increases to 0.748 m at the right end of the tank. The water depth is constant at 0.4 m. Wave gauges 1-4 are located on the slope, 10 m, 11 m, 12 m and 12.3 m away from the wave generation zone respectively. A 5^{th}-order cnoidal wave with wave height $H = 0.128$ m and wave period $T = 5$ s is generated in this simulation, which is supposed to result in a plunging breaker on the slope according to the experiment. A simulation time of 40 s is used.

The simulated wave elevations at different wave gauges with $dx = 0.005$ m are compared to the experimental data in Fig. 4.3. The simulated free surfaces agree with the experimental measurements at all wave gauges. Especially the wave height decrease from wave gauge 2 to wave gauge 3 is accurately captured, indicating a correct energy loss during the wave breaking. Further examination shows that the breaking height of $h_b = 0.208$ m is measured at $x = 21.580$ m in the simulation. In the experiment, the breaking point is detected at $x = 21.595$ m and a breaking height of $h_b = 0.196$ m is measured. Both, the predicted breaking point and the breaking wave height are very close to that in the experiment.

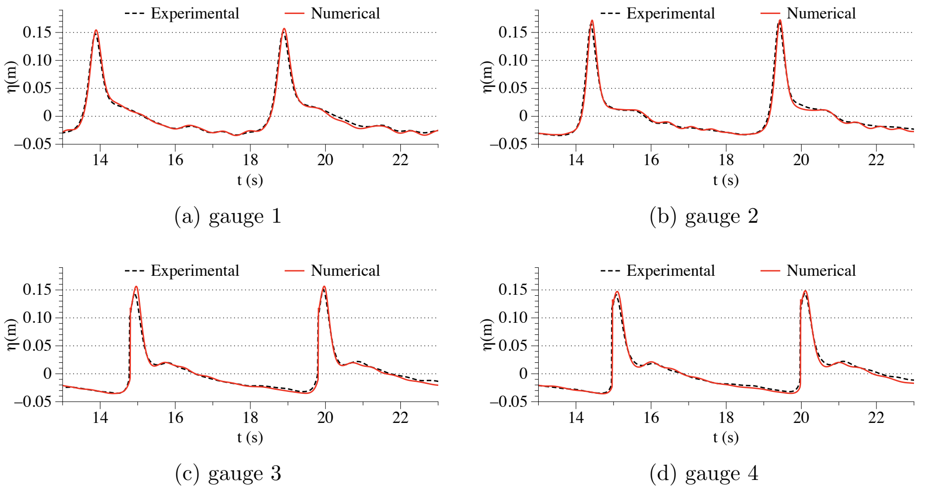

(a) gauge 1

(b) gauge 2

(c) gauge 3

(d) gauge 4

Figure 4.3: Wave surface elevations of wave breaking over a sloping bed. The input wave is a 5^{th}-order cnoidal wave with a wave height of $H = 0.128$ m and a wave period of $T = 5$ s. The cell size is $dx = 0.005$ m and $CFL = 0.2$ is used. Black dashed lines are from laboratory experiments, red solid lines are results from REEF3D::SFLOW.

- The model represents wave shoaling and decomposition over an irregular bottom correctly. However, the limitation of the model regarding water depth is exposed during the wave decomposition process.

The well-known benchmark case of wave propagation over a submerged bar (Beji and Battjes (1993)) is tested. A 2D wave tank of 38 m is equipped with a wave generation zone of 5 m and a wave energy dissipation zone of 9.5 m at the end. The beginning of the submerged bar is located 6 m downstream from the wave generation zone. Eight wave gauges are located above the submerged bar with the x-coordinates being 11 m, 16 m, 17 m, 18 m, 19 m, 20 m, 21 m and 22 m. The incident wave height is $H = 0.021$ m, and the wave period is $T = 2.525$ s. A cell size of $dx = 0.02$ m is found to sufficiently represent the phenomena and shows good agreement with the experimental data. A simulation time of 60 s is used. The time series of free surface at wave gauges 3, 4, 7 and 8 are shown in Fig. 4.4

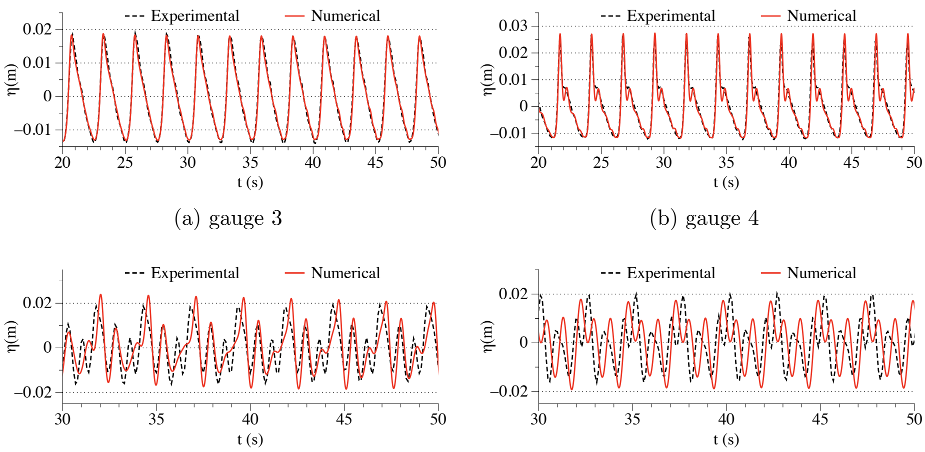

(a) gauge 3

(b) gauge 4

(c) gauge 7

(d) gauge 8

Figure 4.4: The surface elevations of the wave transformation over a submerged bar. Black lines are from laboratory experiments, red lines are results of REEF3D::SFLOW. The cell size $dx = 0.02$ m and $CFL = 0.2$.

The good agreement between the simulation and experiment at wave gauge 3 and 4 shows the model's capacity to capture wave shoaling and decomposition. However, during the de-shoaling process at wave gauges 7 and 8, higher frequency harmonics with shorter wave lengths appear. These emerging short waves are exposed to a deep water condition which exceeds the validity of the model.

- The model demonstrate its ability for large-scale wave modelling

A simulation of swell propagation into Mehamn harbour in the north of Norway is performed. The computational domain is 10.5 km in the east-west direction and 14 km in the north-south direction, with the deepest water depth being 147.5 m. The site is exposed to swell from the open sea. An estimated regular wave of height $H = 4.5$ m and period $T = 15$ s is generated at the northern boundary. The wetting and drying scheme over the complex bathymetry is included. A cell size of 5 m is used in the simulation, resulting in 5.88 million cells. The simulation of wave propagation in Mehamn harbour takes about 4.2 hours for 1000 s simulation time

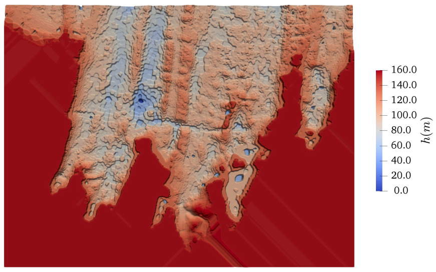

(a)

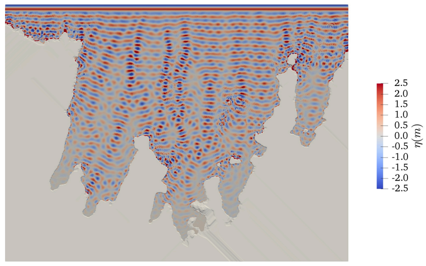

(b)

Figure 4.5: The wave propagation towards the Mehamn harbour in the numerical simulation with a 2^{nd}-order Stokes wave of wave height $H = 4.5$ m and wave period $T = 15$ s. The cell size is $dx = 5.0$ m and $CFL = 0.2$ is used. (a) The topography in the simulation; (b) The surface elevation at simulation time $t = 650$ s.

with 256 cores on the Vilje supercomputer. The free surface elevation at the end of the simulation is shown in Fig. 4.5.

In conclusion, the accuracy gain from the quadratic pressure approximation and the high-order discretisation schemes in REEF3D enable the model to simulate a large range of wave transformations including wave breaking with great numerical performance. However, the improvement of the quadratic pressure approximation does not enable the model to simulate deepwater waves as in the Norwegian fjords.

4.2 REEF3D::FNPF model description

4.2.1 Paper 2: REEF3D::FNPF - a flexible fully nonlinear potential flow solver

Potential flow theory based wave models are not limited by water depth. The development of a fully non-linear potential flow model REEF3D::FNPF is described in the paper. The model solves the Laplace equation tougher with the kinematic and dynamics free surface boundary conditions and bottom boundary condition on a σ-coordinate grid. The grid follows the variation of the bottom topography and the evolution of free surface. It offers great flexibility regarding varying bathymetry. A stretching function is used in the vertical direction that enables a refined vertical grid closer to the free surface. The 5th-order WENO scheme (Jiang and Shu (1996)) and TVD 3^{rd}-order Runge-Kutta scheme Shu and Osher (1988) is used at the free surface boundary conditions. Parallel computation is made possible using the domain decomposition strategy with MPI.

- The model is able to represent the complex free surface and wave transformations without water depth limits.

The wave propagation over a submerged bar (Beji and Battjes (1993)) is tested. The 2D wave tank of 35 m is equipped with a wave generation zone of one wavelength 3.73 m long at the inlet and a numerical beach of two wavelengths 8.73 m at the outlet. The still water level is 0.4 m. The submerged bar begins at $x = 6$ m and elevates following a slope of $1 : 20$ until it reaches the top platform at $x = 12$ m, with a height of 0.3 m. It remains at a height for 2 m before it starts a downwards slope of $1 : 10$ and reaches the bottom of the tank at $x = 17$ m. Nine wave gauges are located at $x = 4.0$ m, 10.5 m, 12.5 m, 13.5 m, 14.5 m, 15.7 m, 17.3 m, 19.0 m and 21.0 m. The incident wave height is $H = 0.02$ m and the wavelength is $L = 3.73$ m. Similar to the study with REEF3D::SFLOW, the surface elevations at wave gauges 3, 4, 7 and 8 in the simulation are compared to the experiment in Fig. 4.6.

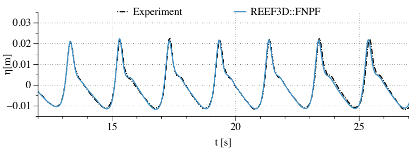

(a) wave gauge 3 at $x = 12.5$ m

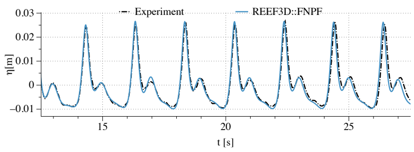

(b) wave gauge 3 at $x = 13.5$ m

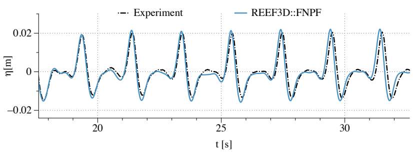

(c) wave gauge 3 at $x = 17.3$ m

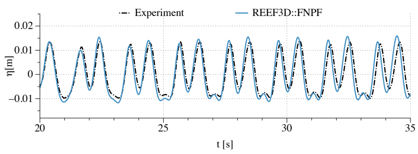

(d) wave gauge 3 at $x = 19.0$ m

Figure 4.6: The comparison between the simulated time series and the experimental measurements at wave gauges 3, 4, 7 and 8 with the grid resolution $L/dx = 212$ in the numerical wave tank for the wave propagation over a submerged bar.

It is seen that good agreement is achieved at all wave gauges, indicating a good representation of wave shoaling, decomposition and de-shoaling. Especially after the de-shoaling, the emerging short waves are well represented in the deep water condition.

- The model demonstrates high computational efficiency even for three-hour irregular wave simulations.

The advantage of the potential flow solver is more prominent for long-duration simulations for obtaining statistical properties of a sea state. The proposed potential flow model is used to simulate a three-hour irregular sea state at intermediate water depth. The input spectrum is a JONSWAP spectrum with a peak enhancement factor of 3.0. The input wave has a significant wave height of $H_s = 4.5$ m, and peak period of $T_p = 12.0$ s. A constant water depth of 40 m is used. The two-dimensional wave tank is 1760 m long, corresponding to 8 wavelengths based on the peak period. The frequency range of $[0.75\omega_p, 2\omega_p]$ is used. The frequency limits represent the wave energy from 0.5% of the total energy to 99.5% of the total energy. Therefore, the chosen frequency range represents 99% of the total wave energy. 30 vertical cells are used with vertical stretching in the σ-coordinate system. The horizontal resolution is 30 cells per wave length corresponding to the shortest wave with the highest frequency. The configuration results in a horizontal cell size of 2 m. The total number of cells is 26400. The simulation time is 12800 s, where the three-hour window from 2000 s to 12800 s is used for the data analysis. The wave elevation at the wave probe located five wave lengths (using the peak period) away is investigated for the chosen time window. The simulated spectrum is compared with the theoretical spectrum in Fig. 4.7. With 16 cores on supercomputer Vilje, the 12800 s simulation takes only 1.13 hour, which is three times faster than real time. The calculated significant wave height in the numerical wave tank is 4.456 m, the peak period is 11.95 s. With a compensation of 1% wave energy, the significant wave height becomes 4.50 m, exactly the same as the input value. The simulated irregular wave match the input H_s, T_p and the shape of the spectrum with high accuracy. In the current setup, the simulation is faster that real time, showing a very high computational efficiency of the model.

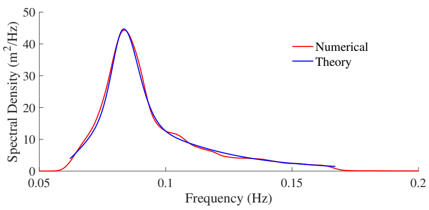

Figure 4.7: Simulated wave spectrum in comparison to the theoretical spectrum for the three-hour irregular wave simulation.

4.3 REEF3D::FNPF applications for deepwater conditions

4.3.1 Paper 3: Investigation of focusing wave properties in a numerical wave tank with a fully nonlinear potential flow model

With the new model REEF3D::FNPF, some of the design concerns of the floating bridges can be investigated. Extreme sea state is one of the major concerns. Here, both the wave packet method (Hennig (2005)) and the NewWave theory(Tromans et al. (1991)) are used to generate rogue waves in the numerical wave tank. The parametric study on different factors that influence the focused wave generation helps to predict the rogue wave in a numerical wave tank more accurately. Some of the main results are summarised in the following:

- The numerical model is more accurate in capturing the correct wave focusing location than physical experiments due to the continuous outputs rather than discrete measurements.

A focused irregular wave group is generated with the wave packet method and the numerical results are compared with the experimental data measured in the Large Wave Flume (GWK), Hannover, Germany (Clauss and Steinhagen (1999)). The physical wave tank in the experiments is 300 m long with a constant water depth of $h = 4.01$ m. A piston-type wavemaker is used to generate the wave packet that focuses at the designated location at $x_F = 126.21$ m and time at $t_F = 103$ s. Though the time series of the surface elevation match well with the experiments, the geometry of the focused wave is not symmetric, indicating that the real wave focusing is may have not been captured during the experiment. Further study is performed by comparing the geometry of the surface elevation every time step to finds out the real focusing location where the wave crest is the highest and the geometry of the crest is symmetric. This lead to the finding out a delayed wave focusing, as shown in Fig. 4.8.

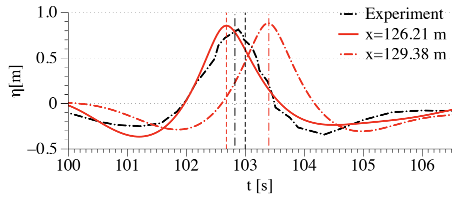

Figure 4.8: The comparison of the time series at the designated focusing location at $x = 126.21$ m and at the real focusing location at $x = 129.38$ m as detected in the numerical simulation. The black dash-dot curve is the time series measured in the experiment at $x = 126.21$ m and the vertical black dash-dot line indicates the measured focusing time at $t = 102.825$ s. The red solid curve is the time series at $x = 126.21$ m in the NWT, and the vertical red dashed line indicates the corresponding numerical focusing time $t = 102.7$ s. The red dash-dot curve is time series at the real focusing location $x = 129.38$ m in the NWT and the vertical red dash-dot line indicates the real focusing time $t = 103.4$ s. The vertical black dashed line is the designated focusing time at $t = 103$ s.

- Increasing nonlinearity postpones the wave focusing in comparison to the designed locations.

The delayed wave focusing in the GWK test case reveals further clues that increasing nonlinearity lead to further delay of the wave focusing. Therefore, waves of higher steepness are simulated in the same numerical wave tank to quantify the shift of wave focusing. The delay in space and time in relation to wave steepness is shown in Fig. 4.9. A near linear delay of focusing is observed in relation to wave steepness.

- Different frequency bands in the input wave spectrum create different focusing wave geometry.

The NewWave theory is used to reproduce the wave field as described by Ning et al. (2009). Here, an additional test is made by using five various frequency band

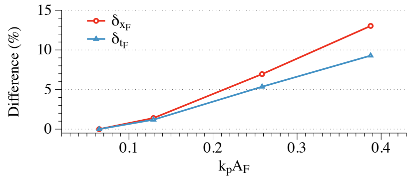

Figure 4.9: The relative spatial differences in focusing location δx_F and temporal differences in focusing time δt_F in relation to wave steepness in the simulation with the wave packet.

widths. NB1 represents the narrowest frequency band, NB5 represents the widest frequency band width. The focused wave profiles produced with different frequency band widths are then compared in Figure. 4.10. It shows that the narrow frequency band produces higher focused wave crests as well as higher secondary crests in the adjacency of the focused wave crests.

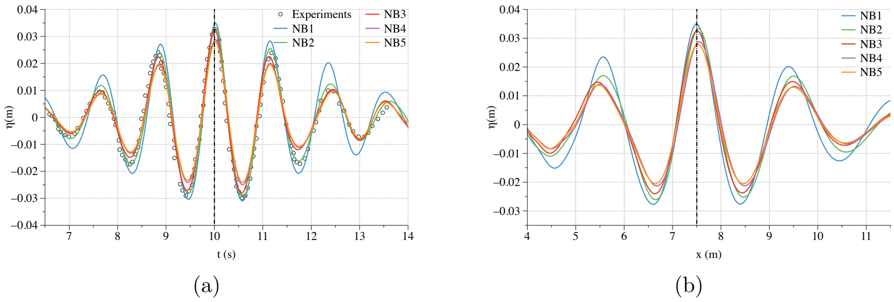

Figure 4.10: Comparison of the wave surface elevations with five different frequency bandwidths. (a) the time series at the designated focusing location $x = 7.5$ m, (b) the spatial wave profile in the longitudinal direction at the designated focusing time $t = 10$ s.

- A Neumann boundary is seen to predict the wave focusing location better than a relaxation wave generation boundary.

In the relaxation method for wave generation, usually only linear dispersion is represented inside the generation zone, which might result in errors in wave phases and the location and time of the focusing point. To test the hypothesis, both Newmann boundary and relaxation method are used to generate the focused wave trains resented by Ning et al. (2009). Two cases are compared, with NING1 representing a wave train of linear nature and NING3 representing a steeper wave train. The results are shown in Fig. 4.11. It is seen that both wave generation methods produce similar wave profiles at the focusing point. However, with increasing nonlinearity, the Newman boundary predicts focusing location and wave height more accurately in comparison to the experiment.

- In a directional sea state, the directional spreading function also influences the 3D focused wave profile. In a more spreading sea, the focused wave crest height is reduced and the wave profile in the transversal plane becomes narrower.

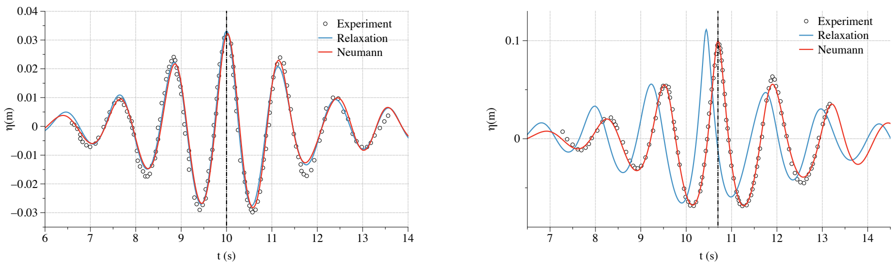

(a) (b)

Figure 4.11: Comparison of the time series at the focusing location of 7.5 m generated by a relaxation method and a Neumann boundary. (a) for the simulation case NING1, (b) for the simulation case NING3.

A three-dimensional (3D) focusing wave is produced in the numerical wave tank. The simulation domain is 20 m long, 20 m wide and 0.5 m deep. The designated wave focusing takes place at x =7.5 m and y =10 m at 35 s. By changing the directional spreading factor, the effect of directional spreading is observed, as shown in Fig. 4.12. As can be seen, a wider directional spreading leads to a lower focusing wave height and a narrower wave profile in the y-direction. This effect can influence the calculation of wave forces on structures tremendously.

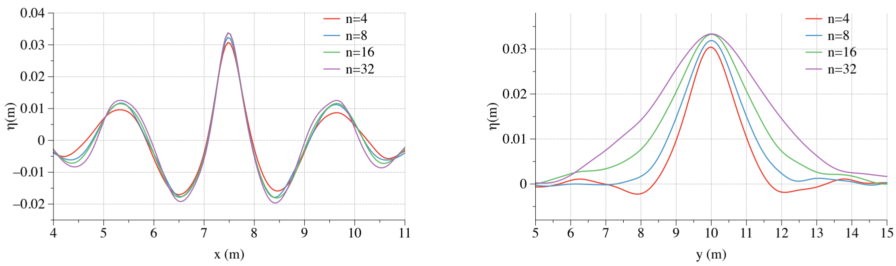

(a) (b)

Figure 4.12: Comparison of the wave free surface elevations with four different spreading functions, (a) comparison of the wave profiles in the longitudinal x-z plane at $y = 10$ m, (b) comparison of wave profiles in the transverse y-z plane at $x = 7.5$ m.

4.3.2 Paper 4: A fully nonlinear potential flow wave modelling procedure for full-scale simulations of sea states with various wave breaking scenarios

In order to ensure an accurate representation of the wave fields inside the fjord, the first critical step is to ensure a high fidelity representation of an irregular wave sea state over a three-hour duration. In this paper, several irregular sea states with different input waves, water depth conditions and severity of wave breaking are simulated. A breaking wave algorithm is introduced to detect both steepness induced wave breaking in deep water and depth induced wave breaking in shallow water. A geometric filtering method (Jensen et al. (1999))and viscous damping method (Baquet et al. (2017)) can be used alone or in combination to dissipate wave energy. A constant truncation error method (Pakozdi et al. (2019b)) is used to optimise the vertical grid arrangement. A working procedure for an accurate simulation of an irregular sea state is concluded especially for a fully non-linear potential flow on a σ-coordinate grid. The procedure is summarised in Fig. 4.13

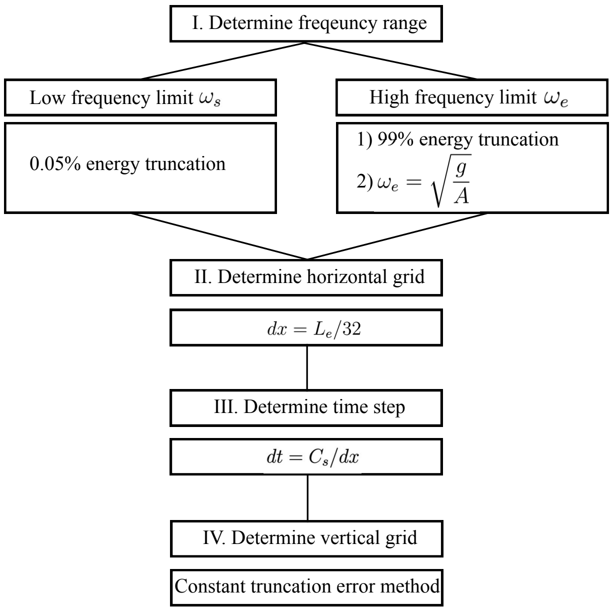

Figure 4.13: Procedure of the numerical setup for the simulation using a potential flow model with a σ-coordinate grid.

Four wave conditions are simulated in a 2D numerical wave tank for 12800 s where the time series from the wave gauge $12.5L_p$ (L_p is the wavelength corresponding to the peak period) away from the inlet boundary is used to obtain short-term wave statistics. The reproduced wave spectra as well as the wave height distribution match the theoretical input wave spectra and the analytical wave height distribution well in all simulated cases. However, more wave energy loss and more tendency of exceeding the upper bound of the wave height distribution are also observed with increasing severity of breaking waves. As an example of the simulated results, the simulated wave spectra in the test case with mild wave breaking in intermediate water depth (JMB) using the equal energy method (EEM) for spectrum discretisation is shown in Fig. 4.14. In addition, the wave height distributions at wave gauges G3 to g7 between $10L_p$ to $15L_p$ with a $1.25L_p$ interval are shown in Fig. 4.15.

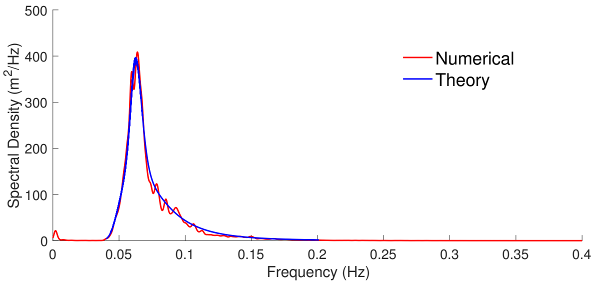

Figure 4.14: Comparison of the numerically reproduced wave spectra and the input theoretical wave spectra in the case with mild wave breaking in intermediate water depth using the EEM discretisation method and viscous damping wave breaking method.

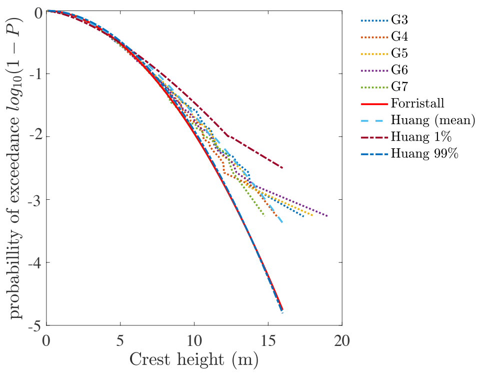

Figure 4.15: Wave crest distribution at G3-G7 in the case with mild wave breaking in intermediate water depth using the EEM discretisation method and viscous damping wave breaking method.

4.4 REEF3D::FNPF applications for Norwegian coastal conditions

4.4.1 Paper 5: A flexible fully nonlinear potential flow model for wave propagation over the complex topography of the Norwegian coast

In this paper, a novel coastline algorithm is introduced into REEF3D::FNPF. The coastline algorithm consists of three steps:

- The wet and dry cells are identified. The computational cells are identified as wet cells and dry cells following a relative-depth criterion. If the local water depth h is smaller than a threshold h, then the local cell is identified as a dry cell. When a cell is identified as a dry cell, the velocities in the cell are set to be zero.
- The wet cells are assigned with a value + 1 and the dry cells are assigned with a value - 1. With the signed initial values, the coastline is captured using a level-set function (Osher and Sethian (1988)). Using the level-set method, the computational grid remains a uniform structured grid in the horizontal plane even though complex topography is included in the computational domain.
- Relaxation zones are applied along the the wet side of the coastline covering a given distance from the coastline. This way, extreme run-ups are avoided and therefore eliminate numerical instabilities in the free surface boundary conditions at shallow regions.

With the novel coastline algorithm and the high computational efficiency as demonstrated previously, REEF3D::FNPF is tested with challenging wave transformations with strongly varying bathymetry and irregular natural topography. Some of the most important results are summarised here:

- The wave model predicts wave propagation over steep underwater slope with high accuracy

One of the challenging scenarios follows the experiment conducted at SINTEF Ocean in Trondheim (Pakozdi et al. (2019a)). Here a bi-chromatic wave propagates over a steep submerged ramp, the first segment of which has a slope of 70° and the second segment has a slope of 45°. This condition closely resembles the natural under water topography in several locations inside the Norwegian fjords. With the chosen grid and time step, the free surface in the simulation is compared to the experiment. As an example, the comparison at wave gauge G3 is shown here. A good agreement is achieved between the experiment and the simulation. In addition, all theoretical frequency components are represented in the frequency spectra from both the experiment and the simulation. The simulation captures the two principal frequencies ω_1 and ω_2 and the low frequency ω_3 exactly as the theoretical values and the corresponding energy densities are nearly identical to the experiment. The high frequencies represented in the numerical simulation are slightly different from the experiment, and the relevant energy densities show a different of $10 - 25\%$. However, the energy densities at the high frequency range are very small (10^{-5} to 10^{-4}) in comparison to the principal frequencies (10^{-2}). The energy differences between the simulation and the experiment at the high frequency range is negligible when they are compared in the same scale as the principal frequencies. For further details, please refer to **Paper 5**.

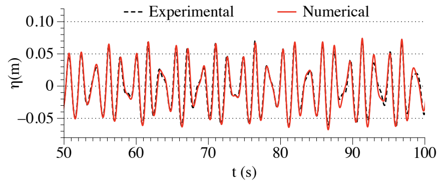

Figure 4.16: Comparison of free surface time series between the simulated waves and experimental measurements. (a) the input wave signal in the numerical simulation at G3.

- The wave breaking algorithm together with the coastline algorithm enables the model to simulate breaking waves nearshore.

The experiment of plunging breaking waves over a mild slope are used for validation of the breaking wave algorithm (Ting and Kirby (1995)). The surface elevation at the wave gauges before (G2) and after the breaking (G3) are selected to be shown in Fig. 4.17. The wave crest has a sudden decrease at wave gauge 3, indicating that wave breaking occurs between wave gauge 2 and 3. The simulated wave crests match the experiment well both before and after the breaking, showing the correct energy dissipation in the implemented breaking algorithm.

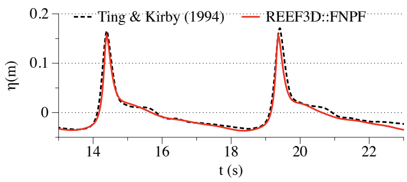

(a) wave gauge 2

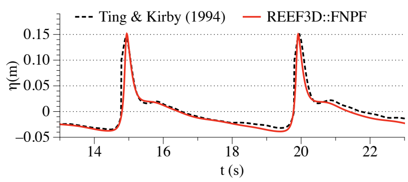

(b) wave gauge 3

Figure 4.17: Time series of surface elevation at gauge 2 before the wave breaking and gauge 3 after the wave breaking in the simulation of wave breaking over a mild-slope.

- The numerical model shows the capability of simulating large-scale wave propagation over irregular bathymetry and irregular coastlines accurately and efficiently.

Full-scale simulations of wave propagation into Mehamn harbour with natural topography are performed for 12800 s. The domain size is 1760 m in the x-direction and 1440 m in the y-direction. The 12800 s simulation takes 7.9 h to finish with 128 Intel Sandy Bridge processors (2.6 GHz) on the supercomputer Vilje. The coastline algorithm captures the coastlines and the topography accurately and efficiently. The detected coastline and the coast-following relaxation zone are shown in Fig. 4.18. The simulations capture the complicated wave transformation inside the harbour, including diffraction around the breakwaters. The free surface at 12800 s is shown in Fig. 4.19. The significant wave height H_s matches the experiment even with both breakwaters . The comparison of H_s is shown in Fig. 4.20.

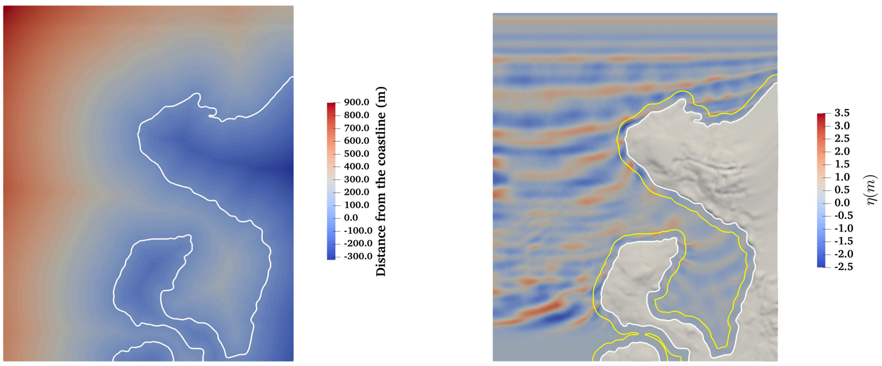

(a) (b)

Figure 4.18: Detection of the coastline and calculation of distance from the coastline for a complicated topography using the proposed coastline algorithm. The white contour in (a) is the detected coastline, the colour shows the distance aways from the coastline, with negative values indicating inland and positive values indicated offshore. The yellow contour in (b) is the boundary of the coast-following relaxation zone to reduce numerical instability and customise reflection properties of the coastline.

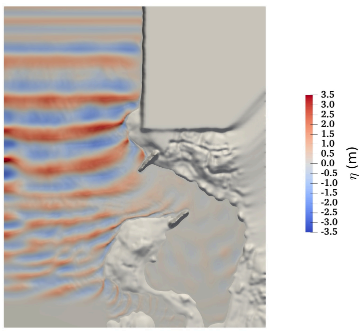

Figure 4.19: Free surface elevation in the simulations of wave propagation into Mehamn harbour at $t = 12800$ s with both breakwater BW1 and BW2.

- Phase-resolved models predict wave diffraction better than phase-averaged

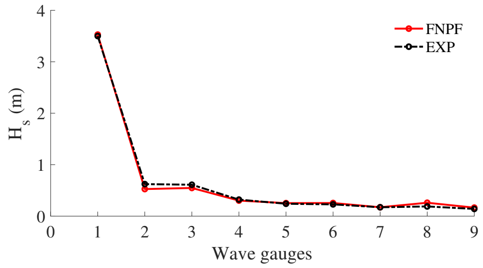

Figure 4.20: Comparison of H_s at the wave gauges between the experimental measurements and numerical simulations for wave propagation in Mehamn harbour with both breakwaters BW1 and BW2.

wave models.

Finally a large-scale simulation of wave propagation over an archipelago towards a fish farm is simulated. The H_s behind the archipelago are compared with the phase-averaged model SWAN (Booij et al. (1999)). The relative differences are calculated as the absolute differences divided by the corresponding values from REEF3D::FNPF. The wave heights from SWAN are underestimated by 20% to 50%. These comparisons confirm the advantage of the proposed phase-resolved wave model in representing some of the nonlinear phenomena such as strong diffraction (Thomas and Dwarakish (2015)). Fergstad et al. (2018) also reported an underestimation of phase-avbrgead model in comparison with the in-situ measurement.

4.4.2 Paper 6: Phase-resolved wave modelling in the Norwegian fjords for the ferry-free E39 project

In this paper, REEF3D::FNPF is first tested for several benchmark cases to further ensure the wave quality in relevant scenarios. Then, the model is applied to simulate the wave field inside the fjords along E39 route. The first study object is the Sulafjord that is located in the Møre and Romsdal county. The fjord is relatively exposed to the open ocean, as there are no archipelagos outside the fjord to prevent offshore swell waves from entering the inner channel of the fjord. The other fjord is Bjørnafjord that is located in the county of Vestland. The fjord is well sheltered from the ocean swell from the Atlantic due to the arrays of archipelagos outside the fjord entry. These fjords have a domain of interest with dimensions of tens of kilometres. Phase-resolved wave modelling for a three-hour duration has not been performed before for these type of applications.

Both long-crested and narrow-spreading short-crested swell waves from offshore are used for both fjords. The chosen domain is 25 km in the x-direction and 16 km wide in the y-direction with its maximum water depth of 500 m. With the chosen grid resolution, 17.8 million cells are used in the simulations at Sulafjord. The simulations with long-crested and host-crested waves are completed in 15.1 and

15.7 hours with 256 Intel Sandy Bridge cores (2.6 GHz) on the supercomputer Vilje. Surface elevation at 12800 s in the simulations of wave propagation into Sulafjord with narrow spreading short-crested irregular wave input is shown in Fig. 4.21.

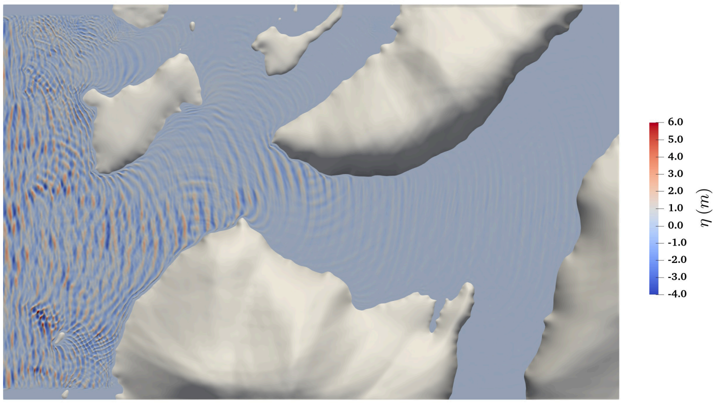

Figure 4.21: Surface elevation at 12800 s in the simulations of wave propagation into Sulafjord with narrow spreading short-crested irregular wave input.

The variation of the frequency components is one of the main findings from the simulations. The dominating frequencies tend to shift away from the peak frequency of the input wave spectrum towards the lower and higher frequency range. As an example, the wave spectra at wave gauge B inside the fjord is shown in Fig. 4.22. At wave gauge B, the short-crested wave shows a main peak near 0.06 Hz while a significant percentage of wave energy is concentrated near 0.08 Hz. For the long-crested wave, the majority of wave energy is concentrated near the new peak of the spectrum at 0.08 Hz. The shift of wave energy towards 0.08 Hz in both wave conditions shows that 0.08 Hz is the critical frequency when considering structure egen frequency, given the input wave properties.

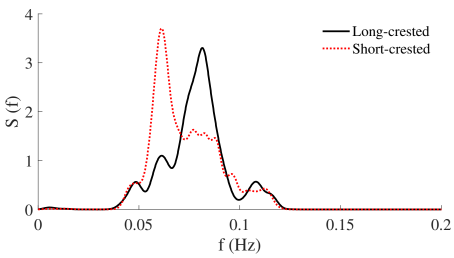

Figure 4.22: Wave spectra at wave gauge B inside Sulafjord.

At Bjørnafjord, the chosen computational domain is 45 km in the x-direction and 35 km in the y-direction with the maximum water depth of 675 m. With the chosen grid arrangement, the final number of cells for the simulations is 39.4 million. All simulations are performed with 256 Intel Sandy Bridge cores (2.6 GHz) on the supercomputer Vilje for 12800 s. The long-crested wave and short-crested wave simulations take 32.0 and 32.1 hours respectively. The free surface at 12800 s in the simulations of wave propagation into Bjørnafjord with narrow spreading short-crested irregular wave input is shown in Fig. 4.23. The frequency of the field also varies significantly inside the fjord at wave gauges G16 to G18, especially in the low frequency range. The new wave spectrum inside the fjord is shown in Fig. 4.24. The emerging new wave frequencies create significant challenges for the floating structures. The low frequency waves contribute to the low frequency drift (Faltinsen (1999)) for the mooring system and the high frequency waves might cause resonant excitations such as ringing (Faltinsen et al. (1995); Faltinsen (1999)).

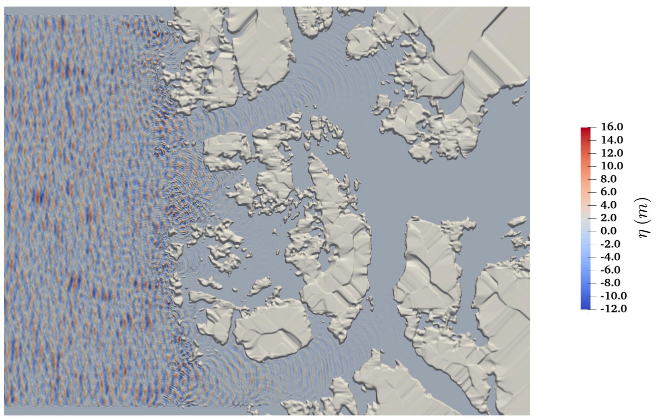

Figure 4.23: Free surface elevation at 12800 s in the simulations of wave propagation into Bjørnafjord with narrow spreading short-crested irregular wave.

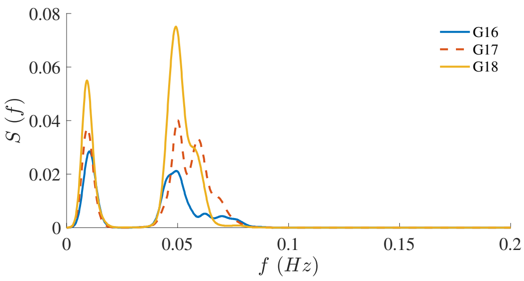

Figure 4.24: Variation of wave spectra during narrow spreading short-crested irregular wave propagation into Bjørnafjord at wave gauges G16-G18 at the second possible crossing location.

4.5 REEF3D open-source hydrodynamics framework

4.5.1 Paper 7: A comparison of different wave modelling techniques in an open-source hydrodynamic framework

The three models, REEF3D::CFD, REEF3D::SFLOW and REEF3D::FNPF are compared in this paper. Since they all share the same numerical framework, the comparison should be relatively objective and offer insights on the differences in numerical performance and their most suitable area of applications.

For example, the test case of wave propagation over a submerged bar (Beji and Battjes (1993)) is simulated with all models with the same setting. The time series are plotted together in Fig. 4.25. Both REEF3D::CFD and REEF3D::FNPF are able to represent the de-shoaling process while REEF3D::SFLOW is restricted by the water depth.

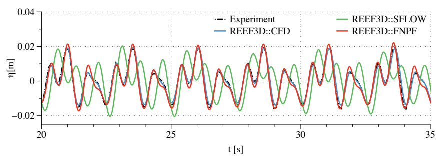

Figure 4.25: Comparison of the time histories of the free surface elevations at the wave gauges in the simulations of wave propagation over a submerged bar using the cell sizes achieving grid convergence.

The test case of wave breaking over a mild slope (Ting and Kirby (1995)) is also simulated with all models. The comparison of the free surface at wave gauge 2 and 3 before and after breaking show that all models are able to capture the correct location of wave breaking and dissipate the correct amount of energy near the shoreline. The comparison is shown in Fig. 4.26. However, the coastline algorithm in REEF3D::FNPF does not allow wave run-up over the slope.

A 3D wave breaking over a fringe reef is also simulated with all models. Here, REEF3D::CFD is the only wave model that is able to represent the geometry of the overturning wave breaker, which is shown in Fig. 4.27.

In terms of computational performance, the computational speed gains from REEF3D::SFLOW and REF3D::FNPF in comparison to REEF3D::CFD are found to be by factors of about 10 and 40 respectively on average for 2D simulations and 60 and 800 respectively for the 3D simulation. The higher computational demands of the CFD model is compensated by that fact that it is the only model capable of representing the geometry of an overturning wave breaker accurately, which is important for studies on slamming load on structures.

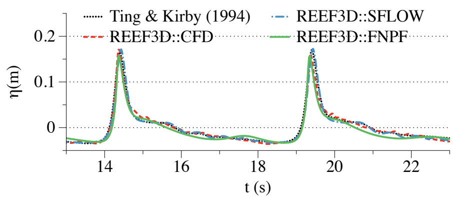

(a) Wave gauge 2

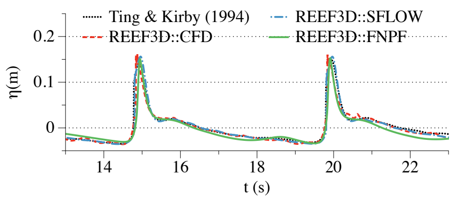

(b) Wave gauge 3

Figure 4.26: Comparison between the simulated free surface elevation time series from the three REEF3D modules and the experiment measurements at all four wave gauges in the simulations of wave breaking over a mild slope.

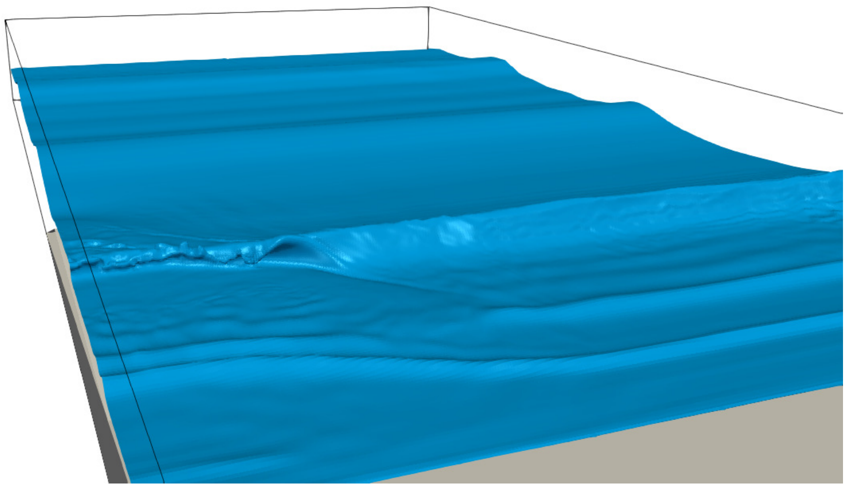

Figure 4.27: Three-dimensional wave breaking over the reef in the numerical wave tank calculated using REEF3D::CFD

Chapter 5

Conclusions and Outlooks

5.1 Conclusions

The Ph.D. study was tasked with developing a numerical wave model that is computationally efficient, accurate, flexible and phase-resolved. The development includes the shallow water equations model REEF3D::SFLOW with a quadratic non-hydrostatic pressure profile and the fully non-linear potential flow model REEF3D::FNPF with a novel coastline algorithm. Both models show computational speed gains by factors of 10 to 800 in comparison to REEF3D::CFD, enabling large-scale simulations over long durations. The performance of REEF3D::SFLOW is limited by the water depth. However, the model shows high computational efficiency and accuracy in the shallow to intermediate water depth regions and allows wave run-up at the shoreline, making it a faster alternative for the study of swash zone dynamics. REEF3D::FNPF is found to be an ideal wave model that is fast, accurate and not restricted by water depth, bathymetry changes and irregular coastlines. Though the coastline algorithm solves the difficulty of including irregular coastlines, it also prohibits wave run-up. Therefore, the model is a wave propagation model that is not suitable for studies on swash zone dynamics.

It is concluded that REEF3D::FNPF is the ideal numerical wave model for the E39 fjord-crossing project as it fulfils all criteria that are required for accurate large-scale simulations of wave propagation into the Norwegian fjords:

- The model is computationally efficient. For example, the model completed the simulation of a 2D irregular wave field for a 12800 s (slightly longer than 3-hour) duration within 1.13 hours using 16 cores on the supercomputer Vilje (see details in **Paper 2**). The large-scale 3D short-crested wave modelling in Bjørnafjord with the duration of 12800 s is completed within 32 hours using 256 cores on the supercomputer Vilje (see details in **Paper 6**). In this case, the domain size is 45 km in the x-direction and 35 km in the y-direction and the total number of cells is almost 40 million. It indicates a maximum simulation time to real time ratio of 10 for most Norwegian fjords using the available supercomputer resources in Norway.

- The model provides phase-resolved solutions. All simulation results using REEF3D::FNPF provide information on surface elevation and particle velocities. They represent all wave transformation phenomena including strong diffraction (for example, the wave propagation into Mehamn harbour with breakwaters. See details in **Paper 5**) and provide time domain information.

- The model is accurate in representing a large range of wave propagation transformation phenomena. The model has been verified and validated with several benchmark cases (see details in **Papers 2, 5** and **6**) as well as large-scale engineering scenarios (see details in **Papers 5** and **6**). These tests prove the modelling capability of accurately simulating regular waves, bi-chromatic waves and long-crested and short-crested irregular wave propagation, wave shoaling, wave decomposition, wave de-shoaling, wave refraction, wave diffraction as well as wave breaking.

- The model is very flexible regarding the coastal topography. The model is not limited by water depth conditions, varying bathymetry and irregular shorelines. The effective coastline algorithm provides a universal solution for irregular coastline inclusion and distinguishes REEF3D::FNPF from other potential flow models. The flexibility is demonstrated with the simulations of Mehamn harbour and Flatøya in **Paper 5** and Sulafjord and Bjørnafjord in **Paper 6**.

- The model is open-source. Just as all models developed in the REEF3D framework, the source code of the model is made freely available from www.reef3d.com. This brings the research transparency and maximises the impact on academics, industry and society.

The procedure for numerical wave analysis in the Norwegian fjords is suggested as the following: The results from the phase-averaged wave models, the in-situ measurements and the hindcast wave data in the offshore area can be used as input waves in REEF3D::FNPF. Then REEF3D::FNPF carries out the phase-resolved simulation in the nearshore area as well as inside the fjords. Here, a customisable number of wave gauges can be arranged in the numerical wave model that provide time series at multiple locations. This information can then be used for the analysis of many properties of the wave fields as well as floating structure response. The schematics of the wave modelling in the Norwegian fjord is shown in Fig. 5.1

During the Ph.D. study, REEF3D has been transformed from an open-source CFD code to an open-source hydrodynamics framework. Even though REEF3D::CFD and REEF3D::SFLOW are not suggested for the large-scale wave modelling at the Norwegian coast for the E39 project, their own features enable the research results to be applied to a wider range of applications beyond the E39 project. For example REEF3D::SFLOW can also be sued for shallow water coastal wave modelling as well as the study on morphology along the coastline. REEF3D::CFD can be used for wave-structure interaction (WSI). As a summary, the characteristics and featured applications of the present models are summarised in Table. 5.1.

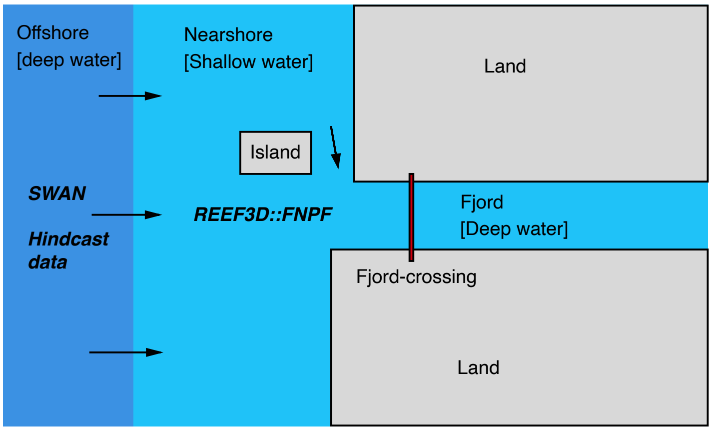

Figure 5.1: Wave propagation strategy for E39.

REEF3D::	Dim.	Br.	Tub.	Visc.	O.B.			Featured Application
CFD	3D	Yes	Yes	Yes	Yes	Low	High	WSI and O.B.
SFLOW	2D	Yes	Yes	No	No	Speed	Detail	Swash zone
FNPF	3D	Yes	No	No	No	High	Low	Wave propagation
*	Dim.: Dimension; Br.: Breaking wave; Tub.:Turbulence; Visc.: viscosity; O.B.: Overturning breaking wave							

Table 5.1: Summary of wave models in REEF3D

5.2 Outlook

In the future, the proposed wave propagation model REEF3D::FNPF will be further tested with engineering scenarios. The numerical results will be compared with in-situ measurements as well as industrial standards. These studies will bring further improvement to the model. Every model in REEF3D has its own features, the coupling among them is beneficial for many applications. Other marine environmental factors such as wind and current should be included in the wave models. The suggested further works are summarised as below:

- Coupling between REEF3D models. Different models have their own strengths and limitations, the coupling between the models combine their advantages. For example, the coupling between REEF3D::FNPF and REEF3D::CFD will transfer the wave field information from REEF3D::FNPF to REEF3D::CFD and thus allow for the representation of wave slamming and the consequent studies on the impact loads on structures.

- Including wind and current in the wave propagation model. Wind waves and current are two of the main factors that influence the wave field inside the fjords. Including the effects of wind and current on the wave fields is one of the demanding features to be implemented in the framework.

- Further applications of REEF3D::FNPF in engineering scenarios and compare the results with in-situ measurements.
- Further development with REEF3D::SFLOW for coastal morphology studies.

Bibliography

Aarnes, O.J., 2019. Wave conditions in Bjørnafjorden. Technical Report. Norwegian Meteorological Institute.

Abbott, M.B., McCowan, A.D., Warren, I.R., 1984. Accuracy of short-wave numerical models. Journal of Hydraulic Engineering 110, 1287–1301.

Aggarwal, A., Bihs, H., Shirinov, S., Myrhaug, D., 2019. Estimation of breaking wave properties and their interaction with a jacket structure. Journal of Fluids and Structures 91, 102722.

Aggarwal, A., Pkozdi, C., Bihs, H., Myrhaug, D., Alagan Chella, M., 2018. Free surface reconstruction for phase accurate irregular wave generation. Journal of Marine Science and Engineering 6.

Ahmad, N., Bihs, H., Myrhaug, D., Kamath, A., Arntsen, Ø.A., 2018. Three-dimensional numerical modelling of wave-induced scour around piles in a side-by-side arrangement. Coastal Engineering Volume 138, 132–151.

Alagan Chella, M., Bihs, H., Myrhaug, D., 2019. Wave impact pressure and kinematics due to breaking wave impingement on a monopile. Journal of Fluids and Structures 86, 94 – 123.

Altomare, C., Domnguez, J., Crespo, A., Gonzlez-Cao, J., Suzuki, T., Gmez-Gesteira, M., Troch, P., 2017. Long-crested wave generation and absorption for SPH-based DualSPHysics model. Coastal Engineering 127, 37 – 54.

Altomare, C., Suzuki, T., Dominguez, J., Crespo, A., 2014. Coupling between Swash and SPH for real coastal problems, in: 9th International Spheric workshop, Proceedings, pp. 1–6.

Arunakumar, H.S., Suvarna, P., Abhijith, P.A., Prabhu, A.S., Pruthviraj, U., Kamath, A., 2019. Effect of emerged coastal vegetation on wave attenuation using open source CFD tool: REEF3D, in: Proceedings of the Fourth International Conference in Ocean Engineering (ICOE2018), Springer Singapore. pp. 591–603.

Ashby, S., Flagout, R., 1996. A parallel mulitgrid preconditioned conjugate gradient algorithm for groundwater flow simulations. Nuclear Science and Engineering Volume 124(1), 145–159.

Ashby, S.F., Flagout, R.D., 1996. A parallel mulitgrid preconditioned conjugate gradient algorithm for groundwater flow simulations. Nuclear Science and Engineering 124, 145–159.

Baquet, A., Kim, J., Huang, Z.J., 2017. Numerical modeling using CFD and potential wave theory for three-hour nonlinear irregular wave simulations, in: International Conference on Offshore Mechanics and Arctic Engineering, Trondheim, Norway.

Beji, S., Battjes, J.A., 1993. Experimental investigation of wave propagation over a bar. Coastal Engineering 19, 151–162.

Berkhoff, J., 1972. Computation of combined refraction - diffraction. Coastal Engineering Proceedings 1, 23.

Berkhoff, J., 1976. Mathematical models for simple harmonic linear water waves: Wave diffraction and refraction. Ph.D. thesis. Delft University of Technology. Delft, the Netherlands.

Berthelsen, P., Faltinsen, O., 2008. A local directional ghost cell approach for incompressible viscous flow problems with irregular boundaries. Journal of Computational Physics Volume 227, 4354–4397.

Bihs, H., Heveling, K., Kamath, A., 2018. REEF3D:NSEWAVE, a three-dimensional non-hydrostatic wave model on a fixed grid. Coastal Engineering Proceedings 1, waves.8.

Bihs, H., Kamath, A., 2017. A combined level set/ghost cell immersed boundary representation for floating body simulations. Int. J. Numer. Meth. Fluids Volume 83, 905–916.

Bihs, H., Kamath, A., Alagan Chella, M., Aggarwal, A., Arntsen, Ø.A., 2016. A new level set numerical wave tank with improved density interpolation for complex wave hydrodynamics. Computers & Fluids 140, 191 – 208.

Bihs, H., Wang, W., Pákozdi, C., Kamath, A., 2020. REEF3D::FNPF-a flexible fully nonlinear potential flow solver. Journal of Offshore Mechanics and Arctic Engineering 142.

Bingham, H.B., Zhang, H., 2007. On the accuracy of finite-difference solutions for nonlinear water waves. Journal of Engineering Mathematics , 211–228.

Bonnefoy, F., Touz, D.L., Ferrant, P., 2006a. A fully-spectral 3d time-domain model for second-order simulation of wavetank experiments. part a: Formulation, implementation and numerical properties. Applied Ocean Research 28, 33 – 43.

Bonnefoy, F., Touz, D.L., Ferrant, P., 2006b. A fully-spectral 3d time-domain model for second-order simulation of wavetank experiments. part b: Validation, calibration versus experiments and sample applications. Applied Ocean Research 28, 121 – 132.

Booij, N., Ris, R.C., Holthuijsen, L.H., 1999. A third-generation wave model for coastal regions, 1. model description and validation. Journal of Geophysical Research 104, 7649–7666.

Brackbill, J., Kothe, D., Zemach, C., 1992. A Continuum Method for Modeling Surface Tension. Journal of Computational Physics Volume 100(2), 335–354.

Chen, W., Panchang, V., Demirbilek, Z., 2005. On the modeling of wavecurrent interaction using the elliptic mild-slope wave equation. Ocean Engineering 32, 2135 – 2164.

Cheng, Z., Svangstu, E., Gao, Z., Moan, T., 2019. Field measurements of inhomogeneous wave conditions in bjørnafjorden. Journal of Waterway, Port, Coastal, and Ocean Engineering 145, 05018008.

Chorin, A., 1968. Numerical solution of the Navier-Stokes equations. Mathematics of Computation Volume 22, 745–762.

Chorin, A., 1968. Numerical solution of the Navier-Stokes equations. Mathematics of Computation 22, 745–762.

Clauss, G.F., Steinhagen, U., 1999. Numerical Simulation of Nonlinear Transient Waves and its Validation by Laboratory Data, in: 9th International Offshore and Polar Engineering Conference.

Crespo, A., Domnguez, J., Rogers, B., Gmez-Gesteira, M., Longshaw, S., Canelas, R., Vacondio, R., Barreiro, A., Garca-Feal, O., 2015. DualSPHysics: Open-source parallel CFD solver based on Smoothed Particle Hydrodynamics (SPH). Computer Physics Communications 187, 204 – 216.

Crespo, A., Gmez-Gesteira, M., Dalrymple, R., 2007a. 3D SPH simulation of large waves mitigation with a dike. Journal of Hydraulic Research 45, 631–642.

Crespo, A.J.C., Gmez-Gesteira, M., Dalrymple, R.A., 2007b. Boundary conditions generated by dynamic particles in SPH methods. Computers, Materials & Continua 5, 173–184.

Dai, J., Leira, B.J., Moan, T., Kvittem, M.I., 2020. Inhomogeneous wave load effects on a long, straight and side-anchored floating pontoon bridge. Marine Structures 72, 102763.

Dean, R.G., Dalrymple, R.A., 1991. Water Wave Mechanics for Engineers and Scientists. WORLD SCIENTIFIC.

Demirbilek, Z., Panchang, V., 1998. CGWAVE: A Coastal Surface Water Wave Model of the Mild Slope Equation. Technical Report CHL-98-26. US Army Corps. of Engineers Waterways Expt. Stn.. Vicksburg, MS 39180.

DHI, 2016. Wave and current measurements in Bjørnafjorden, Hordaland, Norway. Technical Report. DHI AS. Trondheim, Norway.

DHI, 2017a. MIKE 21 BW, Boussinesq Wave Module User Guide. Technical Report. DHI.

DHI, 2017b. MIKE 21 Spectral Waves FM, Sectral Wave Module User Guide. Technical Report. DHI.

DHI, 2017. MIKE 3 Flow Model Hydrodynamic Module Scintific Documentation. Technical Report. DHI.

Dickenson, P., 2009. The feasibility of smoothed particle hydrodynamics for multiphase oilfield systems, in: Seventh International Conference on CFD in the Minerals and Process Industries, CSIRO, Melbourne, Australia.

DNV-GL, 2018. Wave Loads. Standard DNVGL-CG-0130. DNV-GL. Veritasveien 1, Høvik, Norway.

Dommermuth, D.G., Yue, D.K.P., 1987. A high-order spectral method for the study of nonlinear gravity waves. Journal of Fluid Mechanics 184, 267288.

Domnguez, J., Crespo, A., Valdez-Balderas, D., Rogers, B., Gmez-Gesteira, M., 2013. New multi-gpu implementation for smoothed particle hydrodynamics on heterogeneous clusters. Computer Physics Communications 184, 1848 – 1860.

Ducrozet, G., Bonnefoy, F.e.l., Le Touz é, D., Ferrant, P., 2012. A modified High-Order Spectral method for wavemaker modeling in a numerical wave tank. European Journal of Mechanics - B/Fluids 34.

Dunham, K.K., 2016. Coastal highway route e39 extreme crossings. Transportation Research Procedia 14, 494 – 498. Transport Research Arena TRA2016.

Durbin, P., 2009. Limiters and wall treatments in applied turbulence modeling. Fluid Dyn Res Volume 41, 1–18.

Eckart, C., 1952. The propagation of gravity waves from deep to shallow water. National Bureau of Standards NBS Circular 521, 165173.

Eidem, M.E., 2018. Wasatch Solar Project Final Report. Technical Report. The Norwegian Road Administration.

Engsig-Karup, A., Bingham, H., 2009. Boundary-fitted solutions for 3d nonlinear water wave-structure interaction, in: IWWWFB24, p. 20.

Engsig-Karup, A., Eskilsson, C., Bigoni, D., 2016a. A stabilised nodal spectral element method for fully nonlinear water waves. Journal of Computational Physics 318, 1 – 21.

Engsig-Karup, A.P., Eskilsson, C., 2019. Spectral Element FNPF Simulation of Focused Wave Groups Impacting a Fixed FPSO-type Body. International Journal of Offshore and Polar Engineering 29, 141–148.

Engsig-Karup, A.P., Eskilsson, C., Bigoni, D., 2016b. Unstructured Spectral Element Model for Dispersive and Nonlinear Wave Propagation, in: The 26th International Ocean and Polar Engineering Conference, International Society of Offshore and Polar Engineers, Rhodes, Greece. p. 8.

Engsig-Karup, A.P., Glimberg, S.L., Nielsen, A.S., Lindberg, O., 2013. Fast hydrodynamics on heterogenous many-core hardware. Taylor Francis. p. 251294. 2013;11.

Engsig-Karup, A.P., Madsen, M.G., Glimberg, S.L., 2012. A massively parallel gpu-accelerated model for analysis of fully nonlinear free surface waves. International Journal for Numerical Methods in Fluids 70.

Faltinsen, O.M., 1999. Ringing Loads on a Slender Vertical Cylinder of General Cross- Section. Journal of Engineering Mathematics 35, 199–217.

Faltinsen, O.M., Newman, J.N., Vinje, T., 1995. Nonlinear wave loads on a slender vertical cylinder. Journal of Fluid Mechanics 289, 179–198.

Fenton, J.D., 1985. A fifth-order Stokes theory for steady waves. Journal of Waterway, Port, Coastal and Ocean Engineering 111, 216–234.

Fenton, J.D., 1999. The cnoidal theory of water waves. chapter 2. Developments in Offshore Engineering, Gulf, Houston, J. B. Herbich edition. pp. 55–100.

Fergstad, D., Økland, O., Stefanakos, C., Stansberg, C., Croonenborghs, E., Eliassen, L., Eidnes, G., 2018. LFCS Review report - Environmental conditions. Technical Report. SINTEF Ocean.

Fructus, D., Clamond, D., Grue, J., Kristiansen, Ø., 2005. An efficient model for three-dimensional surface wave simulations: Part i: Free space problems. Journal of Computational Physics 205, 665 – 685.

Gingold, R.A., Monaghan, J.J., 1977. Smoothed particle hydrodynamics: theory and application to non-spherical stars. 181, 375–389.

Glimberg, L.S., Engsig-Karup, A.P., Nielsen, A.S., Dammann, B., 2013. Development of software components for heterogeneous many-core architectures, in: Couturier, R. (Ed.), Designing Scientific Applications on GPUs, CRC Press / Taylor & Francis Group. pp. 73–104.

Gobbi, M.F., Kirby, J.T., Wei, G., 2000. A fully nonlinear boussinesq model for surface waves. part 2. extension to o(kh)4. Journal of Fluid Mechanics 405, 181210.

Gomez-Gesteira, M., Crespo, A., Rogers, B., Dalrymple, R., Dominguez, J., Barreiro, A., 2012a. SPHysics development of a free-surface fluid solver Part 2: Efficiency and test cases. Computers Geosciences 48, 300 – 307.

Gomez-Gesteira, M., Rogers, B., Crespo, A., Dalrymple, R., Narayanaswamy, M., Dominguez, J., 2012b. SPHysics development of a free-surface fluid solver Part 1: Theory and formulations. Computers Geosciences 48, 289 – 299.

Gouin, M., Ducrozet, G., Ferrant, P., 2016. Development and validation of a non-linear spectral model for water waves over variable depth. European Journal of Mechanics - B/Fluids 57, 115 – 128.

Gouin, M., OGER, G., Le Touzé, D., 2018. Simulation of a fixed cylinder in waves using the SWENSE method within a weakly-compressible approach, in: 33rd International Workshop on Water Waves and Floating Bodies, Guidel-Plages, France.

Grilli, S.T., Guyenne, P., Dias, F., 2001. A fully non-linear model for three-dimensional overturning waves over an arbitrary bottom. International Journal for Numerical Methods in Fluids 35, 829–867.

Grilli, S.T., Horrillo, J., 1997. Numerical generation and absorption of fully nonlinear periodic waves. Journal of Engineering Mechanics 123, 1060–1069.

Grilli, S.T., Subramanya, R., Svendsen, I.A., Veeramony, J., 1994. Shoaling of solitary waves on plane beaches. Journal Waterway Port Coastal and Ocean Enigneering 120, 609–628.

Grimshaw, R., 1971. The solitary wave in water of variable depth. part 2. Journal of Fluid Mechanics 46, 611–622.

Guyenne, P., Nicholls, D.P., 2008. A high-order spectral method for nonlinear water waves over moving bottom topography. SIAM Journal on Scientific Computing 30, 81–101.

Harlow, F., Welch, J., 1965. Numerical calculation of time dependent viscous incompressible flow of fluid with a free surface. Physics of Fluids 8, 2182–2189.

Hennig, J., 2005. Generation and Analysis of Harsh Wave Environments. Ph.D. thesis. Technical University Berlin.

Higuera, P., Lara, J.L., Losada, I.J., 2013. Realistic wave generation and active wave absorption for NavierStokes models: Application to OpenFOAM. Coastal Engineering 71, 102 – 118.

Hirt, C., Nichols, B., 1981. Volume of fluid VOF method for the dynamics of free boundaries. Journal of Computational Physics 39, 201–225.

Hossain, M., Rodi, W., 1980. Mathematical modeling of vertical mixing in stratified channel flow. Second Symposium on Stratified Flows, Trondheim, Norway.

Hughes, S.A., 1993. Physical models and laboratory techniques in coastal engineering (Advanced series on ocean engineering, volume 7). Advanced Series On Ocean Engineering, World Scientific Publishing Co. Pte. Ltd, Singapore.

hypre, 2015. hypre high performance preconditioners - User's Manual. Center for Applied Scientific Computing, Lawrence Livermore National Laboratory.

Ivicsics, L., 1980. Hydraulic Models. Water Ressources Publications .

Jacobsen, N.G., Fuhrman, D.R., Fredsøe, J., 2012. A wave generation toolbox for the open-source CFD library: OpenFOAM. International Journal for Numerical Methods in Fluids 70, 1073–1088.

Jensen, J.H., Madsen, E.Ø., Fredsøe, J., 1999. Oblique flow over dredged channels. ii: Sediment transport and morphology. Journal of Hydraulic Engineering 125, 1190–1198.

Jeschke, A., Pedersen, G.K., Vater, S., Behrens, J., 2017. Depth-averaged non-hydrostatic extension for shallow water equations with quadratic vertical pressure profile: equivalence to boussinesq-type equations. International Journal for Numerical Methods in Fluids 84, 569–583.

Jiang, G., Peng, D., 2000. Weighted ENO schemes for Hamilton Jacobi equations. SIAM Journal of Scientific Computing Volume 21, 2126–2143.

Jiang, G., Shu, C., 1996. Efficient implementation of weighted ENO schemes. Journal of Computational Physics Volume 126(1), 202–228.

Jiang, G.S., Shu, C.W., 1996. Efficient implementation of weighted ENO schemes. Journal of Computational Physics 126, 202–228.

Kamath, A., Fleit, G., Bihs, H., 2019. Investigation of free surface turbulence damping in rans simulations for complex free surface flows. Water 11, 456.

Kim, S.H., Yamashiro, M., Yoshida, A., 2010. A simple two-way coupling method of bem and vof model for random wave calculations. Coastal Engineering 57, 1018 – 1028.

Kirby, J.T., Wei, G., Chen, Q., Kennedy, A.B., Dalryple, R.A., 1998. FUNWAVE 1.0 Fully Nonlinear Boussineq Wave Model Documentation and User's Manual. Technical Report. Center for Applied Coastal Research, Department of Civil Engineering, University of Delaware, Newark.

Komen, G.J., Cavaleri, L., Donelan, M., Hasselmann, K., Hasselmann, S., Janssen, P.A.E.M., 1994. Dynamics and modelling of ocean waves , 532.

Lam, D., Simpson, R., 1976. Centered differencing and the box scheme for diffusion convection problems. Journal of Computational Physics 22, 486 – 500.

Le, H., Moin, P., 1991. An improvement of fractional step methods for the incompressible navier-stokes equations. Journal of Computational Physics 92, 369 – 379.

Le Méhauté, B., 1976. An introduction to hydrodynamics and water waves. Springer-Verlag, New York.

Li, B., Fleming, C.A., 1997. A three dimensional multigrid model for fully nonlinear water waves. Coastal Engineering 30, 235 – 258.

Lindstrøm, E.K., Pedersen, G.K., Jensen, A., Glimsdal, S., 2014. Experiments on slide generated waves in a 1:500 scale fjord model. Coastal Engineering 92, 12 – 23.

Lynett, P., Liu, P.L., 2004. A two-layer approach to wave modelling. Proceedings of the Royal Society of London. Series A: Mathematical, Physical and Engineering Sciences 460, 2637–2669.

Lynett, P.J., Liu, P., Sitanggang, K., Kim, D., 2008. Modeling Wave Generation, Evolution, and Interaction with Depth-Integrated, Dispersive Wave Equations COULWAVE Code Manual Cornell University Long and Intermediate Wave Modeling Package v. 2.0. Technical Report. Cornell University.

Ma, G., Shi, F., Kirby, J.T., 2012. Shock-capturing non-hydrostatic model for fully dispersive surface wave processes. Ocean Modelling 43-44, 22 – 35.

Madsen, P.A., Bingham, H.B., Liu, H., 2002. A new Boussinesq method for fully nonlinear waves from shallow to deep water. Journal of Fluid Mechanics 462, 1–30.

Madsen, P.A., Murray, R., Sørensen, O.R., 1991. A new form of the Boussinesq equations with improved linear dispersion characteristics. Coastal Engineering 15, 371–388.

Madsen, P.A., Schäffer, H.A., 1998. Higher-order boussinesq-type equations for surface gravity waves: derivation and analysis. Philosophical Transactions of the Royal Society of London. Series A: Mathematical, Physical and Engineering Sciences 356, 3123–3181.

Madsen, P.A., Sørensen, O.R., 1992. A new form of the Boussinesq equations with improved linear dispersion characteristics. Part 2. A slowly-varying bathymetry. Coastal Engineering 18, 183 – 204.

Martin, T., Kamath, A., Bihs, H., 2018. Numerical simulation of interactions between water waves and a moored-floating breakwater. Coastal Engineering Proceedings 1.

Martin, T., Kamath, A., Bihs, H., 2019. Modeling and simulation of moored-floating structures using the tension element method. Journal of Offshore Mechanics and Arctic Engineering 142.

Massey, T.C., Anderson, M.E., Smith, J., Gomez, J., Jones, R., 2011. STWAVE: Steady-State Spectral Wave Model User's Manual for STWAVE, Version 6.0. Technical Report. US Army Corps of Engineers. Washington, DC 20314-1000.

Mayer, S., Garapon, A., Sørensen, L.S., 1998. A fractional step method for unsteady free surface flow with applications to non-linear wave dynamics. International Journal for Numerical Methods in Fluids 28, 293–315.

Mei, C.C., Stiassnie, M., Yue, D.K.P., 2005. Theory and Applications of Ocean Surface Waves. World Scientific. volume 23 of *Advanced Series on Ocean Engieering*. chapter 1.

Monteban, D., 2016. Numerical modelling of wave agitation in ports and access channels. Master's thesis. Delft University of Technology. Delft, the Netherlands.

Monteserin, C., Engsig-Karup, A.P., Eskilsson, C., 2018. Nonlinear Wave-Body Interaction Using a Mixed-Eulerian-Lagrangian Spectral Element Model, in: International Conference on Offshore Mechanics and Arctic Engineering.

Naot, D., Rodi, W., 1982. Calculation of secondary currents in channel flow. Journal of the Hydraulics Division, ASCE Volume 108, 948–968.

Narayanaswamy, M., Crespo, A.J.C., Gmez-Gesteira, M., Dalrymple, R.A., 2010. SPHysics-FUNWAVE hybrid model for coastal wave propagation. Journal of Hydraulic Research 48, 85–93.

Navionics, . Bathymetry at haringvliet. `https://webapp.navionics.com/`, year = 2020, note = Accessed: 2020-06-20.

Navionics, 2020. Bathymetry at sulafjord. `https://webapp.navionics.com/`. Accessed: 2020-06-20.

Ning, D.Z., Zang, J., Liu, S.X., Eatock Taylor, R., Teng, B., Taylor, P.H., 2009. Free-surface evolution and wave kinematics for nonlinear uni-directional focused wave groups. Ocean Engineering 36, 1226—1243.

Nwogu, O., 1993. Alternative form of Boussinesq equations for nearshore wave propagation. Journal of Waterways, Port, Coastal, and Ocean Engineering 119, 618–638.

OpenFOAM, 2019. OpenFOAM User Guide Version 7. Technical Report. The OpenFOAM Foundation.

Osher, S., Sethian, J.A., 1988. Fronts propagating with curvature-dependent speed: Algorithms based on Hamilton-Jacobi formulations. Journal of Computational Physics 79, 12–49.

Pakozdi, C., Wang, W., Bihs, H., Fouques, S., 2019a. Validation of a high-performance computing nonlinear potential theory based numerical wave tank for wave structure interaction, in: Proceedings of the Coastal Structures Conference 2019, pp. 127–137.

Pakozdi, C., Wang, W., Kamath, A., Bihs, H., 2019b. Definition of the vertical spacing of a sigma grid based on the constant truncation error, in: 10th National Conference on Computational Mechanics, MekIT19.

Patera, A.T., 1984. A spectral element method for fluid dynamics: Laminar flow in a channel expansion. Journal of Computational Physics 54, 468 – 488.

Paulsen, B.T., Bredmose, H., Bingham, H.B., 2014. An efficient domain decomposition strategy for wave loads on surface piercing circular cylinders. Coastal Engineering 86, 57–76.

Peng, D., Merriman, B., Osher, S., Zhao, H., Kang, M., 1999. A pde-based fast local level set method. Journal of Computational Physics 155.

Peregrine, D.H., 1967. Long waves on a beach. Journal of Fluid Mechanics 27, 815827.

Raoult, C., Benoit, M., Yates, M.L., 2016. Validation of a fully nonlinear and dispersive wave model with laboratory non-breaking experiments. Coastal Engineering 114, 194 – 207.

Ris, R.C., Holthuijsen, L.H., Booij, N., 1999. A third-generation wave model for coastal regions: 2. verification. Journal of Geophysical Research: Oceans 104, 7667–7681.

Rouse, H., Ince, S., 1957. History of Hydraulics .

Shu, C., Osher, S., 1988. Efficient implementation of essentially non-oscillatory shock-capturing schemes. Journal of Computational Physics Volume 77(2), 439–471.

Shu, C.W., Osher, S., 1988. Efficient implementation of essentially non-oscillatory shock capturing schemes. Journal of Computational Physics 77, 439–471.

Siemens, 2019. Simcenter STARCCM+ User Guide. Technical Report. Siemens.

Simon, B., Papoutsellis, C.E., Benoit, M., Yates, M.L., 2019. Comparing methods of modeling depth-induced breaking of irregular waves with a fully nonlinear potential flow approach. Journal of Ocean Engineering and Marine Energy .

Stansby, P.K., Zhou, J.G., 1998. Shallow-water flow solver with non-hydrostatic pressure: 2d vertical plane problems. International Journal for Numerical Methods in Fluids 28, 541–563.

Statens Vegvesen, 2019. Fjordcrossing illustrations. `https://www.vegvesen.no/vegprosjekter/ferjefriE39/illustrasjonar`. Accessed: 2020-06-05.

Statistics Norway, 2020. 11342: Areal og befolkning, etter region, statistikkvariabel og år. `https://www.ssb.no/statbank/table/11342/tableViewLayout1/`. Accessed: 2020-06-20.

Stelling, G.S., Duinmeijer, S.P.A., 2003a. A staggered conservative scheme for every froude number in rapidly varied shallow water flows. International Journal for Numerical Methods in Fluids 43, 1329–1354.

Stelling, G.S., Duinmeijer, S.P.A., 2003b. A staggered conservative scheme for every froude number in rapidly varied shallow water flows. International Journal for Numerical Methods in Fluids 43, 1329–1354.

Sussman, M., Smereka, P., Osher, S., 1994. A level set approach for computing solutions to incompressible two-phase flow. Journal of Computational Physics Volume 114, 146–159.

Sussman, M., Smereka, P., Osher, S., 1994. A level set approach for computing solutions to incompressible two-phase flow. Journal of Computational Physics 114, 146 – 159.

SWAN, 2016. SWAN USER MANUAL. 2600 GA Delft, The Netherlands.

SWASH developers, 2017. SWASH User Manual version 4.01A .

The Wamdi Group, 1988. The WAM ModelA Third Generation Ocean Wave Prediction Model. Journal of Physical Oceanography 18, 1775–1810.

Thomas, T.J., Dwarakish, G., 2015. Numerical wave modelling a review. Aquatic Procedia 4, 443 – 448.

Ting, F., Kirby, J., 1994. Observation of undertow and turbulence in a laboratory surf zone. Coastal Engineering 24, 51 – 80.

Ting, F., Kirby, J., 1996. Dynamics of surf-zone turbulence in a spilling breaker. Coastal Engineering 27, 131 – 160.

Ting, F.C.K., Kirby, J.T., 1995. Dynamics of surf-zone turbulence in a strong plunging breaker. Coastal Engineering 24, 177–204.

Tromans, P.S., Anaturk, A.R., Hagemeijer, P., 1991. A new model for the kinematics of large ocean waves-application as a design wave, in: The First International Offshore and Polar Engineering Conference, International Society of Offshore and Polar Engineers, Edinburgh, The United Kingdom. p. 8.

Vaz, G., Jaouen, F., Hoekstra, M., 2009. Free-Surface Viscous Flow Computations: Validation of URANS Code FreSCo, pp. 425–437.

Vegvesen, S., 2019. Ferjefri E39. Technical Report. The Norwegian Road Administration.

Vold, S., Lothe, A.E., 2009. Mehamn - modellforsøk. Technical Report SBF IN F09203. SINTEF Byggforsk. Trondheim.

van der Vorst, H., 1992. BiCGStab: A fast and smoothly converging variant of Bi-CG for the solution of nonsymmetric linear systems. SIAM Journal of Scientific Computing Volume 13, 631–644.

van der Vorst, H., 1992. BiCGStab: A fast and smoothly converging variant of Bi-CG for the solution of nonsymmetric linear systems. SIAM Journal of Scientific Computing 13, 631–644.

Wang, W., Bihs, H., Kamath, A., Arntsen, Ø.A., 2017. Large scale CFD modelling of wave propagation in Sulafjord for the E39 project. Proceedings of MekIT17 - 9th national conference on Computational Mechanics .

Wang, W., Martin, T., Kamath, A., Bihs, H., 2020. An improved depth-averaged non-hydrostatic shallow water model with quadratic pressure approximation. International Journal for Numerical Methods in Fluids .

Wei, G., Kirby, J.T., Grilli, S.T., Subramanya, R., 1995. A fully nonlinear boussinesq model for surface waves. part 1. highly nonlinear unsteady waves. Journal of Fluid Mechanics 294, 7192.

West, B.J., Brueckner, K.A., Janda, R.S., Milder, D.M., Milton, R.L., 1987. A new numerical method for surface hydrodynamics. Journal of Geophysical Research: Oceans 92, 11803–11824.

Wilcox, D.C., 1988. Reassessment of the scale-determining equation for advanced turbulence models. AIAA Journal 26, 1299–1310.

Yang, J., Stern, F., 2013. Robust and Efficient Setup Procedure for Complex Triangulations in Immersed Boundary Simulations. Journal of Fluids Engineering Volume 135 (10), 101107.1–101107.11.

Yates, M.L., Benoit, M., 2015. Accuracy and efficiency of two numerical methods of solving the potential flow problem for highly nonlinear and dispersive water waves. International Journal for Numerical Methods in Fluids 77, 616–640.

Zakharov, V.E., 1968. Stability of periodic waves of finite amplitude on the surface of a deep fluid. Journal of Applied Mechanics and Technical Physics 9, 190–194.

Zhang, F., Crespo, A., Altomare, C., Domínguez, J., Marzeddu, A., Shang, S.p., Gómez-Gesteira, M., 2018. DualSPHysics: A numerical tool to simulate real breakwaters. Journal of Hydrodynamics 30, 95–105.

Zhang, J., Benoit, M., Kimmoun, O., Chabchoub, A., Hsu, H.C., 2019. Statistics of extreme waves in coastal waters: Large scale experiments and advanced numerical simulations. Fluids 4.

Zhou, J., Stansby, P., 1999. An arbitrary lagrangian-eulerian σ (ales) model with non-hydrostatic pressure for shallow water flows. Computer Methods in Applied Mechanics and Engineering 178, 199 – 214.

Zijlema, M., Stelling, G., 2008. Efficient computation of surf zone waves using the nonlinear shallow water equations with non-hydrostatic pressure. Coastal Engineering 55, 780 – 790.

Zijlema, M., Stelling, G., Smit, P., 2011a. SWASH: An operational public domain code for simulating wave fields and rapidly varied flows in coastal waters. Coastal Engineering 58, 992–1012.

Zijlema, M., Stelling, G., Smit, P., 2011b. SWASH: An operational public domain code for simulating wave fields and rapidly varied flows in coastal waters. Coastal Engineering 58, 992 – 1012.

Zijlema, M., Stelling, G.S., 2005. Further experiences with computing non-hydrostatic free-surface flows involving water waves. International Journal for Numerical Methods in Fluids 48, 169–197.

Chapter 6

Appended Publications

Paper 1 Wang W., Martin T., Kamath A. and Bihs H. 2020. **An improved depth-averaged non-hydrostatic shallow water model with quadratic pressure approximation**. *International Journal for Numerical Methods in Fluids*, 1-22.

Paper 2 Bihs H., Wang W., Pákozdi C. and Kamath A. 2020. **REEF3D::FNPF - a flexible fully nonlinear potential flow solver**. *Journal of Offshore Mechanics and Arctic Engineering* 142(4).

Paper 3 Wang W., Kamath A., Pákozdi C. and Bihs H. 2019. **Investigation of focusing wave properties in a numerical wave tank with a fully nonlinear potential flow model**. *Journal of Marine Science and Engineering* 7(10), 375.

Paper 4 Wang W., Pákozdi C, Kamath A. and Bihs H. **A fully nonlinear potential flow wave modelling procedure for full-scale simulations of sea states with various wave breaking scenarios**. Submitted to *Ocean Engineering* 2020.

Paper 5 Wang W., Pákozdi C., Kamath A., Fouques S. and Bihs H. **A flexible fully nonlinear potential flow model for wave propagation over the complex topography of the Norwegian coast**. Submitted to *Applied Ocean Research* 2020.

Paper 6 Wang W., Pákozdi C, Kamath A. and Bihs H. **Phase-resolved wave modelling in the Norwegian fjords for the ferry-free E39 project**. Submitted to *Journal of Ocean Engineering and Marine Energy* 2020.

Paper 7 Wang W., Kamath A., Pákozdi C. and Bihs H. **A comparison of different wave modelling techniques in an open-source hydrodynamic framework**. Submitted to *Journal of Marine Science and Engineering* 2020.

Paper 1

An improved depth-averaged non-hydrostatic shallow water model with quadratic pressure approximation

Wang W., Martin T., Kamath A. and Bihs H. (2020)
International Journal for Numerical Methods in Fluids, 1-22.

An Improved Depth-Averaged Non-Hydrostatic Shallow Water Model with Quadratic Pressure Approximation

Weizhi Wang*, Tobias Martin, Arun Kamath and Hans Bihs

Department of Civil and Environmental Engineering
Norwegian University of Science and Technology (NTNU)
7491 Trondheim, Norway

International Journal For Numerical Methods In Fluids, 2020, pp. 1-22.
DOI: http://dx.doi.org/10.1002/fld.4807

Abstract

Phase-resolved information is necessary for many coastal wave problems, for example, for the wave conditions in the vicinity of harbour structures. Two-dimensional (2D) depth-averaging shallow water models are commonly used to obtain a phase-resolved solution near the coast. These models are in general more computationally effective compared to computational fluid dynamics (CFD) software and will be even more capable if equipped with a parallelised code. In the current paper, a 2D wave model solving the depth-averaged continuity equation and the Euler equations is implemented in the open-source hydrodynamic code REEF3D. The model is based on a non-hydrostatic extension and a quadratic vertical pressure profile assumption which provides a better approximation of the frequency dispersion. It is the first model of its kind to employ high-order discretisation schemes and to be fully parallelised following the domain decomposition strategy. Wave generation and absorption are achieved with a relaxation method. The simulations of non-linear long wave propagations and transformations over non-constant bathymetries are presented. The results are compared to benchmark wave propagation cases. A large-scale wave propagation simulation over realistic irregular topography is shown to demonstrate the model's capability of solving operational large-scale problems.

Keywords: wave modelling; numerical simulation; shallow water equations; dynamic pressure; quadratic profile

*Corresponding author, weizhi.wang@ntnu.no
Postprint, published in International Journal For Numerical Methods In Fluids, doi:http://dx.doi.org/10.1002/fld.4807

1 Introduction

Phase-resolved wave modelling is required for many applications in coastal engineering. It enables a time-domain analysis and presents more details for complex free-surface phenomena. Many efforts have been made to solve the Navier-Stokes equations for water waves with the fast development of computational infrastructures and the application of parallel computation techniques. Various methods have been used to capture the free-surface, such as the volume-of-fluid method (Jacobsen et al. (2012); Higuera et al. (2013a); Hirt and Nichols (1981)), the level set method (Bihs et al. (2016); Osher and Sethian (1988)) and the smooth particle hydrodynamics method (Dalrymple and Rogers (2006); Altomare et al. (2017); Chow et al. (2019)). Navier-Stokes solvers in combination with one of the aforementioned free-surface treatment methods are able to provide high-resolution results for complicated marine free-surface flows and near-field wave hydrodynamics. One example that is closely related to the current work is the open-source hydrodynamics model REEF3D. In Kamath et al. (2016), the solver was used to analyse non-breaking wave forces on various configurations of multiple vertical circular cylinders. Further simulations of marine fluid-structure interaction were performed for semi-submerged horizontal circular cylinders in tandem (Ong et al. (2017)), and non-linear marine hydrodynamics were investigated in detail (Aggarwal et al. (2018)). Broader applications of the model are also seen on the sediment transport analysis (Ahmad et al. (2018)) and the coastal infrastructure design (Sasikumar et al. (2018)). Typically, these simulations require relatively fine three-dimensional grids and are, therefore, more computationally demanding.

Phase-resolved modelling of the far-field wave field is important for delivering a realistic wave generation boundary condition for higher resolution near-field wave modelling. However, the far-field wave propagation towards the coast is a large-scale phenomenon, which puts a limitation on the application of the Navier-Stokes approach in spite of the increasing computational capacities. Less computationally demanding models are required to model the far-field large-scale phase-resolved wave propagation efficiently. As most coastal areas share relatively shallower water conditions, depth-averaged shallow water models have been favoured for the coastal wave modelling. These models are essentially two-dimensional and, thus, require less cells. The advances of such models have been focused on developing numerical methods to accurately capture the frequency dispersion relation and the non-linearity when the water depth increases or a rapidly varying bathymetry is involved. A common representative of shallow water models is the Boussinesq-type wave model (Madsen et al. (1991); Nwogu (1993)). Here, the lack of vertical flow information is compensated through the Boussinesq terms which help to calculate the correct frequency dispersion of the waves. This approach is valid from shallow to deep water, depending on the order of the Boussinesq terms (Lynnett and Liu (200451)). However, higher-order mixed time-space derivatives in the Boussinesq equations tend to cause numerical instabilities. More recently, the possibility of using non-hydrostatic shallow equations with a single layer or multiple layers in the vertical direction has been explored by Zijlema and Stelling (Stelling and Zijlema (2003); Zijlema et al. (2005); Zijlema and Stelling (2008); Zijlema et al. (2011a)). With an increasing number of vertical layers, the flow information in the vertical direction is better resolved. However, it has been shown previously that the increase of vertical layers leads to a significant increase in computational costs. For example, Monteban (2016) observed that the simulation time using two layers is nearly 10 times compared to that using a single layer. Cui et al. (2014) improved the two-layer approach such that it has similar computational efficiency as a one-layer counterpart and, yet, maintaining a high linear dispersion accuracy. While the commonly used vertical pressure profile is linear, a quadratic pressure approach has been presented by Jeschke et al. (2017). It is stated that, with an approximation of a proposed quadratic vertical pressure profile, the model can achieve at least a good equivalence to existing fully non-linear weakly dispersive Boussinesq models (Jeschke et al. (2017)). This method presents itself as an attractive alternative for modelling shallow water waves, while potentially avoiding the numerical instabilities due to higher-order terms in a Boussinesq-type model and the increased computational costs from a larger number of vertical layers in a multi-layer non-hydrostatic model. However, only simple scenarios such as one-dimensional (1D) standing waves and progressive solitary waves over a flat bottom have been investigated previously (Jeschke et al. (2017)). Here, several terms of the derived equations are neglected which leaves the final question of reliability open. It is reported by Jeschke (2018) that it is challenging to incorporate the vital term involving the varying bathymetry into her numerical model. As a result, the model's accuracy is seen to be less ideal than the theoretical expectations when changing bottom is present. Therefore, this paper includes a numerical procedure to discretise this term appropriately. This enables the authors to emphasise the accuracy gain from the quadratic pressure approximation for non-constant bathymetries.

The accuracy of shallow water models has been improved over the last years. High-order numerical schemes are employed in the development of Boussinesq-types models. Wei and Kirby (1995) applied a 4^{th}-order accurate AdamsBashforthMoulton (ABM) scheme for the time discretisation and a mixed 4^{th}-order and 2^{nd}-order scheme for the spatial discretisation. Shi et al. (2012) employed a mixed finite volume and finite difference method using a 4^{th}-order accurate MUSCL (Monotone Upstream-centered Schemes for Conservation Laws) reconstruction technique for the advection term and a 3^{rd}-order Runge-Kutta scheme for temporal discretisation. However, few high-order implementations are presented for non-hydrostatic models. Zijlema et al. (2011*b*) present their model using a 2^{nd}-order discretisation scheme in space and a 2^{nd}-order leapfrog algorithm in time. Jeschke et al. (2017) implement the quadratic pressure model with the 2^{nd}-order ${P_1}^{NC} - P_1$ finite element method (Hanert et al. (2005); Roux and Pouliot (2008)) for the advection terms and a Leapfrog method for the time stepping. In a recent development, Jeschke (2018) also implemented a 2^{nd}-order discontinuous Galerkin scheme in the model. Thus, high-order numerical implementations are left to be fulfilled in order to advance the development of non-hydrostatic models.

In addition, parallel computations are incorporated in many shallow water models in case of computationally demanding simulations. Shi et al. (2012) presents a parallelized Boussinesq model following the domain decomposition strategy with a Message Passing Interface (MPI). Good scaling characteristic is observed up to 48 cores. Zijlema et al. (2011*b*) also uses the same parallelisation technique and achieve linear scalability up to 8 cores. However, the newly proposed quadratic pressure approximation (Jeschke et al. (2017)) has not been incorporated into any parallel code. A good scalability up to hundreds of processors is also not presented in the literature regarding shallow water models in general. For large-scale operational engineering applications, such scalability is in great demand.

Ensuring high-quality input waves is another important aspect in the development of a shallow water model. The typical practice is to impose the surface elevation and the depth-averaged velocities to the boundary (Madsen et al. (1991); Nwogu (1993); Wei et al. (1995); Zijlema et al. (2011*b*); Shi et al. (2012); Chen et al. (2003)). Periodic boundary conditions are also widely used, for example, a spatial periodic boundary condition is applied by Madsen et al. (2002), and a double periodic boundary condition is implemented in (Jeschke et al. (2017)). Another popular wave generation method is the relaxation method (Mayer et al. (1998); Jacobsen et al. (2012)) which has high flexibility and tends to result in less reflected waves (Miquel et al. (2018)). This method has been widely implemented in Navier-Stokes solvers (Azimi et al. (2014)) but remains absent in the development of shallow water models. The feasibility of using a relaxation method for the wave generation and absorption in a non-hydrostatic shallow water model remains to be explored.

In the presented paper, REEF3D::SFLOW is introduced as a novel non-hydrostatic shallow water model following the quadratic pressure approximation (Jeschke et al. (2017)). Developed as a part of the REEF3D framework, the proposed model has direct access to all the existing numerical schemes and parallelisation algorithms in REEF3D. Thus, the model presents itself as the first non-hydrostatic shallow water model with high-order discretisation schemes, for example, a 5^{th}-order Weighted-Essentially-Non-Oscillatory (WENO) scheme in spatial discretisation and a 3^{rd} to 4^{th}-order Runge-Kutta scheme for the temporal discretisation. The model also innovatively employs the relaxation method (Jacobsen et al. (2012)) for the wave generation and absorption. With a model equipped with high-order numerical methods, this paper presents for the first time the simulations of non-linear long wave propagations over varying bathymetries using the quadratic pressure approximation. In these simulations, the equations with the depth-related terms are solved and the overall performance gain from the quadratic pressure approximation is investigated comprehensively. Computational scalability up to multi-hundred cores is demonstrated with the proposed model. An expanded validation process is then presented, including several well-known benchmark cases incorporating wave propagation over changing topographies and wave-structure interactions. Additionally, a large-scale coastal wave propagation over a natural topography is presented to demonstrate the model's capability for engineering applications.

2 Numerical Theory

The mass and momentum conservation for an incompressible inviscid flow leads to the continuity and Euler equations in three dimensions:

$$\frac{\partial U}{\partial x} + \frac{\partial V}{\partial y} + \frac{\partial W}{\partial z} = 0, \tag{1}$$

$$\frac{\partial U}{\partial t} + U\frac{\partial U}{\partial x} + V\frac{\partial U}{\partial y} + W\frac{\partial U}{\partial z} = -\frac{1}{\rho}\frac{\partial P_T}{\partial x}, \tag{2}$$

$$\frac{\partial V}{\partial t} + U\frac{\partial V}{\partial x} + V\frac{\partial V}{\partial y} + W\frac{\partial V}{\partial z} = -\frac{1}{\rho}\frac{\partial P_T}{\partial y}, \tag{3}$$

$$\frac{\partial W}{\partial t} + U\frac{\partial W}{\partial x} + V\frac{\partial W}{\partial y} + W\frac{\partial W}{\partial z} = -\frac{1}{\rho}\frac{\partial P_T}{\partial z} - g. \tag{4}$$

where U, V and W are velocities in x, y and z directions, ρ is the constant density, P_T represents the total pressure and g is the gravitational acceleration. Additional source terms such as bottom friction and turbulent stresses are omitted here but are straightforward to include if needed.

The water depth $h = d+\zeta$ consists of two parts: the still water depth d and the free-surface elevation ζ, as displayed in Fig. 1. Defining the horizontal velocity vector as $\boldsymbol{U} = (U, V)$, the kinematic boundary conditions at the free-surface and the bottom are:

$$W|_\zeta = \frac{\partial \zeta}{\partial t} + \boldsymbol{U}|_\zeta \cdot \nabla \zeta, \tag{5}$$

$$W|_{-d} = -\boldsymbol{U}|_{-d} \cdot \nabla d. \tag{6}$$

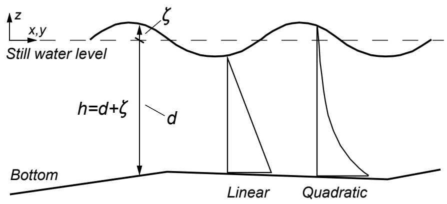

Figure 1: Basic definitions in the shallow water model: the water depth h, the still water depth d, the free-surface elevation ζ, the coordinates system and the schematics of the assumed linear pressure profile and quadratic pressure approximation

The shallow water assumption, i.e. the horizontal acceleration is much greater than the vertical acceleration, implies a hydrostatic pressure. In order to get a hydrodynamic pressure correction, the total pressure P_T is assumed to consist of a hydrostatic part P and a hydrodynamic part Q. The pressure and its boundary condition at the free-surface is given by:

$$P_T = P + Q = \rho g(\zeta - z) + Q, \tag{7}$$

$$P_T|_\zeta = P|_\zeta = Q|_\zeta = 0. \tag{8}$$

The velocities and the dynamic pressure are depth-averaged by integrating over the water depth:

$$\boldsymbol{u} = (u, v) = \frac{1}{h}\int_{-d}^{\zeta} \boldsymbol{U}\,\mathrm{d}\,z; \quad w = \frac{1}{h}\int_{-d}^{\zeta} W\,\mathrm{d}\,z; \quad q = \frac{1}{h}\int_{-d}^{\zeta} Q\,\mathrm{d}\,z \tag{9}$$

In contrast to previous models (Zijlema et al. (2011*b*)), where the pressure is solved at the bottom, the proposed model consists of only depth-averaged quantities. A relation between the depth-averaged pressure q and the pressure at the bottom $Q|_{-d}$ needs to be defined in order to close the system. If the linear pressure profile (Stelling and Zijlema (2003); Zijlema et al. (2011*b*)) is assumed, the pressure at the bottom is simply twice the depth-averaged pressure, or:

$$Q|_{-d} = 2q. \tag{10}$$

Consequently, the governing equations with only depth-averaged variables are:

$$\frac{\partial \zeta}{\partial t}+\frac{\partial hu}{\partial x}+\frac{\partial hv}{\partial y}=0, \tag{11}$$

$$\frac{\partial u}{\partial t}+u\frac{\partial u}{\partial x}+v\frac{\partial u}{\partial y}=-g\frac{\partial \zeta}{\partial x}-\frac{1}{\rho h}\left(\frac{\partial hq}{\partial x}-2q\frac{\partial d}{\partial x}\right), \tag{12}$$

$$\frac{\partial v}{\partial t}+u\frac{\partial v}{\partial x}+v\frac{\partial v}{\partial y}=-g\frac{\partial \zeta}{\partial y}-\frac{1}{\rho h}\left(\frac{\partial hq}{\partial y}-2q\frac{\partial d}{\partial y}\right), \tag{13}$$

$$\frac{\partial w}{\partial t}+u\frac{\partial w}{\partial x}+v\frac{\partial w}{\partial y}=-\frac{2q}{\rho h}. \tag{14}$$

Jeschke et al. (2017) replaces the linear assumption with a quadratic vertical pressure profile as shown in Eqn. (15).

$$Q|_{-d}=\frac{3}{2}q+\frac{1}{4}\rho h\Phi, \tag{15}$$

$$\Phi=-\nabla d\cdot(\partial_t \boldsymbol{u}+(\boldsymbol{u}\cdot\nabla)\boldsymbol{u})-\boldsymbol{u}\cdot\nabla(\nabla d)\cdot\boldsymbol{u}. \tag{16}$$

Following the quadratic assumption, the governing equations with depth-averaged variables become:

$$\frac{\partial \zeta}{\partial t}+\frac{\partial hu}{\partial x}+\frac{\partial hv}{\partial y}=0, \tag{17}$$

$$\frac{\partial u}{\partial t}+u\frac{\partial u}{\partial x}+v\frac{\partial u}{\partial y}=-g\frac{\partial \zeta}{\partial x}-\frac{1}{\rho h}\left(\frac{\partial hq}{\partial x}-\left(\frac{3}{2}q+\frac{1}{4}\rho h\Phi\right)\frac{\partial d}{\partial x}\right), \tag{18}$$

$$\frac{\partial v}{\partial t}+u\frac{\partial v}{\partial x}+v\frac{\partial v}{\partial y}=-g\frac{\partial \zeta}{\partial y}-\frac{1}{\rho h}\left(\frac{\partial hq}{\partial y}-\left(\frac{3}{2}q+\frac{1}{4}\rho h\Phi\right)\frac{\partial d}{\partial y}\right), \tag{19}$$

$$\frac{\partial w}{\partial t}+u\frac{\partial w}{\partial x}+v\frac{\partial w}{\partial y}=\frac{1}{\rho h}\left(\frac{3}{2}q+\frac{1}{4}\rho h\Phi\right). \tag{20}$$

The governing equations with the boundary conditions are solved on a structured staggered grid using a finite difference method (FDM). Chorin's projection method (Chorin (1968)) is applied for the solution of the velocities. The 5^{th}-order conservative finite difference Weighted-Essentially-Non-Oscillatory (WENO) scheme proposed by Jiang and Shu (1996) is used for the discretisation of convective terms for the velocities u,v and w. The Total-Variation-Diminishing (TVD) 3^{rd}-order Runge-Kutta explicit time scheme developed by Shu and Osher (1988) is employed for time discretisation. It involves the calculation of the spatial derivatives and the dynamics pressure three times per time step. The information containing pressure is solved using the Poisson equation:

$$\frac{h_p}{\rho}\left(\frac{\partial^2 q}{\partial x^2}+\frac{\partial^2 q}{\partial y^2}\right)+\frac{2q}{\rho h_p}=\frac{1}{\partial x\partial t}\left(-h_p\left(\frac{\partial u}{\partial x}+\frac{\partial v}{\partial y}\right)-2w-u\frac{\partial d}{\partial x}-v\frac{\partial d}{\partial y}\right) \tag{21}$$

Here, the parameter h_p denotes the water level in the centre of the cell. In a staggered grid arrangement, this is where the dynamic pressure q, the vertical velocities w and the free surface location ζ are solved. The horizontal velocities are solved at the faces of the cells. The high-performance solver library HYPRE (Hypre (2015)) is employed to solve the Poisson pressure equation using the PFMG-preconditioned BiCGStab algorithm (Ashby and Flagout

(1996)). The dynamic pressure q is then used to correct the velocities in a correction step. Hence, the corrections of the velocities with the quadratic pressure approximation are

$$u^{n+1} = u^* + \Delta t \left(\frac{3}{2} \frac{q^{n+1}}{\rho h_p} \frac{\partial d}{\partial x} + \frac{1}{4} \Phi \frac{\partial d}{\partial x} \right), \tag{22}$$

$$v^{n+1} = v^* + \Delta t \left(\frac{3}{2} \frac{q^{n+1}}{\rho h_p} \frac{\partial d}{\partial y} + \frac{1}{4} \Phi \frac{\partial d}{\partial y} \right), \tag{23}$$

$$w^{n+1} = w^* + \Delta t \left(\frac{3}{2} \frac{q^{n+1}}{\rho h_p} + \frac{1}{4} \Phi \right). \tag{24}$$

where u^*, v^*, w^* are intermediate-step velocities with only hydrostatic pressure.

The term Φ on the right-hand side of Eqn. (18) to Eqn. (20) is treated with a procedure following the principles of the fractional step method of Le and Moin (1991). Assuming the dynamic pressure does not change significantly within one Runge-Kutta sub-step, the intermediate velocities u^*, v^*, w^* are corrected with the dynamic pressure gradients of the previous sub-step:

$$u^{**} = u^* - \frac{\partial q^{n,rk}}{\partial x}, \tag{25}$$

$$v^{**} = v^* - \frac{\partial q^{n,rk}}{\partial y}, \tag{26}$$

$$w^{**} = w^* - \frac{\partial q^{n,rk}}{\partial z}, \tag{27}$$

where $q^{n,rk}$ is the dynamic pressure from the previous Runge-Kutta sub-step. The spatial derivatives of Φ are updated with the corrected velocities u^{**}, v^{**} and w^{**} in equation Eqn. 16, which is then inserted into Eqn. (22) to Eqn. (24) to obtain the velocities at the new time step. The time derivative term inside Φ is then calculated with simple finite differences:

$$\partial_t \boldsymbol{u} = \frac{u^{**} - u^{n,rk}}{\alpha \Delta t}, \tag{28}$$

$$\partial_t \boldsymbol{v} = \frac{v^{**} - v^{n,rk}}{\alpha \Delta t}, \tag{29}$$

$$\partial_t \boldsymbol{w} = \frac{w^{**} - w^{n,rk}}{\alpha \Delta t}, \tag{30}$$

$$\tag{31}$$

where α is the increment factor of the corresponding Runge-Kutta sub-step and $u^{n,rk}$, $v^{n,rk}$, $w^{n,rk}$ are the velocities from the previous Runge-Kutta sub-step.

Parallel computation is enabled by decomposing the simulation domain into smaller sub-domains. The communication between these domains is achieved through a ghost cell approach. The message passing interface (MPI) is then used for the communication at the sub-domain boundaries.

The location of the free-surface ζ is determined based on the divergence of the depth-integrated horizontal velocities as given in Eqn. (17). The free-surface is reconstructed using the 5^{th}-order WENO scheme (Jiang and Shu (1996)). The solutions of the stencils are weighted, i.e. a coefficient or weight is assigned to the solution of each stencil. The scheme assigns the largest weight to the smoothest solution and can therefore handle large-gradient free-surface changes caused by the varying bathymetry. As an example, the discretised form of Eqn. (17) in x-direction is presented in Eqn. (32).

$$\frac{\zeta_i^{n+1}-\zeta_i^n}{\triangle t}+\frac{\widehat{h}^n_{i+1/2}u^{n+1/2}_{i+1/2}-\widehat{h}^n_{i-1/2}u^{n+1/2}_{i-1/2}}{\triangle x}=0, \tag{32}$$

where $\widehat{h}_{i+1/2}$ is the water level at the cell face $i+1/2$. $\widehat{h}_{i+1/2}$ is reconstructed with the WENO procedure:

$$\widehat{h}^{\pm}_{i+1/2}=\omega_1^{\pm}\widehat{h}^{1\pm}_{i+1/2}+\omega_2^{\pm}\widehat{h}^{2\pm}_{i+1/2}+\omega_3^{\pm}\widehat{h}^{3\pm}_{i+1/2}. \tag{33}$$

The $\pm$ sign indicates the upwind direction. The nonlinear weights $\omega_n^{\pm}$ are calculated for each ENO stencil based on the smoothness indicators (Jiang and Shu (1996)). For the upwind direction in the positive i-direction, the three possible ENO stencils $\widehat{h}^1$, $\widehat{h}^2$ and $\widehat{h}^3$ are:

$$\widehat{h}^{1-}_{i+1/2}=\frac{1}{3}h_{i-2}-\frac{7}{6}h_{i-1}+\frac{11}{6}h_i, \tag{34}$$

$$\widehat{h}^{2-}_{i+1/2}=-\frac{1}{6}h_{i-1}+\frac{5}{6}h_i+\frac{1}{3}h_{i+1}, \tag{35}$$

$$\widehat{h}^{3-}_{i+1/2}=\frac{1}{3}h_i+\frac{5}{6}h_{i+1}-\frac{1}{6}h_{i+2}. \tag{36}$$

Wetting and drying are handled by setting the velocities in cells below a certain user-defined threshold of the water level to zero:

$$\begin{cases} u=0, & if\ \widehat{h}_x < threshold, \\ v=0, & if\ \widehat{h}_y < threshold. \end{cases} \tag{37}$$

The default threshold is set to be 0.00005 m, which is used throughout the presented work. The approach tracks the variation of the shoreline accurately and avoids numerical instabilities by ensuring non-negative water depth (Stelling and Duinmeijer (2003); Zijlema and Stelling (2008)).

Wave generation and absorption are carried out with the relaxation method as described in Bihs et al. (2016). The relaxation function formulated by Jacobsen (Jacobsen et al. (2012)) is used in the proposed model:

$$\Gamma(\widetilde{x})=1-\frac{e^{(\widetilde{x}^{3.5})}-1}{e-1}\ for\ \widetilde{x}\in[0;1], \tag{38}$$

where $\widetilde{x}$ is scaled to the length of the relaxation zone. The velocities u, v, the surface elevation ζ and the pressure p are increased to the analytical values in the wave generation zone and reduced to zero or initial still wave values in the wave energy dissipation zone:

$$u(\widetilde{x})_{relaxed}=\Gamma(\widetilde{x})u_{analytical}+(1-\Gamma(\widetilde{x}))u_{computational}, \tag{39}$$

$$v(\widetilde{x})_{relaxed}=\Gamma(\widetilde{x})v_{analytical}+(1-\Gamma(\widetilde{x}))v_{computational}, \tag{40}$$

$$\zeta(\widetilde{x})_{relaxed}=\Gamma(\widetilde{x})\zeta_{analytical}+(1-\Gamma(\widetilde{x}))\zeta_{computational}, \tag{41}$$

$$p(\widetilde{x})_{relaxed}=\Gamma(\widetilde{x})p_{analytical}+(1-\Gamma(\widetilde{x}))p_{computational}. \tag{42}$$

All types of wave theories, type of wavemakers and wave signal input available in the existing code are applicable to the proposed shallow water model as well.

A breaking wave criterion is introduced (The SWASH Team (2017)) to represent the wave breaking process. The wave breaking is initialised when the vertical velocity of the free-surface exceeds a fraction of the shallow water celerity:

$$\frac{\partial \zeta}{\partial t} > \alpha \sqrt{gh}. \tag{43}$$

At the same time, the dynamic pressure is neglected and remains so at the front of the breaker. For the persistence of the wave breaking, the coefficient β $(0 < \beta < \alpha)$ is introduced in Eqn. (43) instead of α to stop the wave breaking process. The computations become non-hydrostatic again when the vertical velocity of the free-surface falls out of the range of the criterium. $\alpha = 0.6$ and $\beta = 0.3$ are recommended as they work well with most of the waves (The SWASH Team (2017)). By introducing the wave breaking criterion and removing the dynamic pressure during breaking, the momentum is well conserved, the energy dissipation is well represented and the asymmetry and skewness of non-linearity are respected (The SWASH Team (2017)).

3 Verification

The proposed numerical model REEF3D::SFLOW is first verified for the wave propagation in a 28 m long one-dimensional flume as shown in Fig. 2. The wave generation zone of one wavelength is at the inlet of the flume, and a wave energy dissipation zone of two wavelengths is located at the outlet. Four different wave cases are simulated with the proposed model.

3.1 Linear progressive wave propagation over constant bathymetry

First, a linear wave (Dean and Dalrymple (1991*b*)) of wave height $H = 0.02$ m and wavelength $L = 4$ m is simulated for 60 s. The water depth is constant at 0.5 m, correspondingly $kd = 0.25\pi$. A grid convergence study is initially performed with the cell sizes of 0.01 m, 0.02 m, 0.04 m and 0.08 m. Only one cell exits in the y-direction and its size equals to that in the x-direction. The Courant-Friedrichs-Lewy (CFL) number is kept constant at 0.2 for all cases. The wave profiles obtained using different cell sizes at $t = 90$ s are compared in Fig. 3a. As can be seen, $dx = 0.04$ m and $dx = 0.08$ m under-predict the wave height and show minor phase differences. The cell size of $dx = 0.02$ m represents the wave propagation sufficiently well, with a similar result as $dx = 0.01$ m. The average wave heights of the last ten wave periods in the time series at the wave gauge at $x = 14.5$ m from the inlet boundary are used to quantify the grid convergence property. The relative error between the averaged wave height and the theoretical value together with the L2 norm of the absolute errors are summarised in Table 2. A monotonic reduction of the error can be observed with the refinement of the grids.

Further, a series of simulations are performed with different CFL numbers of 0.1, 0.2, 0.3 and 0.4 to investigate the impact of the time step. For this purpose, a constant cell size of 0.02 m is utilized. The different wave profiles at $t = 90$ s are compared in Fig. 3b. All tested CFL numbers represent the phase information well in comparison to the theoretical wave. For $CFL = 0.3$ and 0.4, the wave height seems to reduce. The wave height information is better represented for $CFL = 0.1$ and 0.2, while an over-estimation of wave crest is noticed with $CFL = 0.1$ in the chosen time frame. The relative errors and the L2 norms of errors are summarised in Table 1. CFL number of 0.2 matches both the trough and crest well and errors approach to the ones with CFL number 0.1. As a result, $CFL = 0.2$ will be used in all the following simulations of this paper. Fig. 4a shows that the linear progressive wave is well represented by the solver at an intermediate water depth. Both, the wave height and phase are matching satisfactorily. It is also noticeable that the relaxation method dissipates the wave energy well at the wave energy dissipation zone where the surface elevation remains constant at the still water level and no artificial reflection is observed.

The advantage of the quadratic pressure approximation is demonstrated by comparing the surface elevation with quadratic pressure approximation with the linear pressure profile in Stelling and Zijlema (2003); Zijlema et al. (2011*b*) (see Fig. 4b). It is observed that, with a linear pressure assumption, the wave phase starts to shift shortly after the waves propagate outside the generation zone. In contrast, the quadratic pressure approximation improves the phase accuracy significantly and approximates the theoretical value more precisely due to a better representation of dispersion.

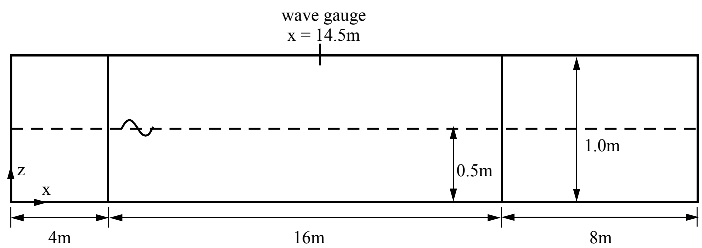

Figure 2: The numerical wave tank set-up of the 1D flume for linear progressive waves, view from the side. The left-hand side is the wave generation zone of one wavelength, the right-hand side is the wave energy dissipation zone of two wavelengths. The water depth is constant at 0.5 m.

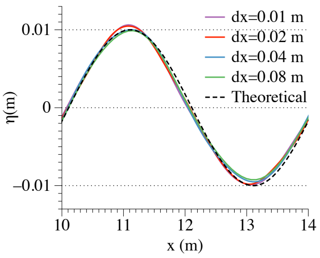

(a) Grid convergence study

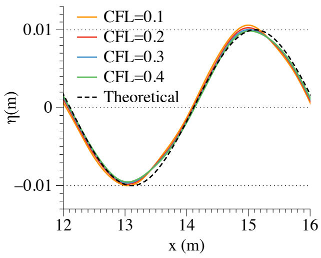

(b) Time step convergence study

Figure 3: The convergence study of the linear progressive wave simulation in a 1D wave flume with REEF3D::SFLOW: (a) grid convergence study (CFL number is kept constant 0.2), (b) time step convergence study.

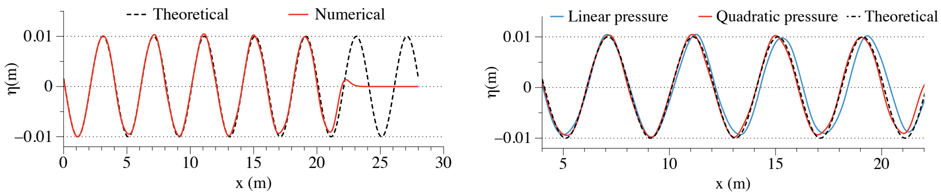

(a) (b)

Figure 4: The wave surface elevation profiles at $t = 90$ s with a linear wave of wave height $H = 0.02$ m, wavelength $L = 4$ m, cell size $dx = 0.02$ m and $CFL = 0.2$: (a) quadratic pressure approximation in the vertical direction; (b) comparison between quadratic pressure approximation and linear pressure profile in the vertical direction.

Table 1: The spatial discretisation error analysis for the progressive linear wave simulation.

dx (m)	$\overline{H}$ (m)	relative error	L2 error
0.08	0.0186	-7.00 %	0.0046
0.04	0.0193	-3.50 %	0.0023
0.02	0.0196	-2.00 %	0.0014
0.01	0.0197	-1.50%	0.0010

Table 2: The CFL error analysis for progressive linear wave simulation.

CFL	$\overline{H}$ (m)	relative error	L2 error
0.4	0.0192	-4.00 %	0.0024
0.3	0.0194	-3.00 %	0.0019
0.2	0.0196	-2.00 %	0.0014
0.1	0.0197	-1.50%	0.0009

3.2 2^{nd}-order Stokes wave propagation over constant bathymetry

Next, a 2^{nd}-order Stokes wave (Dean and Dalrymple (1991*b*)) of $H = 0.1$ m and $L = 4$ m is simulated in the same 1D numerical flume. The grid convergences study is presented in Fig. 5a. Similar to the previous study, the cell size $dx = 0.02$ m is found to be suitable for this case. The average wave height of the last ten periods are again used for the convergence study. The relative errors and L2 norms of the absolute error for different grids are summarised in Table. 3. With the quadratic pressure approximation, the asymmetry due to the high-order approximation is well presented, and both, the wave height and phase match well with the theory. It shows that the model provides a good representation of the non-linearity of progressive waves. In comparison, the simulation with linear pressure profile shows an increasing difference in phase over time compared to the theoretical result.

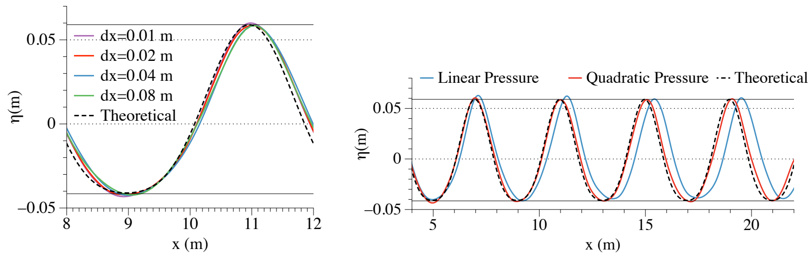

(a) (b)

Figure 5: (a) Grid convergence study for the 2^{nd}-order Stokes progressive wave with the wave height $H = 0.1$ m, the wavelength $L = 4$ m and $CFL = 0.2$. (b) The wave surface elevation profile at $t = 90$ s with the cell size $dx = 0.02$ m. The two horizontal solid black lines represent the theoretical wave envelope.

Table 3: The spatial discretisation error analysis for progressive 2^{nd}-order Stokes wave simulation.

dx (m)	$\overline{H}$ (m)	relative error	L2 error
0.08	0.0957	-4.30 %	0.0136
0.04	0.0991	-0.90 %	0.0030
0.02	0.1003	0.30 %	0.0010
0.01	0.1011	1.10 %	0.0035

3.3 Cnoidal wave propagation over constant bathymetry

A 5^{th}-order cnoidal wave (Korteweg and de Vries (1895); Dean and Dalrymple (1991*b*)) of $H = 0.21$ m and $L = 4$ m is investigated in the 1D numerical flume to test steep periodic wave propagation in shallow water. The steepness of the wave is $H/L = 0.0525$, the wave length to depth ratio is $H/d = 0.42$ which is about 65% of the breaking limit suggested by Laitone (1960). As shown in Fig. 6a, $dx = 0.02$ m is still a suitable cell size to capture the wave surface elevation accurately despite the increased wave steepness. Following the same methodology as in section 3.1, the relative error and L2 norms are computed and shown in Table 4. The wave profiles obtained with the quadratic pressure approximation and the linear pressure assumption are also compared in Fig. 6b. The wave troughs start to show slight deformation while the crests are still well preserved with the wave height to depth ratio closer to the breaking limit. The geometry of the steep cnoidal wave is kept constant during the propagation. It is also observed that the phase misalignment from the linear pressure assumption amplifies with the increase of wave steepness because the linear pressure profile assumption deviates further from the physical pressure distribution.

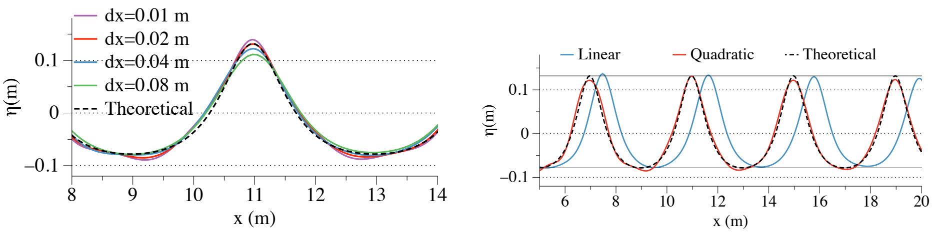

(a) (b)

Figure 6: (a) The grid convergence study for the 5^{th}-order cnoidal progressive wave with the wave height $H = 0.21$ m, the wavelength $L = 4$ m and $CFL = 0.2$. (b) The wave surface elevation profile at $t = 90$ s with the cell size $dx = 0.02$ m. The two horizontal solid black lines represent the theoretical wave envelope.

Table 4: The spatial discretisation error analysis for progressive cnoidal wave simulation.

dx (m)	$\overline{H}$ (m)	relative error	L2 error
0.08	0.1719	-18.14 %	0.0978
0.04	0.1958	-6.76 %	0.0449
0.02	0.2047	-2.52 %	0.0168
0.01	0.2110	0.48 %	0.0031

3.4 Solitary wave propagation over constant bathymetry

A solitary wave (Munk (1949); Dean and Dalrymple (1991*b*)) propagation over a constant bathymetry is simulated for 60 s in a 1D flume of 100 m length. The input wave height is is $H = 0.05$ m, and the constant water depth is $d = 0.5$ m. A wave generation zone of 4 m and a wave energy dissipation zone of 8 m are allocated at the inlet and the outlet of the flume. The comparison of the wave profiles at $t = 90$ s simulated with different grids is shown in Fig. 7a. The relative errors and L2 norms are also computed and shown in Table 5.

Further, simulations with the quadratic pressure approximation and the linear pressure assumption are simulated with $dx = 0.02$ m. The numerical computations are compared to the analytical values at propagation time 10 s, 20 s, 30 s and 40 s, shown in Fig. 7b. It is seen that the numerical results with the quadratic pressure remain in good agreement during the entire wave propagation process. Small amplitude waves propagate in opposite direction and trailing waves start to form during the simulation with the linear pressure. Simultaneously, the wave height increases during the process due to weaker dispersion from the linear assumption. These findings are in agreement with the investigations of Jeschke et al. (2017).

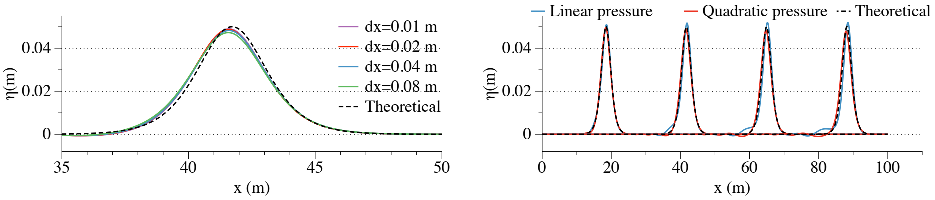

(a) (b)

Figure 7: (a) The grid convergence study for the solitary wave propagation with the wave height $H = 0.05$ m, the wavelength $L = 100$ m and $CFL = 0.2$. (b) Comparison of the analytical surface elevation of the solitary wave with the simulation results of the quadratic and linear vertical pressure profile after a propagation time of 10 s, 20 s, 30 s and 40 s (from left to right).

Table 5: The spatial discretisation error analysis for progressive solitary wave simulation.

dx (m)	$\overline{H}$ (m)	relative error	L2 error
0.08	0.0473	-5.40 %	0.0027
0.04	0.0483	-3.40 %	0.0017
0.02	0.0487	-2.60 %	0.0013
0.01	0.0490	-2.00 %	0.0010

The model's scaling capacity is investigated by conducting a series of simulations for 500 time step iterations with the number of processors being 16, 32, 64, 128, 256 and 512 on the supercomputer Vilje. The dimension of the computational domain is (10000 m × 1000 m × 10 m). The input wave is a 2^{nd}-order Stokes wave of wave height $H = 5$ m and wavelength $L = 100$ m. A cell size of $dx = 1$ m is used, resulting in 10 million cells in total. It is empirically assumed that the scaling is linear within 16 processors, i.e. one physical node on the cluster. Therefore, the computation time with one processor is linearly extrapolated from the 16-processor simulation. The computational speed of the one-processor simulation is considered as the base reference. The simulation time on one processor divided by the simulation time on multiple processors is defined as a speed-up factor. The relation between the speed-up factor and the number of processors as well as the number of cells per processor are plotted in Fig. 8. It shows that the performance increases almost linearly with the number of processors within the chosen range.

4 Validations and Applications

The evolution of waves over a non-constant bathymetry is complicated, and the performance gain from the quadratic pressure approximation in a general setting was recommended as future work by Jeschke et al. (2017). To fill the research gap, wave propagations over non-constant bathymetries of various configurations are simulated and validated with the available experimental data. A wave-structure interaction study is also validated against the bench-

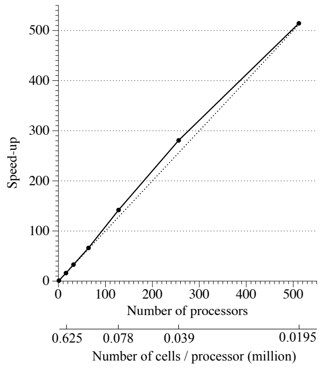

Figure 8: The performance of the parallel computation, shown as a relation between the speed-up factor in reference to the single-processor simulation for 500 iterations versus the number of processors and the number of cells per processor

mark. Jeschke et al. (2017) suggest the quadratic pressure approximation has the best performance when the water depth to wave length ratio is below 0.25. The selected benchmark cases all share the water depth condition within the suggested range. In addition, a large-scale wave propagation over a natural topography is presented based on an engineering scenario.

4.1 Wave propagation over a submerged bar

First, the well-known benchmark case of wave propagation over a submerged bar (Beji and Battjes (1993)) is tested. The configuration of the numerical set-up based on the experiment is shown in Fig. 9. A 2D wave tank of 38 m is equipped with a wave generation zone of 5 m to the left end and a wave energy dissipation zone of 9.5 m to the right end. The beginning of the submerged bar is located 6 m downstream from the wave generation zone. Eight wave gauges are located above the submerged bar with the x-coordinates being 11 m, 16 m, 17 m, 18 m, 19 m, 20 m, 21 m and 22 m, as shown in Fig. 9. The incident wave height is $H = 0.021$ m, and the wave period is $T = 2.525$ s. A grid convergence study is performed at gauge 2 and 6, before and after the crest of the submerged bar, as shown in Fig. 10i and Fig. 10j. A cell size of $dx = 0.02$ m is found to sufficiently represent the phenomena and shows good agreement with the experimental data. A simulation time of 60 s is used.

The numerically predicted time series of the surface elevations at gauge 1 to gauge 8 are compared with the experimental data in Fig. 10. The results match well with the experimental measurements before the waves reach the submerged bar and during the shoaling process, for example at gauges 1 and 2. It demonstrates that the model can represent the dispersion relations well with changing bathymetry. At the crest of the bar, no wave breaking happens but the wave decomposition takes place and results in higher harmonic wave components. The wave decomposition phenomenon is observed at wave gauges 3 to 5, where the numerical results show accurate agreement with the experimental measurements as well. On top of the relatively steep downslope, the waves undergo a de-shoaling process as the water depth increases. During this process, it is observed that the numerical results start to show differences in phase from the experimental data. The discrepancies accumulate from wave gauge 6 to wave gauge 7. When the waves reach wave gauge 8, a significant difference is observed. This shows a less discussed limitation of existing shallow water approximations for de-shoaling processes. Furthermore, the results are also compared between the quadratic and the linear pressure profile assumptions. As an example, the comparisons of the surface elevations at gauge 3 and 5 are shown in Fig. 11. At both gauges, the quadratic assumption shows good alignment in phase with the experiment, while the linear assumption tends to predict a faster moving wave front. The observation is consistent with the investigation in section 3.

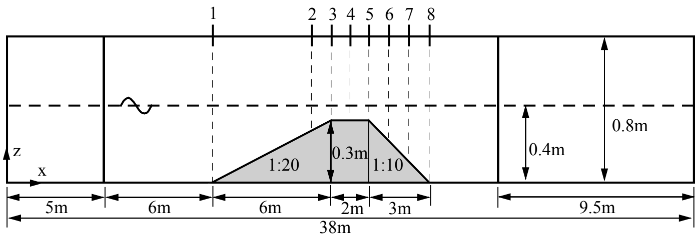

Figure 9: The numerical wave tank set-up of the wave propagation over a submerged bar, view from the side. The water depth is constant at 0.4 m. The locations of the wave elevation gauges are marked with short vertical line segments from 1 to 8. The grey-shaded object is the submerged bar. A wave generation zone of 5 m and a wave energy dissipation zone of 9.5 m are located at the left end and right end of the tank respectively.

4.2 Solitary wave interaction with a rectangular abutment

In this benchmark study, the solitary wave interaction with a surface-piercing rectangular abutment is investigated. Based on the experiments (Higuera et al. (2013*b*); Lara et al. (2012)), the numerical wave tank is defined as shown in Fig. 12. The tank is 23.86 m long, 0.58 m wide and 0.9 m deep. The still water level is constant at 0.45 m. A wave generation zone of 3.93 m is placed at the left end of the numerical wave tank to cover the effective wave length of the solitary wave (Dean and Dalrymple (1991*a*)), and a fully reflective wall is placed at the right end. A 3^{rd}-order solitary wave (Grimshaw (1971)) with a wave height of 0.1 m is generated in the wave generation zone. The front face of the abutment is located 14.86 m from the beginning of the tank. Nine wave gauges are located upstream, sideways and downstream of the abutment, as shown in Fig. 12. For the grid convergence study, three different cell sizes $dx = 0.05$ m, 0.1 m and 0.2 m are used. All cases are simulated for 30 s to allow enough time for the reflected wave to interact with the abutment and propagate back to the generation zone.

The simulated time series at all wave gauges are compared to those from the experiments as shown in Fig. 13. The first peak in the distributions is the result of the incoming solitary wave impact on the abutment. After the incident solitary wave passes the abutment, it is reflected from the wall at the end of the tank and interact with the abutment again, resulting in the second peak. The grid convergence study shown in Fig. 13j is performed at gauge 7, which is located at the downstream side of the abutment. At this location, both, the

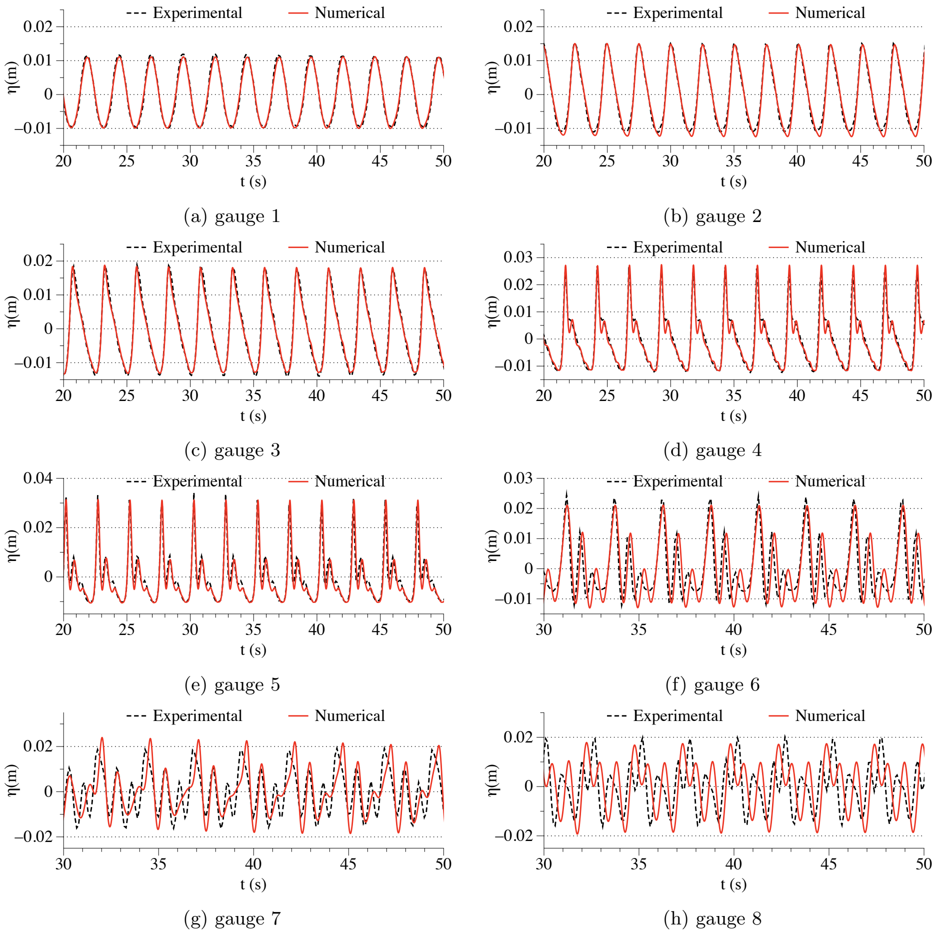

(a) gauge 1 (b) gauge 2 (c) gauge 3 (d) gauge 4 (e) gauge 5 (f) gauge 6 (g) gauge 7 (h) gauge 8

Figure 10: The surface elevations of the wave transformation over a submerged bar. (a)-(h) show the surface elevations at different wave gauges at $t = 60$ s, black lines are from laboratory experiments, red lines are results of REEF3D::SFLOW. The cell size $dx = 0.02$ m and $CFL = 0.2$. (i) and (j) are grid convergence study at wave gauge 4 and 6. (part 1)

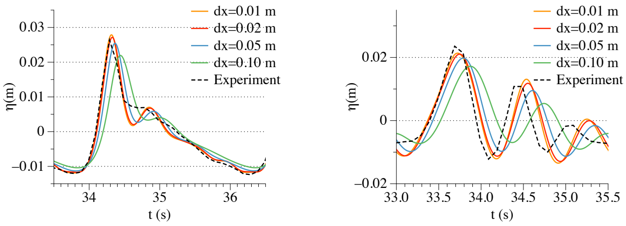

(i) Grid Convergence at the wave gauge 4

(j) Grid Convergence at the wave gauge 6

Figure 10: The surface elevations of the wave transformation over a submerged bar. (a)-(h) show the surface elevations at different wave gauges at $t = 60$ s, black lines are from laboratory experiments, red lines are results of REEF3D::SFLOW. The cell size $dx = 0.02$ m and $CFL = 0.2$. (i) and (j) are grid convergence study at wave gauge 4 and 6. (part 2)

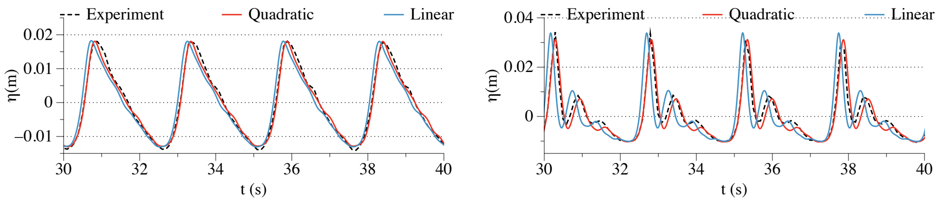

(a)

(b)

Figure 11: The comparison of the surface elevation between the quadratic and linear pressure profile assumptions at gauge 3 (a) and gauge 5 (b) in the simulation of wave propagation over a submerged bar.

interaction between the structure and the incoming waves and the properties of the reflected waves can be well observed. It indicates that the cell size $dx = 0.05$ m sufficiently captures the details of the wave pattern and gives good results compared to the experiments. At gauge 1 and 2, the first peaks show the solitary wave propagates without much interruption and, therefore, preserves its wave height. A second minor peak is noticed right after the peak which is due to the partially reflected waves from the abutment. Gauge 3 shows an increase of the wave height due to the narrowing of the channel, while gauge 4 presents a further increase of the peak because of the interaction with the abutment. The peaks increase to about 0.11 m and 0.13 m at gauge 3 and 4 respectively. Since gauge 5 is located in the constricted part of the channel, the flow velocity increases and the pressure decreases. As a consequence, the wave surface drops. At gauge 6, the first peak occurs right after the wave crest passes the abutment while the depth-averaged solution tends to smooth out the results in the sheltered region behind the abutment. At gauge 8 and 9, two peaks of equal heights are observed, indicating that the reflected wave shares the same wave height as the incoming wave. This shows that there is no damping of the soliton and the model provides an accurate representation of the solitary wave propagation. Similarly, the two peaks also share similar height at gauge 7, where no wave transformations occur before and after the wave reflects from the vertical wall. When the reflected wave reaches the abutment, a second peak occurs at gauge 6. After the reflected wave passes the abutment, gauge 4 also witnesses the second peak. In general, the wave patterns from gauge 6 and gauge 4 mirror each other.

Finally, the second peak at wave gauge 5 and the first peak at wave gauge 7 are compared with the quadratic and the linear pressure approximation in Fig. 14. Similar to the previous observations, the linear approximation predicts a increased phase velocity while the quadratic approximation matches the experiment well in phase.

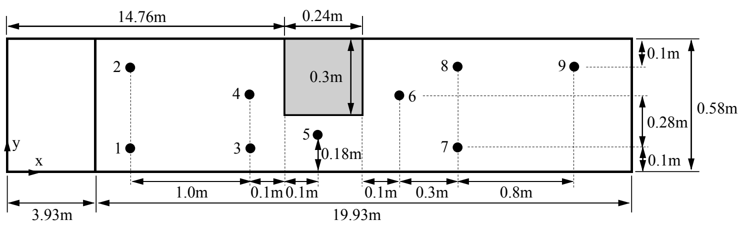

Figure 12: The numerical wave tank set-up of the solitary wave interaction with a rectangular abutment in a view from above. The grey-shaded object is the abutment. The following three groups of wave gauges share the same y-coordinate: wave gauges 1,3,7; wave gauges 4,6 and the wave gauges 2,8,9. A wave generation zone of 3.93 m is located on the left-hand side, the solid wall is located on the right-hand side to allow full reflection of the waves.

The details of the free-surface during this process is also visualised in Fig. 15. Fig. 15a shows the free-surface at simulation time $t = 7$ s, right before the solitary wave reaches the abutment. The solitary wave preserves its waveform. After the wave passes the abutment, a vortex is observed at the downstream behind the abutment, as can be seen in Fig. 15b. When the reflected wave reaches back towards the abutment from the right-hand side, the wave crest meets the vortex from the last interaction before a second interaction, as seen in

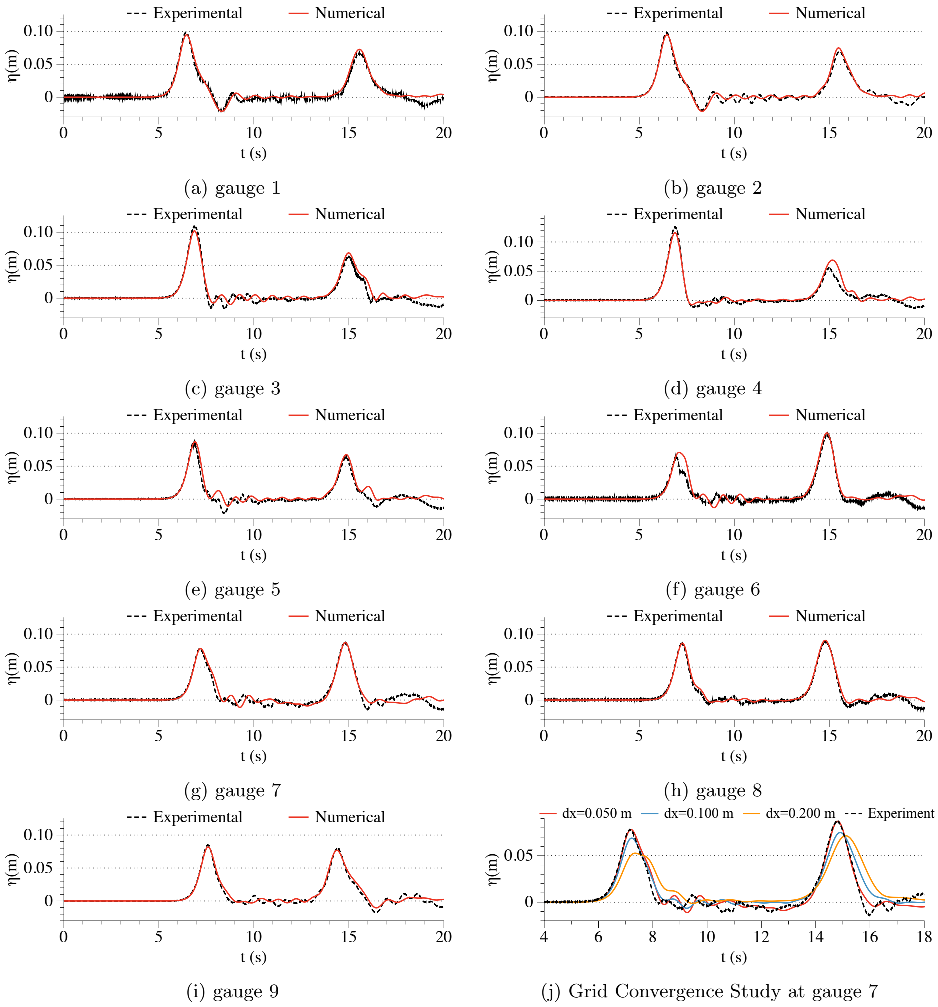

Figure 13: Wave surface elevation at the wave gauges are shown in (a)-(i). The input solitary wave has a wave height of $H = 0.1$ m. The black dashed lines are from laboratory experiments, red solid lines are results from REEF3D::SFLOW. The cell size is $dx = 0.05$ m and $CFL = 0.2$ is used. (j) shows the grid convergence study.

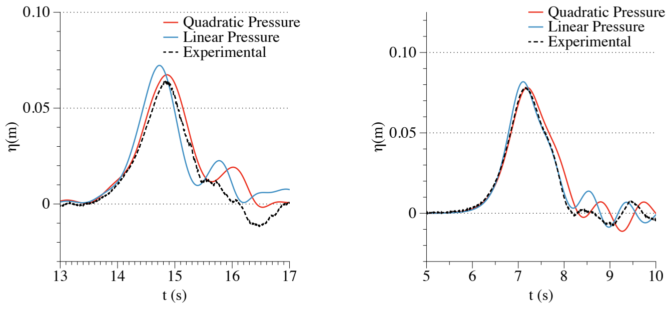

(a)

(b)

Figure 14: The comparison of the surface elevation between the quadratic and linear pressure profile approximation at gauge 5 (a) and gauge 7 (b) in the simulation of solitary wave interaction with a rectangular abutment.

Fig. 15c. After the reflected wave passes the abutment, two vortices are observed on both sides of the abutment. Fig. 13 reveals that the resolution of the vortex is smoothed out at gauge 4 and 6, while the other wave gauges are well represented.

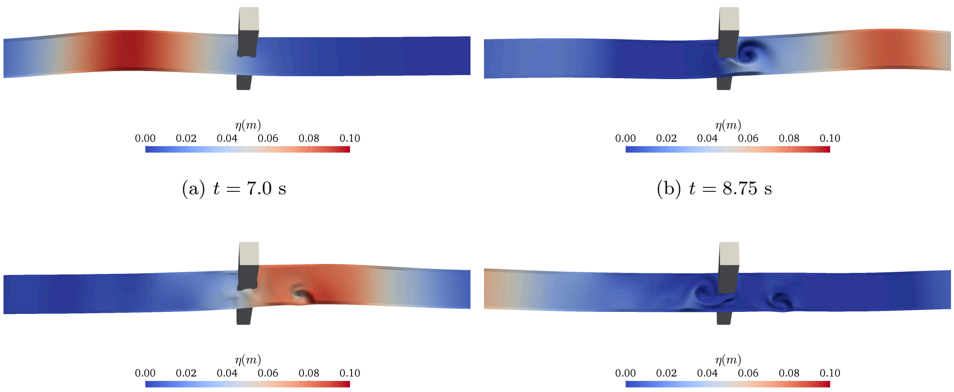

(a) $t = 7.0$ s

(b) $t = 8.75$ s

(c) $t = 15.25$ s

(d) $t = 17.5$ s

Figure 15: Surface elevation of the input and reflected wave interaction with the rectangular abutment, (a) right before the input solitary wave reaches the abutment, (b) right after the input solitary wave passes the abutment, (c) right before the reflected wave reaches the abutment from the right-hand side, (d) right after the reflected wave passes the abutment.

It might be interesting to notice that the 2D shallow water model is as accurate as the CFD study in (Bihs et al. (2016)) except for the vortices representation in the wakes of the abutment. Here, the results of simulations based on the 3D Navier-Stokes equations show a slightly better match with the experiments. The cost of the computational resource, however, is significantly lower using the proposed shallow water model. This benchmark case is simulated with 16 processors on the Vilje supercomputer about 56 times faster than the 3D simulation with the same configuration.

4.3 Plunging breaking waves over a sloping bed

In section 4.1, non-breaking waves over a submerged bar are modelled. In a more extreme situation, where the shoaling is so strong that the wave steepness increases over a certain threshold, the wavefront becomes unstable and breaking takes place. The numerical wave tank is initialised based on the experiments in (Ting and Kirby (1994, 1996)) to model a breaking wave scenario. The wave tank has a total length of 40 m and a height of 1 m. A wave generation zone of 9.8 m is located at the inlet of the tank; a wave energy dissipation zone of the same length is arranged at the outlet. An inclined bed with a slope of 1:35 is located 4 m away from the wave generation zone. The obstacle increases to 0.748 m at the right end of the tank. The water depth is constant at 0.4 m. Wave gauges 1-4 are located on the slope, 10 m, 11 m, 12 m and 12.3 m away from the wave generation zone respectively. A 5^{th}-order cnoidal wave with wave height $H = 0.128$ m and wave period $T = 5$ s is propagated in this simulation, which is supposed to result in a plunging breaker on the slope according to the experiment. A simulation time of 40 s is used.

The sensitivity to the grid resolution is investigated with different cell sizes of $dx = 0.0025$ m, 0.005 m, 0.01 m, 0.02 m and 0.05 m. The wave surface elevation at wave gauge 4 is chosen for comparing the results from different cell sizes. As can be seen in Fig. 17e, the simulations capture very steep wavefronts as well as instabilities at the wave crest with all cell sizes. It is not possible to observe the over-turning process because the shallow water model represents the free-surface with a single-valued function. Though, a vertical wavefront and instability at the wave crest indicates the breaking process. The view on the wave crest is shown in more detail in Fig. 17f, where it is visible that $dx = 0.005$ m captures the peak values most accurately. The simulated wave elevations at different wave gauges with $dx = 0.005$ m are compared to the experimental data in Fig. 17 in order to assess the model's capacity to resolve the surf-zone wave transformations. The wave crests increase significantly when the waves propagate from gauge 1 to gauge 2, showing an increasing shoaling process. As the waves evolve on the slope, an unstable wave crest is seen at gauge 3 and the wave height decreases slightly compared to that at gauge 2. The instability at the crest remains as the waves approach gauge 4 and a further decrease of the wave crest is noticed. These time series suggest that the breaking happens between gauge 2 and 3. To identify the breaking point, the wave elevation profile at different time are compared in the same plot (Fig. 18). It is seen that at $x = 21.580$ m, the wave crest is the highest while the wavefront becomes vertical for the first time indicating the location of the breaking point. Correspondingly, a breaking height of $h_b = 0.208$ m is measured at $x = 21.580$ m. In the experiment, the breaking point is detected at $x = 21.595$ m and a breaking height of $h_b = 0.196$ m is measured. Both, the predicted breaking point and are very close to that in the experiment. The wave surface elevation profile is illustrated in Fig. 19. As can be seen in Fig. 19a, the wave height increases significantly, the wave shape becomes narrower, the crest becomes unstable and the wavefront becomes vertical, indicating a breaking process. At a later time, the wave energy dissipates and the wave height decreases dramatically. An attempt to simulate the breaking wave using the linear pressure approximation leads to a numerical failure. It indicates that the quadratic pressure approximation is superior for the simulation of breaking waves.

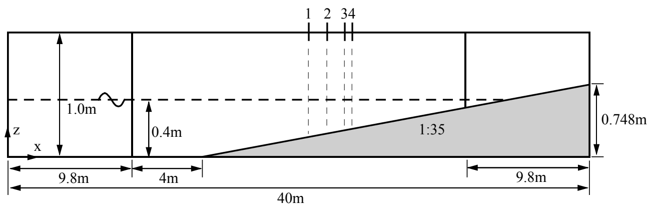

Figure 16: The numerical wave tank set-up of the wave breaking over a sloping bed, view from the side. The water depth is constant at 0.5 m, the grey-shaded object is the sloping bed with a slope of 1:35. Four wave gauges are arranged near the breaking point.

4.4 Large scaling numerical modelling of coastal waves near Mehamn harbour

The previous benchmark studies have quantitatively examined the capacities of the proposed model. In this section, the wave propagation in a large domain with real topography is simulated to show the model's computational efficiency and its capacity for operational engineering applications. The chosen scenario is Mehamn harbour in northern Norway, highlighted by a black box in Fig. 20. The harbour is the north-most Hutigruten harbour and it is connected to the open sea to the north and relatively well protected from the west and the east. The bathymetry outside the harbour has a mostly intermediate water depth condition with moderate changes of topography. The computational domain is 10.5 km in the east-west direction and 14 km in the north-south direction, with the deepest water depth being 147.5 m. The site is exposed to swell from the open sea. An estimated regular wave of height $H = 4.5$ m and period $T = 15$ s is generated at the northern boundary. The wetting and drying scheme over the complex bathymetry is included. A cell size of 5 m is used in the simulation, resulting in 5.88 million cells. In the case of a 3D simulation with Navier-Stokes solver, such a configuration will result in 246.96 million cells assuming a uniform grid. This simulation of wave propagation in Mehamn harbour takes about 4.2 hours for 1000 s simulation time with 256 cores on the Vilje supercomputer.

The wave surface elevation at simulation time $t = 650$ s is shown in Fig. 21b. Strongly reflected waves can be seen at the tips of the peninsulas that reach out northwards into the ocean. Stripes of submerged reefs in the north-south directions create strong shoaling, as higher waves are shown to be following the same pattern of the submerged reefs. When the waves propagate southwards, refraction occurs and bend the wave rays towards the shore. When the waves start to reach the harbour, the narrowing entry causes diffraction. A fraction of the diffracted waves manages to bypass the curve-shaped peninsulas and enter the inner harbour. The complicated wave transformations and their interactions are well demonstrated in the simulation results.

Finally, the model's computational performance including a complicated bathymetry with wetting and drying and the breaking algorithm is determined in a similar manner as described

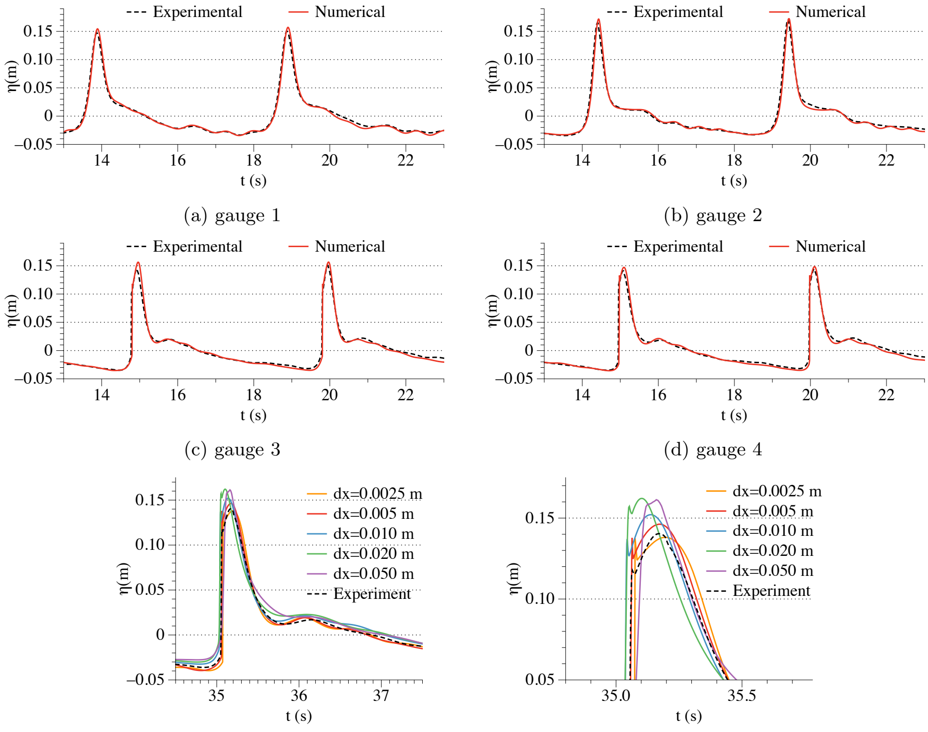

(a) gauge 1

(b) gauge 2

(c) gauge 3

(d) gauge 4

(e) Grid convergence study at gauge 4

(f) Grid convergence study at gauge 4 with the wave crest zoomed in

Figure 17: Wave surface elevations of wave breaking over a sloping bed. The input wave is a 5^{th}-order cnoidal wave with a wave height of $H = 0.128$ m and a wave period of $T = 5$ s. The cell size is $dx = 0.005$ m and $CFL = 0.2$ is used. Black dashed lines are from laboratory experiments, red solid lines are results from REEF3D::SFLOW.

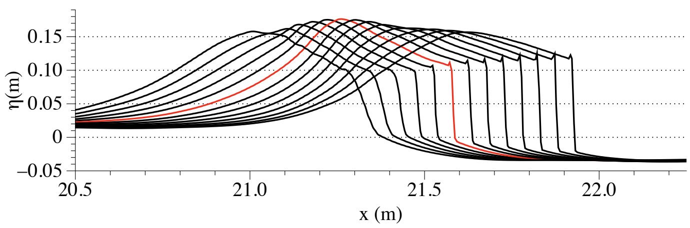

Figure 18: The wavefront evolution near the wave breaking point, from the numerical simulation with $dx = 0.005$ m. When the wavefront turns vertical for the first time, shown as a red curve, the breaking and overturning process starts.

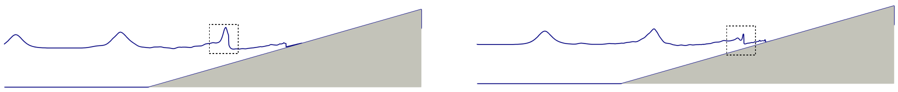

(a) (b)

Figure 19: The wave surface elevation profiles along the x-direction. (a) the breaking wave at $t = 34.75$ s, as highlighted by a box of a dashed frame. (b) after the wave breaking, at $t = 37.50$ s, the wave height reduces and the wave keeps running up the sloping bed, as highlighted by a box of dashed lines.

in section 2. The simulations are conducted for 500 iterations with the number of processors fixed to 16, 32, 64, 128, 256 and 512 on the supercomputer Vilje. The computational time with one processor is linearly extrapolated from the 16-processor simulation and is used as a base reference for the speed-up factor. The relation between the speed-up factor and the number of processors as well as the number of cells per processor are then plotted in Fig. 22. It shows that with the presence of a complex topography and the wetting-drying scheme, the model is as computationally efficient as with a constant bottom within 200 processors, while it slows down compared to the ideal scaling characteristics afterwards.

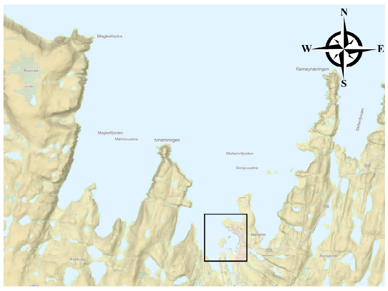

Figure 20: The illustration of the simulated region outside Mehamn harbour in northern Norway. The harbour is highlighted by a black box.

5 Conclusion

The shallow water model REEF3D::SFLOW has been presented in this paper. The model solves the depth-averaged shallow water equations with non-hydrostatic extensions and a quadratic vertical pressure profile approximation (Jeschke et al. (2017)). In comparison to well-known Boussinesq-type models, the proposed model treats the pressure terms differently. A typical Boussinesq model adds higher-order terms to express the hydrodynamic pressure. The proposed model adds non-hydrostatic extensions to the shallow water equations and

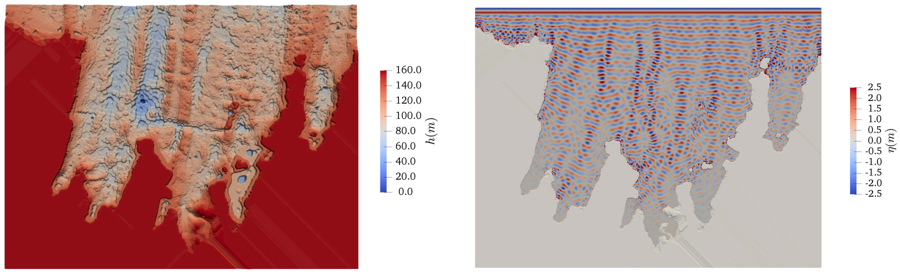

(a) (b)

Figure 21: The wave propagation towards the Mehamn harbour in the numerical simulation with a 2^{nd}-order Stokes wave of wave height $H = 4.5$ m and wave period $T = 15$ s. The cell size is $dx = 5.0$ m and $CFL = 0.2$ is used. (a) The topography in the simulation; (b) The surface elevation at simulation time $t = 650$ s.

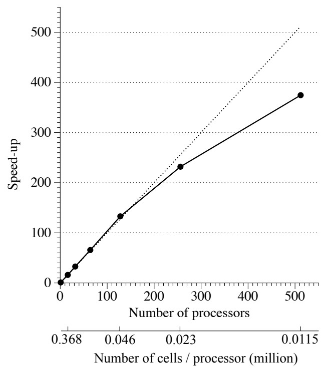

Figure 22: The performance of the parallel computation, shown as a relation between the speed-up factor in reference to the single-processor simulation for 500 iterations versus the number of processors and the number of cells per processor

solves for the hydrodynamic pressure explicitly from a Poisson equation. This equation is solved iteratively using an implicit scheme. Thus, the proposed model offers simpler numerics and indicates higher numerical stability by avoiding the high-order pressure terms of a Boussinesq model. The current model assumes a quadratic pressure approximation for a better representation of dispersion and always solves the depth-averaged pressure. This is in contrast to the multi-layer approach that uses vertical layers to represent dispersion and solves the pressure at the lower layer interface. Thereby, the presented approach saves the additional computational costs from the increasing number of layers.

High-order numerical methods are incorporated into the new model. Consequently, it is the first model with the quadratic pressure approximation that combines high-order schemes and fully parallelised computation. The wave generation and absorption are achieved using a relaxation method, which is absent in the current literature. The approach proves to generate various wave types with correct amplitude and dispersion, and no artificial reflections are observed in the numerical wave tank. The accuracy of the high-order scheme is confirmed for 1D and 2D wave propagation cases with a constant bathymetry. The 2D large-scale simulation of a wave propagation over constant bathymetry presents a near-linear scaling of the computational speed with an increasing number of processors up to 512. Further, the model shows an almost linear scaling up to 128 processors if a natural topography is included in the numerical wave tank. The speed-up is reduced with a further increase of computational units due to the complex boundary treatment from the topography.

Overall, the study confirms the advantage of the quadratic pressure approximation over the linear pressure assumption for multiple validation cases. The linear pressure assumption leads to an overshooting phase velocity for all the regular wave tests in the manuscripts. It also causes a secondary wave during the solitary wave propagation. The quadratic pressure approximation improves the phase information for progressive waves significantly and removes the unrealistic free-surface disturbances.

A key advancement presented in the current work is the inclusion of the varying bathymetry and structures in a non-hydrostatic shallow water model with the quadratic pressure approximation. A fractional step method is applied in the proposed numerical model in order to meet the challenge of incorporating the term Φ that appears in the bottom pressure calculation. Thus, the simulations of the nonlinear long wave propagation over varying topographies using a non-hydrostatic model with the quadratic pressure assumption are possible for the first time. The wave transformations over varying topography are well represented and in good agreement with the experimental data. The model can represent the complex free-surface during wave-structure interactions and predicts the breaking wave height and locations accurately. The quadratic pressure approximation again provides a better representation of the free-surface than the linear pressure assumption for the wave propagation over varying bathymetries. The challenges of representing the de-shoaling process using a non-hydrostatic shallow water model is also discussed, and the study confirms the findings from previous research (Dingemans (1994)).

It can be concluded that, within the applicable range of the quadratic assumption (Jeschke et al. (2017)), the quadratic pressure approximation presents better results both with a constant and a varying bathymetry. The large-scale engineering application shows a good computational scaling character with the wetting and drying of complex topography included. In general, the model presents itself as a good alternative to shallow water modelling with robust and efficient numerical methods. The model also serves as an additional option within the hydrodynamics code REEF3D. As a consequence, an integrated wave modelling cascade is more easily adaptable because different sub-models are developed on a single platform and the information exchange can be made more convenient.

Acknowledgements

This study has been carried out under the E39 fjord crossing project (No. 304624), and the authors are grateful to the grants provided by the Norwegian Public Roads Administration. This study was supported in part with the computational facility Vilje (https://www.sigma2.no/content/vilje) at the Norwegian University of Science and Technology (NTNU) provided by The Norwegian Metacenter for Computational Sciences (NOTUR, http://www.notur.no) under project no. NN2620K.

References

Aggarwal, A., Pkozdi, C., Bihs, H., Myrhaug, D. and Alagan Chella, M. (2018). Free surface reconstruction for phase accurate irregular wave generation. *Journal of Marine Science and Engineering*, **6**(3). ISSN 2077-1312. 10.1002/fld.480710.3390/jmse6030105.

Ahmad, N., Bihs, H., Myrhaug, D., Kamath, A. and ivind A. Arntsen (2018). Three-dimensional numerical modelling of wave-induced scour around piles in a side-by-side arrangement. *Coastal Engineering*, **138**, 132 – 151. ISSN 0378-3839. 10.1002/fld.4807https://doi.org/10.1016/j.coastaleng.2018.04.016.

Altomare, C., Domínguez, J., Crespo, A., González-Cao, J., Suzuki, T., Gómez-Gesteira, M. and Troch, P. (2017). Long-crested wave generation and absorption for sph-based dualsphysics model. *COASTAL ENGINEERING*, **127**, 37–54. ISSN 0378-3839.

Ashby, S.F. and Flagout, R.D. (1996). A parallel mulitgrid preconditioned conjugate gradient algorithm for groundwater flow simulations. *Nuclear Science and Engineering*, **124**(1), 145–159.

Azimi, A.H., Rajaratnam, N. and Zhu, D.Z. (2014). Submerged flows over rectangular weirs of finite crest length. *Journal of Irrigation and Drainage Engineering*, **140**(5), 06014001–1 –06014001–12.

Beji, S. and Battjes, J.A. (1993). Experimental investigation of wave propagation over a bar. *Coastal Engineering*, **19**, 151–162.

Bihs, H., Kamath, A., Alagan Chella, M., Aggarwal, A. and Arntsen, Ø.A. (2016). A new level set numerical wave tank with improved density interpolation for complex wave hydrodynamics. *Computers & Fluids*, **140**, 191–208.

Chen, Q., Kirby, J.T., Dalrymple, R.A., Shi, F. and Thornton, E.B. (2003). Boussinesq modeling of longshore currents. *Journal of Geophysical Research: Oceans*, **108**(C11). 10.1002/fld.480710.1029/2002JC001308.

Chorin, A. (1968). Numerical solution of the Navier-Stokes equations. *Mathematics of Computation*, **22**, 745–762.

Chow, A.D., Rogers, B.D., Lind, S.J. and Stansby, P.K. (2019). Numerical wave basin using incompressible smoothed particle hydrodynamics (isph) on a single gpu with vertical cylinder test cases. *Computers & Fluids*, **179**, 543 – 562. ISSN 0045-7930. 10.1002/fld.4807https://doi.org/10.1016/j.compfluid.2018.11.022.

Cui, H., Pietrzak, J. and Stelling, G. (2014). Optimal dispersion with minimized poisson equations for non-hydrostatic free surface flows. *Ocean Modelling*, **81**, 1 – 12. ISSN 1463-5003. 10.1002/fld.4807https://doi.org/10.1016/j.ocemod.2014.06.004.

Dalrymple, R. and Rogers, B. (2006). Numerical modeling of water waves with the sph method. *Coastal Engineering*, **53**(2), 141 – 147. ISSN 0378-3839. 10.1002/fld.4807https://doi.org/10.1016/j.coastaleng.2005.10.004. Coastal Hydrodynamics and Morphodynamics.

Dean, R. and Dalrymple, R. (1991*a*). *Water Wave Mechanics for Engineers and Scientists*. Advanced series on ocean engineering. World Scientific. ISBN 9789810204211.

Dean, R.G. and Dalrymple, R.A. (1991*b*). *Water Wave Mechanics for Engineers and Scientists*. WORLD SCIENTIFIC. 10.1002/fld.480710.1142/1232.

Dingemans, M.W. (1994). Comparison of computations with Boussinesq-like models and laboratory measurements. *Igarss 2014*, 1–30. ISSN 13514180. 10.1002/fld.480710.1007/s13398-014-0173-7.2.

Grimshaw, R. (1971). The solitary wave in water of variable depth. part 2. *Journal of Fluid Mechanics*, **46**(3), 611622. 10.1002/fld.480710.1017/S0022112071000739.

Hanert, E., Roux, D.Y.L., Legat, V. and Deleersnijder, E. (2005). An efficient eulerian finite element method for the shallow water equations. *Ocean Modelling*, **10**(1), 115 – 136. ISSN 1463-5003. 10.1002/fld.4807https://doi.org/10.1016/j.ocemod.2004.06.006. The Second International Workshop on Unstructured Mesh Numerical Modelling of Coastal, Shelf and Ocean Flows.

Higuera, P., Lara, L.J. and Losada, I.J. (2013*a*). Realistic wave generation and active wave absorption for Navier-Stokes models application to OpenFOAM. *Coastal Engineering*, **71**, 102–118.

Higuera, P., Lara, L.J. and Losada, I.J. (2013*b*). Simulating coastal engineering processes with OpenFOAM. *Coastal Engineering*, **71**, 119–134.

Hirt, C. and Nichols, B. (1981). Volume of fluid (vof) method for the dynamics of free boundaries. *Journal of Computational Physics*, **39**(1), 201 – 225. ISSN 0021-9991. 10.1002/fld.4807https://doi.org/10.1016/0021-9991(81)90145-5.

Hypre (2015). *hypre high performance preconditioners - User's Manual*. Center for Applied Scientific Computing, Lawrence Livermore National Laboratory.

Jacobsen, N., Fuhrman, D. and Jrgen, F. (2012). A wave generation toolbox for the opensource cfd library: Openfoam. *International Journal for Numerical Methods in Fluids*, **70**(9), 1073–1088. ISSN 0271-2091. 10.1002/fld.480710.1002/fld.2726.

Jeschke, A. (2018). *Second Order Convergent Discontinuous Galerkin Projection Method for Dispersive Shallow Water Flows.* Ph.D. thesis, Universitt Hamburg.

Jeschke, A., Pedersen, G.K., Vater, S. and Behrens, J. (2017). Depth-averaged non-hydrostatic extension for shallow water equations with quadratic vertical pressure profile: equivalence to boussinesq-type equations. *International Journal for Numerical Methods in Fluids*, **84**(10), 569–583. 10.1002/fld.480710.1002/fld.4361.

Jiang, G.S. and Shu, C.W. (1996). Efficient implementation of weighted ENO schemes. *Journal of Computational Physics*, **126**, 202–228.

Kamath, A., Bihs, H., Alagan Chella, M. and Arntsen, Ø.A. (2016). Upstream-cylinder and downstream-cylinder influence on the hydrodynamics of a four-cylinder group. *Journal of Waterway, Port, Coastal, and Ocean Engineering.* 10.1002/fld.480710.1061/(ASCE)WW.1943-5460.0000339.

Korteweg, D.J. and de Vries, G. (1895). On the change of form of long waves advancing in a rectangular canal, and on a new type of long stationary waves. *Philosophical Magazine*, **39**(240), 422–443. 10.1002/fld.480710.1080/14786449508620739.

Laitone, E.V. (1960). The second approximation to cnoidal and solitary waves. *Journal of Fluid Mechanics*, **9**(3), 430444. 10.1002/fld.480710.1017/S0022112060001201.

Lara, J., del Jesus, M. and Losada, I. (2012). Three-dimensional interaction of waves and porous coastal structures: Part ii: Experimental validation. *Coastal Engineering*, **64**, 26 – 46. ISSN 0378-3839. 10.1002/fld.4807https://doi.org/10.1016/j.coastaleng.2012.01.009.

Le, H. and Moin, P. (1991). An improvement of fractional step methods for the incompressible navier-stokes equations. *Journal of Computational Physics*, **92**(2), 369 – 379. ISSN 0021-9991. 10.1002/fld.4807https://doi.org/10.1016/0021-9991(91)90215-7.

Lynnett, P.J. and Liu, P.L.F. (200451). Linear analysis of the multi-layer model. *Coastal Engineering*, 439–454.

Madsen, P.A., Bingham, H.B. and Liu, H. (2002). A new boussinesq method for fully nonlinear waves from shallow to deep water. *Journal of Fluid Mechanics*, **462**, 130. 10.1002/fld.480710.1017/S0022112002008467.

Madsen, P.A., Murray, R. and Sørensen, O.R. (1991). A new form of the boussinesq equations with improved linear dispersion characteristics. *Coastal Engineering*, **15**, 371–388.

Mayer, S., Garapon, A. and Srensen, L.S. (1998). A fractional step method for unsteady free-surface flow with applications to non-linear wave dynamics. *International Journal for Numerical Methods in Fluids*, **28**(2), 293–315. 10.1002/fld.480710.1002/(SICI)1097-0363(19980815)28:2¡293::AID-FLD719¿3.0.CO;2-1.

Miquel, A.M., Kamath, A., Alagan Chella, M., Archetti, R. and Bihs, H. (2018). Analysis of different methods for wave generation and absorption in a cfd-based numerical wave tank. *Journal of Marine Science and Engineering*, **6**(2). ISSN 2077-1312. 10.1002/fld.480710.3390/jmse6020073.

Monteban, D. (2016). Numerical modelling of wave agitation in ports and access channels.

Munk, W.H. (1949). The solitary wave theory and its application to surf problems. *Annals of the New York Academy of Sciences*, **51**(3), 376–401. 10.1002/fld.480710.1111/j.1749-6632.1949.tb27281.x.

Nwogu, O. (1993). Alternative form of boussinesq equations for nearshore wave propagation. *Journal of Waterways, Port, Coastal, and Ocean Engineering*, **119**(6), 618–638.

Ong, M.C., Kamath, A., Bihs, H. and Afzal, M.S. (2017). Numerical simulation of free-surface waves past two semi-submerged horizontal circular cylinders in tandem. *Marine Structures*, **52**, 1 – 14. ISSN 0951-8339. 10.1002/fld.4807https://doi.org/10.1016/j.marstruc.2016.11.002.

Osher, S. and Sethian, J.A. (1988). Fronts propagating with curvature- dependent speed: algorithms based on Hamilton-Jacobi formulations. *Journal of Computational Physics*, **79**, 12–49.

Roux, D.Y.L. and Pouliot, B. (2008). Analysis of Numerically Induced Oscillations in Two-Dimensional Finite-Element Shallow-Water Models Part II: Free Planetary Waves. *SIAM Journal on Scientific Computing*. ISSN 1064-8275. 10.1002/fld.480710.1137/060650106.

Sasikumar, A., Kamath, A., Musch, O., Bihs, H. and Arntsen, Ø.A. (2018). Numerical Modeling of Berm Breakwater Optimization With Varying Berm Geometry Using REEF3D. *Journal of Offshore Mechanics and Arctic Engineering*, **141**(1), 011801. ISSN 0892-7219. 10.1002/fld.480710.1115/1.4040508.

Shi, F., Kirby, J.T., Harris, J.C., Geiman, J.D. and Grilli, S.T. (2012). A high-order adaptive time-stepping tvd solver for boussinesq modeling of breaking waves and coastal inundation. *Ocean Modelling*, **43-44**, 36 – 51. ISSN 1463-5003. 10.1002/fld.4807https://doi.org/10.1016/j.ocemod.2011.12.004.

Shu, C.W. and Osher, S. (1988). Efficient implementation of essentially non-oscillatory shock capturing schemes. *Journal of Computational Physics*, **77**, 439–471.

Stelling, G. and Zijlema, M. (2003). An accurate and efficient finite-difference algorithm for non-hydrostatic free-surface fow with application to wave propagation. *International Journal for Numerical Methods in Fluids*, **43**, 1–23.

Stelling, G.S. and Duinmeijer, S.P.A. (2003). A staggered conservative scheme for every froude number in rapidly varied shallow water flows. *International Journal for Numerical Methods in Fluids*, **43**(12), 1329–1354. 10.1002/fld.480710.1002/fld.537.

The SWASH Team (2017). SWASH User Manual version 4.01A.

Ting, F. and Kirby, J. (1994). Observation of undertow and turbulence in a laboratory surf zone. *Coastal Engineering*, **24**(1), 51 – 80. ISSN 0378-3839. 10.1002/fld.4807https://doi.org/10.1016/0378-3839(94)90026-4.

Ting, F. and Kirby, J. (1996). Dynamics of surf-zone turbulence in a spilling breaker. *Coastal Engineering*, **27**(3), 131 – 160. ISSN 0378-3839. 10.1002/fld.4807https://doi.org/10.1016/0378-3839(95)00037-2.

Wei, G. and Kirby, J.T. (1995). Time-dependent numerical code for extended boussinesq equations. *Journal of Waterway, Port, Coastal, and Ocean Engineering*, **121**(5), 251–261. 10.1002/fld.480710.1061/(ASCE)0733-950X(1995)121:5(251).

Wei, G., Kirby, J.T., Grilli, S.T. and Subramanya, R. (1995). A fully nonlinear boussinesq model for surface waves. part 1. highly nonlinear unsteady waves. *Journal of Fluid Mechanics*, **294**, 7192. 10.1002/fld.480710.1017/S0022112095002813.

Zijlema, M. and Stelling, G. (2008). Efficient computation of surf zone waves using the nonlinear shallow water equations with non-hydrostatic pressure. *Coastal Engineering*, **55**(780–790).

Zijlema, M., Stelling, G. and Smit, P. (2005). Further experiences with computing non-hydrostatic free-surface flows involving water waves. *International Journal for Numerical Methods in Fluids*, **48**, 169–197.

Zijlema, M., Stelling, G. and Smit, P. (2011*a*). SWASH: An operational public domain code for simulating wave fields and rapidly varied flows in coastal waters. *Coastal Engineering*, **58**, 992–1012.

Zijlema, M., Stelling, G. and Smit, P. (2011*b*). Swash: An operational public domain code for simulating wave fields and rapidly varied flows in coastal waters. *Coastal Engineering*, **58**(10), 992 – 1012. ISSN 0378-3839. 10.1002/fld.4807https://doi.org/10.1016/j.coastaleng.2011.05.015.

Paper 2

REEF3D::FNPF - a flexible fully nonlinear potential flow solver

Bihs H., Wang W., Pákozdi C. and Kamath A. (2020)
Journal of Offshore Mechanics and Arctic Engineering, 142(4).

REEF3D::FNPF - A Flexible Fully Nonlinear Potential Flow Solver

Hans Bihs[1], Weizhi Wang[1]*, Csaba Pákozdi[2] and Arun Kamath[1]

[1] Department of Civil and Environmental Engineering
Norwegian University of Science and Technology
Høgskoleringen 7A, 7491 Trondheim, Norway

[2] SINTEF Ocean, Otto Nielsens veg 10, 7052 Trondheim, Norway

Journal of Offshore Mechanics and Arctic Engineering, 2020, **142** 4.
DOI: http://dx.doi.org/10.1115/1.4045915

Abstract

In situations where the calculation of ocean wave propagation and impact on structures is required, fast numerical solvers are desired in order to find relevant wave events. Computational Fluid Dynamics (CFD) based Numerical Wave Tanks (NWT) emphasize on the hydrodynamic details such as fluid-structure interaction, which make them less ideal for the event identification due to the large computational resources involved. Therefore, a computationally efficient numerical wave model is needed to identify the events both for offshore deep-water wave fields and coastal wave fields where the bathymetry and coastline variations have strong impact on wave propagation. In the current paper a new numerical wave model is represented that solves the Laplace equation for the flow potential and the nonlinear kinematic and dynamics free surface boundary conditions. This approach requires reduced computational resources compared to CFD based NWTs. The resulting fully nonlinear potential flow solver REEF3D::FNPF uses a σ-coordinate grid for the computations. This allows the grid to follow the irregular bottom variation with great flexibility. The free surface boundary conditions are discretized using fifth-order WENO finite difference methods and the third-order TVD Runge-Kutta scheme for time stepping. The Laplace equation for the potential is solved with Hypres stabilized biconjugated gradient solver preconditioned with geometric multi-grid. REEF3D::FNPF is fully parallelized following the domain decomposition strategy and the MPI communication protocol. The numerical results agree well with the experimental measurements in all tested cases and the model proves to be efficient and accurate for both offshore and coastal conditions.

Keywords: Fully non-linear potential flow; Numerical wave modelling; Irregular topography; REEF3D

*Corresponding author, weizhi.wang@ntnu.no
Postprint, published in Journal of Offshore Mechanics and Arctic Engineering, doi:http://dx.doi.org/10.1115/1.4045915

1 Introduction

In the study of wave propagation and wave loads on offshore and coastal structures, phase-resolved wave modeling is often required, because it presents the details of the complicated free surface phenomena and enables a time domain analysis. A closer investigation of wave-structure interaction usually requires a Navier-Stokes solver to represent the complicated events involving turbulent flows. REEF3D is developed as an open-source hydrodynamic model specializing in the simulations of complex free surface flows (Bihs et al. (2016)). Its Navier-Stokes solver REEF3D::CFD has been widely used for various hydrodynamic studies. For example, the model is used for the regular wave interaction with surface piercing circular cylinder arrays (Kamath et al. (2016)), wave interaction with horizontal semi-submersible cylinders in tandem (Ong et al. (2017)) and multi-directional irregular wave interaction with a large-diameter cylinder (Wang et al. (2018)). The modular design of the model enables a flexible implementation of extensions. As a result, the model is also seen in a broader range of applications, such as the sediment transport analysis (Ahmad et al. (2018)) and the coastal infrastructure design (Sasikumar et al. (2018)). However, such computations tend to require a high resolution of the computational domain and therefore require more computational resources and longer simulation time. In order to identify relevant wave events close to the structures, a large-scale simulation is demanded, where a faster numerical model is needed.

In the far-field wave domain, fast two-dimensional shallow water models have been developed for fast phase-resolving wave modeling, such as widely used Boussinesq-type models (Madsen et al. (1991); Nwogu (1993)). However, the representation of the dispersion relation remains a challenge in deep water regions with such models. Turbulence and viscosity are normally not significant in the far-field domain. Therefore, a potential flow solver is ideal for a fast calculation of wave propagation in the far-field, especially in deep water conditions. The development of the potential flow solvers has focused on the representation of nonlinearity. One nonlinear wave model in the potential flow domain is the high-order spectrum (HOS) model (Ducrozet et al. (2012); Ducrozet et al. (2016)) where a high level of accuracy and computational efficiency are provided by a Fast Fourier Transform (FFT) solution. The model is proven to be efficient both in a numerical wave tank and in an open-ocean scenario. However, the development is challenged by an efficient representation of the fast varying bottom geometry.

Another approach is solving the Laplace equation with an enclosure of free surface boundary conditions and the bottom boundary condition. In the studies of Grilli et al. (1996) (Grilli (1996)), a high-order boundary element method (BEM) is used for various applications including wave propagation, shoaling, breaking and wave run-up. Correct representations of both the geometry and kinematics of strongly nonlinear waves are achieved with the highly nonlinear model where no approximations are introduced for the free surface boundary conditions. However, BEM approaches usually require explicit knowledge of a fundamental solution of the differential equations and case-specific mathematical analysis. A sharp discontinuity at the boundary, such as corners and edges may introduce singularities in the solution. In contrast to the BEM approach, Li and Fleming (1997) (Li and Fleming (1997)) were the first to propose a finite difference method (FDM) for the solution of the Laplace equation throughout the whole domain. A low-order multi-grid method is developed for an efficient and scalable solution of the fully nonlinear potential flow (FNPF) equations for water wave applications. Bingham et al. (2007) (Bingham and Zhang (2007)) further improved the model using high-order finite differences. In 2008, OceanWave3D (Engsig-Karup et al. (2009)) was introduced as a fully nonlinear and dispersive free surface wave model for 3D nonlinear water waves. Adaptive and curvilinear meshes are employed in the model, offering flexibilities with respect to geometry. The model has also been extended to study wave-structure interactions (Engsig-Karup and Bingham (2009); Ducrozet et al. (2014)). However, the mesh generation with curvilinear mesh can be challenging with the appearance of complicated solid boundaries in the computational domain. Other FNPF models have also been developed in 2D or 3D, as presented in (Janssen et al. (2010); Mehmood et al. (2015, 2016)). These FNPF models are able to simulate strongly nonlinear wave generation, propagation and transformation, up to wave overturning (Janssen et al. (2010)). Recently, much attention has also been put on improving the computational capacity of the FNPF models. For example, an OceanWave3D version equipped with a GPU-based parallelization was introduced in 2012 (Engsig-Karup et al. (2012)). Further explanations of the GPU implementations on heterogeneous many-core architectures can be found in (Engsig-Karup et al. (2013)) and (Glimberg et al. (2013)). The model achieves an applaudable computational efficiency, but also requires specific GPU infrastructure.

There is a lack of potential flow model that represents both non-linear wave phenomena at offshore and wave transformation at coastal area with irregular varying topography, as well as supporting High Performance Computation (HPC) with multiple processors. In this paper, a fully nonlinear potential flow solver REEF3D::FNPF is introduced in the numerical framework of REEF3D. The computations are performed with a finite difference method on a σ-coordinate grid. Since the model is coded in REEF3D, the existing robust numerical schemes in REEF3D are straightforward accessible to the proposed model. For example, the model is equipped with high-order discretization schemes and is fully parallelized with an MPI-based domain decomposition method. The presented paper describes the governing equations and the numerical implementations of the model. Then four test cases are shown to demonstrate its numerical performance. First, a linear progressive wave propagation over constant water depth is simulated. Then, the wave propagation over irregular topography is investigated by simulating the wave transformation over a submerged bar. Next, the evolution of a wave packet and the wave focusing is presented. Finally, a three-hour irregular wave simulation is performed. The simulated results are compared to theoretical values and experimental measurements. In the presented studies, the model shows a robust accuracy and cheerful computational efficiency.

2 Numerical Model

Governing equations

The governing equation for the flow calculations in the open-source fully non-linear potential flow code REEF3D::FNPF is the Laplace equation:

$$\frac{\partial^2 \phi}{\partial x^2} + \frac{\partial^2 \phi}{\partial y^2} + \frac{\partial^2 \phi}{\partial z^2} = 0 \tag{1}$$

In order to solve for the velocity potential ϕ, this elliptic equation requires boundary conditions, where especially the ones at the free surface and the bed are of importance. At the free surface, the fluid particles should remain at the surface and the pressure in the fluid is equal to the atmospheric pressure. These conditions must hold true at the free surface at all times and they form the kinematic and dynamic boundary conditions at the free surface respectively:

$$\frac{\partial \eta}{\partial t} = -\frac{\partial \eta}{\partial x}\frac{\partial \widetilde{\phi}}{\partial x} - \frac{\partial \eta}{\partial y}\frac{\partial \widetilde{\phi}}{\partial y} + \widetilde{w}\left(1 + \left(\frac{\partial \eta}{\partial x}\right)^2 + \left(\frac{\partial \eta}{\partial y}\right)^2\right), \tag{2}$$

$$\frac{\partial \widetilde{\phi}}{\partial t} = -\frac{1}{2}\left(\left(\frac{\partial \widetilde{\phi}}{\partial x}\right)^2 + \left(\frac{\partial \widetilde{\phi}}{\partial y}\right)^2\right) + \frac{1}{2}\widetilde{w}^2\left(1 + \left(\frac{\partial \eta}{\partial x}\right)^2 + \left(\frac{\partial \eta}{\partial y}\right)^2\right) - g\eta. \tag{3}$$

where $\widetilde{\phi} = \phi(\mathbf{x}, \eta, t)$ is the velocity potential at the free surface, $\mathbf{x} = (x, y)$ represents the horizontal location and $\widetilde{w}$ is the vertical velocity at the free surface.

At the bottom, the fluid particle cannot penetrate the solid boundary, and therefore the vertical water velocity must be zero at all times. This gives the bottom boundary condition:

$$\frac{\partial \phi}{\partial z} + \frac{\partial h}{\partial x}\frac{\partial \phi}{\partial x} + \frac{\partial h}{\partial y}\frac{\partial \phi}{\partial y} = 0, \quad z = -h. \tag{4}$$

where $h = h(\mathbf{x})$ is the water depth from the seabed to the still water level.

The Laplace equation, together with the enclosure of the boundary conditions are solved on a flexible-order finite difference scheme on a σ-coordinate. The σ-coordinate can be transferred from a Cartesian grid following:

$$\sigma = \frac{z + h\left(\mathbf{x}\right)}{\eta(\mathbf{x}, t) + h(\mathbf{x})} \tag{5}$$

The velocity potential is denoted as Φ after the σ-coordinate transformation. Then the governing equations and boundary conditions in the σ-coordinate become:

$$\Phi = \widetilde{\phi}, \qquad \sigma = 1; \tag{6}$$

$$\begin{aligned}&\frac{\partial^2 \Phi}{\partial x^2} + \frac{\partial^2 \Phi}{\partial y^2} + \left(\frac{\partial^2 \sigma}{\partial x^2} + \frac{\partial^2 \sigma}{\partial y^2}\right)\frac{\partial \Phi}{\partial \sigma} + 2\left(\frac{\partial \sigma}{\partial x}\frac{\partial}{\partial x}\left(\frac{\partial \Phi}{\partial \sigma}\right)\right.\\ &\left. + \frac{\partial \sigma}{\partial y}\frac{\partial}{\partial y}\left(\frac{\partial \Phi}{\partial \sigma}\right)\right) + \left(\left(\frac{\partial \sigma}{\partial x}\right)^2 + \left(\frac{\partial \sigma}{\partial y}\right)^2 + \left(\frac{\partial \sigma}{\partial z}\right)^2\right)\frac{\partial^2 \Phi}{\partial \sigma^2} = 0, \qquad 0 \leq \sigma < 1;\end{aligned} \tag{7}$$

$$\left(\frac{\partial \sigma}{\partial z} + \frac{\partial h}{\partial x}\frac{\partial \sigma}{\partial x} + \frac{\partial h}{\partial y}\frac{\partial \sigma}{\partial y}\right)\frac{\partial \Phi}{\partial \sigma} + \frac{\partial h}{\partial x}\frac{\partial \Phi}{\partial x} + \frac{\partial h}{\partial y}\frac{\partial \Phi}{\partial y} = 0, \qquad \sigma = 0. \tag{8}$$

Once the velocity potential Φ is obtained in the σ-domain, the velocities can be calculated as follows:

$$u(\mathbf{x},z) = \frac{\partial \Phi(\mathbf{x},z)}{\partial x} = \frac{\partial \Phi(\mathbf{x},\sigma)}{\partial x} + \frac{\partial \sigma}{\partial x}\frac{\partial \Phi(\mathbf{x},\sigma)}{\partial \sigma}, \tag{9}$$

$$v(\mathbf{x},z) = \frac{\partial \Phi(\mathbf{x},z)}{\partial y} = \frac{\partial \Phi(\mathbf{x},\sigma)}{\partial y} + \frac{\partial \sigma}{\partial y}\frac{\partial \Phi(\mathbf{x},\sigma)}{\partial \sigma}, \tag{10}$$

$$w(\mathbf{x},z) = \frac{\partial \Phi(\mathbf{x},z)}{\partial z} = \frac{\partial \sigma}{\partial z}\frac{\partial \Phi(\mathbf{x},\sigma)}{\partial \sigma}. \tag{11}$$

The waves are generated at the wave generation zone using the relaxation method (Mayer et al. (1998)). The relaxation function proposed by Jacobsen (Jacobsen et al. (2012)) is used in the model, as shown in Eqn. (12). In the wave generation zone, the free-surface elevation and velocities are ramped up to the designed theoretical values. In the numerical beach, a reverse process takes place and the flow properties are restored to hydrostatic values following the relaxation method.

$$\Gamma(\widetilde{x}) = 1 - \frac{e^{(\widetilde{x}^{3.5})} - 1}{e - 1} \; for \; \widetilde{x} \in [0;1] \tag{12}$$

where $\widetilde{x}$ is scaled to the length of the relaxation zone.

The Laplace equation is solved using the parallelized geometric multi-grid algorithm provided by hypre (van der Vorst (1992)). Second-order central differences are used for the discretization of the Laplace equation.

The calculation of wave propagation can be challenging because insufficient grid resolution can cause numerical diffusion which consequently leads to unphysical damping of the waves. In order to achieve the balance between the order of accuracy of the discretization methods and the numerical stability and efficiency, the model chooses the fifth-order WENO (weighted essentially non-oscillatory) scheme (Jiang and Shu (1996)) in the conservative finite-difference framework for the discretization of the convection terms. This scheme can handle large gradients accurately by taking local smoothness into account. The overall WENO discretization stencil consists of three local ENO-stencils, which are weighted depending on their smoothness, with the smoothest stencil contributing the most significantly.

For the time treatment for the freesurface boundary conditions, a third-order accurate TVD Runge-Kutta scheme (Shu and Osher (1988)) is used. Adaptive time stepping is used in order to determine the time step size while keeping a constant CFL number which is based on phase velocity.

The model is fully parallelized following the domain decomposition strategy. Ghost cells are used within the implemented domain decomposition framework for the parallelization. These ghost cells are updated with the values from the neighboring processors via MPI (Message Passing Interface).

3 Results

Linear wave propagation

At first, the proposed model is tested with wave propagation over a constant bottom. The two-dimensional (2D) numerical wave tank is 35 m long. The still water level is constant at

0.4 m. The input wave is a linear wave at intermediate water depth. The wave height is 0.02 m and the wavelength is 3.73 m. A wave generation zone of one wavelength is located at the inlet of the tank to the left-hand side. A numerical beach of two wavelengths is located at the outlet of the tank to the right-hand side. The schematics of the numerical wave tank's configuration is shown in Fig. 1.

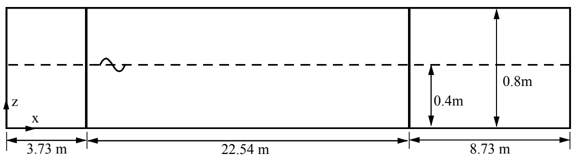

Figure 1: The configuration of the numerical wave tank for the linear wave propagation.

To study the grid convergence property of the model, three simulations are performed with three different grid sizes. The finest grid uses 85 cells per wavelength, the intermediate grid allows 53 cells per wavelength, while the coarsest grid consists of 26 cells per wavelength. The wave profiles at $t = 35$ s from the three simulations are compared to the theoretical value in Fig. 2:

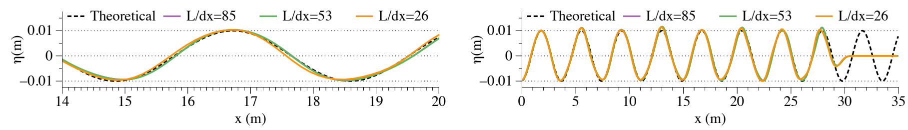

(a) (b)

Figure 2: The comparison of the wave profile at $t = 35$ s for the linear wave propagation. (a) the comparison along the whole tank, (b) a closer view at the wave profile.

A Richardson extrapolation method is used to estimate the grid-independent numerical result, the spatial discretization error and the convergence rate. The average wave heights during 30 s simulations are used for the grid-convergence study. The fitted curve of the Richardson extrapolation is shown in Fig. 3. It is seen that the grid-independent average wave height is 0.01983 m, with an error of -0.833% compared to the input theoretical value of 0.01983 m. The monotonic convergence rate is found to be 2.64, higher than second order.

Wave propagation over a submerged bar

In this section, the wave propagation over a submerged bar (Beji and Battjes (1993)) is tested. The 2D wave tank of 35 m is equipped with a wave generation zone of one wavelength 3.73 m at the inlet and a numerical beach of two wavelengths 8.73 m at the outlet. The still water level is 0.4 m. The submerged bar begins at $x = 6$ m and elevates following a slope of $1 : 20$ until it reaches the top platform at $x = 12$ m, with a height of 0.3 m. It remains the height for 2 m before it starts a downwards slope of $1 : 10$ and reaches the bottom of the tank at $x = 17$ m. Nine wave gauges are located at $x = 4.0$ m, 10.5 m, 12.5 m, 13.5 m, 14.5 m, 15.7 m, 17.3 m, 19.0 m and 21.0 m. The incident wave height is $H = 0.02$ m and the wavelength is $L = 3.73$ m. The

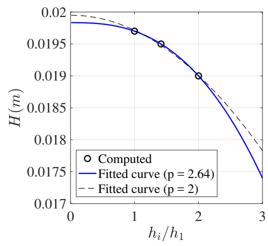

Figure 3: The grid convergence study following a Richardson extrapolation method for the linear wave propagation case.

schematics of the configurations of the numerical wave tank is shown in Fig. 4.

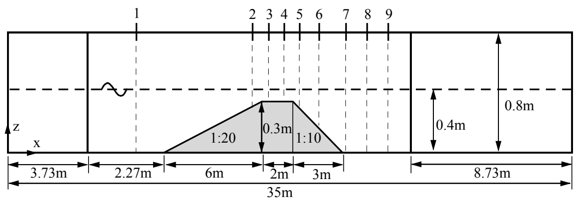

Figure 4: The configuration of the numerical wave tank for wave propagation over a submerged bar.

A grid convergence study is performed at gauge 2 and 6, before and after the crest of the submerged bar, as shown in Fig. 5a and Fig. 5b. Three grids sizes are used in the study, giving 212, 106, 53, and 26 cells per incident wavelength. It is found that 212 cells per wavelength are sufficient to capture the wave transformation. A simulation time of 35 s is used. With 12 2.7 GHz cores on a Mac Pro with 32 GB memory, the simulation only takes 170 s. The time series at all nine wave gauges are compared to the experimental measurements, shown from Fig. 6a to Fig. 6i. The waves shoal over the uprising slope of the submerged bar. A continuous increase of wave height is observed from gauge 1 to gauge 3. Gauge 4 and gauge 5 sees the beginning of the wave decomposition process, where higher frequency short wave components start to emerge. From gauge 6, the de-shoaling takes place, and the wave decomposition becomes more prominent. The velocity potential and the horizontal velocities in the numerical wave tank at $t = 35$ s is also shown in Fig. 7. With the chosen grid resolution, the evolution of the waves is well represented during the entire shoaling and the de-shoaling process, especially the complicated wave decomposition after the top of the bar. It is also noted that in order to resolve those short waves during the decomposition, a finer grid is needed compared to the previous study with a constant bottom in the previous section.

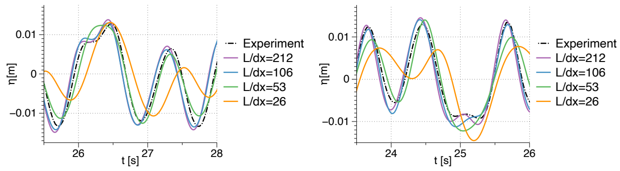

(a) Grid convergence at wave gauge 6

(b) Grid convergence at wave gauge 8

Figure 5: The grid convergence study at wave gauge 6 and wave gauge 8.

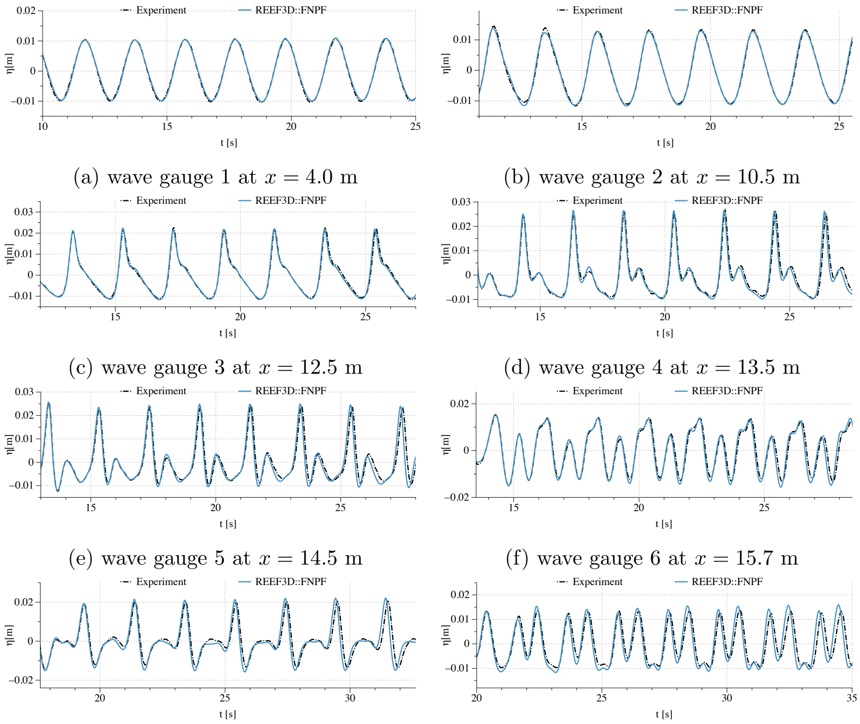

(a) wave gauge 1 at $x = 4.0$ m

(b) wave gauge 2 at $x = 10.5$ m

(c) wave gauge 3 at $x = 12.5$ m

(d) wave gauge 4 at $x = 13.5$ m

(e) wave gauge 5 at $x = 14.5$ m

(f) wave gauge 6 at $x = 15.7$ m

(g) wave gauge 7 at $x = 17.3$ m

(h) wave gauge 8 at $x = 19.0$ m

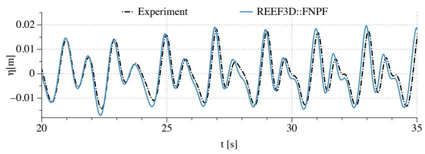

(i) wave gauge 9 at $x = 21.0$ m

Figure 6: The comparison between the simulated time series and the experimental measurements at all wave gauges with the grid resolution $L/dx = 212$ in the numerical wave tank for the wave propagation over a submerged bar.

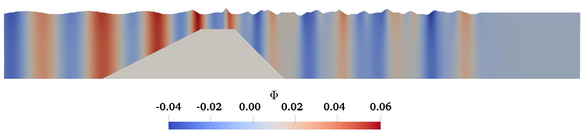

(a) The velocity potential in the wave tank at $t = 35$ s

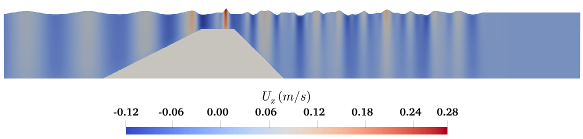

(b) The horizontal velocity in the wave tank at $t = 35$ s

Figure 7: The velocity potential and the horizontal velocity in the numerical wave tank when the waves pass the submerged bar at $t = 35$ s.

In comparison, a CFD simulation requires a much finer grid and smaller time step to resolve the high-frequency wave components. In stead of 20000 cells used in the current simulation, a cell number of 1322000 is needed in a CFD simulation to achieve good representation of the wave propagation. With 12 cores on a Mac Pro, the CFD simulation takes about 17 hours indtead of 170 s as with FNPF, a magnitude of 400 slower than the FNPF simulation for this case.

The focused wave from a wave packet

The model is tested with extreme wave event in this section. An experimental wave packet measured in the LargeWave Flume (GWK), Hannover, Germany (Clauss and Steinhagen (1999)) is used for the validation. Several tests in the experiment have been successfully reproduced with the CFD model REEF3D::CFD (Bihs et al. (2019)), including focused wave breaking. Here, a non-breaking focused wave is to be reproduced with the presented model REEF3D::FNPF. The physical wave tank in the experiment is a 300 m long channel with a still water level of $d = 4.01$ m. A Piston-type wavemaker is used to generate the wave packets such that the waves focus at a designed location and time. In the numerical test, a 2D numerical wave tank 250 m long with a water depth of $d = 4.01$ m is used. Following the arrangement from the experiment, the distance of the focus point and the time of focusing are $x_f = 126.21$ m and $t_f = 83$ s. The free surface elevations are measured at $x = 3.59\text{ m}, 50.5\text{ m}, 79.05\text{ m}, 100.10$ m and 126.21 m in the numerical wave tank. They are compared to the experimental observations as presented from Fig. 8a to Fig. 8e. The grid convergence study is shown in Fig. 9, where 30, 20 and 10 cells per shortest wavelength in the generated ave group are tested. It is found that 30 cells per shortest wavelength shows a nearly grid-independent result. With the chosen resolution, a 110 s simulation takes 1160 s with 2 processors on the same machine as shown in the previous section. At the focus location, the numerical error at the wave peak is 4.8%. In order to show the evolution of the wave packet, the wave profiles and the horizontal velocities in the computational domain are shown in Fig. 10 for the sampled time frames $t = 65\text{ s}, 83$ s and 99 s. At $t = 65$ s, the wave packet propagates from the wave generation zone, where a short wave is leading the wave train while the longer wave is chasing from behind. At $t = 83$ s, all the wave components superimpose into a focused wave with an amplified single peak with high velocities. At $t = 99$ s, the longer wave components surpass the shorter waves and the single peak decomposes into several components again. The entire process is clearly represented by the model.

Three-hour irregular wave

The advantage of the potential flow solver is more prominent for long-duration simulations for obtaining statistical properties of a sea state. In order to gather statistical information on a wave field, it is necessary to perform a three-hour simulation at full scale. This is computationally demanding for Naiver-Stokes solvers. In this section, the proposed potential flow model is used to simulation a three-hour irregular sea state at intermediate water depth. The input spectrum is a JONSWAP spectrum with a peak enhancement factor of 3.0. The input wave has a significant wave height of $H_s = 4.5$ m, and peak period of $T_p = 12.0$ s. A constant water depth of 40 m is used. The two-dimensional wave tank is 1760 m long, corresponding to 8 wavelengths based on the peak period. The frequency range of $[0.75\omega_p, 2\omega_p]$

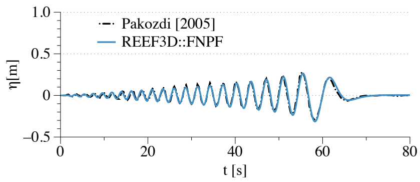

(a) wave gauge 1 at $x = 3.59$ m

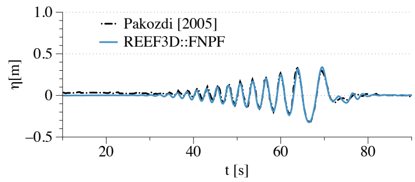

(b) wave gauge 2 at $x = 50.5$ m

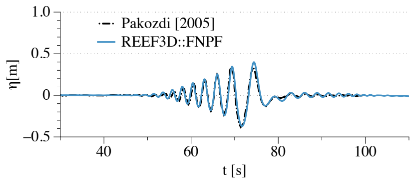

(c) wave gauge 3 at $x = 79.05$ m

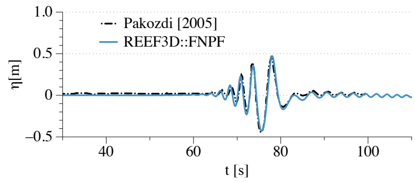

(d) wave gauge 4 at $x = 100.10$ m

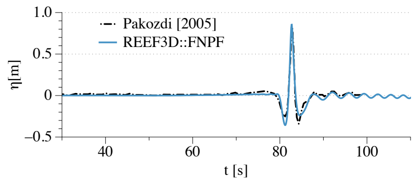

(e) wave gauge at the focus point at $x = 126.21$ m

Figure 8: The comparison between the simulated time series and the experimental measurements at all wave gauges in the numerical wave tank for the focusing wave packet.

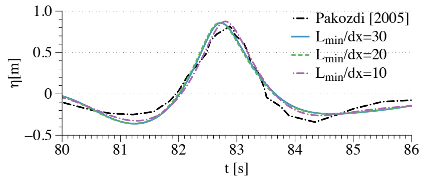

Figure 9: The grid convergence study at the focusing point for the wave packet propagation.

is used. The frequency limits represent the wave energy from 0.5% of the total energy to 99.5% of the total energy. Therefore, the chosen frequency range represents 99% of the total wave energy. The wave generation zone is located at the input boundary with the length of one wavelength corresponding to the lowest frequency. The numerical beach is located at the outlet boundary and has a length twice that of the wave generation zone. 30 vertical cells are used with vertical stretching in the σ-coordinate system. The horizontal resolution is 30 cells per wave length corresponding to the shortest wave with the highest frequency. The configuration results in a horizontal cell size of 2 m. The total number of cells is 26400. The

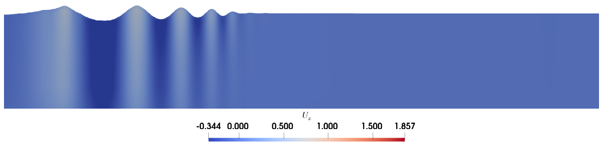

(a) Horizontal velocity at $t = 65$ s

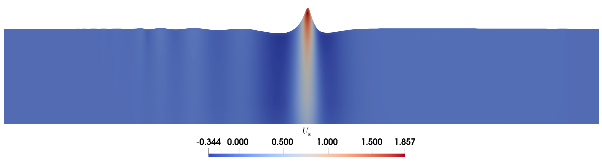

(b) Horizontal velocity at $t = 83$ s at the focusing time

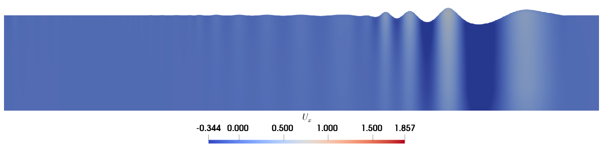

(c) Horizontal velocity at $t = 99$ s

Figure 10: The wave profile and the horizontal velocities (m/s) at different times during the evolution of the wave packet.

simulation time is 12800 s, where the three-hour window from 2000 s to 12800 s is used for the data analysis. The wave elevation at the wave probe located five wave lengths (using the peak period) away is investigated for the chosen time window. The simulated spectrum is compared with the theoretical spectrum in Fig. 11. The horizontal velocity field of the simulation at $t = 12800$ s is shown in Fig. 12, where the surface elevation is amplified with a factor of 10 for visualisation purpose. With 16 cores on supercomputer Vilje, the 12800 s simulation takes only 1.13 hour, which is three times faster than real time. The calculated significant wave height in the numerical wave tank is 4.456 m, the peak period is 11.95 s. With a compensation of 1% wave energy, the significant wave height becomes 4.50 m, exactly the same as the input value. The simulated irregular wave match the input H_s, T_p and the shape of the spectrum with high accuracy.

4 Conclusion

The presented work introduces a new flexible fully-nonlinear potential flow solver REEF3D::FNPF in the numerical framework of the open-source hydrodynamics model REEF3D. The proposed model solves the Laplace equation together with the free surface boundary conditions and the

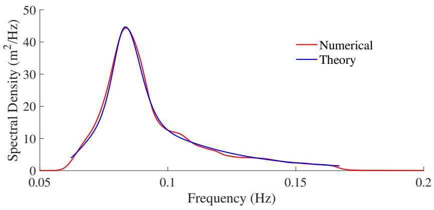

Figure 11: Simulated wave spectrum in comparison to the theoretical spectrum for the three-hour irregular wave simulation.

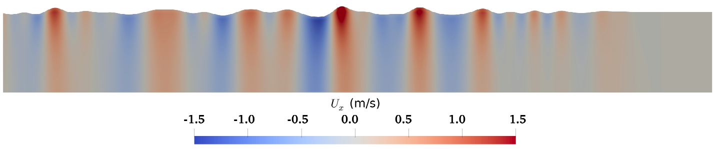

Figure 12: Horizontal velocities in the simulated irregular wave field in the entire numerical wave tank at $t = 12800$ s. Surface elevation is amplified with a factor of 10 for visualisation purpose.

bottom boundary condition using a finite difference method on a σ-coordinate system. The solution for the velocity potential is obtained with Hypres stabilized bi-conjugated gradient solver preconditioned with geometric multi-grid. High-order discretization schemes are used, such as a fifth-order WENO scheme in space and a third-order Runge-Kutta in time. The varying bottom is represented with the sigma coordinate grid. An efficient domain decomposition strategy is used for the parallel computation where the information between sub-domains is exchanged following an MPI protocol. The model is validated for the wave propagation over a submerged bar and the wave focusing from a wave packet. In both studies, the model provides favorable agreements with the experimental data. In addition, the model is able to perform simulations very fast with very limited computational resources, enabling complex simulations on personal computers or desktops. The model takes only one hour for the three-hour irregular wave simulation on 16 processors and obtained near identical statistical wave properties in comparison to the theoretical inputs. The model is proven to be accurate and computationally efficient for diverse and flexible scenarios with non-breaking waves. To further explore the model's potential, large-scale wave propagation over irregular natural topography and irregular coastline are to be investigated. A robust wave breaking algorithm is also to be introduced in the model for future studies.

Acknowledgements

The research work has been funded by the Norwegian Public Roads Administration through the E39 fjord crossing project (No. 304624).

References

Ahmad, N., Bihs, H., Myrhaug, D., Kamath, A. and ivind A. Arntsen (2018). Three-dimensional numerical modelling of wave-induced scour around piles in a side-by-side arrangement. *Coastal Engineering*, **138**, 132 – 151. ISSN 0378-3839. 10.1115/1.4045915https://doi.org/10.1016/j.coastaleng.2018.04.016.

Beji, S. and Battjes, J.A. (1993). Experimental investigation of wave propagation over a bar. *Coastal Engineering*, **19**, 151–162.

Bihs, H., Kamath, A., Alagan Chella, M. and Arntsen, Ø.A. (2019). Extreme Wave Generation, Breaking, and Impact Simulations Using Wave Packets in REEF3D. *Journal of Offshore Mechanics and Arctic Engineering*, **141**(4), 41802–41807. ISSN 0892-7219.

Bihs, H., Kamath, A., Chella, M.A., Aggarwal, A. and ivind A. Arntsen (2016). A new level set numerical wave tank with improved density interpolation for complex wave hydrodynamics. *Computers Fluids*, **140**, 191 – 208. ISSN 0045-7930.

Bingham, H.B. and Zhang, H. (2007). On the accuracy of finite-difference solutions for nonlinear water waves. *Journal of Engineering Mathematics*. ISSN 00220833. 10.1115/1.404591510.1007/s10665-006-9108-4.

Clauss, G.F. and Steinhagen, U. (1999). Numerical Simulation of Nonlinear Transient Waves and its Validation by Laboratory Data. In: *9th International Offshore and Polar Engineering Conference*.

Ducrozet, G., BONNEFOY, F., Le Touzé, D. and Ferrant, P. (2012). A modified High-Order Spectral method for wavemaker modeling in a numerical wave tank. *European Journal of Mechanics - B/Fluids*, **34**, http://dx.doi.org/10.1016/j.euromechflu.2012.01.017. 10.1115/1.404591510.1016/j.euromechflu.2012.01.017.

Ducrozet, G., Bonnefoy, F., Le Touzé, D. and Ferrant, P. (2016). HOS-ocean: Open-source solver for nonlinear waves in open ocean based on High-Order Spectral method. *Computer Physics Communications*, **203**, 245–254. 10.1115/1.404591510.1016/j.cpc.2016.02.017.

Ducrozet, G., Engsig-Karup, A.P., Bingham, H.B. and Ferrant, P. (2014). A non-linear wave decomposition model for efficient wavestructure interaction. part a: Formulation, validations and analysis. *Journal of Computational Physics*, **257**, 863 – 883. ISSN 0021-9991. 10.1115/1.4045915https://doi.org/10.1016/j.jcp.2013.09.017.

Engsig-Karup, A. and Bingham, H. (2009). Boundary-fitted solutions for 3d nonlinear water wave-structure interaction. In: *IWWWFB24*, 20.

Engsig-Karup, A., Bingham, H. and Lindberg, O. (2009). An efficient flexible-order model for 3D nonlinear water waves. *Journal of Computational Physics*, **228**, 2100–2118.

Engsig-Karup, A.P., Glimberg, S.L., Nielsen, A.S. and Lindberg, O. (2013). *Fast hydrodynamics on heterogenous many-core hardware*, 251294. Taylor Francis. ISBN 978-1-4665-7162-4. 2013;11.

Engsig-Karup, A.P., Madsen, M.G. and Glimberg, S.L. (2012). A massively parallel gpu-accelerated model for analysis of fully nonlinear free surface waves. *International Journal for Numerical Methods in Fluids*, **70**(1).

Glimberg, L.S., Engsig-Karup, A.P., Nielsen, A.S. and Dammann, B. (2013). Development of software components for heterogeneous many-core architectures. In: R. Couturier (Editor), *Designing Scientific Applications on GPUs*, Lecture notes in computational science and engineering, 73–104. CRC Press / Taylor & Francis Group.

Grilli, S. (1996). Fully nonlinear potential flow models used for long wave runup prediction. *Long Wave Runup Models*.

Jacobsen, N.G., Fuhrman, D.R. and Fredsøe, J. (2012). A wave generation toolbox for the open-source CFD library: OpenFOAM. *International Journal for Numerical Methods in Fluids*, **70**(9), 1073–1088.

Janssen, C.F., Grilli, T. and Krafczyk, M. (2010). Modeling of Wave Breaking and Wave-Structure Interactions by Coupling of Fully Nonlinear Potential Flow and Lattice-Boltzmann Models. *Simulation*. ISSN 10986189. 10.1115/1.404591510.1016/j.jphotobiol.2011.03.017.

Jiang, G.S. and Shu, C.W. (1996). Efficient implementation of weighted ENO schemes. *Journal of Computational Physics*, **126**, 202–228.

Kamath, A., Bihs, H., Alagan Chella, M. and ivind A. Arntsen (2016). Upstream-cylinder and downstream-cylinder influence on the hydrodynamics of a four-cylinder group. *Journal of Waterway, Port, Coastal, and Ocean Engineering*, **142**(4), 04016002. 10.1115/1.404591510.1061/(ASCE)WW.1943-5460.0000339.

Li, B. and Fleming, C.A. (1997). A three dimensional multigrid model for fully nonlinear water waves. *Coastal Engineering*. ISSN 03783839. 10.1115/1.404591510.1016/S0378-3839(96)00046-4.

Madsen, P.A., Murray, R. and Sørensen, O.R. (1991). A new form of the Boussinesq equations with improved linear dispersion characteristics. *Coastal Engineering*, **15**, 371–388.

Mayer, S., Garapon, A. and Sørensen, L.S. (1998). A fractional step method for unsteady free surface flow with applications to non-linear wave dynamics. *International Journal for Numerical Methods in Fluids*, **28**, 293–315.

Mehmood, A., Graham, D.I., Langfeld, K. and Greaves, D.M. (2015). OpenFOAM Finite Volume Method Implementation of a Fully Nonlinear Potential Flow Model for Simulating Wave-Structure Interactions.

Mehmood, A., Graham, D.I., Langfeld, K. and Greaves, D.M. (2016). Numerical Simulation of Nonlinear Water Waves based on Fully Nonlinear Potential Flow Theory in OpenFOAM® -Extend.

Nwogu, O. (1993). Alternative form of Boussinesq equations for nearshore wave propagation. *Journal of Waterways, Port, Coastal, and Ocean Engineering*, **119**(6), 618–638.

Ong, M.C., Kamath, A., Bihs, H. and Afzal, M.S. (2017). Numerical simulation of free-surface waves past two semi-submerged horizontal circular cylinders in tandem. *Marine Structures*, **52**, 1 – 14. ISSN 0951-8339. 10.1115/1.4045915https://doi.org/10.1016/j.marstruc.2016.11.002.

Sasikumar, A., Kamath, A., Musch, O., Bihs, H. and Arntsen, Ø.A. (2018). Numerical Modeling of Berm Breakwater Optimization With Varying Berm Geometry Using REEF3D. *Journal of Offshore Mechanics and Arctic Engineering*, **141**(1), 011801. ISSN 0892-7219. 10.1115/1.404591510.1115/1.4040508.

Shu, C.W. and Osher, S. (1988). Efficient implementation of essentially non-oscillatory shock capturing schemes. *Journal of Computational Physics*, **77**, 439–471.

van der Vorst, H. (1992). BiCGStab: A fast and smoothly converging variant of Bi-CG for the solution of nonsymmetric linear systems. *SIAM Journal of Scientific Computing*, **13**, 631–644.

Wang, W., Kamath, A. and Bihs, H. (2018). CFD Simulations of Multi-Directional Irregular Wave Interaction With a Large Cylinder.

Paper 3

Investigation of focusing wave properties in a numerical wave tank with a fully nonlinear potential flow model

Wang W., Kamath A., Pákozdi C. and Bihs H. (2019) *Journal of Marine Science and Engineering*

Investigation of focusing wave properties in a numerical wave tank with a fully nonlinear potential flow model

Weizhi Wang[1,*], Arun Kamath[1], Csaba Pákozdi[2] and Hans Bihs[1]

[1] Department of Civil and Environmental Engineering
Norwegian University of Science and Technology
Høgskoleringen 7A, 7491 Trondheim, Norway
[2] SINTEF Ocean, Otto Nielsens veg 10, 7052 Trondheim, Norway

Journal of Marine Science and Engineering, 2019, **7** 10.
DOI: http://dx.doi.org/10.3390/jmse7100375

Abstract

Nonlinear wave interactions and superpositions among the different wave components and wave groups in a random sea sometimes produce rogue waves that appear unexpectedly with extremely large wave heights. A good understanding of the generation and evolution of such extreme wave events is of great importance for the analysis of wave forces on marine structures. A fully nonlinear potential flow (FNPF) model is proposed in the presented paper to investigate the different factors that influence the wave focusing location, focusing time and focusing wave height in a numerical wave tank. Those factors include wave steepness, spectrum bandwidth, wave generation method, focused wave spectrum and wave spreading functions. The proposed model solves the Laplace equation together with the boundary conditions on a σ-coordinate grid using high-order discretisation schemes on a fully parallel computational framework. The model is validated against the focused wave experiments and thereafter used to obtain insights into the effects of the different factors. It is found that the wave steepness contributes to changing the location and time of focus significantly. Spectrum bandwidth and directional spreading affect the focusing wave height and profile, for example, a wider bandwidth and a wider directional spread lead to lower focusing wave height. A Neumann boundary condition represents the nonlinearity of the wave groups better than a relaxation method for wave generation.

Keywords: fully nonlinear potential flow; extreme wave; focused waves

*Corresponding author, weizhi.wang@ntnu.no
Postprint, published in Journal of Marine Science and Engineering, doi:http://dx.doi.org/10.3390/jmse7100375

1 Introduction

Random seas consist of many incident wave components of different amplitudes, frequencies and phases. The nonlinear interactions among them may result in extreme waves that are much higher than that expected from the sea state in the region. Such large and unexpected extreme waves can exert tremendous forces on offshore structures. Understanding the generation and evolution of such waves is important for determining the wave loads on marine structures. One of the most renowned extreme events is the 'New Year Wave' recorded at the Draupner platform (Haver (2004)) where a maximum wave height of nearly 26 m was observed in a sea state with an measured significant wave height of 12 m. Afterwards, many efforts have been made to generate and reproduce such extreme events in both physical experiments and numerical wave tanks. Among those efforts, focused wave groups are considered as an efficient method to replicate extreme wave events.

Due to the stochastic nature of the sea state and extreme events, the basis for the generation of focused waves is the irregular wave theory. Lindgren (1970) presented a theoretical explanation for the wave generation through empirically studying the propagation of irregular wave groups. Based on his results, Tromans et al. (1991) suggested a practical spectrum for focused wave groups. The spectrum has a shape that is proportional to the auto-correlation function of the underlying random processes. This type of compact wave spectrum was later named the NewWave model. The NewWave model is based on the linear wave theory and wave spectra such as the JONSWAP and PM spectrum can be used to generate the irregular wave components for linear superposition. The NewWave method has been successfully applied to investigate irregular large waves both in deep (Jonathan and Taylor (1997)) and intermediate water depths (Taylor and Williams (2004)). The method has also been used for the studies of directional irregular seas and three-dimensional (3D) wave focusing in spreading seas (Jonathan and Taylor (1997); Bateman et al. (2001); Johannessen and Swan (2001)). Recently, researchers have further extended the NewWave theory to coastal applications in the shallow water domain, for example, wave run-up and flow kinematics at plane beaches (Borthwick et al. (2006); Whittaker et al. (2017)) and focused wave overtopping and forces on seawalls (Hunt (2003); Hunt-Raby et al. (2011); Whittaker et al. (2016, 2018); Hofland et al. (2014)). Another method for extreme wave generation is to use the transient wave packet approach, which has been validated during an experimental study in a wave flume (Clauss and Bergmann (1986)). The approach was later improved with increased flexibility, allowing a prediction of the wave train at any instant and location in a wave tank (Clauss and Kühhnlein (1995)). It was further optimised to avoid premature breaking by adjusting the high-frequency components (Clauss and Kuhnlein (1997)). Compared to the NewWave theory, the spectrum for the wave packet has a wider bandwidth and consists of more harmonic components of lower amplitudes relative to the focusing wave height. Consequently, a larger focusing wave height can be achieved and premature breaking is avoided.

Using different wave focusing theories, researchers have conducted many experiments to investigate different aspects of the evolution of focusing wave groups. Ning et al. (2009) performed an experiment in a wave flume to study the propagation of transient focusing wave groups with a range of different steepness. It is shown that the focusing point in time and space changes with varying wave steepnesses. Clauss and Steinhagen (1999) reported an experimental study on the evolution of a wave packet at the Large Wave Flume (GWK) in Hannover and demonstrated a similar finding. Sriram et al. (2015) investigated the evolution of focused wave packet in intermediate and deep water condition using different paddle displacements for a piston-type wavemaker. The results using second-order corrected paddle motion and linear paddle motion are compared and it is found that the difference is more prominent for a broadband spectrum. Bai et al. (2018) reported an experiment to generate focused waves in a wave flume and used the measured data for the validation of a numerical model. Taylor and Williams (2004) analyzed the data set from the WACSIS measurement program (Forristall et al. (2004)). The authors paid special attention to the average shape of large crests and troughs and the vertical and horizontal asymmetry. It was shown that the NewWave theory fits the average shape of large waves well when the trough-crest asymmetry is accounted for. Buldakov et al. (2017) introduced a linearized amplitude spectrum methodology following the NewWave theory to produce focused waves up to weak breaking waves in a physical wave flume. They found that the steepness of the limiting breaking wave depends strongly on the choice of the wave group spectrum. Focused wave group interaction with offshore and coastal structures and the impact forces are also investigated in several experiments (Zang et al. (2010, 2006)). In a 3D wave basin, Johannessen and Swan (2001) performed a laboratory study on the influence of directionality on the transient focusing wave groups in a spreading sea. The experiments prove the effectiveness of the focusing wave theories and provide fundamental insights into the generation and evolution of focused waves. However, experiments are also limited by the capability of continuous measurement. Wave focusing is a transient phenomenon with a short duration, therefore, demands more dense measurements.

Many numerical models have been employed to investigate focusing wave groups. Ning et al. (2009) used the local surface elevation measurements from a physical experiment to drive the numerical solution in their numerical model using a high-order boundary element method (HOBEM). Bai and Taylor (2007) report their numerical study on the diffraction of a focusing wave group around a circular cylinder using a HOBEM model with a mixed Eulerian-Lagrangian approach. A similar approach has been discussed in detail by Grilli et al. (2001) and used for the modeling of different 3D focusing wave groups (Grilli et al. (2010)). Other studies on the 3D energy focusing in a spreading sea have also been performed following the BEM approach (Brandini and Grilli (2001); Fochesato et al. (2007)). However, the BEM approaches generally involve mathematic expressions that make them less flexible for handling complex boundaries. Wu and Taylor (1994) suggest that a finite element method requires less memory than a BEM method and is more computationally efficient as a result. Following the suggestions and formulations of Wu and Taylor (1995), Clauss and Steinhagen (1999) performed numerical simulations of nonlinear transient waves using a potential flow solver with a moving boundary finite element method. Good agreements were achieved in the validation process against their laboratory data. Boussinesq-type models (Madsen et al. (1991); Nwogu (1993)) can also be used for extreme sea states, especially for shallow water region. With higher order terms for hydrodynamic pressure, Boussinesq-type models can resolve better dispersion relation in deeper wave condition (Madsen et al. (2002)), often with increasing risks of numerical instabilities due to higher order derivatives. The double-layer approach developed by Chazel et al. (2009) reduces the order of derivatives in comparison to the traditional high-order Boussinesq models and still shows the ability of modelling deep water waves up to $kh = 10$. Other numerical methods based on Fast Fourier Transforms

(FFT) are also explored for a further increase in computational efficiency. A fully-nonlinear spectral model is applied systematically for simulating the focusing of directionally spread surface water waves in 3D (Bateman et al. (2001, 2003, 2012)). The model is based on a Neumann operator similar to the G-operator (Craig and Sulem (1993)) and only the velocity potential at the free surface is needed for the solution. Both the free surface elevation η and velocity potential Φ are represented by a Fourier series and are advanced in time. The model is computationally efficient, as necessary spatial derivatives can be calculated rapidly using the FFT. However, the periodicity assumption is necessary to ensure that the spatial derivatives can be evaluated rapidly using FFT and this requirement is not necessarily physically realistic. Similarly, a high-order spectral (HOS) model is described and used in the simulation of 2D and 3D focused wave groups (Ducrozet et al. (2012); Bonnefoy et al. (2006*a*,*b*)). The spectral based methods are generally effective but also require certain criteria for the boundary conditions. Another approach is to solve the Laplace equation directly. Bingham and Zhang (2007) used a finite difference scheme for solving the Laplace equation and recommended using stretched grid that is clustered towards the free surface in the vertical direction. Based on the research, Engsig-Karup and Bingham (2009) introduced a general purpose fully nonlinear potential flow model OceanWave3D for wave propagation over varying bottom with no water depth limits. The model uses curvilinear grid in the horizontal plane for irregular boundaries. This approach requires sophisticated grid treatment when the boundary geometry becomes complicated. Efforts have been made to combine the usage of finite difference methods and spectral methods. Yates and Benoit (2015) compared a spectral approach with a finite difference approach in the vertical direction and found that the spectral approach is more accurate and efficient in one-dimensional tests. Based on that, Raoult et al. (2016) and Zhang et al. (2019) introduced the model Whisper3D that combines a finite difference scheme in the horizontal direction with a spectral approach in the vertical with Chebyshev polynomial. Clamond and Grue (2001) and Fructus et al. (2005) introduced another approach to evaluate the Dirichlet to Neumann operator, where the global terms of the operator are computed using FFT and the local terms are evaluated by numerical integration. However, the model also limits itself to periodic boundary conditions (Fructus et al. (2005)) as many others that reply on FFT. The coupled-mode Hamiltonian approach of Belibassakis and Athanassoulis (2011) and Athanassoulis et al. (2017) also shows a good representation of non-linear high waves over varying bottom in finite depth. For example, Athanassoulis et al. (2017) studied a focused wave evolution both over constant finite water depth and sloping bottom. The model has an efficient treatment of the bottom boundary and is most suitable for shallow to intermediate water depth simulations. In a recent development, a spectral element method (SEM) is used for the study of focused wave groups (Engsig-Karup and Eskilsson (2018)). The aforementioned numerical models are all based on potential flow theory and represent the free surface with a single-value and therefore cannot represent overturning breaking waves. For an accurate representation of overturning breaking waves, computational fluid dynamic (CFD) models are usually needed. Efforts to model the steep near-breaking focused wave group using a finite volume method (FVM) and a volume of fluid (VOF) technique for the free surface have been reported (Chen et al. (2014); Bai et al. (2018); Vyzikas et al. (2018)). Westphalen et al. (2012) compared the focused wave impact forces modeled by Navier-Stokes solvers with FVM and with a control-volume finite element method(CV-FE). To accurately capture the overturning breaker, the finite difference CFD model REEF3D::CFD (Bihs et al. (2016*b*)) has been used for extreme wave generation. With this model, focused breaking wave impact on structures is investigated with transient wave packets (Bihs et al. (2017*b*, 2019*b*)) and the NewWave theory (Bihs et al. (2016*a*, 2017*a*)). A level-set method is used to capture the free surface and overturning breakers are well represented. The modeled free surface elevations and impact loads are validated against experimental measurements and good agreement is achieved. CFD methods generally require high spatial resolution and present high demands on computational power. To reduce the computational cost associated with the CFD simulations, a one-way coupling between a CFD model and a fully nonlinear potential flow (FNPF) solver is presented by Paulsen et al. (2014) to study focusing wave groups. In this approach, the wave propagation is modeled rapidly in the FNPF domain and the breaking wave is resolved in a smaller CFD domain. However, special attention is needed for the coupling error at the boundaries of information exchange.

The presented paper attempts to offer insights into the different numerical configurations and aspects that influence the generation and evolution of non-breaking focused wave groups in a comprehensive manner. The work focuses on the time domain analysis and the geometric study of focusing wave groups. The changes of focusing time, focusing location, wave height and wave profile of the focused waves due to the effects of the wave generation method, bandwidth, wave nonlinearity, choice of focusing wave spectrum and wave spreading are investigated in detail. After examining the existing numerical approaches, a fully nonlinear potential flow model with a flexible boundary treatment is considered as a reliable and efficient alternative for non-breaking nonlinear steep focusing waves. Therefore, the paper proposes a new FNPF model for this investigation. Compared to the boundary integral method and the spectral-based method, the proposed FNPF model solves the Laplace equation on a σ-coordinate with a finite difference method. The model is developed as a part of the open-source hydrodynamic code REEF3D. The code uses high-order discretization schemes in space and time and provides fully parallel computation using Message Passing Interface (MPI). The code has been widely used for various hydrodynamic studies, for example, wave interactions with surface piercing cylinders (Chella et al. (2019); Kamath et al. (2015)), extreme wave generation (Bihs et al. (2019*b*)), free falling objects into water (Kamath et al. (2017)), local scour around a pipeline (Ahmad et al. (2019)) and new developments of a non-hydrostatic Navier-Sokes solver (Bihs et al. (2019*a*)). The proposed potential flow model REEF3D::FNPF inherits the high-order schemes and parallel computation from the REEF3D framework. In comparison to the CFD solvers, the presented model is much less computationally demanding and therefore is ideal for the time domain analyses of different factors. For example, in order to obtain the same accuracy for the simulation of the wave propagation over a submerged bar (Beji and Battjes (1993)), a CFD simulation takes 17 hours while the FNPF solver takes only 54 s in the work presented by Bihs et al. (2019 in press).

The structure for the presented work is arranged as follows: First, the mathematical model and numerical methods are presented. The model is then validated against the experimental data using a wave packet input (Clauss and Steinhagen (1999)). A detailed time domain analysis is applied to identify the real focusing point and further studies are performed using different wave steepnesses and wave generation methods. Next, the model is validated against the experiments performed by Ning et al. (2009) using the NewWave theory input. Similarly, the effect of wave generation method and wave steepness are investigated. In addition, various bandwidths of the input JONSWAP spectrum are used to obtain a better understanding of the frequency bandwidth effect. Finally, a 3D focusing wave in a directional sea is simulated and the effects of the directional spreading function on the focused wave evolution in the longitudinal and transverse direction are studied. With high efficiency and accuracy, the proposed model is able to offer insights into 2D and 3D wave groups and from low steepness wave groups up to near-breaking. The effects of the different factors are helpful for future configurations of numerical wave tanks and physical experiments when studying focused wave groups.

2 Numerical model

2.1 Governing equations

The governing equation for the proposed fully nonlinear potential flow model is the Laplace equation:

$$\frac{\partial^2 \phi}{\partial x^2} + \frac{\partial^2 \phi}{\partial y^2} + \frac{\partial^2 \phi}{\partial z^2} = 0. \tag{1}$$

Boundary conditions are required in order to solve for the velocity potential ϕ from this elliptic equation, especially at the free surface and at the bed. The fluid particles at the free surface should remain at the surface where the pressure in the fluid should be equal to the atmospheric pressure. These conditions must be fulfilled at all times and they form the kinematic and dynamic boundary conditions at the free surface respectively:

$$\frac{\partial \eta}{\partial t} = -\frac{\partial \eta}{\partial x}\frac{\partial \widetilde{\phi}}{\partial x} - \frac{\partial \eta}{\partial y}\frac{\partial \widetilde{\phi}}{\partial y} + \widetilde{w}\left(1 + \left(\frac{\partial \eta}{\partial x}\right)^2 + \left(\frac{\partial \eta}{\partial y}\right)^2\right), \tag{2}$$

$$\frac{\partial \widetilde{\phi}}{\partial t} = -\frac{1}{2}\left(\left(\frac{\partial \widetilde{\phi}}{\partial x}\right)^2 + \left(\frac{\partial \widetilde{\phi}}{\partial y}\right)^2 - \widetilde{w}^2\left(1 + \left(\frac{\partial \eta}{\partial x}\right)^2 + \left(\frac{\partial \eta}{\partial y}\right)^2\right)\right) - g\eta. \tag{3}$$

where η is the free surface elevation, $\widetilde{\phi} = \phi(\mathbf{x}, \eta, t)$ is the velocity potential at the free surface, $\mathbf{x} = (x, y)$ represents the location at the horizontal plane and $\widetilde{w}$ is the vertical velocity at the free surface.

At the bottom, the component of the velocity normal to the bottom must be zero at all times since the fluid particle cannot penetrate the solid boundary. This gives the bottom boundary condition:

$$\frac{\partial \phi}{\partial z} + \frac{\partial h}{\partial x}\frac{\partial \phi}{\partial x} + \frac{\partial h}{\partial y}\frac{\partial \phi}{\partial y} = 0, \quad z = -h. \tag{4}$$

where $h = h(\mathbf{x})$ is the water depth measured from the still water level to the seabed.

The Laplace equation, together with the boundary conditions are solved with a finite difference method on a σ-coordinate system. The σ-coordinate system follows the water depth changes and offers flexibility for irregular boundaries. The transformation from a Cartesian grid to a σ-coordinate is expressed as follows:

$$\sigma = \frac{z + h\left(\mathbf{x}\right)}{\eta(\mathbf{x}, t) + h(\mathbf{x})}. \tag{5}$$

In the model, the vertical coordinates also follow a stretching function so that the grid becomes denser close to the free surface:

$$\sigma_i = \frac{\sinh\left(-\alpha\right) - \sinh\left(\alpha\left(\frac{i}{N_z} - 1\right)\right)}{\sinh\left(-\alpha\right)}, \tag{6}$$

where α is the stretching factor and i and N_z stand for the index of the grid point and the total number of cells in the vertical direction.

The velocity potential after the σ-coordinate transformation is denoted as Φ. The boundary conditions and the governing equation in the σ-coordinate are then written in the following format:

$$\Phi = \widetilde{\phi} \qquad ,\sigma = 1; \tag{7}$$

$$\frac{\partial^2\Phi}{\partial x^2} + \frac{\partial^2\Phi}{\partial y^2} + \left(\frac{\partial^2\sigma}{\partial x^2} + \frac{\partial^2\sigma}{\partial y^2}\right)\frac{\partial\Phi}{\partial\sigma} + 2\left(\frac{\partial\sigma}{\partial x}\frac{\partial}{\partial x}\left(\frac{\partial\Phi}{\partial\sigma}\right) + \frac{\partial\sigma}{\partial y}\frac{\partial}{\partial y}\left(\frac{\partial\Phi}{\partial\sigma}\right)\right) + \left(\left(\frac{\partial\sigma}{\partial x}\right)^2 + \left(\frac{\partial\sigma}{\partial y}\right)^2 + \left(\frac{\partial\sigma}{\partial z}\right)^2\right)\frac{\partial^2\Phi}{\partial\sigma^2} = 0 \quad ,0 \le \sigma < 1; \tag{8}$$

$$\left(\frac{\partial\sigma}{\partial z} + \frac{\partial h}{\partial x}\frac{\partial\sigma}{\partial x} + \frac{\partial h}{\partial y}\frac{\partial\sigma}{\partial y}\right)\frac{\partial\Phi}{\partial\sigma} + \frac{\partial h}{\partial x}\frac{\partial\Phi}{\partial x} + \frac{\partial h}{\partial y}\frac{\partial\Phi}{\partial y} = 0 \qquad ,\sigma = 0. \tag{9}$$

Once the velocity potential Φ is obtained in the σ-domain, the velocities can be calculated as follows:

$$u\left(\mathbf{x}, z\right) = \frac{\partial\Phi\left(\mathbf{x}, z\right)}{\partial x} = \frac{\partial\Phi\left(\mathbf{x}, \sigma\right)}{\partial x} + \frac{\partial\sigma}{\partial x}\frac{\partial\Phi\left(\mathbf{x}, \sigma\right)}{\partial\sigma}, \tag{10}$$

$$v\left(\mathbf{x}, z\right) = \frac{\partial\Phi\left(\mathbf{x}, z\right)}{\partial y} = \frac{\partial\Phi\left(\mathbf{x}, \sigma\right)}{\partial y} + \frac{\partial\sigma}{\partial y}\frac{\partial\Phi\left(\mathbf{x}, \sigma\right)}{\partial\sigma}, \tag{11}$$

$$w\left(\mathbf{x}, z\right) = \frac{\partial\Phi\left(\mathbf{x}, z\right)}{\partial z} = \frac{\partial\sigma}{\partial z}\frac{\partial\Phi\left(\mathbf{x}, \sigma\right)}{\partial\sigma}. \tag{12}$$

The waves are generated at the inlet using a Neumann boundary condition where the spatial derivatives of the velocity potential are defined. In this way, the velocity potential at the boundary is calculated using the desired analytical horizontal velocity:

$$\varphi_{i-1} = -u(\boldsymbol{x}, z, t)\triangle x + \varphi_i. \tag{13}$$

where $u(\boldsymbol{x}, z, t)$ is the analytical horizontal velocity.

The numerical beach uses the relaxation method (Mayer et al. (1998)) to mitigate wave reflection. The relaxation function used in the model:

$$\Gamma(\widetilde{x}) = 1 - \frac{e^{(\widetilde{x}^{3.5})} - 1}{e - 1} \; for \; \widetilde{x} \in [0; 1]. \tag{14}$$

where $\widetilde{x}$ is scaled to the length of the relaxation zone.

The Laplace equation is discretized using second-order central differences and solved using a parallelized geometric multigrid preconditioned conjugated gradient solver provided by Hypre (van der Vorst (1992)).

Insufficient grid resolution can lead to numerical diffusion which causes unphysical damping of the waves as a result. In order to achieve the balance between numerical accuracy, stability and efficiency, the convection terms at the free-surface boundary conditions are discretized with the 5-order Hamilton-Jacobi version of the weighted essentially non-oscillatory (WENO) scheme (Jiang and Shu (1996)). The WENO discretization stencil consists of three local ENO-stencils based on the smoothness indicators. A large smoothness indicator means a non-smooth solution in a local stencil. The scheme is designed such that the local stencil with the highest smoothness is assigned the largest weight and therefore contributes the most significantly. In this way, the scheme is able to handle large gradients up to shock with good accuracy. For example, let u represent the convective quantities, which include the $\partial\eta/\partial x$ and $\partial\widetilde{\Phi}/\partial x$ terms in the free surface boundary conditions and U represents the stencils used in the discretisation. At the cell face $i+1/2$, $u_{i+1/2}$ is reconstructed with the WENO procedure:

$$U^{\pm}_{i+1/2} = \omega^{\pm}_1 U^{1\pm}_{i+1/2} + \omega^{\pm}_2 U^{2\pm}_{i+1/2} + \omega^{\pm}_3 U^{3\pm}_{i+1/2}. \tag{15}$$

U^1, U^2 and U^3 represent the three possible ENO stencils, and the $\pm$ sign indicates the upwind direction. For upwind direction in the positive i-direction, they are:

$$\begin{aligned} U^{1-}_{i+1/2} &= \frac{1}{3}u_{i-2} - \frac{7}{6}u_{i-1} + \frac{11}{6}u_i, \\ U^{2-}_{i+1/2} &= -\frac{1}{6}u_{i-1} + \frac{5}{6}u_i + \frac{1}{3}u_{i+1}, \\ U^{3-}_{i+1/2} &= \frac{1}{3}u_i + \frac{5}{6}u_{i+1} - \frac{1}{6}u_{i+2}. \end{aligned} \tag{16}$$

For the time treatment, a third-order accurate TVD Runge-Kutta scheme (Shu and Osher (1988)) is used. Adaptive time stepping is used by controlling a constant time factor as an equivalence to the CFL number:

$$
\begin{aligned}
c_u &= \frac{dx}{\left|max(u_{max}, 1.0\sqrt{9.81 * h_{max}})\right|},\\
c_v &= \frac{dx}{\left|max(v_{max}, 1.0\sqrt{9.81 * h_{max}})\right|},\\
c_{tot} &= min(c_u, c_v),\\
dt &= c_{tot} CFL.
\end{aligned} \tag{17}
$$

where u_{max}, v_{max} are the maximum particle velocities in x and y directions, h_{max} is the maximum water depth.

The model is fully parallelized following the domain decomposition strategy where ghost cells are used to exchange information between adjacent domains. These ghost cells are updated with the values from the neighboring processors via Message Passing Interface (MPI).

2.2 Focused wave generation

The focusing irregular wave generation is achieved by a linear superposition of a finite number of individual regular wave components with different amplitudes, frequencies and phases. The phase of each wave component is adjusted so that the wave components focus at the pre-defined focusing time and focusing location. The first-order free surface $\eta^{(1)}$ is defined as

$$\eta^{(1)} = \sum_{i=1}^{N} A_i \cos\alpha_i. \tag{18}$$

where A_i is the amplitude of each wave component and α_i is the phase of each component, which is defined as

$$\theta_i = k_i x - \omega_i t - \varepsilon_i. \tag{19}$$

where ω_i is the angular frequency, k_i is the wave number and ε_i is the phase angle of each component. For irregular waves, the phases are randomly distributed with a uniform probability distribution function over the $[-\pi, \pi]$ range. In the case of focused waves, ε_i is designed so that each individual wave focuses at a specified time t_F and location x_F:

$$\varepsilon_i = k_i x_F - \omega_i t_F. \tag{20}$$

In the case of a 3D focusing wave group, the propagation angle is also included in the phase adjustment:

$$\varepsilon_i = k_i x_F \cos(\beta_i) + k_i y_F \sin(\beta_i) - \omega_i t_F. \tag{21}$$

The amplitude of the individual wave components are calculated based on the different methods for the focused waves. The wave packet generation uses a dimensionless amplitude spectrum of the form (Hennig (2005)):

$$\left|A^{'}(\omega)\right| = \frac{27\left(\omega - \omega_{beg}\right)\left(\omega - \omega_{end}\right)^2}{4\left(\omega_{end} - \omega_{beg}\right)^3}. \tag{22}$$

Here, ω is the angular frequency and the subscripts *beg* and *end* define the frequency range for the Fourier spectrum. The absolute magnitude of the resulting wave amplitude $A_i^{'}$ does not represent the given focused wave input at this point, therefore a scaling factor f is calculated:

$$f = \frac{A_F}{\sum_{i=1}^{N} A_i^{'}}. \tag{23}$$

Then the amplitudes of the harmonic components can be calculated as:

$$A_i = f A_i^{'}. \tag{24}$$

When using the NewWave theory, a JONSWAP spectrum is used to describe the distribution of the wave energy as a function of the angular frequency ω. The required significant wave height H_s, the peak angular frequency ω_p, and the number of components N are given as input values to the JONSWAP spectrum (DNV-GL (2000)):

$$S\left(\omega\right) = \frac{5}{16} H_s^2 \omega_p^4 \omega_i^{-5} exp\left(-\frac{5}{4}\left(\frac{\omega_i}{\omega_p}\right)^{-4}\right) \gamma^{exp\left(\frac{-(\omega-\omega_p)^2}{2\sigma^2\omega_p^2}\right)} A_\gamma. \tag{25}$$

where the peak-shape parameter $\gamma = 3.3$ and the spectral width parameter σ is 0.07 for $\omega_i \leq \omega_p$ and 0.09 for $\omega_i > \omega_p$. The normalising facor $A_\gamma = 1 - 0.287 ln(\gamma)$.

The Pierson-Neumann-James (PNJ) directional spreading function (Pierson et al. (1955)) is used to describe the directionality in the wave field:

$$G(\beta) = \begin{cases} \frac{2}{\pi}\cos^n(\beta_j - \overline{\beta}) & \text{, if } \left|\beta_j - \overline{\beta}\right| < \frac{\pi}{2} \\ 0 & \text{, else.} \end{cases} \tag{26}$$

where $\overline{\beta}$ is the principal direction representing the major energy propagation direction and β_j is the direction of each incident wave component measured counterclockwise from the principal. The shape parameter n is subject to change in order to study the effect of different angular spreading properties.

By multiplying Eqn. (25) and Eqn. (26), the directional spectrum is obtained. An equal energy method is used to discretize the frequency spectrum and the spreading function to prevent phase-locking in the directional wave field and ensure ergodicity (Duarte et al. (2014); Jefferys (1987)). With the equal energy method, the amplitude of each wave component can be expressed in terms of the wave spectrum $S_i(\omega)$ and the amplitude at the focus point A_F:

$$A_i = A_F \frac{S_i\left(\omega\right)\triangle\omega}{\sum_{i=1}^{N} S_i\left(\omega\right)\triangle\omega}. \tag{27}$$

Following the first-order wave theory, the particle velocities $u^{(1)}, v^{(1)}$ and $w^{(1)}$ are defined as the sum of individual wave components

$$u^{(1)} = \sum_{i=1}^{N} A_i \omega_i \frac{\cosh\left(k_i\left(z+h\right)\right)}{\sinh\left(k_i h\right)} \cos\theta_i, \tag{28}$$

$$v^{(1)} = \sum_{i=1}^{N} A_i \omega_i \frac{\cosh\left(k_i\left(z+h\right)\right)}{\sinh\left(k_i h\right)} \sin\theta_i, \tag{29}$$

$$w^{(1)} = \sum_{i=1}^{N} A_i \omega_i \frac{\sinh\left(k_i\left(z+h\right)\right)}{\sinh\left(k_i h\right)} \sin\theta_i. \tag{30}$$

With increasing wave steepness, it is necessary to take the second-order effects into account. In the presented study, the second-order component is added to the first-order component of the free surface elevation, velocity potential and the particle velocities.

$$\eta = \eta^{(1)} + \eta^{(2)}, \tag{31}$$

$$\phi = \phi^{(1)} + \phi^{(2)}, \tag{32}$$

$$u = u^{(1)} + u^{(2)}, \tag{33}$$

$$w = w^{(1)} + w^{(2)}. \tag{34}$$

In the presented model, the second-order wave components are implemented following the formulations presented in (Ning et al. (2009)) using second-order irregular wave theory (Schäffer (1996)).

3 Results and Discussions

The proposed model is first validated against two experiments with a wave packet spectrum and NewWave theory respectively. The differences between the numerical and experimental data are analyzed and the advantages of the numerical simulations are discussed. Then, different wave generation methods, wave steepnesses, frequency bandwidths and wave spreading are investigated with the numerical tool.

3.1 Validation of the focused wave group generation in the NWT

The focused irregular wave group is generated with the wave packet method and the numerical results are compared with the experimental data measured in the Large Wave Flume (GWK), Hannover, Germany (Clauss and Steinhagen (1999)). The physical wave tank in the experiments is 300 m long with a constant water depth of $h = 4.01$ m. A piston-type wavemaker is used to generate the wave packet that focuses at the designated location at $x_F = 126.21$ m and time at $t_F = 103$ s. Following the experimental setup, a 2D numerical wave tank (NWT) 250 m long with a water depth of $h = 4.01$ m is used in the numerical test. A Neumann boundary is used at the inlet of the NWT to generate the wave packet that focuses at $x_F = 126.21$ m and $t_F = 103$ s. A 50 m long numerical beach is located at the outlet to absorb the wave energy. A linear wavemaker theory is used in the experiment (Clauss and Steinhagen (1999)), therefore a 1st-order focused wave theory is used in the numerical wave tank. The free surface elevations are measured at $x = 3.59$ m, 90.30 m and 126.21 m in both the physical and the numerical wave tank. The grid convergence study is shown in Fig. 1. The time series at the focusing location and the wave profiles at the focusing time are nearly identical when a further grid refinement is made from $dx = 0.25$ m to $dx = 0.167$ m in the horizontal direction. Therefore, the grid size of $dx = 0.25$ m is considered sufficient for the simulation. A vertical grid convergence study with the σ-coordinate arrangement is also shown in Fig. 2. With more than 10 cells, the focused wave shape, focusing time and focused wave crest height are nearly identical. It is therefore concluded that 10 cells in the water depth are sufficient to capture the extreme event accurately. Ning et al. (2009) captured the focused wave shape in their NWT with only 16 frequency components due to the transient nature of the focusing event. In this study, the free surface time series with different numbers of frequency components are also compared in Fig. 3. At the wave focusing event, 25 wave components appear to be sufficient to capture the focusing crest geometry very well as shown in Fig. 3a. However, away from the crest, 50 components are needed to achieve convergence in the time domain. With a grid size of 0.25 m in the horizontal direction, 10 cells in the vertical direction and 50 wave components, a 180 s simulation takes 553 s on a Mac pro with with 2 Intel Xeon E5 processors (2.7 GHz). The simulated results are compared to the experimental observations in Fig. 4. A favourable match is achieved at all wave probes. At the focusing point, the absolute difference between the simulated and measured wave peak height $|H_{F(sim)} - H_{F(exp)}|$ is divided by the measured wave peak height $H_{F(exp)}$ to quantify the relative numerical error, which is found to be limited to 4.5%.

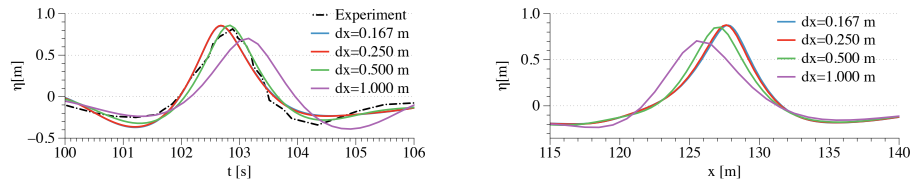

(a) (b)

Figure 1: Grid convergence study of the focusing wave group generated using a wave packet method. (a) Comparison of time series at the designated focusing location with different grid sizes. The time series are also compared to the measurements. (b) Comparison of wave profiles at the designated focusing time with different grid sizes. Four grid sizes are investigated: $dx = 0.167$ m, 0.25 m, 0.5 m and 1.0 m. 10 vertical cells are used in the study.

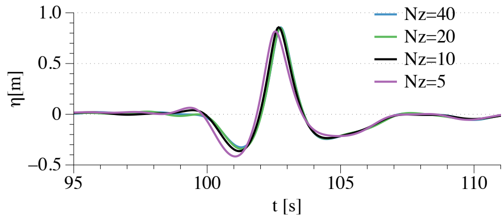

Figure 2: The grid convergence study of the vertical grid resolution in a σ-coordinate arrangement for the focusing wave group generated using a wave packet method.

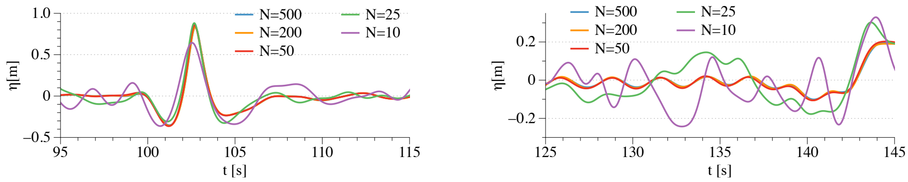

(a) (b)

Figure 3: Convergence study for the number of frequency components for the generation of the focused wave group using the wave packet approach, (a) time series near the focusing event with different number of frequency components, (b) time series away from the focusing event with different number of frequency components.

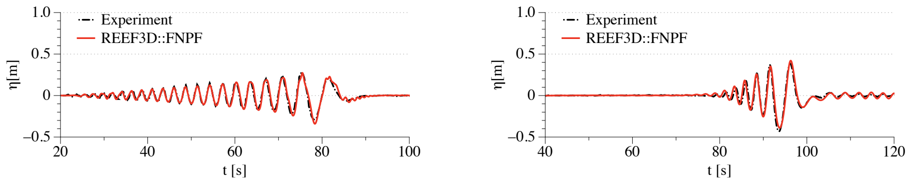

(a) Wave gauge 1, x=3.59 m (b) Wave gauge 2, x=90.30 m

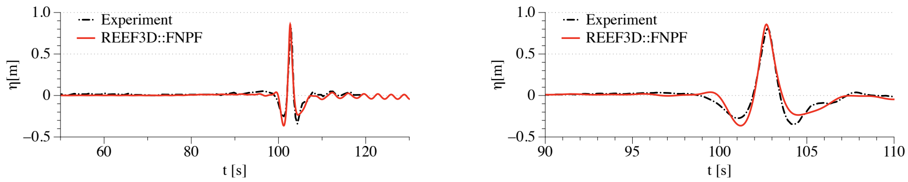

(c) Wave gauge 3, x=126.21 m (d) Wave gauge 3, x=126.21 m

Figure 4: Comparison of the wave elevation time series at the three wave probes between the numerical wave tank and the experiment for the wave packet study. d) is the close-up view of the wave profile near the focusing region.

The velocity potential, the vertical velocities at the focusing point and the grid are shown in Fig. 5a and Fig. 5b. It is seen that the σ-grid follows the free surface well at the focusing peak with a sharp curvature. The velocity potential and the velocity field inside the water volume are also presented and the vertical velocity distribution for the intermediate water depth is demonstrated. The evolution of the wave packet and its vertical velocities are shown in Fig. 6 for the sampled time frames $t = 59.5$ s, 103.0 s and 126.0 s. At $t = 59.5$ s, the wave packet propagates from the wave generating Neumann boundary with shorter waves leading the wave train and the trailing longer waves. At $t = 103.0$ s, all the wave components propagate to the focusing location at the same time, creating an amplified single peak with high velocities. At $t = 126.0$ s, the longer wave components surpass the shorter waves and the single peak decomposes into several smaller components of different frequencies.

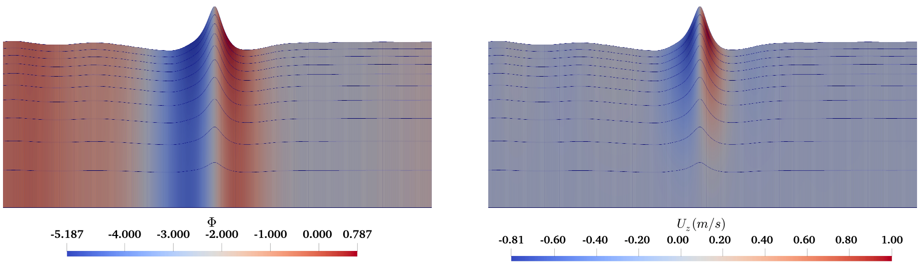

(a) (b)

Figure 5: Flow information and σ-grid near the focusing event, (a) velocity potential in the water volume, (b) The vertical velocity component in the water volume.

(a) t=59.5 s

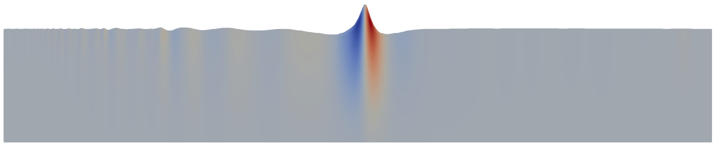

(b) t=103.0 s

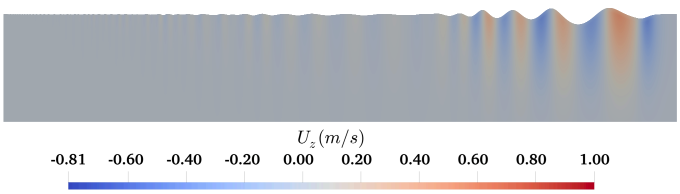

(c) t=126.0 s

Figure 6: Vertical velocity component during the evolution of the focused wave group generated by the wave packet method, (a) $t = 59.5$ s, (b) $t = 103.0$ s, (c) $t = 126.0$ s.

In spite of the agreement between the experimental and numerical results, the asymmetry of the time series at the focusing location indicates that the real focusing event might not happen at the measured location in the experiment, i.e. not all the wave components superimpose simultaneously at the designated point. As can be observed in Fig. 1a, both the simulated and physically measured focused wave at the designated focusing location at $x = 126.21$ m take place slightly ahead of the designated focusing time $t = 103$ s. In addition, at the designated focusing time, the waves in the numerical wave tank focus at $x = 127.5$ m, 1.29 m after the designated focusing location. These discrepancies indicate that there is a possibility that the real focusing event is delayed in comparison to the designated focusing location and time. Since it is challenging to perform a continuous measurement at very fine spatial intervals in the experiment, it is likely that there are no wave probes located at the real focusing point in the experiment. With the flexibility of the NWT, the spatial wave profiles along the longitudinal direction of the wave tank are plotted in one graph with a small interval of 0.06 s near $t = 103.0$ s as shown in Fig. 7.

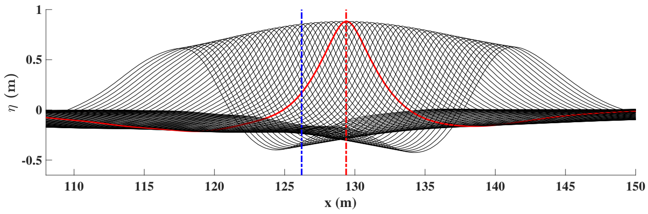

Figure 7: Wave profiles along the longitudinal direction of the wave tank are plotted in one graph at an interval of 0.06 s near t = 103.0 s. The red dash-dot line indicates the real focusing location in the NWT at x = 129.38 m. The blue dash-dot line indicates the designated focusing location at x = 126.21 m.

As can be seen from Fig. 7, the highest peak appears at the location x = 129.38 m, reaching 0.8845 m, 8.5% higher than the measured peak in the experiment. It indicates that the real focusing location is x = 129.38 m, 3.17 m after the designated focusing location, and the corresponding focus time is t = 103.4 s, 0.4 s after the designated focusing time. This finding is also illustrated in time domain, as shown in Fig. 8.

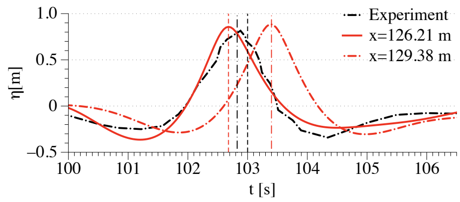

Figure 8: The comparison of the time series at the designated focusing location at x = 126.21 m and at the real focusing location at x = 129.38 m as detected in the numerical simulation. The black dash-dot curve is the time series measured in the experiment at x = 126.21 m and the vertical black dash-dot line indicates the measured focusing time at t = 102.825 s. The red solid curve is the time series at x = 126.21 m in the NWT, and the vertical red dashed line indicates the corresponding numerical focusing time t = 102.7 s. The red dash-dot curve is time series at the real focusing location x = 129.38 m in the NWT and the vertical red dash-dot line indicates the real focusing time t = 103.4 s. The vertical black dashed line is the designated focusing time at t = 103 s.

Previous research on focusing waves also found that the focusing time and location is delayed with increasing nonlinearity (Baldock et al. (1996)). A detailed discussion on the influence of nonlinearity on the focusing wave group in time and space is presented in section 3.2.

The input wave packet is a strictly defined wave train with a very specific spectrum. To investigate a more general wave focusing mechanism, the widely used NewWave theory (Lindgren (1970); Tromans et al. (1991)) is also implemented in the proposed model. The numerical results are validated against the experiments performed by Ning et al. (2009). The experiments were conducted at Dalian University of Technology in a wave flume 69 m long and 3 m wide. A constant water depth of 0.5 m is used during the tests. A 4 m region of foam is located at the outlet of the tank to reduce wave reflections. The experimental setup has been modified by (Bihs et al. (2017*a*)) considering the computational convenience. The equivalence of the modified NWT to the original experimental setup has been demonstrated in (Bihs et al. (2017*a*)). The current study adopts the modified configuration of the NWT in a two-dimensional arrangement by removing the transverse dimension. Two of the physical tests are used for the validation in the study, the input wave conditions are summarized in Table. 1. The Neumann boundary condition is used for the wave generation. The input wave in case NING1 has a more linear behaviour, while the input wave in NING3 is expected to show more nonlinearity with higher steepness. As described by Ning et al. (2009), a second-order wave theory is implemented in the wave generation to account for higher nonlinearity.

Table 1: The focusing wave inputs and the real focusing properties for the validation cases

Case No.	T_p (s)	A_F (m)	x_F (m)	t_F (s)	x_{Fr} (m)	t_{Fr} (s)
NING1	1.20	0.0313	7.5	10.0	7.5	10.0
NING3	1.25	0.0875	7.2	10.0	8.475	10.7

To begin with, the grid convergence studies in the x-direction are performed for both NING1 and NING3, which are shown in Fig. 9 and Fig. 10. Since the numerical wave tank length and the designated focusing location are modified from the original experiment, the experimental time series are shifted 0.6 s and 0.2 s respectively for NING1 and NING3 cases to match the numerical focusing time in the numerical wave tank. These shifts are kept constant in all following comparisons. For both cases, further refinements of the horizontal grid from $dx = 0.05$ m to $dx = 0.025$ m do not improve the results further and the time series with both grid sizes match well with the experimental measurements. The location, time and crest height at focusing and the wave group shape adjacent to the focused crest are almost identical between the experimental and numerical results with the grid size of $dx = 0.05$ m. Consequently, the horizontal grid size of $dx = 0.05$ m is used in all the following simulations. In the vertical direction, the grid convergence study is shown in Fig. 11. As can be seen in these two plots, the vertical grid resolution has a low influence on the accuracy of the model and a resolution of ten cells is found to be sufficient for both cases. As reported by Ning et al. (2009), 20 frequency components are seen to be sufficient for all the tested wave conditions. To confirm this finding with the proposed model, the time series using different numbers of frequency components are compared at the focusing location in Fig. 12. It is seen that 20 components are sufficient to capture the focusing wave group shape. All the following results are obtained with $dx = 0.05$ m in the horizontal plane, 10 cells in the vertical direction and 20 wave components for the irregular wave generation. The simulation time for the case NING1 is 20 s and it takes 37 s to finish the simulation with 2 Intel Xeon E5 processors (2.7 GHz) on a Mac Pro. On the same computer, the 32 s simulation for the case NING3 takes 76 s.

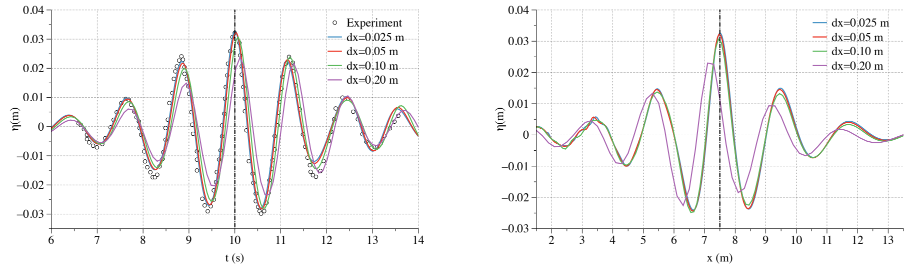

(a) (b)

Figure 9: Grid convergence study in the x-direction for the case NING1, where four grid sizes are tested $dx = 0.025,\ 0.05,\ 0.1$ and 0.2 m. 10 vertical cells are used in the study. (a) the time series at the focusing location $x = 7.5$ m, (b) the spatial wave profiles at the focusing time $t = 10.0$ s.

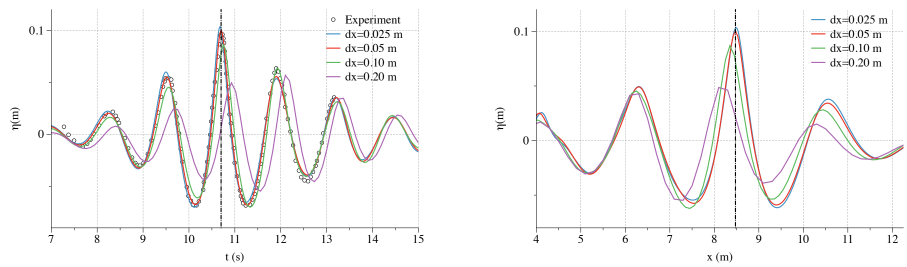

(a) (b)

Figure 10: Grid convergence study in the x-direction for the case NING3, where four grid sizes are tested $dx = 0.025,\ 0.05,\ 0.1$ and 0.2 m. 10 vertical cells are used in the study. (a) the time series at the focusing location $x = 8.475$ m, (b) the spatial wave profiles at the focusing location $t = 10.7$ s.

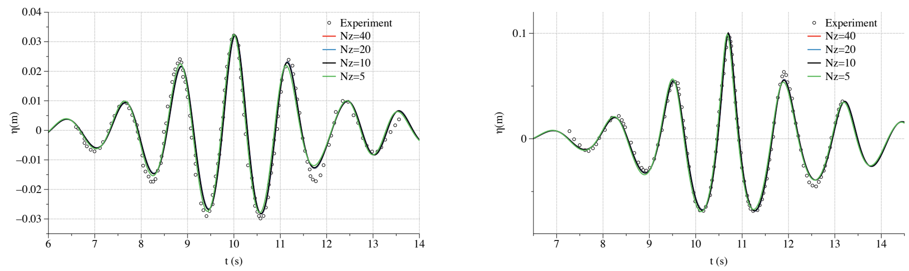

(a) (b)

Figure 11: Grid convergence study in the z-direction, (a) the time series at the focusing location $x = 7.5$ m for case NING1, (b) the time series at the focusing location $x = 8.475$ m for case NING3. The tested numbers of grid in the vertical direction are $N_z = 5,\ 10,\ 20$ and 40.

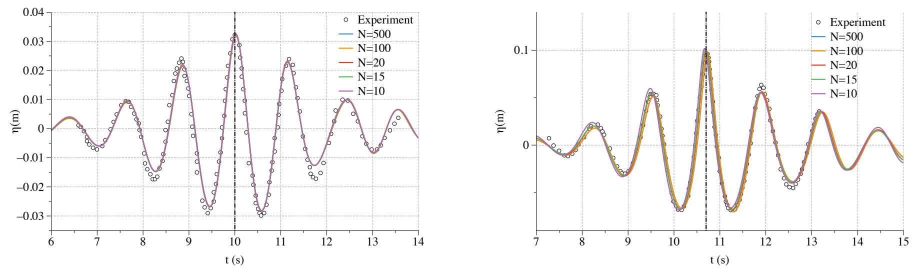

(a) (b)

Figure 12: Convergence study of the number of frequency components, (a) the time series at the focusing location $x = 7.5$ m for case NING1, (b) the time series at the focusing location $x = 8.475$ m for case NING3. The tested numbers of frequency components are $N = 10,\ 15,\ 20,\ 100$ and 500.

For the first case NING1, the wave focuses at nearly the exact designated focusing time at $t = 10$ s both in the experiment and the numerical simulation, as shown in Fig. 9a. Correspondingly, the focusing location is found to be also nearly as designated at $x = 7.5$ m, as shown in Fig. 9b. However, with a higher wave steepness and consequently stronger nonlinearity, both the focusing time and the focusing location are delayed for case NING3. These observations are again confirmed by both the experiment and the simulations. In the case NING3, the wave group actually focuses at $x = 8.475$ m instead of focusing at $x = 7.2$ m as designated. The numerical wave tank is able to provide a continuous output of the wave evolution at close time intervals. By plotting the wave profiles along the tank together at a time interval of 0.06 s near $t = 10.7$ s in Fig. 13, one can clearly observe the real focusing location marked in red in comparison to the designated focusing location marked in blue. Similarly, the focusing time is delayed to $t = 10.7$ s rather than $t = 10.0$ s. The difference in the focusing location and time is mainly due to the nonlinear wave-wave interaction in the process of the wave group evolution. With stronger nonlinearity in NING3 case, the effect becomes more prominent. To demonstrate the evolution of the two different wave groups, the vertical velocity in the flow field for the two cases are illustrated in Fig. 14. The focusing amplitude is much higher and the wave profile is much narrower with the steeper wave in NING3 in comparison to NING1. The difference in the focusing location is also visible when the two simulations are laid side by side. The vertical velocity magnitude of steeper waves is comparatively higher. This finding of the shifted focusing point due to nonlinear wave-wave interaction confirms the previous research reported by (Baldock et al. (1996); Westphalen et al. (2012); Ning et al. (2009); Bateman et al. (2001)).

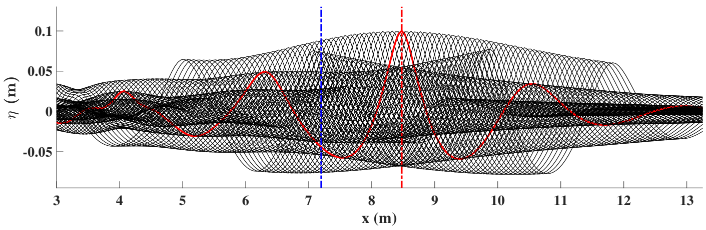

Figure 13: The wave profiles along the longitudinal direction of the wave tank are plotted in one graph at an interval of 0.06 s near t = 10.7 s for the simulation case NING3. The red dash-dot line indicates the real focusing location in the NWT at x = 8.475 m. The blue dash-dot line indicates the designated focusing location at x = 7.2 m. The red curve is the wave profile at the real focusing time.

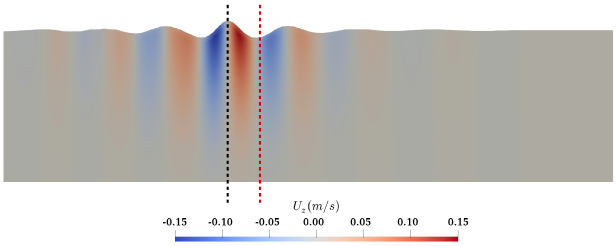

(a)

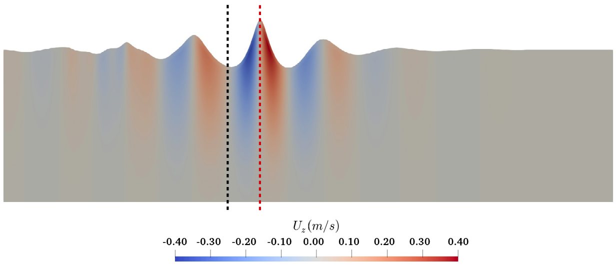

(b)

Figure 14: The vertical velocity in the wave fields at the focusing time, (a) for the simulation case NING1 with a less steep input wave, (b) for the simulation case NING3 with a more steep input wave. The black vertical dashed line in (a) indicates the location of the focused wave crest in the case NING1, and the red vertical dashed line in (b) indicates the location of the focused wave crest in the case NING3. The black dashed line in (a) is extended to (b), and the red dashed line in (b) is extended to (a) so that the horizontal distance between the focused wave crests in the two cases is straightforwardly observable.

3.2 Effects of nonlinearity

As found in the previous section, nonlinearity has a strong impact on the focused wave group evolution in time and space. In order to investigate the effect of wave nonlinearity, four wave groups with varying wave steepness are generated with the wave packet method, as shown in Table. 2. The NWT configurations and designated focusing locations and times are the same as in the experiment shown in section 3.1. The wave length L_p is calculated based on linear wave theory with the corresponding peak period T_p. The wave steepness is then defined as $\epsilon_p = k_p A_F$, where A_F is the input value for the focusing amplitude, and $k_p = 2\pi/L_p$ is the corresponding wave number at the peak period.

Table 2: The wave inputs and the absolute differences in the focusing points for the wave groups generated using the wave packet with different wave steepnesses

Case No.	A_F (m)	T_p (s)	L_p (m)	ϵ_p	$\triangle x_F$ (m)	$\triangle t_F$ (s)
Case PK1	0.25	4.20	24.32	0.0646	0.00	0.00
Case PK2	0.50	4.20	24.32	0.1292	0.09	0.05
Case PK3	1.00	4.20	24.32	0.2584	0.54	0.15
Case PK4	1.50	4.20	24.32	0.3875	1.29	0.31

The wave profiles in the longitudinal direction at the designated focusing time $t = 103$ s in the four cases are compared in Fig. 15a. The time series at the designated focusing location $x = 126.21$ m in the four cases are compared in Fig. 15b. As can be seen from the figure, stronger asymmetries are observed with steeper waves at the designated focusing time and location, indicating that the wave is not really focused at this location. As can be seen further in Fig. 16a and Fig. 16b, the wave profiles and time series are more symmetric at their respective real focus locations and time. It is also seen that the focusing location and focusing time of the simulated waves approach the designed values for lower wave steepness. For example, the simulated focusing location and time are almost identical with the designed input at the wave steepness $\epsilon_p = 0.0646$, as shown in Fig. 17. The spatial and temporal differences at the designated focusing points are listed in Table. 2. The relative differences in time and space are then defined as $\delta x_F = \Delta x_F / L_p$ and $\delta t_F = \Delta t_F / L_p$. The general trend of increasing relative differences with increasing wave steepnesses is further demonstrated in Fig. 18. The finding confirms the previous investigations and justifies the differences between the measured and real focusing point in the experiment of Clauss and Steinhagen (1999).

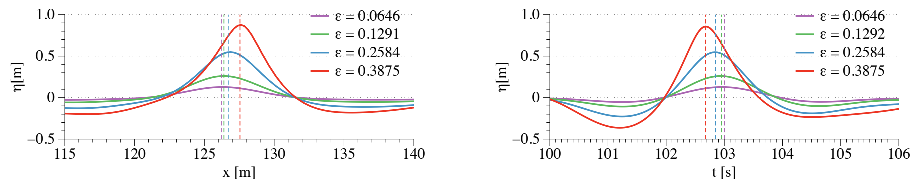

(a) (b)

Figure 15: Comparison of the wave surface elevations at the designated focusing time and location with four different wave steepnesses, (a) the wave profiles in the longitudinal direction at $t = 103$ s, (b) the time series at $x = 126.21$ m.

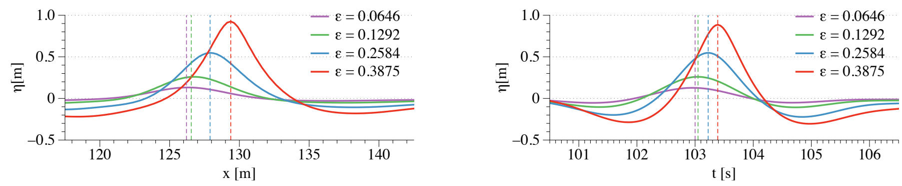

(a)

(b)

Figure 16: Comparison of the wave surface elevations at the respective real focusing time and location with four different wave steepnesses, (a) the wave profiles in the longitudinal direction, (b) the time series at respective real focusing location.

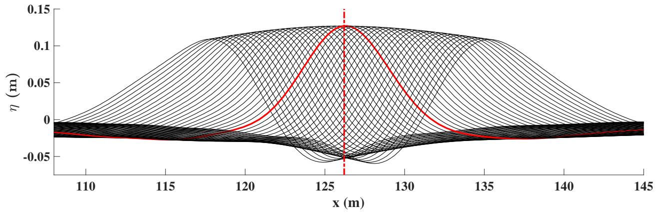

Figure 17: The wave profiles along the longitudinal direction of the wave tank with the wave steepness $\epsilon_p = 0.0646$ are plotted in one graph at an interval of 0.06 s near $t = 103.0$ s. The red dash-dot line indicates the real focusing location in the NWT at $x = 126.21$ m, which align with the designated focusing locations.

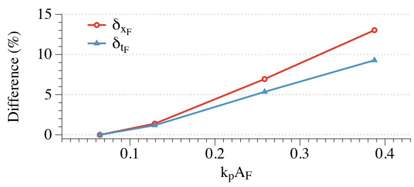

Figure 18: The relative spatial differences in focusing location δx_F and temporal differences in focusing time δt_F in relation to wave steepness in the simulation with the wave packet.

Similarly, the influence of wave steepness on the focusing location and focusing time is also investigated with the NewWave theory. The designated input wave parameters are listed in Table. 3. While keeping the same peak period, the focusing wave amplitude increases consistently. The time series at the respective focusing location and the wave profiles at the respective focusing time are plotted in Fig. 19. It is seen that the differences between the real and designated focusing location and focusing time increase monotonically with increasing steepnesses. This finding agrees with the previous observations with the wave packet in the previous section. The absolute differences of focusing time and focusing location for each case are also listed in Table. 3 and the relative differences are plotted in Fig. 20. It is shown that there are almost no differences in the first two cases with lower steepnesses. As larger waves evolve, the focusing location and focusing time of the wave group shift downstream due to the highly nonlinear wave-wave interactions. After a certain threshold, the differences start to increase dramatically following a near-linear trend.

Table 3: The wave inputs and the absolute differences in the focusing points for the wave groups generated using the NewWave theory with different wave steepnesses

Case No.	A_F (m)	T_p (s)	L_p (m)	ϵ_p	$\triangle x_F$ (m)	$\triangle t_F$ (s)
NS1	0.0391	1.20	2.00	0.1229	0.000	0.000
NS2	0.0470	1.20	2.00	0.1475	0.075	0.015
NS3	0.0626	1.20	2.00	0.1967	0.375	0.165
NS4	0.0783	1.20	2.00	0.2458	1.025	0.520

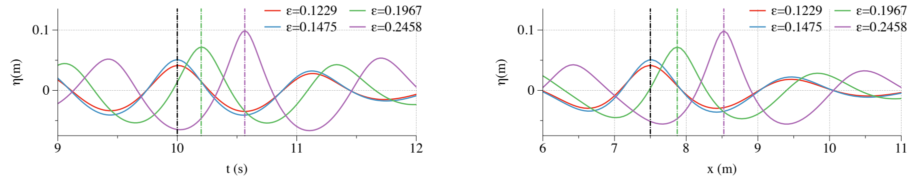

(a) (b)

Figure 19: Comparison of wave surface elevations at the respective real focusing time and location with four different wave steepnesses (a) the time series at respective real focusing time, (b) The comparison of the wave profiles in the longitudinal direction at the respective real focusing locations.

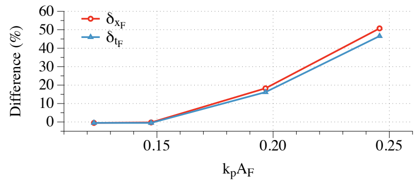

Figure 20: The relative spatial differences in focusing location δx_F and temporal differences in focusing time δt_F in relation to wave steepness in the simulation with the NewWave theory.

3.3 Effects of frequency bandwidth

Another factor influencing the properties of the focusing wave group is the frequency bandwidth. The combined effects of the nonlinearity and bandwidth (randomness) have been investigated previously by (Alber and Stewartson (1978); Socquet-Juglard et al. (2005); Dysthe et al. (2003)). In this study, instead of focusing on the statistical properties, the authors focus on the geometrical properties and the general shape of the evolving wave train. Since the frequency range of a wave packet spectrum is strictly defined, the frequency bandwidth effects are only studied with the NewWave theory. Five different bandwidths are tested with the same peak frequency. The detailed specifications are listed in Table. 4. The input wave height is the same as that defined in NING1. The focusing wave time series and wave profiles are plotted together in Fig. 21. The focusing wave height decreases as the frequency bandwidth gets wider, the differences between the focusing wave height in comparison to the designated wave height are also listed in Table. 4. It is seen that the focusing wave height decreases by 12% with the widest bandwidth in case NB5. However, it is also noticed that the bandwidth does not have an influence on the focusing location and time.

Table 4: The input wave properties with different bandwidth for the wave spectrum

Case No.	ω range (rad/s)	bandwidth (rad/s)	H_F (m)	$\delta H_F(\%)$
NB1	[5.02, 6.54]	1.52	0.06191	1.10
NB2	[4.27, 7.04]	2.77	0.06142	1.88
NB3	[3.77, 7.54]	3.77	0.06143	1.87
NB4	[2.77, 9.54]	6.77	0.05690	9.11
NB5	[1.77, 11.04]	9.27	0.05495	12.22

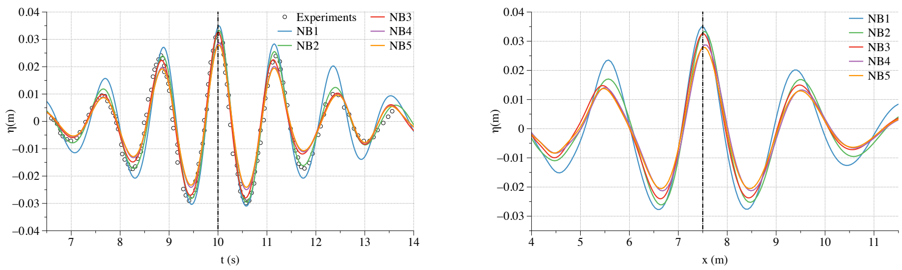

(a) (b)

Figure 21: Comparison of the wave surface elevations with five different frequency bandwidths. (a) the time series at the designated focusing location $x = 7.5$ m, (b) the spatial wave profile in the longitudinal direction at the designated focusing time $t = 10$ s.

3.4 Effects of wave generation method

The presented waves are generated using a Neumann boundary when the gradient of the velocity potential changes are defined at the wave generation boundary. Another widely used wave generation method is the relaxation method (Mayer et al. (1998)). Following the configurations in the experiments, a linear irregular wave theory and a second-order wave theory are used in the relaxation zones for the simulations using the wave packet method and the NewWave theory respectively. However, in both theories, only linear dispersion is represented inside the generation zone, which might result in errors in wave phases and the location and time of the focusing point. To demonstrate the difference between the two different wave generation methods, the validation cases presented in section 3.1 are simulated with relaxation wave generation zone and the results are compared to the corresponding results from the Neumann boundary condition. It is seen that the two wave generation methods show similar results for waves of relative weaker nonlinearity as in Fig. 22 and Fig. 23a. However, with increasing wave steepness and nonlinearity, the wave focusing properties are significantly different between the two wave generation methods, as shown in Fig. 23b. The wave group generated by the relaxation method focuses earlier and overpredicts the focusing wave crest. In contrast, the waves groups generated with the Neumann method match the experiments very well.

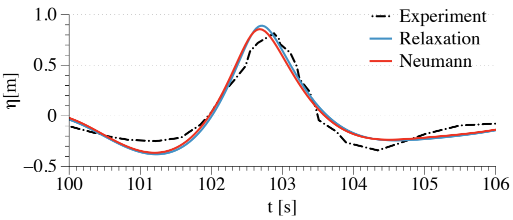

Figure 22: Comparison of the time series at the focusing location of 126.21 m generated by a relaxation method and a Neumann boundary using the wave packet input.

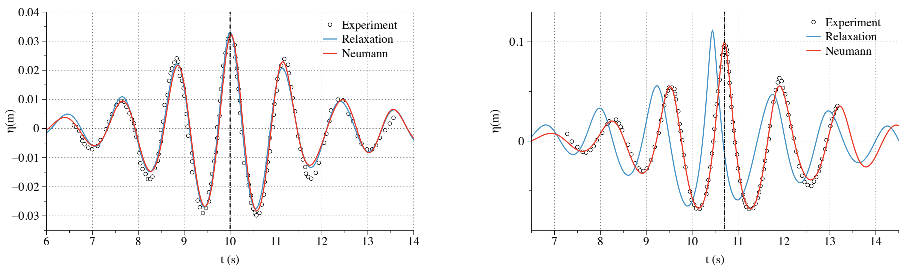

(a) (b)

Figure 23: Comparison of the time series at the focusing location of 7.5 m generated by a relaxation method and a Neumann boundary. (a) for the simulation case NING1, (b) for the simulation case NING3.

3.5 Effects of directional spreading on 3D focused wave group

Rogue waves are more likely to happen in a crossing sea state (Kharif et al. (2009)). To study the wave-wave interaction in a 3D sea-state, the JONSWAP spectrum and the PNJ directional spreading function are used to generate a multi-directional irregular wave field. The NewWave theory is used for wave focusing. A numerical wave basin 20 m long, 20 m wide with a constant water depth of 0.5 m is used in the study. Numerical beaches of 2 m width are arranged along the side walls and at the outlet of the tank. To fully resolve the 3D wave field, an Equal Energy method is used to discretise the frequency spectrum and spreading function. In this study, 500 frequency components and 20 directions are used, i.e.

10000 wave components in total are generated at the boundary. The wave height and peak period in NING1 are used as the input wave properties in this simulation. The designated focusing location is $(x, y) = (7.5, 10)$ m and the focusing time is set to be 35 s. The wave profiles along the x-axis and the y-axis at the designated focusing time together with the free surface elevation time series are compared with different grid sizes in Fig. 24. It is found that a grid size of 0.05 m is sufficient to achieve convergence. Ten cells are used in the vertical direction, resulting in 1.76 million cells in total. With 256 processors on NOTUR's supercomputer Fram, the 70 s simulation is finished in 5 h. The wave envelope is shown in Fig. 25 by plotting the wave profile along the centre of the tank with a small time interval around $t_F = 35$ s. It is seen that the highest peak of the wave envelope emerges at $x = 7.5$ m, indicating that the wave group focuses at the designated location. The evolution of the 3D focusing wave field is demonstrated in Fig. 26 by showing the velocity magnitude in the wave field at the chosen time frames at $t = 30$ s, $t = 35$ s and $t = 40$ s. The 3D wave train forms several curved wave fronts asymmetric along the centreline of the tank and approaches the focusing point in a wedge-shape pattern in the x-y plane. At the focusing location, the wave profile along the x-axis is similar to the 2D NewWave profile as shown in Fig. 24a and the wave profile along the y-axis is a single crested peak.

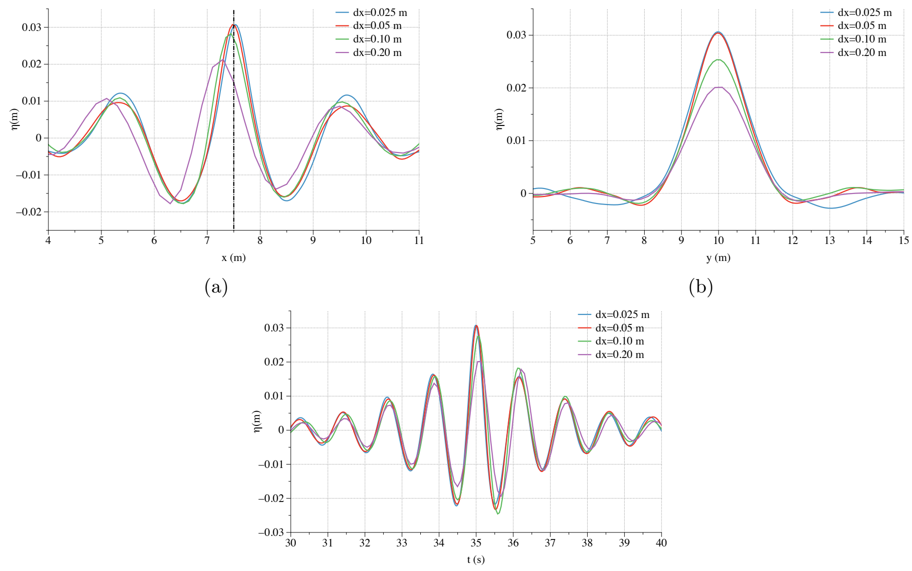

Figure 24: Grid convergence study for the 3D wave focusing simulation with four grid sizes $dx = 0.025,\ 0.05,\ 0.1$ and 0.2 m, 10 vertical cells are used in the study. (a) wave profile along the x-axis at $y = 10$ m and $t_F = 35$ s , (b) wave profile along the y-axis at $x = 7.5$ m and $t_F = 35$ s, (c) free surface elevation time series at $(x, y) = (7.5, 10)$ m.

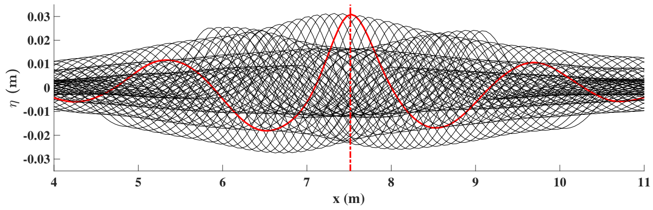

Figure 25: Wave profile envelop along the x-axis at $y = 10$ m, plotted with short time intervals around $t_F = 35$ s.

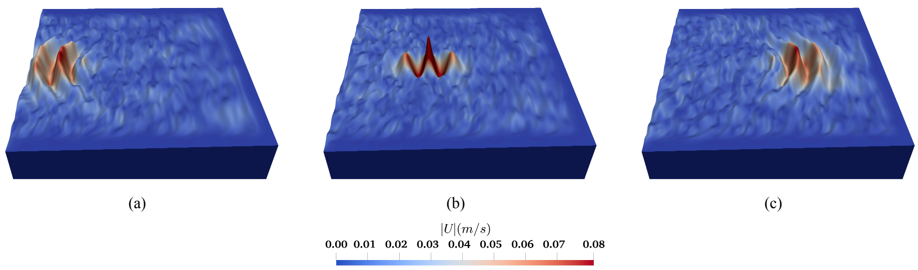

Figure 26: Velocity magnitude in the 3D focusing wave field. The time frames are $t = 30$ s, $t = 35$ s and $t = 40$ s from left to right.

Different energy spreading conditions are investigated in the study with various values of the spreading parameter n, as shown in Eqn. (26). The wave profile along $y = 10.0$ m and $x = 7.5$ m are plotted in Fig. 27 with different spreadings. A larger value of n signifies higher energy concentration and less spreading. It is seen from Fig. 27a that the focused wave height slightly decreases with stronger energy spreading. The two secondary peaks adjacent to the focused peak also follow the same trend. The directional spreading function tends to redistribute the energy in the horizontal plane more evenly and leads to smaller waves near the focusing point. Fig. 27a shows the wave profile in the y-direction at the focusing location. The focusing peak is higher and the wave profile is wider with more energy concentration. In contrast, with stronger directional spreading, the focused peak reduces and profile becomes narrower. The investigation indicates that different spreading conditions might lead to different load scenarios for marine structures due to varying peak height and the transverse dimension of the wavefront.

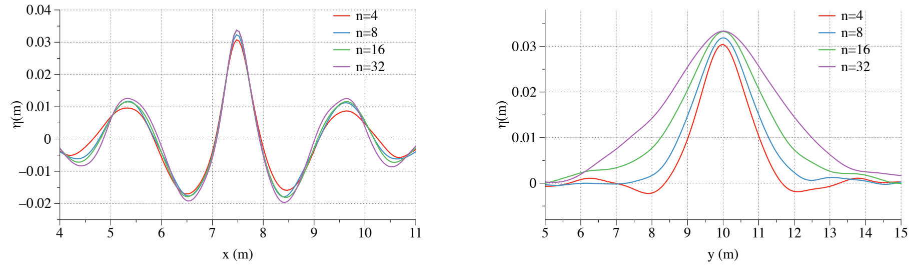

(a) (b)

Figure 27: Comparison of the wave free surface elevations with four different spreading functions, (a) comparison of the wave profiles in the longitudinal x-z plane at $y = 10$ m, (b) comparison of wave profiles in the transverse y-z plane at $x = 7.5$ m.

4 Conclusions

In this paper, an efficient fully-nonlinear potential flow model is introduced. The model solves the Laplace equation with a finite difference method on a σ-grid. The model employs high-order discretisation schemes in space and time which allows for larger grid sizes and time steps and ensures both the computational efficiency and accuracy. Ten vertical grids in the σ-coordinate system are usually found to be sufficient for surface wave applications. The focusing wave generated by the proposed model is validated against experiments using both the wave packet input and the NewWave theory. Favourable agreements are achieved with different wave conditions for both methods. The model is also used to create a 3D focusing wave group and the wave group focuses at the designated time and location. Further studies are performed to investigate the change of focusing location, focusing time, the geometry of the wave group and wave height in relation to the wave steepness, wave generation method, bandwidth and directional spreading. The focus of the study has been on the time domain analysis and geometry near the focusing point. The following findings are derived from the studies:

1) Wave steepness and the nonlinearity affects the wave focusing location and time significantly. As a steeper wave group evolves, both the focusing location and the focusing time are shifted downstream due to stronger nonlinear wave-wave interactions.

2) The close relation between the wave nonlinearity and the downstream shift of the focusing time and location challenges the physical test arrangement to allocate the wave probe at the exact focusing point. Instead of repeated attempts in a physical wave tank, a numerical wave model proves to be a useful tool to predict the exact real focusing time and location due to its flexibility and near-continuous output capacity.

3) The frequency bandwidth does not have an influence on the focusing time and location but affects the focusing wave crest height. A wider bandwidth tends to reduce the focusing wave crest height.

4) The focusing wave evolution is a very nonlinear phenomenon, the wave generation using a relaxation method does not represent the nonlinearity correctly as the wave steepness increases. Therefore, a Neumann boundary is recommended for the generation of the focusing wave group in an NWT.

5) In a directional sea state, the directional spreading function also influences the 3D focused wave profile. In a more spreading sea, the focused wave crest height is reduced and the wave profile in the transversal plane becomes narrower.

In conclusion, the proposed FNPF model is efficient and flexible to investigate the focusing wave evolution comprehensively. The finding of the study offers insights into the numerical tank configurations for future studies on focused waves both numerically and experimentally.

Acknowledgements

This study has been carried out as part of the E39 fjord crossing project (No. 304624) and the authors are grateful for the grants provided by the Norwegian Public Roads Administration. This study was also supported by the computational resources at the Norwegian University of Science and Technology (NTNU) provided by NOTUR, http://www.notur.no.

References

Ahmad, N., Bihs, H., Myrhaug, D., Kamath, A. and ivind A. Arntsen (2019). Numerical modelling of pipeline scour under the combined action of waves and current with free-surface capturing. *Coastal Engineering*, **148**, 19 – 35. ISSN 0378-3839. 10.3390/jmse7100375https://doi.org/10.1016/j.coastaleng.2019.02.008.

Alber, I.E. and Stewartson, K. (1978). The effects of randomness on the stability of two-dimensional surface wavetrains. *Proceedings of the Royal Society of London. A. Mathematical and Physical Sciences*, **363**(1715), 525–546. 10.3390/jmse710037510.1098/rspa.1978.0181.

Athanassoulis, G.A., Belibassakis, K.A. and Papoutsellis, C.E. (2017). An exact hamiltonian coupled-mode system with application to extreme design waves over variable bathymetry. *Journal of Ocean Engineering and Marine Energy*, **3**(4), 373–383. ISSN 2198-6452. 10.3390/jmse710037510.1007/s40722-017-0096-4.

Bai, J., Ma, N. and Gu, X. (2018). Numerical simulation of focused wave and its uncertainty analysis. *Journal of Shanghai Jiaotong University (Science)*, **23**(4), 475–481. ISSN 1995-8188. 10.3390/jmse710037510.1007/s12204-018-1970-5.

Bai, W. and Taylor, R.E. (2007). Numerical simulation of fully nonlinear regular and focused wave diffraction around a vertical cylinder using domain decomposition.

Baldock, T.E., Swan, C. and Taylor, P.H. (1996). A laboratory study of nonlinear surface waves on water. *Philosophical Transactions of the Royal Society A: Mathematical, Physical and Engineering Sciences*. ISSN 1364503X. 10.3390/jmse710037510.1098/rsta.1996.0022.

Bateman, W., Katsardi, V. and Swan, C. (2012). Extreme ocean waves. part i. the practical application of fully nonlinear wave modelling. *Applied Ocean Research*, **34**, 209 – 224. ISSN 0141-1187. 10.3390/jmse7100375https://doi.org/10.1016/j.apor.2011.05.002.

Bateman, W., Swan, C. and Taylor, P. (2001). On the efficient numerical simulation of directionally spread surface water waves. *Journal of Computational Physics*, **174**(1), 277 – 305. ISSN 0021-9991. 10.3390/jmse7100375https://doi.org/10.1006/jcph.2001.6906.

Bateman, W., Swan, C. and Taylor, P. (2003). On the calculation of the water particle kinematics arising in a directionally spread wavefield. *Journal of Computational Physics*, **186**(1), 70 – 92. ISSN 0021-9991. 10.3390/jmse7100375https://doi.org/10.1016/S0021-9991(03)00012-3.

Beji, S. and Battjes, J.A. (1993). Experimental investigation of wave propagation over a bar. *Coastal Engineering*, **19**, 151–162.

Belibassakis, K. and Athanassoulis, G. (2011). A coupled-mode system with application to nonlinear water waves propagating in finite water depth and in variable bathymetry regions. *Coastal Engineering*, **58**(4), 337 – 350. ISSN 0378-3839. 10.3390/jmse7100375https://doi.org/10.1016/j.coastaleng.2010.11.007.

Bihs, H., Alagan Chella, M., Kamath, A. and Arnsten, Ø.A. (2016*a*). Wave-Structure Interaction of Focussed Waves With REEF3D. 49934, V002T08A027.

Bihs, H., Chella, M.A., Kamath, A. and Arntsen, Ø.A. (2017*a*). Numerical Investigation of Focused Waves and Their Interaction With a Vertical Cylinder Using REEF3D. *Journal of Offshore Mechanics and Arctic Engineering*, **139**(4), 41101–41108. ISSN 0892-7219.

Bihs, H., Kamath, A., Aggarwal, A. and Pakozdi, C. (2019*a*). Efficient Wave Modeling using Nonhydrostatic Pressure Distribution and Free Surface Tracking on Fixed Grids. *Journal of Offshore Mechanics and Arctic Engineering*, **141**(4), 41805–41806. ISSN 0892-7219.

Bihs, H., Kamath, A., Alagan Chella, M. and Arntsen, Ø. (2017*b*). Extreme Wave Generation, Breaking and Impact Simulations With REEF3D. In: *Proceeding of 36th International Conference on Ocean, Offshore Arctic Engineering*.

Bihs, H., Kamath, A., Alagan Chella, M. and Arntsen, Ø.A. (2019*b*). Extreme Wave Generation, Breaking, and Impact Simulations Using Wave Packets in REEF3D. *Journal of Offshore Mechanics and Arctic Engineering*, **141**(4), 41802–41807. ISSN 0892-7219.

Bihs, H., Kamath, A., Chella, M.A., Aggarwal, A. and ivind A. Arntsen (2016*b*). A new level set numerical wave tank with improved density interpolation for complex wave hydrodynamics. *Computers Fluids*, **140**, 191 – 208. ISSN 0045-7930. 10.3390/jmse7100375https://doi.org/10.1016/j.compfluid.2016.09.012.

Bihs, H., Wang, W., Martin, T. and Kamath, A. (2019 in press). REEF3D::FNPF - A Flexible Fully Nonlinear Potential Flow Solver. In: *Proceeding of 38th International Conference on Ocean, Offshore Arctic Engineering*.

Bingham, H.B. and Zhang, H. (2007). On the accuracy of finite-difference solutions for nonlinear water waves. *Journal of Engineering Mathematics*, **58**(1), 211–228. ISSN 1573-2703. 10.3390/jmse710037510.1007/s10665-006-9108-4.

Bonnefoy, F., Touz, D.L. and Ferrant, P. (2006*a*). A fully-spectral 3d time-domain model for second-order simulation of wavetank experiments. part a: Formulation, implementation and numerical properties. *Applied Ocean Research*, **28**(1), 33 – 43. ISSN 0141-1187. 10.3390/jmse7100375https://doi.org/10.1016/j.apor.2006.05.004.

Bonnefoy, F., Touz, D.L. and Ferrant, P. (2006*b*). A fully-spectral 3d time-domain model for second-order simulation of wavetank experiments. part b: Validation, calibration versus experiments and sample applications. *Applied Ocean Research*, **28**(2), 121 – 132. ISSN 0141-1187. 10.3390/jmse7100375https://doi.org/10.1016/j.apor.2006.05.003.

Borthwick, A.G., Hunt, A.C., Feng, T., Taylor, P.H. and Stansby, P.K. (2006). Flow kinematics of focused wave groups on a plane beach in the u.k. coastal research facility. *Coastal Engineering*, **53**(12), 1033 – 1044. ISSN 0378-3839. 10.3390/jmse7100375https://doi.org/10.1016/j.coastaleng.2006.06.007.

Brandini, C. and Grilli, S.T. (2001). *Three-Dimensional Wave Focusing in Fully Nonlinear Wave Models*, 1102–1111. 10.3390/jmse710037510.1061/40604(273)112.

Buldakov, E., Stagonas, D. and Simons, R. (2017). Extreme wave groups in a wave flume: Controlled generation and breaking onset. *Coastal Engineering*, **128**, 75 – 83. ISSN 0378-3839. 10.3390/jmse7100375https://doi.org/10.1016/j.coastaleng.2017.08.003.

Chazel, F., Benoit, M., Ern, A. and Piperno, S. (2009). A double-layer boussinesq-type model for highly nonlinear and dispersive waves. *Proceedings of the Royal Society A: Mathematical, Physical and Engineering Sciences*, **465**(2108), 2319–2346. 10.3390/jmse710037510.1098/rspa.2008.0508.

Chella, M.A., Bihs, H. and Myrhaug, D. (2019). Wave impact pressure and kinematics due to breaking wave impingement on a monopile. *Journal of Fluids and Structures*, **86**, 94 – 123. ISSN 0889-9746. 10.3390/jmse7100375https://doi.org/10.1016/j.jfluidstructs.2019.01.016.

Chen, L.F., Zang, J., Hillis, A.J., Morgan, G.C.J. and Plummer, A.R. (2014). Numerical investigation of wave–structure interaction using openFOAM. *Ocean Engineering*, **88**, 91—109.

Clamond, D. and Grue, J. (2001). A fast method for fully nonlinear water-wave computations. *Journal of Fluid Mechanics*, **447**, 337355. 10.3390/jmse710037510.1017/S0022112001006000.

Clauss, G.F. and Bergmann, J. (1986). Gaussian wave packets a new approach to seakeeping testsof ocean structures. *Applied Ocean Research*, **8**(4), 190 – 206. ISSN 0141-1187. 10.3390/jmse7100375https://doi.org/10.1016/S0141-1187(86)80036-0.

Clauss, G.F. and Kühhnlein, W.L. (1995). Numerical Simulation of Nonlinear Transient Waves and its Validation by Laboratory Data. In: *3rd International Conference on Fast Sea Transport*, volume 2, 1193–1204. Lubeck-Travemunde, Germany.

Clauss, G.F. and Kuhnlein, W.L. (1997). A new tool for seakeeping tests - nonlinear transient wave packets. volume 2, 269–285. Delft, the Netherlands.

Clauss, G.F. and Steinhagen, U. (1999). Numerical Simulation of Nonlinear Transient Waves and its Validation by Laboratory Data. In: *9th International Offshore and Polar Engineering Conference*.

Craig, W. and Sulem, C. (1993). Numerical simulation of gravity waves. *Journal of Computational Physics*, **108**(1), 73 – 83. ISSN 0021-9991. 10.3390/jmse7100375https://doi.org/10.1006/jcph.1993.1164.

DNV-GL (2000). DNV Recommended Practice RP-C205 Environmental Conditions and Environmental Loads . Technical report.

Duarte, T., Gueydon, S., Jonkman, J. and Sarmento, A. (2014). Computation of Wave Loads under Multidirectional Sea States for Floating Offshore Wind Turbines. *Proceedings of the 33rd International conference on Ocean, Offshore and Arctic Engineering*, (June). 10.3390/jmse710037510.1115/OMAE2014-24148.

Ducrozet, G., Bonnefoy, F., Le Touzé, D. and Ferrant, P. (2012). A modified High-Order Spectral method for wavemaker modeling in a numerical wave tank. *European Journal of Mechanics - B/Fluids*, **34**, http://dx.doi.org/10.1016/j.euromechflu.2012.01.017. 10.3390/jmse710037510.1016/j.euromechflu.2012.01.017.

Dysthe, K.B., Trulsen, K., Krogstad, H.E. and Socquet-Juglard, H. (2003). Evolution of a narrow-band spectrum of random surface gravity waves. *Journal of Fluid Mechanics*, **478**, 110. 10.3390/jmse710037510.1017/S0022112002002616.

Engsig-Karup, A. and Bingham, H. (2009). Boundary-fitted solutions for 3d nonlinear water wave-structure interaction. In: *IWWWFB24*, 20.

Engsig-Karup, A.P. and Eskilsson, C. (2018). Spectral Element FNPF Simulation of Focused Wave Groups Impacting a Fixed FPSO. In: *The 28th International Ocean and Polar Engineering Conference*, 8. International Society of Offshore and Polar Engineers, Sapporo, Japan. ISBN 978-1-880653-87-6.

Fochesato, C., Grilli, S. and Dias, F. (2007). Numerical modeling of extreme rogue waves generated by directional energy focusing. *Wave Motion*, **44**(5), 395 – 416. ISSN 0165-2125. 10.3390/jmse7100375https://doi.org/10.1016/j.wavemoti.2007.01.003.

Forristall, G.Z., Barstow, S.F., Krogstad, H.E., Prevosto, M., Taylor, P.H. and Tromans, P.S. (2004). Wave Crest Sensor Intercomparison Study: An Overview of WACSIS. *Journal of Offshore Mechanics and Arctic Engineering*, **126**(1), 26–34. ISSN 0892-7219.

Fructus, D., Clamond, D., Grue, J. and yvind Kristiansen (2005). An efficient model for three-dimensional surface wave simulations: Part i: Free space problems. *Journal of Computational Physics*, **205**(2), 665 – 685. ISSN 0021-9991. 10.3390/jmse7100375https://doi.org/10.1016/j.jcp.2004.11.027.

Grilli, S.T., Dias, F., Guyenne, P., Fochesato, C. and Enet, F. (2010). *Progress in Fully Nonlinear Potential Flow Modeling of 3D Extreme Ocean Waves*, chapter 1, 75–128. World Scientific.

Grilli, S.T., Guyenne, P. and Dias, F. (2001). A fully non-linear model for three-dimensional overturning waves over an arbitrary bottom. *International Journal for Numerical Methods in Fluids*, **35**(7), 829–867. 10.3390/jmse710037510.1002/1097-0363(20010415)35:7¡829::AID-FLD115¿3.0.CO;2-2.

Haver, S. (2004). A possible freak wave event measured at the Draupner jacket January 1 1995. In: *proceedings in Rogue waves 2004*.

Hennig, J. (2005). *Generation and Analysis of Harsh Wave Environments*. Ph.D. thesis, Technical University Berlin.

Hofland, B., Wenneker, I. and Van Steeg, P. (2014). Short test durations for wave overtopping experiments. *Proceedings of the 5th International Conference on the Application of Physical Modelling to Port and Coastal Protection*, 349–358. Cited By 3.

Hunt, A. (2003). *Extreme waves, overtopping and flooding at sea defences*. Ph.D. thesis.

Hunt-Raby, A.C., Borthwick, A.G., Stansby, P.K. and Taylor, P.H. (2011). Experimental measurement of focused wave group and solitary wave overtopping. *Journal of Hydraulic Research*, **49**(4), 450–464. 10.3390/jmse710037510.1080/00221686.2010.542616.

Jefferys, E.R. (1987). Directional seas should be ergodic. *Applied Ocean Research*. ISSN 01411187. 10.3390/jmse710037510.1016/0141-1187(87)90001-0.

Jiang, G.S. and Shu, C.W. (1996). Efficient implementation of weighted ENO schemes. *Journal of Computational Physics*, **126**, 202–228.

Johannessen, T.B. and Swan, C. (2001). A laboratory study of the focusing of transient and directionally spread surface water waves. *Proceedings: Mathematical, Physical and Engineering Sciences*, **457**(2008), 971–1006. ISSN 13645021.

Jonathan, P. and Taylor, P.H. (1997). On Irregular, Nonlinear Waves in a Spread Sea. *Journal of Offshore Mechanics and Arctic Engineering*, **119**(1), 37–41. ISSN 0892-7219.

Kamath, A., Bihs, H. and Arntsen, Ø.A. (2017). Study of Water Impact and Entry of a Free Falling Wedge Using Computational Fluid Dynamics Simulations. *Journal of Offshore Mechanics and Arctic Engineering*, **139**(3), 31802–31806. ISSN 0892-7219.

Kamath, A., Chella, M.A., Bihs, H. and ivind A. Arntsen (2015). Evaluating wave forces on groups of three and nine cylinders using a 3d numerical wave tank. *Engineering Applications of Computational Fluid Mechanics*, **9**(1), 343–354. 10.3390/jmse710037510.1080/19942060.2015.1031318.

Kharif, C., Pelinovsky, E. and Slunyaev, A. (2009). *Rogue Waves in the Ocean*. Advances in Geophysical and Environmental Mechanics and Mathematics. Springer Berlin Heidelberg, Berlin, Heidelberg. ISBN 978-3-540-88418-7. 10.3390/jmse710037510.1007/978-3-540-88419-4.

Lindgren, G. (1970). Some properties of a normal process near a local maximum. *The Annals of Mathematical Statistics*, **41**(6), 1870–1883. ISSN 00034851.

Madsen, P.A., Bingham, H.B. and Liu, H. (2002). A new Boussinesq method for fully nonlinear waves from shallow to deep water. *Journal of Fluid Mechanics*, **462**, 1–30.

Madsen, P.A., Murray, R. and Sørensen, O.R. (1991). A new form of the Boussinesq equations with improved linear dispersion characteristics. *Coastal Engineering*, **15**, 371–388.

Mayer, S., Garapon, A. and Sørensen, L.S. (1998). A fractional step method for unsteady free surface flow with applications to non-linear wave dynamics. *International Journal for Numerical Methods in Fluids*, **28**, 293–315.

Ning, D.Z., Zang, J., Liu, S.X., Eatock Taylor, R., Teng, B. and Taylor, P.H. (2009). Free-surface evolution and wave kinematics for nonlinear uni-directional focused wave groups. *Ocean Engineering*, **36**, 1226—1243.

Nwogu, O. (1993). Alternative form of Boussinesq equations for nearshore wave propagation. *Journal of Waterways, Port, Coastal, and Ocean Engineering*, **119**(6), 618–638.

Paulsen, B.T., Bredmose, H. and Bingham, H. (2014). An efficient domain decomposition strategy for wave loads on surface piercing circular cylinders. *Coastal Engineering*, **86**, 57–76.

Pierson, W.J., Neumann, G. and James, R.W. (1955). Practical methods for observing and forecasting ocean waves by means of wave spectra and statistics.

Raoult, C., Benoit, M. and Yates, M.L. (2016). Validation of a fully nonlinear and dispersive wave model with laboratory non-breaking experiments. *Coastal Engineering*, **114**, 194 – 207. ISSN 0378-3839. 10.3390/jmse7100375https://doi.org/10.1016/j.coastaleng.2016.04.003.

Schäffer, H.A. (1996). Second-order wavemaker theory for irregular waves. *Ocean Engineering*, **23**(1), 47–88.

Shu, C.W. and Osher, S. (1988). Efficient implementation of essentially non-oscillatory shock capturing schemes. *Journal of Computational Physics*, **77**, 439–471.

Socquet-Juglard, H., Dysthe, K., Trulsen, K., Krogstad, H.E. and Liu, J. (2005). Probability distributions of surface gravity waves during spectral changes. *Journal of Fluid Mechanics*, **542**, 195216. 10.3390/jmse710037510.1017/S0022112005006312.

Sriram, V., Schlurmann, T. and Schimmels, S. (2015). Focused wave evolution using linear and second order wavemaker theory. *Applied Ocean Research*, **53**, 279 – 296. ISSN 0141-1187. 10.3390/jmse7100375https://doi.org/10.1016/j.apor.2015.09.007.

Taylor, P.H. and Williams, B.A. (2004). Wave Statistics for Intermediate Depth Water-NewWaves and Symmetry. *Journal of Offshore Mechanics and Arctic Engineering*, **126**(1), 54–59. ISSN 0892-7219.

Tromans, P.S., Anaturk, A.R. and Hagemeijer, P. (1991). A New Model For The Kinematics Of Large Ocean Waves-Application As a Design Wave. 8.

van der Vorst, H. (1992). BiCGStab: A fast and smoothly converging variant of Bi-CG for the solution of nonsymmetric linear systems. *SIAM Journal of Scientific Computing*, **13**, 631–644.

Vyzikas, T., Stagonas, D., Buldakov, E. and Greaves, D. (2018). The evolution of free and bound waves during dispersive focusing in a numerical and physical flume. *Coastal Engineering*, **132**, 95 – 109. ISSN 0378-3839. 10.3390/jmse7100375https://doi.org/10.1016/j.coastaleng.2017.11.003.

Westphalen, J., Greaves, D., Williams, C., Hunt-Raby, A. and Zang, J. (2012). Focused waves and wavestructure interaction in a numerical wave tank. *Ocean Engineering*, **45**, 9 – 21. ISSN 0029-8018. 10.3390/jmse7100375https://doi.org/10.1016/j.oceaneng.2011.12.016.

Whittaker, C., Fitzgerald, C., Raby, A., Taylor, P. and Borthwick, A. (2018). Extreme coastal responses using focused wave groups: Overtopping and horizontal forces exerted on an inclined seawall. *Coastal Engineering*, **140**, 292 – 305. ISSN 0378-3839. 10.3390/jmse7100375https://doi.org/10.1016/j.coastaleng.2018.08.004.

Whittaker, C., Fitzgerald, C., Raby, A., Taylor, P., Orszaghova, J. and Borthwick, A. (2017). Optimisation of focused wave group runup on a plane beach. *Coastal Engineering*, **121**, 44 – 55. ISSN 0378-3839. 10.3390/jmse7100375https://doi.org/10.1016/j.coastaleng.2016.12.001.

Whittaker, C., Raby, A., Fitzgerald, C. and Taylor, P. (2016). The average shape of large waves in the coastal zone. *Coastal Engineering*, **114**, 253 – 264. ISSN 0378-3839. 10.3390/jmse7100375https://doi.org/10.1016/j.coastaleng.2016.04.009.

Wu, G. and Taylor, R.E. (1994). Finite element analysis of two-dimensional non-linear transient water waves. *Applied Ocean Research*, **16**(6), 363 – 372. ISSN 0141-1187. 10.3390/jmse7100375https://doi.org/10.1016/0141-1187(94)00029-8.

Wu, G. and Taylor, R.E. (1995). Time stepping solutions of the two-dimensional nonlinear wave radiation problem. *Ocean Engineering*, **22**(8), 785 – 798. ISSN 0029-8018. 10.3390/jmse7100375https://doi.org/10.1016/0029-8018(95)00014-C.

Yates, M.L. and Benoit, M. (2015). Accuracy and efficiency of two numerical methods of solving the potential flow problem for highly nonlinear and dispersive water waves. *International Journal for Numerical Methods in Fluids*, **77**(10), 616–640. 10.3390/jmse710037510.1002/fld.3992.

Zang, J., Gibson, R., Taylor, P., Eatock Taylor, R. and Swan, C. (2006). Second order wave diffraction around a fixed ship-shaped body in unidirectional steep waves. *Journal of Offshore Mechanics and Arctic Engineering*, **128**(2), 89–99. 10.3390/jmse710037510.1115/1.2185130.

Zang, J., Taylor, P.H. and Tello, M. (2010). Steep wave and breaking wave impact on offshore wind turbine foundations - ringing re-visited. *25th International Workshop on Water Waves and Floating Bodies, Harbin, China*.

Zhang, J., Benoit, M., Kimmoun, O., Chabchoub, A. and Hsu, H.C. (2019). Statistics of extreme waves in coastal waters: Large scale experiments and advanced numerical simulations. *Fluids*, **4**(2). ISSN 2311-5521. 10.3390/jmse710037510.3390/fluids4020099.

Paper 4

A fully nonlinear potential flow wave modelling procedure for full-scale simulations of sea states with various wave breaking scenarios

Wang W., Pákozdi C, Kamath A. and Bihs H.
Submitted to *Ocean Engineering* 2020.

This Paper is awaiting publication and is not included in NTNU Open

Paper 5

A flexible fully nonlinear potential flow model for wave propagation over the complex topography of the Norwegian coast

Wang W., Pákozdi C., Kamath A., Fouques S. and Bihs H.
Submitted to *Applied Ocean Research* 2015

This Paper is awaiting publication and is not included in NTNU Open

Paper 6

Phase-resolved wave modelling in the Norwegian fjords for the ferry-free E39 project

Wang W., Pákozdi C, Kamath A. and Bihs H.

Submitted to *Journal of Ocean Engineering and Marine Energy* 2020.

This Paper is awaiting publication and is not included in NTNU Open

Paper 7

A comparison of different wave modelling techniques in an open-source hydrodynamic framework

Wang W., Kamath A., Pákozdi C. and Bihs H.
Journal of Marine Science and Engineering 2020.

A comparison of different wave modelling techniques in an open-source hydrodynamic framework

Weizhi Wang[1]*, Arun Kamath[1], Tobias Martin [1], Csaba Pákozdi [2] and Hans Bihs [1]

[1] Department of Civil and Environmental Engineering
Norwegian University of Science and Technology
Høgskoleringen 7A, 7491 Trondheim, Norway

[2] SINTEF Ocean, Otto Nielsens veg 10, 7052 Trondheim, Norway

Journal of Marine Science and Engineering Under Review.

Abstract

Modern design for marine and coastal activities place increasing focus on numerical simulations. Several numerical wave models have been developed in the past decades with various techniques and assumptions. Those numerical models have their own advantages and disadvantages. The proper choice of the most useful numerical tool depends on the understanding of the validity and limitations of each model. In the past years, REEF3D has been developed into an open-source hydrodynamic numerical toolbox that consists of several modules based on the Navier-Stokes equations, the shallow water equations and the fully non-linear potential theory. All modules share a common numerical basis which consists of rectilinear grids with an immersed boundary method, high-order finite differences and high-performance computing capabilities. The numerical wave tank of REEF3D utilises a relaxation method to generate waves at the inlet and dissipate them at the numerical beach. In combination with the choice of the numerical grid and discretisation methods, high accuracy and stability can be achieved for the calculation of free surface wave propagation and transformation. The comparison among those models provide an objective overview of the different wave modelling techniques in terms of their numerical performance as well as validity. The performance of the different modules is validated and compared using several benchmark cases. They range from simple propagations of regular waves to three-dimensional wave breaking over a changing bathymetry. The diversity of the test cases help with an educated choice of wave models for different scenarios.

Keywords: Numerical wave models; High-performance computing; Open-Source; CFD; Navier-Stokes equations; Shallow water equations; Potential flow theory

*Corresponding author, weizhi.wang@ntnu.no
Preprint, under review in Journal of Marine Science and Engineering

1 Introduction

Each fluid flow is subject to the conservation laws of mass, momentum and energy which can be described by several non-linear partial differential equations. Numerical modelling is the method of solving these equations numerically by replacing them with a set of algebraic equations. Today, this powerful technique is used in all industries and research areas, such as aero- and hydrodynamics, weather predictions or mixing processes. In contrast to experiments, numerical simulations are in general cheaper, faster in the preparation and more flexible with respect to specific external conditions or changing geometries.

Free surface flows frequently arise in nature and present an increasingly important subject due to increased sea transport, population growth and changing climate. The correct simulation of the interfaces separating the different fluids is key knowledge in marine and hydraulic engineering. The class of interface phenomena range from current to large-scale waves of varying amplitude to splashing with coalescence and breakup situations. This variety of effects reveals the development of capable numerical models for two-phase flow applications as a difficult task.

The open-source hydrodynamics framework REEF3D (Bihs et al. (2016)) was originally developed to overcome these difficulties by taking the specific challenges in hydraulics, coastal and marine engineering into consideration. This affected the design choices for the grid architecture, the discretization methods of the governing equations, the treatment of the complex free surface and the computational efficiency.

The ever increasing computational resources allow the computation of more and more complex flow problems at a reasonable cost, even for small companies and research institutions. The limiting factor of such simulations becomes less the necessary computational power but rather the time it takes for the engineer to generate the numerical grids and post-process the results. However, these high-performance computations are only possible if the code provides a consistent parallelisation strategy. From the beginning, REEF3D was designed under consideration of high-performance computations (HPC). Therefore, all parts of the code are fully parallelised based on the domain decomposition strategy and the Message Passing Interface (MPI).

The numerical grid affects the range of applicability of numerical methods but also the productivity in usage. REEF3D utilises a rectilinear grid to overcome the limitations from complicated grid generation processes. In each principal direction, user-specified analytical stretching functions enable the refinement of the grid at selected locations. Ray tracing and inverse distance algorithms are included to incorporate natural bathymetries and complicated structures using the STL file format. Together with the directional immersed boundary method of Berthelsen and Faltinsen (2008), this effectively simplifies the user input in pre-processing.

Suitable boundary conditions for the application in hydraulics, coastal and marine engineering have to be given. This particularly includes establishing a numerical wave tank with varies wave generation and dissipation methodologies. The level set method is used for capturing the propagation of the free surface (Osher and Sethian (1988)). The challenge arising from most interface models relates to physical discontinuities of the fluid properties at the interface. Low-order discretization techniques lead to a large amount of numerical diffusion, whereas high-order methods produce oscillatory and non-physical results. In order to keep a high numerical accuracy and stability, the implementation of a high-order weighted essentially non-oscillatory (WENO) scheme is the key step towards the accurate representation of sharp interfaces. The Cartesian grid makes it possible to employ the fifth-order accurate WENO scheme of Jiang and Shu (1996) for all convection terms in REEF3D. Also for the discretization in time, a high-order method is selected with the third-order total variation diminishing (TVD) RungeKutta scheme (Shu and Osher (1988)). The equations of fluid motion are solved on a staggered grid which ensures tight velocity-pressure coupling and avoids unphysical high air velocity above waves. As a result, wave propagation and transformation can be calculated throughout the wave steepness range up to the point of wave breaking and beyond, with no artificially high air velocities impacting the quality of the free surface. In the past, multiple applications proved the validity of this approach for wave propagation and wave-structure interaction. In Moreno Miquel et al. (2018), the wave generation and absorption were validated and compared to other CFD codes. Bihs et al. (2019) analysed the generation, propagation and impact of wave packets using REEF3D. Breaking waves and their interaction with a complex jacket structure were investigated by Aggarwal et al. (2019). Multi-directional irregular waves were subject of the studies in Wang et al. (2018). Alternative approaches for a numerical wave tank based on CFD were presented in e.g. Jacobsen et al. (2012) and Higuera et al. (2013). Both utilise a volume of fluid method with interface-compression (Weller (2008)) to capture the free surface and a collocated unstructured grid with second-order accuracy for the spatial and temporal discretization. The models were applied to experiments for wave propagation, and all results indicated the applicability of CFD for these kind of problems (Higuera et al. (2014); Paulsen et al. (2014); Seiffert et al. (2014)).

The source code of REEF3D is available at http://www.reef3d.com and is published under the GPL license, version 3. REEF3D is written in an object-oriented C++ structure which enables a module-based design. This led to the development of several extensions of the main code. For applications near the coast and in rivers, a dynamic sediment transport model and porous structures were incorporated. The simulated flow field is coupled with the morphological module in REEF3D to simulate e.g. the scouring process around piles (Ahmad et al. (2018)). The morphological evolution of the sediment bed is based on the Exner formula, a modified calculation of the critical bed shear stress and a sand slide algorithm. The porous medium module solves the volume-averaged Navier-Stokes equations by adding appropriate terms and coefficients to the common Reynolds-averaged Navier-Stokes equations solved in REEF3D::CFD (Kamath et al. (2018)). The model is also adapted for vegetation (Arunakumar et al. (2019)). In Bihs and Kamath (2017), a floating algorithm was presented which utilises the same directional immersed boundary method developed for fixed structures. Recently, a mooring model based on finite elements (Martin et al. (2019)) was added which improves the capabilities of the model for the simulation of moored-floating structures in waves (Martin et al. (2018)).

The phase-resolved modelling of the far-field is important for providing a realistic wave boundary condition for near-field CFD wave modelling. REEF3D, with its distinct numerical basis of high-order finite differences on rectilinear grids, is capable of incorporating simplified phase-resolving wave models for these type of problems.

For very large scale wave modelling, such as the wave transformation from the ocean to the coast, spectral wave models such as SWAN (Booji et al. (1999)) are applicable. SWAN solves the wave action or energy balance equation, which describes the wave spectrum evolution in space and time. The model lacks the ability to resolve phases which is necessary information for more detailed analyses. Here, depth-averaged shallow water models have been favoured for the coastal and harbour wave modelling because most coastal areas share relatively shallow water conditions. Shallow water models are essentially two-dimensional and, thus, require fewer computational resources. One possible approach is based on the Boussinesq equations (Madsen et al. (1991)) which can accurately model wave reflection and diffraction as well as non-dispersive linear wave propagation. Extended versions of the Boussinesq equations enable the prediction of wave propagation and transformation from deep to shallow water using improved dispersive terms (Madsen et al. (2002)). In contrast, REEF3D::SFLOW was introduced as a novel non-hydrostatic shallow water model following the quadratic pressure profile assumption. It benefits from the high-order discretization schemes and good scaling properties of REEF3D. Thus, large-scale coastal wave propagations over natural topography are possible.

The specific characteristic of Norwegian fjords and the general demand for fast far-field solutions in marine engineering require an alternative approach due to the changing dispersion relation in deep water regions. A potential flow solver is ideal for the fast calculation of wave propagation in deep water conditions as viscous effects are not important in the far-field domain. The general potential problem for waves is described by the Laplace equation with boundary conditions for the free surface and the bottom. This system of equations is highly non-linear and describes a one-phase three-dimensional flow field. High-order spectral (HOS) methods (Dommermuth and Yue (1987)), which solve the fully non-linear potential problem in deep water, have gained popularity (West et al. (1987)). HOS methods are capable of capturing non-linear wave interaction at a reasonable computational cost, though they are dependent on empirical input for wind forcing and wave breaking. Amongst others, Seiffert and Ducrozet (2018) incorporated a wave breaking parameter in HOS-NWT (Ducrozet and Bonnefoy (2012)) and simulated irregular breaking waves in 2D without wind or current. They could successfully compare surface elevation, wave spectra and energy dissipation with experiments. An alternative approach is the fully non-linear potential flow (FNPF) model, which is based on the solution of the potential problem in physical space and time. The direct numerical solution of the Laplace equation using the method of finite differences is the basis of the model OceanWave3D (Ensig-Karup et al. (2008)). This model has been used to simulate wave-structure interaction (Ducrozet et al. (2010); Paulsen et al. (2014)) and non-linear wave propagation over large spatial scales with variable bathymetry (Belibassakis and Athanassoulis (2011)). The effects of wave steepness, water depth, white-capping, and directional spreading can be included with few assumptions to obtain a better description of the real sea state to calculate extreme wave statistics and wave crest height distributions. Within the REEF3D framework, REEF3D::FNPF combines the approach of solving the Laplace equation on a σ-coordinate system using high-order finite difference methods with its high-performance computing capabilities and natural bathymetry handling.

Previously, different wave models are developed by different developers and institutes, often with various numerical implementations, making a direct comparison among the modelling techniques difficult. Now, REEF3D has evolved into an open-source numerical framework that include several types of numerical wave modelling: a computational fluid dynamic (CFD) solver REEF3D::CFD solving the Naiver-Stokes equations, a shallow water model REEF3D::SFLOW solving the non-hydrostatic shallow water equations and a fully nonlinear potential flow solver REEF3D::FNPF solving the Laplace equation with the fully nonlinear boundary conditions. With such a numerical framework, an objective comparison of the different wave modelling techniques is made possible. The authors attempt to reveal the differences in the three numerical wave modelling methods in terms of their numerical performance and physical validity by explaining the development and numerical implementations of REEF3D and testing its three modules through a series of benchmark cases.

The structure of the manuscript is arranged as the following. First, in section 2, the development and numerical implementation of the REEF3D numerical framework and its three wave modelling modules are introduced. Then an objective comparison among the different types of wave modules is performed using the three REEF3D wave modelling modules through a series of benchmark testings in section 3. In the process, the evidence of the models' strengths and limitations are revealed and explained. Finally, the findings and recommendations for an educated choice of the wave models are summarised in the section 4.

2 Numerical fluid modules

2.1 REEF3D::CFD

Mass and momentum are conserved for an incompressible fluid by solving the continuity and Reynolds-averaged Navier-Stokes (RANS) equations

$$\frac{\partial u_i}{\partial x_i} = 0, \tag{1}$$

$$\frac{\partial u_i}{\partial t} + u_j \frac{\partial u_i}{\partial x_j} = -\frac{1}{\rho}\frac{\partial p}{\partial x_i} + \frac{\partial}{\partial x_j}\left[(\nu + \nu_t)\left(\frac{\partial u_i}{\partial x_j} + \frac{\partial u_j}{\partial x_i}\right)\right] + g_i, \tag{2}$$

with u_i the velocity vector, ρ the fluid density, p the pressure, ν and ν_t the kinematic and turbulent viscosity, and g_i the gravity acceleration vector.

The Boussinesq hypothesis is used to calculate ν_t from the turbulent kinetic energy k and its specific rate of dissipation ω according to

$$\nu_t = \frac{k}{\omega}. \tag{3}$$

In REEF3D::CFD, the two-equations k-ω turbulence model (Wilcox (1988)) is typically applied to propagate the turbulence properties in space and time. Wall functions are taken into account to approximate the boundary layer flow. A limiter for ν_t is introduced to account for eventual overproduction of turbulence in highly strained flows outside the boundary layer (Durbin (2009)):

$$\nu_t = \min\left(\frac{k}{\omega}, \sqrt{\frac{2}{3}}\frac{k}{|\mathbf{S}|}\right) \tag{4}$$

Special attention is paid to the correct turbulence modelling near the free surface as the turbulent length scales in the water are reduced in its proximity. Standard two-phase RANS turbulence models do not account for this which can lead to increased ω and damped fluctuations normal to the surface due to a redistributed to parallel fluctuations. Additionally, standard RANS turbulence closure will incorrectly predict the maximum turbulence intensity at the free surface because the mean rate of strain $\mathbf{S}$ can be large especially in the vicinity of the interface between water and air (Kamath et al. (2019)). A more realistic representation of the free surface effect on the turbulence can be achieved through the replacement of the original equation for ω in the vicinity of the surface by the empirical formula (Naot and Rodi (1982); Kamath et al. (2019)):

$$\omega_s = \frac{c_\mu^{-0.25}}{\kappa} k^{0.5} \left(\frac{1}{y'} + \frac{1}{y^*} \right), \tag{5}$$

with $c_\mu = 0.07$ and $\kappa = 0.4$. The virtual origin of the turbulent length scale y' is empirically found to be 0.07 times the mean water depth (Hossain and Rodi (1980)). y^* is the distance from the nearest wall. Hence, a smooth transition from the free surface value to the wall boundary value of ω is ensured.

The location of the free surface is represented implicitly by the zero level set of a smooth signed distance function φ which can be expressed with the Eikonal equation $|\nabla\varphi| = 1$. The simple advection equation

$$\frac{\partial\varphi}{\partial t} + u_j \frac{\partial\varphi}{\partial x_j} = 0, \tag{6}$$

is applied for propagating the function in space and time. The hyperbolic property of (6) necessitates the usage of conservative numerical schemes. The level set function has to be reinitialized regularly in order to keep its signed distance property. The PDE-based reinitialization algorithm by Sussman et al. (1994) is, therefore, executed after each time step. By solving

$$\frac{\partial\varphi}{\partial\tau} + S(\varphi) \left(\left| \frac{\partial\varphi}{\partial x_j} \right| - 1 \right) = 0, \tag{7}$$

with $\Delta\tau$ an artificial time stepping, the original properties of φ can be retained. $S(\varphi)$ is the smoothed sign function Peng et al. (1999).

The material properties of the two phases are determined for the whole domain in accordance with the continuum surface force model of Brackbill et al. (1992). The properties are defined at any location in the domain as

$$\rho_i = \rho_w H(\varphi_i) + \rho_a(1 - H(\varphi_i)), \tag{8}$$

$$\nu_i = \nu_w H(\varphi_i) + \nu_a(1 - H(\varphi_i)), \tag{9}$$

with w indicating water and a air properties. H is the smoothed Heaviside step function

$$H(\varphi_i) = \begin{cases} 0 & if\ \varphi_i < -\epsilon \\ \frac{1}{2}\left(1 + \frac{\varphi}{\epsilon} + \frac{1}{\pi}\sin\left(\frac{\pi\varphi_i}{\epsilon}\right)\right) & if\ |\varphi_i| \le \epsilon \\ 1 & if\ \varphi_i > \epsilon, \end{cases} \tag{10}$$

Typically the thickness of the smoothed out interface is chosen to be $\epsilon = 2.1\Delta x$ on both sides of the interface. The density is generally determined directly at the cell faces in order to avoid spurious oscillations at the interface (see Bihs et al. (2016) for details).

The numerical discretisation of the different equations is achieved using finite difference methods on rectilinear grids. The coupling of pressure and velocity during the solution of (2) is ensured by staggering the grid. A fifth-order accurate weighted essentially non-oscillatory (WENO) scheme (Jiang and Shu (1996)) adapted to non-uniform cell sizes is applied for the convection terms. In (6), the convection term is discretised by the fifth-order accurate Hamilton-Jacobi WENO method of Jiang and Peng (2000). Diffusion terms are, generally, discretised using second-order accurate central finite differences.

The solution process follows the projection method for incompressible flows of Chorin (1968). In the predictor step, the conservation equation for momentum (2) is solved without considering the pressure gradients

$$\frac{u_i^{(*)} - u_i^{(n)}}{\Delta t} = -u_j \frac{\partial u_i}{\partial x_j} + \frac{\partial}{\partial x_j}\left(\nu \cdot \left(\frac{\partial u_i}{\partial x_j} + \frac{\partial u_j}{\partial x_i}\right)\right) + g_i. \tag{11}$$

Thus, a predicted velocity field $u_i^{(*)}$ is obtained. Here, the time derivatives are solved by applying the third-order accurate Total Variation Diminishing (TVD) Runge-Kutta scheme (Shu and Osher (1988)). The same time discretisation is also used in (6) and (7). Turbulence time advancement is solved using implicit methods due to its source term driven character. The general time-stepping is controlled adaptively under consideration of the CFL condition (see Bihs et al. (2016)). Diffusion terms are treated implicitly to overcome their restrictions on this condition. The insertion of the predicted velocities into the continuity equation leads to the Poisson equation

$$\frac{\partial}{\partial x_i}\left(\frac{1}{\rho(\widehat{\Phi}^{n+1})}\frac{\partial p^{(n+1)}}{\partial x_i}\right) = \frac{1}{\Delta t}\frac{\partial u_i^{(*)}}{\partial x_i}. \tag{12}$$

for the pressure of the new time step. It is solved by the fully parallelized BiCGStab algorithm of the HYPRE library (van der Vorst (1992)) with the geometric multigrid PFMG pre-conditioner (Ashby and Flagout (1996)) to enhance the performance. As the final step, the divergence-free velocity field of the new time step is obtained following

$$u_i^{(n+1)} = u_i^{(*)} - \frac{\Delta t}{\rho(\widehat{\Phi}^{n+1})}\frac{\partial p^{(n+1)}}{\partial x_i}. \tag{13}$$

High-performance computations are enabled in REEF3D::CFD by applying the Message Passing Interface (MPI) and ghost cells as the parallelisation strategy. Three layers of ghost cells are added to each sub-domain due to the fifth-order accurate WENO scheme. Similarly, the directional ghost cell immersed boundary method (GCIBM) of Berthelsen and Faltinsen (2008) is implemented to handle complex solid geometries. Here, the domain is virtually extended into the geometry, and the values at these ghost cells are found through extrapolation and under consideration of a wall boundary condition. Thus, the numerical discretisation of the fluid domain does not need to account for the boundary conditions explicitly. Instead, they are incorporated implicitly. Simple geometries such as boxes, cylinders or prisms can be generated directly through user input. Otherwise, STL files are to be generated. Then a level set function, with the zero level set representing the solid boundary, is generated using a ray-tracing algorithm as presented in Yang and Stern (2013), see above. In the same way, natural bathymetries can be incorporated in a straight forward manner (Shepard (1968)).

2.2 REEF3D::SFLOW

The governing equations for the non-hydrostatic shallow water module are derived from the mass and momentum conservation for an incompressible inviscid fluid. Following the quadratic assumption (Jeschke et al. (2017); Wang et al. (2020)), the governing equations are written with depth-averaged variables:

$$\frac{\partial \zeta}{\partial t} + \frac{\partial hu}{\partial x} + \frac{\partial hv}{\partial y} = 0, \tag{14}$$

$$\frac{\partial u}{\partial t} + u\frac{\partial u}{\partial x} + v\frac{\partial u}{\partial y} = -g\frac{\partial \zeta}{\partial x} - \frac{1}{\rho h}\left(\frac{\partial hq}{\partial x} - \left(\frac{3}{2}q + \frac{1}{4}\rho h \Phi_{nh}\right)\frac{\partial d}{\partial x}\right), \tag{15}$$

$$\frac{\partial v}{\partial t} + u\frac{\partial v}{\partial x} + v\frac{\partial v}{\partial y} = -g\frac{\partial \zeta}{\partial y} - \frac{1}{\rho h}\left(\frac{\partial hq}{\partial y} - \left(\frac{3}{2}q + \frac{1}{4}\rho h \Phi_{nh}\right)\frac{\partial d}{\partial y}\right), \tag{16}$$

$$\frac{\partial w}{\partial t} + u\frac{\partial w}{\partial x} + v\frac{\partial w}{\partial y} = -\frac{1}{\rho h}\left(\frac{3}{2}q + \frac{1}{4}\rho h \Phi_{nh}\right), \tag{17}$$

where u, v, w and q are the depth-averaged velocity components in x, y, z-directions and the depth-averaged dynamic pressure. d is the still water depth, ζ represents the free surface elevation and $h = d + \zeta$. The hydrodynamic pressure at the bottom is represented as $\frac{3}{2}q + \frac{1}{4}\rho h \Phi$, which describes the quadratic vertical pressure profile (Jeschke et al. (2017)). The term Φ is expressed as follows Jeschke et al. (2017):

$$\Phi_{nh} = -\nabla d \cdot (\partial_t \boldsymbol{u} + (\boldsymbol{u} \cdot \nabla)\boldsymbol{u}) - \boldsymbol{u} \cdot \nabla(\nabla d) \cdot \boldsymbol{u}. \tag{18}$$

The governing equations are solved on REEF3D's structured staggered grid using finite differences. The solution of the velocities are obtained using Chorin's projection method (Chorin (1968)). The convective terms for the velocities u,v and w are discretised with the fifth-order accurate WENO scheme. The TVD third-order accurate Runge-Kutta explicit time scheme is used for time discretisation. The pressure information is obtained from the solution of the Poisson equation

$$\frac{h_p}{\rho}\left(\frac{\partial^2 q}{\partial x^2} + \frac{\partial^2 q}{\partial y^2}\right) + \frac{2q}{\rho h_p} = \frac{1}{\partial x \partial t}\left(-h_p\left(\frac{\partial u}{\partial x} + \frac{\partial v}{\partial y}\right) - 2w - u\frac{\partial d}{\partial x} - v\frac{\partial d}{\partial y}\right). \tag{19}$$

Here, the parameter h_p denotes the water level in the centre of the cell, where the dynamic pressure q, the vertical velocities w and the free surface location ζ are solved. The horizontal velocities u and v are solved at the cell faces. The PFMG preconditioned BiCGStab algorithm (Ashby and Flagout (1996)) of HYPRE is applied to solve for pressure. The solution is then utilised to correct the velocities in a correction step:

$$u^{n+1} = u^* + \Delta t \left(\frac{3}{2} \frac{q^{n+1}}{\rho h_p} \frac{\partial d}{\partial x} + \frac{1}{4} \Phi_{nh} \frac{\partial d}{\partial x} \right), \tag{20}$$

$$v^{n+1} = v^* + \Delta t \left(\frac{3}{2} \frac{q^{n+1}}{\rho h_p} \frac{\partial d}{\partial y} + \frac{1}{4} \Phi_{nh} \frac{\partial d}{\partial y} \right), \tag{21}$$

$$w^{n+1} = w^* + \Delta t \left(\frac{3}{2} \frac{q^{n+1}}{\rho h_p} + \frac{1}{4} \Phi_{nh} \right), \tag{22}$$

with u^*, v^*, w^* the intermediate velocities using only the hydrostatic pressure information.

The free-surface elevation ζ is determined from Eqn. (14) using the divergence of the depth-integrated horizontal velocities and the fifth-order WENO scheme.

A straightforward wetting and drying scheme (Stelling and Duinmeijer (2003); Zijlema and Stelling (2008)) is applied at the coastlines. The velocities are set to be zero in cells where the local water level is below a user-defined threshold:

$$\begin{cases} u = 0, & \text{if } \widehat{h}_x < \text{threshold}, \\ v = 0, & \text{if } \widehat{h}_y < \text{threshold}. \end{cases} \tag{23}$$

The default threshold is set to be 0.00005 m. This approach tracks the variations of the coastlines accurately and avoids numerical instabilities by ensuring non-negative water depth (Stelling and Duinmeijer (2003); Zijlema and Stelling (2008)).

Breaking waves are detected when the vertical velocity of the free-surface exceeds a fraction of the shallow water celerity (SWASH developers (2017)):

$$\frac{\partial \zeta}{\partial t} > \alpha \sqrt{gh}. \tag{24}$$

During breaking, the dynamic pressure is removed at the front of the breaker and only the hydrostatic pressure is present in the momentum equations. Another parameter β $(0 < \beta < \alpha)$ is introduced to replace α in Eqn. (24) to stop wave breaking and determine the persistence of the breaking process. $\alpha = 0.6$ and $\beta = 0.3$ are recommended by the SWASH developers (2017). In this combined approach, the momentum is well conserved and the energy is correctly dissipated (SWASH developers (2017)).

2.3 REEF3D::FNPF

The governing equation for the fully non-linear potential flow module REEF3D::FNPF is the Laplace equation (Bihs et al. (2020))

$$\frac{\partial^2 \phi}{\partial x^2} + \frac{\partial^2 \phi}{\partial y^2} + \frac{\partial^2 \phi}{\partial z^2} = 0. \tag{25}$$

Boundary conditions at the free surface and the bottom are required in order to solve for the velocity potential ϕ. The kinematic and dynamic free surface boundary conditions state that the fluid particles at the free surface must remain at the surface and the pressure at the free surface should be equal to the atmospheric pressure. These boundary conditions can be expressed as follows:

$$\frac{\partial \eta}{\partial t} = -\frac{\partial \eta}{\partial x}\frac{\partial \widetilde{\phi}}{\partial x} - \frac{\partial \eta}{\partial y}\frac{\partial \widetilde{\phi}}{\partial y} + \widetilde{w}\left(1+\left(\frac{\partial \eta}{\partial x}\right)^2+\left(\frac{\partial \eta}{\partial y}\right)^2\right), \tag{26}$$

$$\frac{\partial \widetilde{\phi}}{\partial t} = -\frac{1}{2}\left(\left(\frac{\partial \widetilde{\phi}}{\partial x}\right)^2+\left(\frac{\partial \widetilde{\phi}}{\partial y}\right)^2 - \widetilde{w}^2\left(1+\left(\frac{\partial \eta}{\partial x}\right)^2+\left(\frac{\partial \eta}{\partial y}\right)^2\right)\right) - g\eta, \tag{27}$$

where η is the free surface elevation, $\mathbf{x} = (x, y)$ represents the horizontal directions, $\widetilde{\phi} = \phi(\mathbf{x}, \eta, t)$ and $\widetilde{w}$ are the velocity potential and the vertical velocity at the free surface. At the bottom, the component of the velocity normal to the bottom surface must be zero at all times. This gives the bottom boundary condition

$$\frac{\partial \phi}{\partial z} + \frac{\partial h}{\partial x}\frac{\partial \phi}{\partial x} + \frac{\partial h}{\partial y}\frac{\partial \phi}{\partial y} = 0, \quad z = -h, \tag{28}$$

with $h = h(\mathbf{x})$ the water depth measured from the still water level to the bottom.

The Laplace equation is solved iin each time step with the finite difference method on a σ-coordinate system as proposed by Li and Fleming (1997). Here, the σ-coordinate system follows the irregular variation of the water depth. A Cartesian grid can be transformed to a σ-coordinate as follows:

$$\sigma = \frac{z + h(\mathbf{x})}{\eta(\mathbf{x}, t) + h(\mathbf{x})}. \tag{29}$$

The vertical coordinates are clustered towards the free surface by including a stretching function:

$$\sigma_i = \frac{\sinh(-\alpha) - \sinh\left(\alpha\left(\frac{i}{N_z} - 1\right)\right)}{\sinh(-\alpha)}, \tag{30}$$

where α is the stretching factor, i is the index of the vertical grid point and N_z stand for the total number of cells in the vertical direction. The boundary conditions and the governing equation in the σ-coordinate can be written as:

$$\Phi = \widetilde{\phi} \qquad , \sigma = 1; \tag{31}$$

$$\begin{aligned}&\frac{\partial^2 \Phi}{\partial x^2} + \frac{\partial^2 \Phi}{\partial y^2} + \left(\frac{\partial^2 \sigma}{\partial x^2} + \frac{\partial^2 \sigma}{\partial y^2}\right)\frac{\partial \Phi}{\partial \sigma} + 2\left(\frac{\partial \sigma}{\partial x}\frac{\partial}{\partial x}\left(\frac{\partial \Phi}{\partial \sigma}\right) + \right.\\ &\left.\frac{\partial \sigma}{\partial y}\frac{\partial}{\partial y}\left(\frac{\partial \Phi}{\partial \sigma}\right)\right) + \left(\left(\frac{\partial \sigma}{\partial x}\right)^2 + \left(\frac{\partial \sigma}{\partial y}\right)^2 + \left(\frac{\partial \sigma}{\partial z}\right)^2\right)\frac{\partial^2 \Phi}{\partial \sigma^2} = 0 \quad , 0 \leq \sigma < 1;\end{aligned} \tag{32}$$

$$\left(\frac{\partial \sigma}{\partial z} + \frac{\partial h}{\partial x}\frac{\partial \sigma}{\partial x} + \frac{\partial h}{\partial y}\frac{\partial \sigma}{\partial y}\right)\frac{\partial \Phi}{\partial \sigma} + \frac{\partial h}{\partial x}\frac{\partial \Phi}{\partial x} + \frac{\partial h}{\partial y}\frac{\partial \Phi}{\partial y} = 0 \qquad , \sigma = 0, \tag{33}$$

with Φ the velocity potential with a dependency on σ. The fluid velocities can then be calculated using

$$u(\mathbf{x}, z) = \frac{\partial \Phi(\mathbf{x}, z)}{\partial x} = \frac{\partial \Phi(\mathbf{x}, \sigma)}{\partial x} + \frac{\partial \sigma}{\partial x}\frac{\partial \Phi(\mathbf{x}, \sigma)}{\partial \sigma}, \tag{34}$$

$$v(\mathbf{x}, z) = \frac{\partial \Phi(\mathbf{x}, z)}{\partial y} = \frac{\partial \Phi(\mathbf{x}, \sigma)}{\partial y} + \frac{\partial \sigma}{\partial y}\frac{\partial \Phi(\mathbf{x}, \sigma)}{\partial \sigma}, \tag{35}$$

$$w(\mathbf{x}, z) = \frac{\partial \Phi(\mathbf{x}, z)}{\partial z} = \frac{\partial \sigma}{\partial z}\frac{\partial \Phi(\mathbf{x}, \sigma)}{\partial \sigma}. \tag{36}$$

The Laplace equation is discretized using second-order central differences, and the solution is obtained using the geometric multigrid preconditioned conjugated gradient solver provided by HYPRE. The convection terms in the free surface boundary conditions are discretized using the fifth-order accurate Hamilton-Jacobi version of the WENO scheme (Jiang and Peng (2000)). The time-dependent terms in the free surface boundary conditions are treated with the third-order accurate TVD Runge-Kutta scheme (Shu and Osher (1988)). An adaptive time step is included by controlling a constant time factor that is equivalent to the Courant criterion (Courant et al. (1967)):

$$\begin{aligned}
c_u &= \frac{\Delta x}{\left|\max(u_{\max}, \sqrt{9.81 * d_{\max}})\right|}, \\
c_v &= \frac{\Delta x}{\left|\max(v_{\max}, \sqrt{9.81 * d_{\max}})\right|}, \\
c_{\text{tot}} &= \min(c_u, c_v), \\
\Delta t &= c_{\text{tot}} \text{ CFL},
\end{aligned} \tag{37}$$

where c_u, c_v, c_w are the phase velocities in x, y and z directions, and $u_{\max}, v_{\max}$ are the maximum particle velocities in x- and y-direction.

The wetting-drying scheme for detecting coastlines and the shallow water breaking criterium follow the same principle as in REEF3D::SFLOW. For deep water breaking, a wave slope criterion is used. Wave breaking takes place when the ratio between the free surface elevation difference and the horizontal distance difference at adjacent cells is higher than the criterion, which has a default value of 1.25. A filtering scheme is used to smooth the free surface in order to dissipate wave energy when wave breaking is detected (Jacobsen (2015)).

Another challenge in handling coastlines in a potential flow model is the possible numerical instability during the wave run-up process in the swash zone. The derivatives of velocity potential over water depth in Eqn. 32 indicate a possible numerical instability when water depth becomes infinitesimal. Therefore, an innovative coatline lagorithm is introduced to eliminate the instability.

After the wet and dry cells are identified, the wet cells are assigned with $+1$ and the dry cells are assigned with -1. With these initial values, the coastline is captured using the level-set function by Osher and Sethian (1988):

$$\varphi(\vec{x}, t) \begin{cases} > 0 \ if \ \vec{x} \in wet\ cell \\ = 0 \ if \ \vec{x} \in \Gamma \\ < 0 \ if \ \vec{x} \in dry\ cell \end{cases} \tag{38}$$

Γ represents the coastline, and the Eikonal equation $|\nabla\varphi| = 1$ holds valid in the level-set function. From the initial values, the correct signed distance function is obtained by solving the following Partial Differential Equation (PDE) based reinitialisation function (Sussman et al. (1994)):

$$\frac{\partial\varphi}{\partial t} + S(\varphi)\left(\left|\frac{\partial\varphi}{\partial x_j}\right| - 1\right) = 0 \tag{39}$$

where $S(\varphi)$ is the smoothed sign function (Peng et al. (1999)). This equation is solved until convergence and results in the correct signed distance away from the coastline in the whole horizontal plane. The excact coastline location is the zero-contour of the level set function.

Relaxation zones are applied along the the wet side of the coastline. With these relaxation zones, the extreme run-ups are avoided and therefore eliminate numerical instabilities in the free surface boundary conditions at extreme shallow regions.

3 Numerical Results

3.1 Comparison of the different modules for the numerical simulation of progressive waves

The different modules of REEF3D all share high-order numerical schemes for spatial and temporal discretisation and a high-performance computation capacity. To demonstrate the modules' capabilities and limitations, simulations of progressive waves over constant and varying topography are performed using all three modules. First, progressive regular wave propagation over constant intermediate water depth in 2D is simulated. The numerical wave tank is 28 m long and the water depth is 0.5 m. Two input waves are used, one is a linear wave with the wave height $H = 0.01$ m and a wave period of $T = 1.95$ s, and another is a Stokes 2nd-order wave with a wave height of $H = 0.05$ m and the same wave period of $T = 1.95$ s and wavelength 3.936 m. A one-wavelength wave generation zone is located at the inlet boundary, and a two-wavelength numerical beach is arranged at the outlet boundary. All simulations are conducted for a duration of 40 s on a Mac Pro with a four 2.7 GHz Intel Xeon E5 cores. The grid convergence studies of the linear wave simulations are shown in Fig. 1a to Fig. 1c. For REEF3D::FNPF, the vertical grid is determined by keeping a constant truncation error in the vertical direction (Pakozdi et al. (2019)), which results in 10 vertical cells with a stretching factor of 1.25. It is seen that the results for amplitude and phase converge with $\Delta x = 0.05$ m, 0.02 m and 0.1 m for REEF3D::CFD, REEF3D::SFLOW and REEF3D::FNPF respectively. With these cell sizes, the total number of cells N_t and the simulation time T_s are compared in Tab. 2. The spatial free surface profiles are compared against the theoretical wave profile in Fig. 1d. All three modules generate the theoretical wave profile accurately and the numerical beach absorbs the wave energy at the outlet boundary effectively. REEF3D::SFLOW requires the least number of cells due to its two-dimensional grid. Consequently, it is 7.3 times faster as REEF3D::CFD. However, REEF3D::FNPF is the fastest (35 times as fast at REEF3D::CFD), even though it needs more cells than REEF3D::SFLOW.

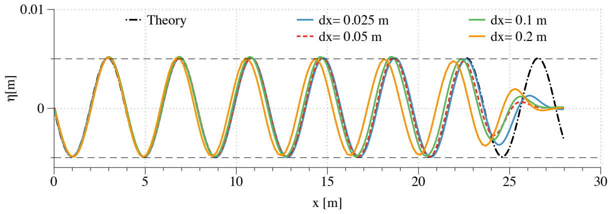

(a) Grid convergence study using REEF3D::CFD

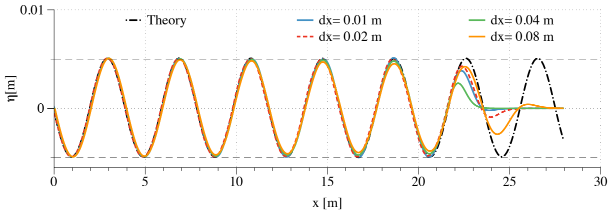

(b) Grid convergence study using REEF3D::SFLOW

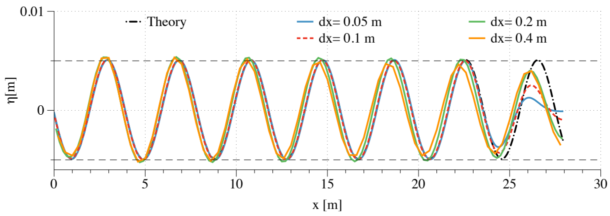

(c) Grid convergence study using REEF3D::FNPF

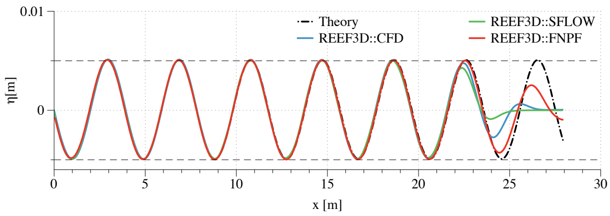

(d) Comparison of the spatial wave profiles

Figure 1: Convergence study on cell sizes for the 2D regular linear wave simulation and the comparison of free surface elevation among the three modules. (a) - (c) grid convergence study, (d) comparison of the spatial wave profiles using the finest cell sizes.

The mean square root errors for wave height in the grid convergence study for the 2D regular linear wave simulation using the three modules are summarised in Table. 1.

Similarly, the grid convergence study and the comparison of the spatial wave profiles for the simulations of the 2nd-order Stokes wave using different modules are shown in Fig. 2. The mean square root errors for wave height in the grid convergence study for the 2D regular Stokes 2nd-order wave simulation using the three modules are summarised in Table. 3. It is seen that the grid convergence is achieved with $\Delta x = 0.05$ m, 0.02 m and 0.1 m for REEF3D::CFD,

Table 1: Mean square root errors on wave height in the grid convergence study for the 2D regular linear wave simulation using the three modules. The notations dx1 to dx4 represent the finest and coarsest cell size in the tests of each of the modules.

dx (m)	REEF3D::CFD	REEF3D::SFLOW	REEF3D::FNPF
dx1	7.889e-05	8.031e-05	5.025e-05
dx2	8.872e-05	9.656-05	5.701e-05
dx3	1.010e-04	1.999e-04	3.303e-04
dx4	1.213e-04	4.251e-04	4.842e-04

Table 2: Comparison of total number of cells N_t and simulation time T_s in seconds for the simulation of progressive linear wave using the three modules.

module	N_t	T_s
REEF3D::CFD	11200	594.9 s
REEF3D::SFLOW	560	81.5 s
REEF3D::FNPF	2800	16.8 s

REEF3D::SFLOW and REEF3D::FNPF. With these cell sizes, all three modules represent the 2nd-order Stokes wave with correct amplitude, phase and asymmetry over the still water level. Similarly, the total number of cells and computational time are summarised in Tab. 4, the computational speed is similar to the linear wave simulations.

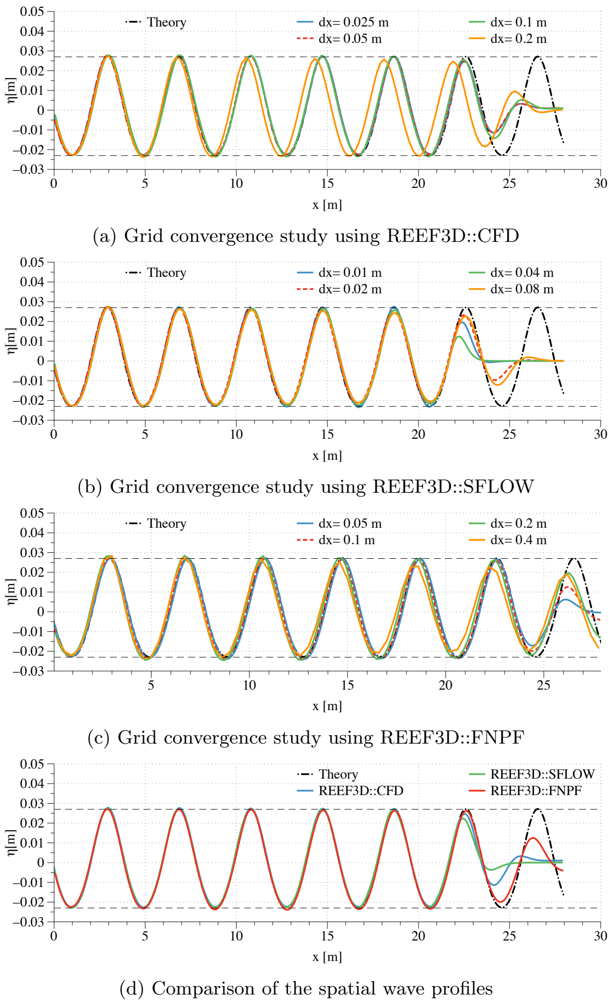

(a) Grid convergence study using REEF3D::CFD

(b) Grid convergence study using REEF3D::SFLOW

(c) Grid convergence study using REEF3D::FNPF

(d) Comparison of the spatial wave profiles

Figure 2: Convergence study on cell sizes for the 2D regular Stokes 2nd-order wave simulation and the comparison of free surface elevation among the three modules. (a) - (c) grid convergence study, (d) comparison of the spatial wave profiles using the cell sizes achieving grid convergence.

3.2 Two-dimensional wave propagation over a submerged bar

Next, the experiment of the wave propagation over a submerged bar (Beji and Battjes (1993)) is reproduced using all three modules. The numerical tank setup is shown in Fig. 3. A wave generation zone of 5 m is located at the inlet boundary and a numerical beach of 9.5 m is

Table 3: Mean square root errors for wave height in the grid convergence study for the 2D regular Stokes 2nd-order wave simulation using the three modules. The notations dx1 to dx4 represent the finest and coarsest cell size in the tests of each of the modules.

dx (m)	REEF3D::CFD	REEF3D::SFLOW	REEF3D::FNPF
dx1	3.581e-04	5.117e-04	4.739e-04
dx2	3.582e-04	7.637e-04	5.483e-04
dx3	4.421e-04	9.529e-04	1.41e-03
dx4	1.109e-03	1.80e-03	2.15e-03

Table 4: Comparison of total number of cells N_t and simulation time T_s in seconds for the simulation of progressive 2nd-order Stokes wave using the three modules

module	N_t	T_s
REEF3D::CFD	11200	638.3 s
REEF3D::SFLOW	560	86.7 s
REEF3D::FNPF	2800	16.9 s

located at the outlet boundary. The submerged bar starts 6 m from the wave generation zone, and 8 wave gauges are located over the horizontal range of the submerged bar. A 2nd-order Stokes wave with a wave height 0.021 m and a wave period of 2.525 s is generated from the inlet boundary and propagates over the bar for 60 s. The simulations are computed with four 2.7 GHz Intel Xeon E5 cores on Mac Pro for REEF3D::FNPF and REEF3D::SFLOW and 128 2.1 GHz Intel E5-2683v4 cores on the supercomputer Fram for REEF3D::CFD.

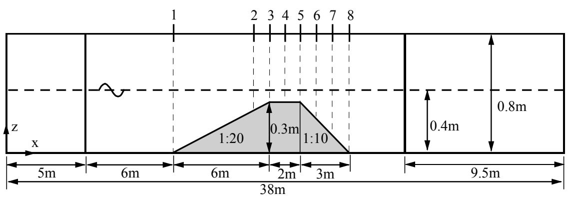

Figure 3: Numerical setup for the simulation of the wave propagation over a submerged bar.

The grid convergence study is shown in Fig. 4. The vertical grid arrangement for REEF3D::FNPF follows the same constant truncation error principle. Here, 10 vertical cells and a stretching factor of 1.2 is used. Only the horizontal grid convergence of REEF3D::FNPF is performed. The last wave gauge 8 is used for the convergence study as high-frequency wave components appear during the de-shoaling process after the waves propagate over the submerged bar. REEF3D::CFD and REEF3D::FNPF are able to capture the high-frequency wave components with cell sizes of 0.005 m and 0.025 m respectively. For REEF3D::SFLOW, even with a converged cell size of 0.02 m, the wave phases are not correctly represented because these high-frequency waves have significantly shorter wavelengths and the water condition is not appropriate for shallow water models at this location.

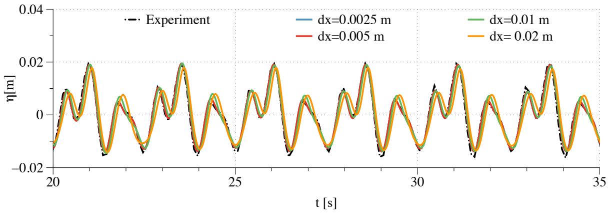

(a) REEF3D::CFD convergence at Gauge 8

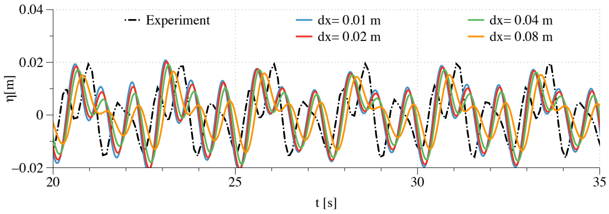

(b) REEF3D::SFLOW convergence at Gauge 8

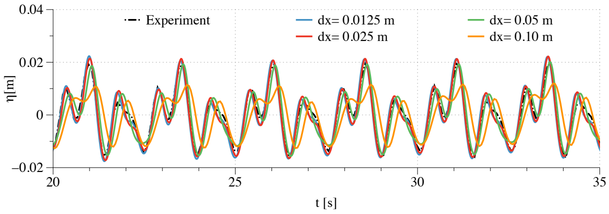

(c) REEF3D::FNPF convergence at Gauge 8

Figure 4: Convergence study on horizontal cell sizes at wave gauge 8 for the simulations of wave propagation over a submerged bar. (a)REEF3D::CFD grid convergence, (b) REEF3D::SFLOW grid convergence, (c) REEF3D::FNPF grid convergence

Using the converged cell sizes, the free surface elevation time history in the simulations are compared against the experimental measurements in Fig. 5. The free surfaces from all simulations agree well with the experimental data during the shoaling process, while REEF3D::SFLOW starts to show phase differences from gauge 6 in the de-shoaling process as the water condition gets deeper due to shorter waves.

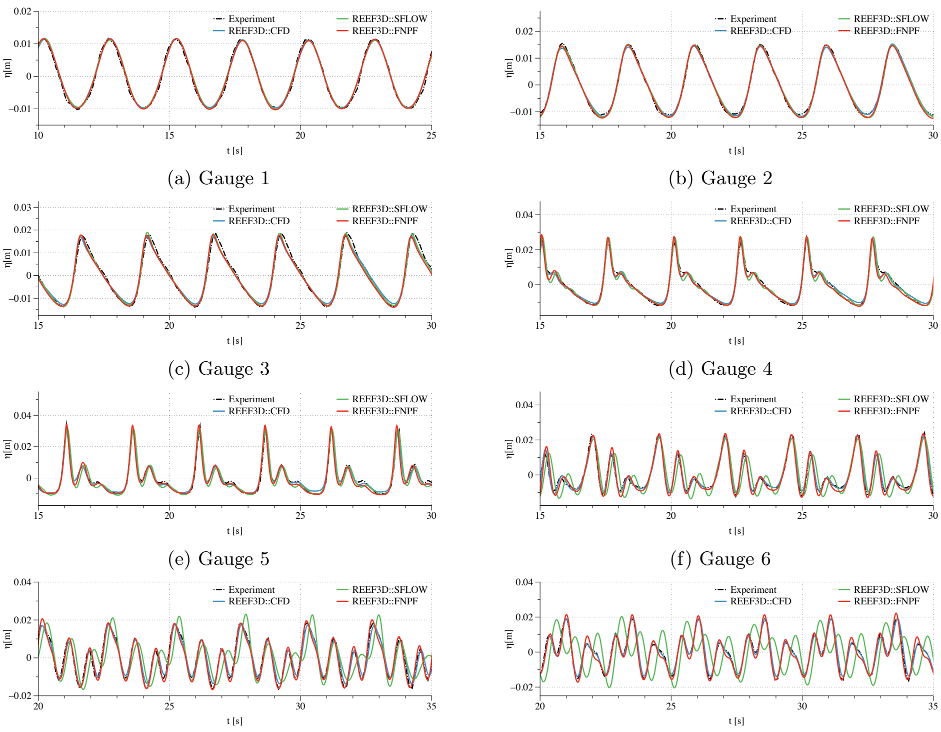

(a) Gauge 1 (b) Gauge 2

(c) Gauge 3 (d) Gauge 4

(e) Gauge 5 (f) Gauge 6

(g) Gauge 7 (h) Gauge 8

Figure 5: Comparison of the time histories of the free surface elevations at the wave gauges in the simulations of wave propagation over a submerged bar using the cell sizes achieving grid convergence. .

The number of cells and computational time for the simulations of the wave propagation over a submerged bar are summarised in Tab. 5. When complicated phenomena are present, CFD often requires a large number of cells, and the speed-up with the shallow water model and the potential flow model is dramatically increased.

Table 5: Comparison of total number of cells N_t and simulation time T_s in seconds for the simulation of wave propagation over a submerged bar using the three modules

module	N_t	T_s
REEF3D::CFD	1216000	10759.5 s
REEF3D::SFLOW	1900	761.7 s
REEF3D::FNPF	15200	282.2 s

The simulations show that for progressive regular waves below the breaking limit, all three modules can represent the frees surface accurately. However, the requirements of the grid resolution are different. It is commonly seen that 80 to 100 cells per wavelength is able to capture the free-surface well with REEF3D::CFD, while only 30 to 40 cells per wavelength are needed in REEF3D::FNPF. The grid resolution in REEF3D::SFLOW might be higher, but the 2D vertical grid structure reduces the total number of cells dramatically. In practice, when the wave steepness is not close to the breaking limit, REEF3D::SFLOW and REEF3D::FNPF are much faster alternatives, especially for large-scale sea states and coastal wave simulations. In shallow to intermediate water condition up to wavelength to water depth ratio 0.25 (Jeschke et al. (2017)), REEF3D::SFLOW has an advantage because it is capable of resolving the run-up process in the swash zone. However, for water conditions with large water depth changes, the de-shoaling process limits the application of REEF3D::SFLOW as seen in the simulation of wave propagation over a submerged bar. In such conditions, REEF3D::FNPF is the optimal choice as its applicability is not limited by large water depth gradients. REEF3D::CFD is slower but contains more information about turbulent effects in the flow. In cases where strong wave-structure interaction take place or waves break, REEF3D::CFD is the only option for numerical modelling of the associated phenomena. The following applications focus on the most suitable applications for each of the modules.

3.3 Two-dimensional wave breaking over a mild slope

In shallow water regions, depth-induced wave breaking is a common phenomenon. All three modules are equipped with breaking wave algorithms to represent the energy dissipation during a wave breaking process, as described in section 2. In this section, a depth-induced breaking wave over a mild slope is simulated with all three modules in a two-dimensional numerical wave tank. In order to reduce the computational cost of the CFD simulation, the original setup from Ting and Kirby (1995) is truncated in its longitudinal direction. The breaking wave zone and swash zone are all remained in the truncated numerical wave tank. The new numerical wave tank setup is shown in Fig. (6). The mild slope starts 13.8 m from the inlet boundary and rises up to 0.463 m at the outlet following a slope of 1:35. The water depth at the wave generator is 0.4 m. A $5th$-order Cnoidal wave with a wave height of 0.128 m and wave period of 5 s is generated at wave generation zone that is 9.8 m long, i.e. one wavelength. Four wave gauges are located on the slope adjacent to the wave breaking location. From wave gauges 1 to 4, the x-coordinates are $x = 19.8, 20.8, 21.8$ and 22.1 m. The simulations are computed with four 2.7 GHz Intel Xeon E5 cores on Mac Pro for REEF3D::FNPF and REEF3D::SFLOW and 128 2.1 GHz Intel E5-2683v4 cores on the supercomputer Fram. The grid convergence study for the three models REEF3D::CFD, REEF3D::SFLOW and REEF3D::FNPF were reported respectively by Bihs et al. (2016), Wang et al. (2020) and Bihs et al. (2020). As a result, the $dx = 0.005$ m, $dx = 0.005$ m and $dx = 0.005$ m are used in the REEF3D::CFD, REEF3D::SFLOW and REEF3D::FNPF simulations respectively. 10 cells are used in the vertical direction for the simulation with REEF3D::FNPF. The simulations are performed for 40 s with adaptive time stepping and $CFL = 0.1, 0.2$ and 1.0 for the REEF3D::CFD, REEFD::SFLOW and REEF3D::FNPF simulations respectively. The simulated free surface elevation time series from all three modules are compared to the experimental measurements in Fig. (7).

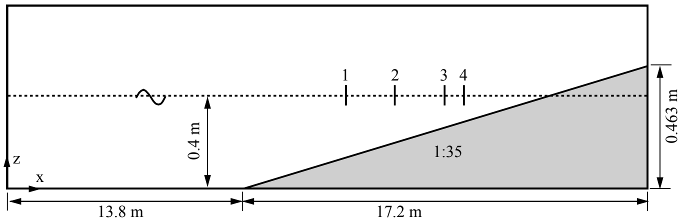

Figure 6: Numerical wave tank setup for wave breaking over a mild slope.

As can be seen in Fig. (7), the results from all three modules achieve a good agreement with the experiment both in wave amplitude and wave phase. The wave amplitudes increase from waver gauge 1 to wave gauge 2 due to the shoaling effect in both the simulations and the experiment. Wave gauge 3 shows a decrease in wave amplitude and the decreasing trend continues to wave gauge 4. This change of amplitude indicates a wave breaking happens between wave gauge 2 and 3 as a result of energy dissipation during the wave breaking process. The correct representation of the amplitude change shows that all three modules produce correct wave energy dissipation.

To compare the computational performance of the three modules, the total number of cells and computational time for each model to finish the simulations are summarised in Table. 6

Table 6: Comparison of total number of cells N_t and simulation time T_s in seconds for the simulation of wave propagation over a submerged bar using the three modules

module	N_t	T_s
REEF3D::CFD	1200000	31578.8 s
REEF3D::SFLOW	6000	5326.62 s
REEF3D::FNPF	6000	639.9 s

Similar to section 3.2, REEF3D::SFLOW and REEF3D::FNPF use much less cells in comparison to REEF3D::CFD to achieve a similar level of accuracy. In this case, both REEF3D::SFLOW and REEF3D::FNPF only need 1/200 the number of cells as used in the REEF3D::CFD simulation. In terms of the computational speed, REEF3D::SFLOWS is seen to be roughly 190 times faster than REEF3D::CFD while REEF3D::FNPF is 1580 times faster. However, the slower computational speed of REEF3D::CFD is compensated by the fact that REEF3D::CFD is the only model that is able to represent a correct geometry of an overturning breaker, which is shown in the next section with a three-dimensional overturning wave breker.

3.4 Three-dimensional wave breaking over a flat-tipped reef

The design of coastal structures such as combined coastal defences, recreational surfing reefs and marine biodiversity enhancement measures such as submerged porous reefs require a detailed analysis of the interaction between the incident waves and the proposed structure.

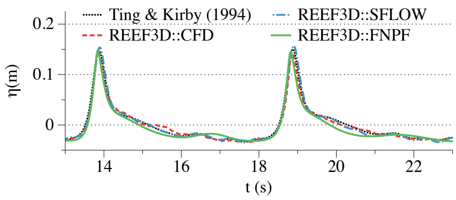

(a) Wave gauge 1

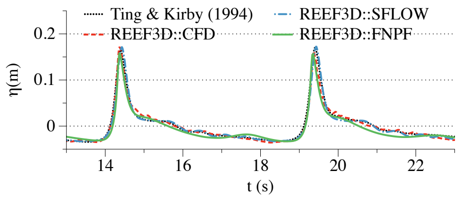

(b) Wave gauge 2

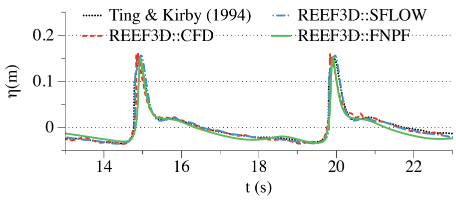

(c) Wave gauge 3

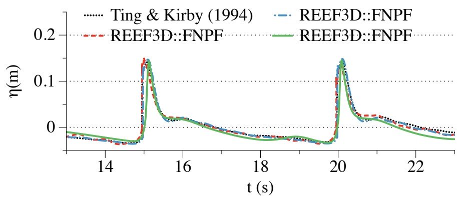

(d) Wave gauge 4

Figure 7: Comparison between the simulated free surface elevation time series from the three REEF3D modules and the experiment measurements at all four wave gauges in the simulations of wave breaking over a mild slope.

The evaluation of the properties of the breaking waves generated due to the presence of the submerged structure is one of the essential analyses in such cases. In this sub-section, three-dimensional wave breaking is investigated using all three models. The free surface elevations at different locations calculated by the two models are also compared. The illustration of the numerical wave tank with the bottom topography used in the simulations is presented in Fig. (8). The bottom topography consists of a 1 in 20 slope over which a flat-tip shaped reef with a reef slope of 1 in 6 is placed. The reef angle, that is the angle between the reef normal and the direction of wave propagation is 60°. A detailed description of the complicated reef geometry is provided in Henriquez (2005). The width of the flat tip is 0.188 m and the width of the reef at the far end is 3.88 m. The numerical wave tank is 20 m long, 9 m wide, 0.8 m wide with a water depth of $d = 0.4$ m. Cnoidal waves with a height of $H = 0.12$ m and period $T = 2.50$ s are generated. The submerged reef will affect the propagation of the incident waves and induce wave breaking with the overturning wave crest first appearing over the slope of the reef as shown in Fig. (9). The rest of the wavefront undergoes overturning as it propagates further along the submerged reef and the bottom slope. All simulations are computed with 128 2.1 GHz Intel E5-2683v4 cores on the supercomputer Fram.

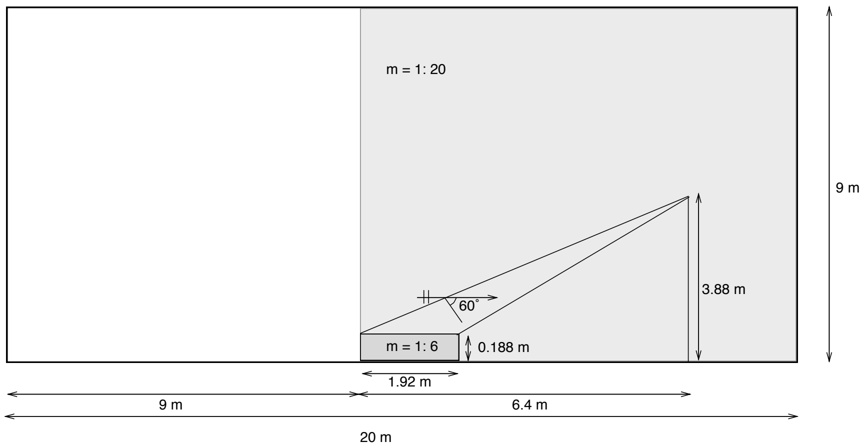

(a)

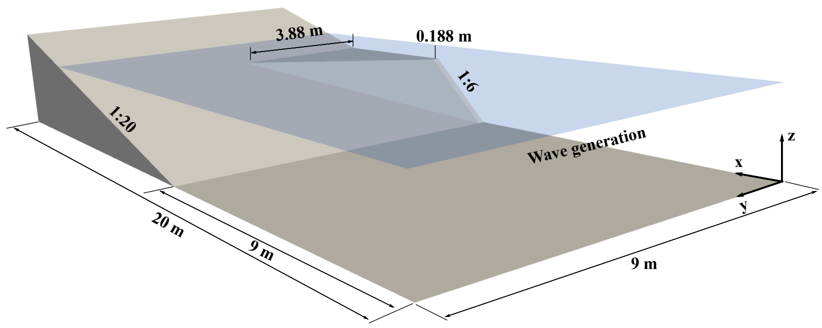

(b)

Figure 8: Numerical wave tank setup for the simulation of three-dimensional wave breaking on a reef. m represents the slopes. (a) schematics from top view, (b) 3D view in the NWT.

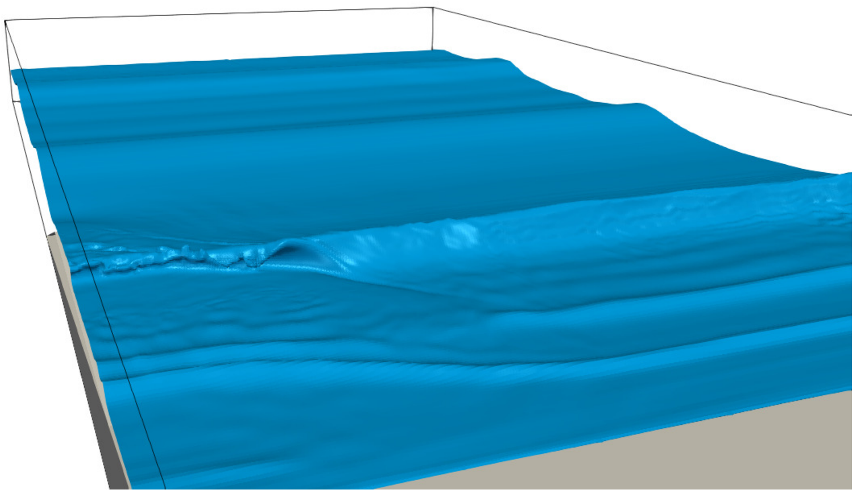

Figure 9: Three-dimensional wave breaking over the reef in the numerical wave tank calculated using REEF3D::CFD

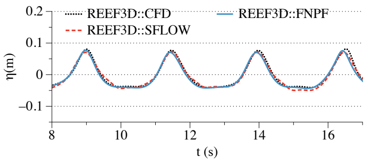

(a) WG1- $x = 9.0$ m, $y = 0.1$ m

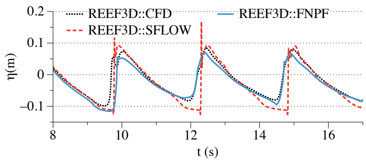

(b) WG2- $x = 11.42$ m, $y = 0.5$ m

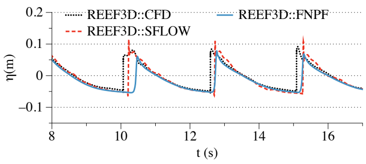

(c) WG3- $x = 11.92$ m, $y = 0.6$ m

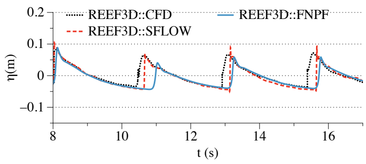

(d) WG4- $x = 12.42$ m, $y = 0.1$ m

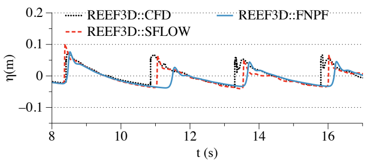

(e) WG5- $x = 12.42$ m, $y = 0.7$ m

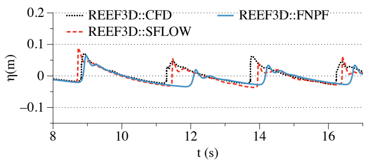

(f) WG6- $x = 13.42$ m, $y = 0.7$ m

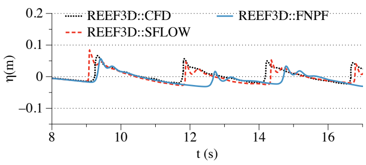

(g) WG7- $x = 13.42$ m, $y = 1.2$ m

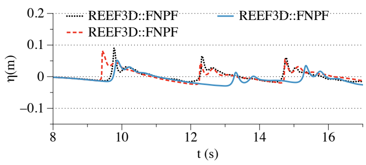

(h) WG8- $x = 13.92$ m, $y = 0.7$ m

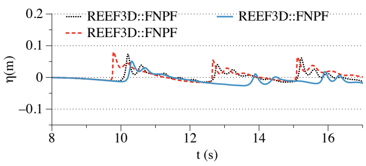

(i) WG9- $x = 14.42$ m, $y = 0.7$ m

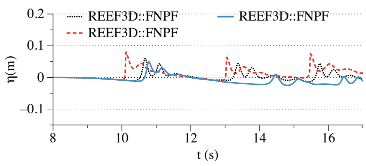

(j) WG10- $x = 14.42$ m, $y = 1.2$ m

Figure 10: Free surface elevations at several locations in the numerical wave tank for three-dimensional wave breaking on a submerged reef calculated using CFD and SFLOW

The free surface elevations at different locations along the reef in the numerical wave tank using the three models are presented in Fig(10). The incident wave at the toe of the slope near the wall is shown in Fig. (10a). The free surface elevation over the reef slope is seen in Figs. (10b) and Figs. (10c). The wave appears to break at these locations as seen from the vertical wave crest front. The difference between the results from the two models are seen in the shape of the wave crest front. The shallow water model, REEF3D::SFLOW and the potential flow model REEF3D::FNPF cannot account for an overturning crest and therefore represent a perfectly vertical wave crest fronts to represent the breaking wave before a sudden reduction in the free surface elevation. In the time series in Figs. (10b) and Figs. (10c), this is seen through the graph retracing its path, before its eventual reduction. In contrast, REEF3D::CFD represents the overturning wave crest. Therefore, the vertical wave crest front is followed by a reduction of the free surface elevation, without a period of retracing of the initial path to the peak. The wave gauges WG 2, 3 and 4 show this process in Figs. (10b), (10c) and (10d) respectively as they are placed in the region of wave breaking over the reef slope. The free surface elevations at WG 5, 6 and 7 in Figs. (10e, 10f and 10g) respectively show the secondary breaking process and the post breaking splash up. This is signified by the reduced free surface elevations and the appearance of secondary crests in the time series. A slight phase difference is seen between the results from REEF3D::SFLOW and REEF3D::CFD. The first secondary breaker in the REEF3D::FNPF simulation is in phase with the other two models. However, significant phase differences are seen in comparison to the other two models after the first secondary breaking. The reason is that the incoming waves start to interact with the wave run-up and run-down on the slope which takes place after the first secondary breaker. In the potential flow model, the wet side of the coastline is covered with a narrow relaxation zone of 0.675 m to avoid numerical instabilities due to the derivatives of the velocity potential over z in the infinitesimal water depth. Therefore, the run-up and run-down are not correctly represented, which lead to a large phase different and smaller wave amplitude in the potential flow simulation. The complex 3D swash zone dynamic and the steeper slope at the end of the numerical wave tank amplify this effect, which is not noticeable in section 3.3. Figures (10h), (10i) and (10j) present the free surface elevations at WG 8, 9 and 10 respectively, which are along the reef slope but in post-breaking region. The free surface elevations are seen to be further reduced and several secondary crests appear in the time series. There is also some phase difference seen among the models. On the other hand, the wave heights calculated by all models are similar for the first breaking wave. This suggests that the loss of wave energy due to wave breaking is well represented in the shallow water model as well as the potential flow model, even though the overturning wave crest is not accounted for.

The free surface elevations in the numerical wave tank with the horizontal velocity contours for the simulations carried out using all three models are presented in Fig. (11). The overturning wave crest at $t/T = 5.5$ is represented in the CFD model in Fig. (11a), whereas only a steep free surface is seen in REEF3D::SFLOW and REEF3D::FNPF in Fig. (11c) and Fig. (11e). The free surface and velocities over the rest of the wavefront are seen to be similar for all the models. The overturning wave crest moves towards the preceding wave trough and the rest of the wavefront gets steeper at $t/T = 5.6$ in Fig. (11b) in REEF3D::CFD model. The REEF3D::SFLOW and REEF3D::FNPF simulations show smoothened free surfaces in the region of the overturning wave crest in Fig. (11d) and Fig. (11f). Wave breaking is seen on the reef slope and wave breaking is initiated away from the reef in Fig. (11g) at $t/T = 5.8$ in the REEF3D::CFD simulation. Figure (11i) and Figure (11k) show steep wavefronts in the region away from the reef for the REEF3D::SFLOW and REEF3D::FNPF simulations. The process of secondary breaking is seen to have started at this time step in the simulations. The overturning wave crest in the region away from the reef at $t/T = 6.1$ is seen in Fig. (11h) in the REEF3D::CFD simulation. The free surfaces in the REEF3D::SFLOW ad REEF3D::FNPF simulations in Fig. (11j) and Fig. (11l) are seen to be similar over the reef in the absence of wave breaking and a steep wavefront are seen away from the reef. However, the post-breaking region is seen to be very different in the simulation of REEF3D::FNPF in comparison to the other models, as seen in Fig. (11k) and Fig. (11l). Less run-up on the slope and some small high-frequency waves are seen only in the simulation of REEF3D::FNPF as the result of the coastal relaxation zone arrangement.

The key difference in the results from REEF3D::CFD and the other two models is that the overturning wave crest is not represented by REEF3D::SFLOW and REEF3D::FNPF. On the other hand, the wave heights after the wave breaking process are seen to be similar in all models. Therefore, if the representation of the overturning wave crest is not critical in a simulation, the shallow water model and potential flow model can provide similar wave kinematics solutions as the three-dimensional and two-phase flow model. However, REEF3D::SFLOW is a better choice when swash zone dynamics result in strong interaction with the incoming waves.

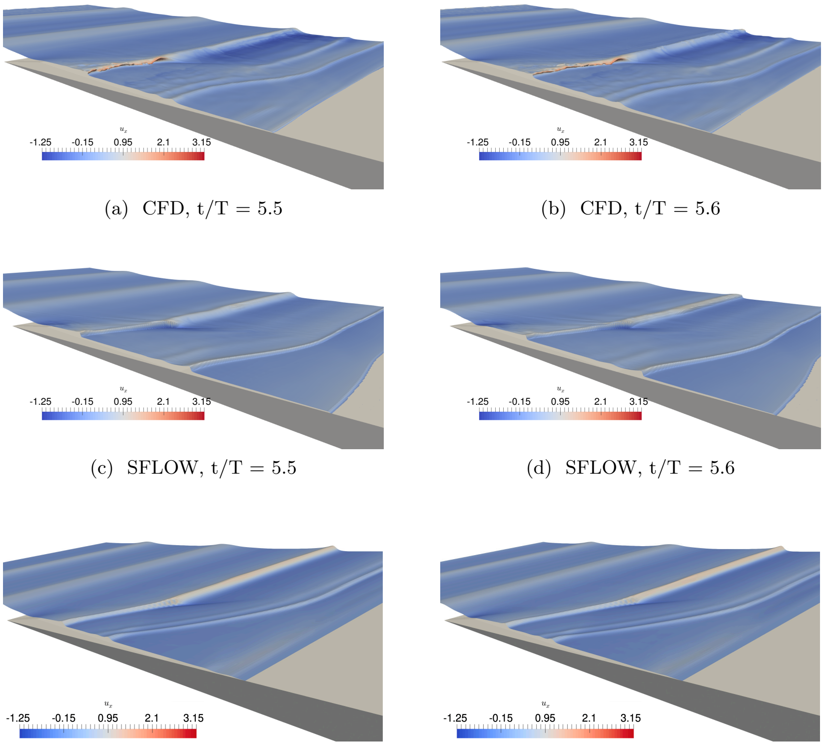

(a) CFD, t/T = 5.5 (b) CFD, t/T = 5.6

(c) SFLOW, t/T = 5.5 (d) SFLOW, t/T = 5.6

(e) FNPF, t/T = 5.5 (f) FNPF, t/T = 5.6

Figure 11: Free surface elevations with velocity contours at different time steps for three-dimensional wave breaking on a reef calculated using CFD and SFLOW (part 1)

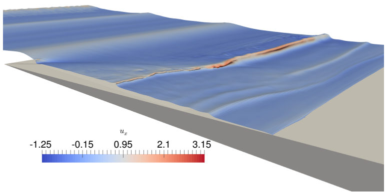

(g) CFD, t/T = 5.8

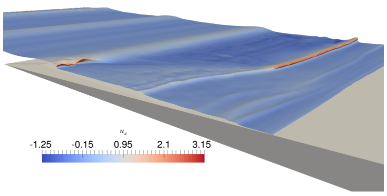

(h) CFD, t/T = 6.1

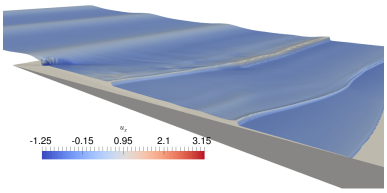

(i) SFLOW, t/T = 5.8

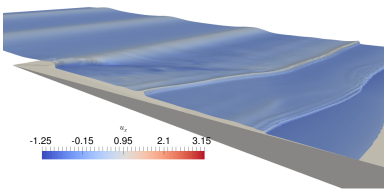

(j) SFLOW, t/T = 6.1

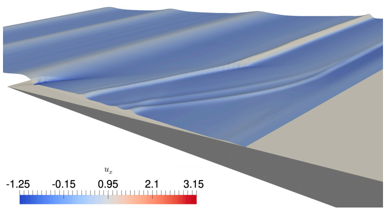

(k) FNPF, t/T = 5.8

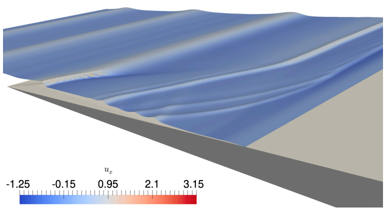

(l) FNPF, t/T = 6.1

Figure 11: Free surface elevations with velocity contours at different time steps for three-dimensional wave breaking on a reef calculated using CFD and SFLOW (part 2)

The computational grid, computational resource and computational time from the three models are compared in Table. 7. The computational speed gains from REEF3D::SFLOW and REEF3D::FNPF in a 3D simulation are seen to be even more prominent in comparison to the CFD solver, with a speedup factor of 60 and 800 respectively. On the other hand, the computational speed of REEF3D::CFD is compensated by the fact that REEF3D::CFD is the only model that is able to represent a correct geometry of an overturning breaker.

Table 7: Comparison of total number of cells N_t and simulation time T_s in seconds for the simulation of wave propagation over a submerged bar using the three modules

module	N_t	T_s
REEF3D::CFD	28700000	90 h
REEF3D::SFLOW	450000	5014.73 s
REEF3D::FNPF	720000	401.34 s

4 Conclusions

In the presented manuscript, a comparative study of the three major types of phase-resolved wave models is presented with the use of the open-source hydrodynamics framework REEF3D. The development and numerical implementation of REEF3D are explained extensively to show the numerical consistency as well as differences among the wave models. The benchmark studies provide an insight into the strengths and limitations of each type of the wave modelling technique in terms of their computational performance as well as their limitations in different types of wave hydrodynamic phenomena. Thanks to the fact that all three models are implemented in the same numerical framework, an objective comparison is presented, which is not influenced by the various numerical implementations from different developers.

REEF3D::CFD solves the incompressible NavierStokes equations with a RANS turbulence model. Here, the pressure is solved on a staggered grid using the projection method. This ensures a tight pressure-velocity coupling. The model benefits from the utilization of a level set function to capture the motion of the free surface implicitly. In the numerical wave tank, the waves are generated and absorbed with either the relaxation method or using Dirichlet boundary conditions.

REEF3D::SFLOW reduces the computational costs significantly by solving the depth-averaged shallow water equations with a non-hydrostatic extension based on a quadratic vertical pressure profile. In comparison to existing approaches, like Boussinesq-type models or multi-layer approaches, the system of equations is solved with the projection method and high-order discretization schemes. This increases the stability of the computation through simpler terms in the equation and semi-implicit calculations for the pressure. Further, the model benefits from the parallelization strategy in REEF3D which enables the simulation of large scale wave propagation near shores.

REEF3D::FNPF closes the gap between the efficient 2D shallow water solver and the accurate CFD solver for wave propagation problems as the FNPF potential flow solver is not restricted by water depth. By solving the three-dimensional Laplace equation with nonlinear boundary conditions for the free surface and the bottom, no simplifying assumptions regarding the wave characteristics or bottom slope are taken into account. At the same time, the use of a σ-coordinate system removes the additional cost of a two-phase approach. The model employs high-order discretization schemes in space and time which allows for larger cell sizes and time steps. Typically, ten cells in the vertical direction are sufficient to obtain accurate wave propagation. Very fast parallelized algorithms for solving the system matrix ensure the computational efficiency and enables the application for large-scale problems in deep and shallow water.

The performance of the presented modules has been tested and compared for several benchmark applications. The direct comparisons for regular waves show that all approaches are capable of predicting the wave propagation in their range of applicability. The challenging submerged bar case revealed very good accuracy of REEF3D::CFD and REF3D::FNPF, whereas the shallow water model fails due to its theoretical limitations. The two-dimensional wave breaking case shows that all three models are able to represent a correct wave energy dissipation during a breaking process. In the case of the three-dimensional wave breaking case, REEF3D::CFD and REEF3D::SFLOW capture the second breaking wave more accurately since both represent the swash zone dynamics better. The CFD based numerical wave tank is the only model that accurately represents the physics of wave propagation including complex overturning wave breaking. The computational speed gains from REEF3D::SFLOW and REF3D::FNPF in comparison to REEF3D::CFD are found to be by factors of about 10 and 40 on average for 2D simulations and 60 and 800 for the 3D simulation. The higher computational demands of the CFD model is compensated by that fact that it is the only model capable of representing the geometry of an overturning wave breaker accurately, which is important for studies on slamming load on structures.

With the strengths and limitations of each numerical models in mind, the future work will focus on the coupling of the different modules within REEF3D. A one-way coupling will use the propagated waves from a potential theory model as input waves in the CFD simulations. Two-way coupling processes will be interesting for applications in marine engineering with strong fluid-structure interactions.

Acknowledgements

The authors are grateful for the grants provided by the Research Council of Norway under the HAVBRUK2 project (no. 267981). This study has also been partially carried out within the E39 fjord crossing project (No. 304624) and the authors are grateful for the grants provided by the Norwegian Public Roads Administration. This research was supported with computational resources at NTNU provided by NOTUR (Norwegian Metacenter for Computational Sciences, http://www.notur.no) under project no. NN2620K.

References

Aggarwal, A., Bihs, H., Shirinov, S. and Myrhaug, D. (2019). Estimation of breaking wave properties and their interaction with a jacket structure. *Journal of Fluids and Structures*, **91**, 102722.

Ahmad, N., Bihs, H., Myrhaug, D., Kamath, A. and Arntsen, Ø.A. (2018). Three-dimensional numerical modelling of wave-induced scour around piles in a side-by-side arrangement. *Coastal Engineering*, **Volume 138**, 132–151.

Arunakumar, H.S., Suvarna, P., Abhijith, P.A., Prabhu, A.S., Pruthviraj, U. and Kamath, A. (2019). Effect of emerged coastal vegetation on wave attenuation using open source CFD tool: REEF3D. In: *Proceedings of the Fourth International Conference in Ocean Engineering (ICOE2018)*, 591–603. Springer Singapore.

Ashby, S. and Flagout, R. (1996). A parallel mulitgrid preconditioned conjugate gradient algorithm for groundwater flow simulations. *Nuclear Science and Engineering*, **Volume 124(1)**, 145–159.

Beji, S. and Battjes, J.A. (1993). Experimental investigation of wave propagation over a bar. *Coastal Engineering*, **19**, 151–162.

Belibassakis, K. and Athanassoulis, G. (2011). A coupled-mode system with application to nonlinear water waves propagating in finite water depth and in variable bathymetry regions. *Coastal Engineering*, **Volume 58(4)**, 337–350.

Berthelsen, P. and Faltinsen, O. (2008). A local directional ghost cell approach for incompressible viscous flow problems with irregular boundaries. *Journal of Computational Physics*, **Volume 227**, 4354–4397.

Bihs, H. and Kamath, A. (2017). A combined level set/ghost cell immersed boundary representation for floating body simulations. *Int. J. Numer. Meth. Fluids*, **Volume 83**, 905–916.

Bihs, H., Kamath, A., Alagan Chella, M., Aggarwal, A. and Arntsen, Ø.A. (2016). A new level set numerical wave tank with improved density interpolation for complex wave hydrodynamics. *Computers & Fluids*, **Volume 140**, 191–208.

Bihs, H., Kamath, A., Alagan Chella, M. and Arntsen, Ø.A. (2019). Extreme wave generation, breaking, and impact simulations using wave packets in REEF3D. *Journal of Offshore Mechanics and Arctic Engineering*, **141 (4)**. 10.1115/1.4042178.

Bihs, H., Wang, W., Pákozdi, C. and Kamath, A. (2020). REEF3D::FNPF-a flexible fully nonlinear potential flow solver. *Journal of Offshore Mechanics and Arctic Engineering*, **142**(4). ISSN 0892-7219. 10.1115/1.4045915.

Booji, N., Ris, R. and Holthuijsen, L. (1999). A third-generation wave model for coastal regions, 1. model description and validation. *J. Geophys Res*, **Volume 104**, 7649–7666.

Brackbill, J., Kothe, D. and Zemach, C. (1992). A Continuum Method for Modeling Surface Tension. *Journal of Computational Physics*, **Volume 100(2)**, 335–354.

Chorin, A. (1968). Numerical solution of the Navier-Stokes equations. *Mathematics of Computation*, **Volume 22**, 745–762.

Courant, R., Friedrichs, K. and Lewy, H. (1967). On the partial difference equations of mathematical physics. *IBM J. Res. Dev.*, **11**(2), 215–234. ISSN 0018-8646. 10.1147/rd.112.0215.

Dommermuth, D. and Yue, D. (1987). A high-order spectral method for the study of nonlinear gravity waves. *Journal of Fluid Mechanics*, **Volume 184(1)**, 267–288.

Ducrozet, G., Bingham, H., Ensig-Karup, A. and Ferrant, P. (2010). High-order finite difference solution for 3D nonlinear wave- structure interaction. *Journal of Hydrodynamics, Ser. B*, **Volume 22(5)**, 225–230.

Ducrozet, G. and Bonnefoy, F. (2012). A modified High-Order Spectral method for wavemaker modeling in a numerical wave tank. *European Journal of Mechanics - B/Fluids*, **Volume 34**, 19–34.

Durbin, P. (2009). Limiters and wall treatments in applied turbulence modeling. *Fluid Dyn Res*, **Volume 41**, 1–18.

Ensig-Karup, A., Hesthaven, J., Bingham, H. and Warburton, T. (2008). DG-FEM solution for nonlinear wave-structure interaction using Boussinesq-type equations. *Coastal Engineering*, **Volume 55(3)**, 197–208.

Henriquez, M. (2005). Artificial surf reefs.

Higuera, P., Lara, L. and Losada, I. (2013). Realistic wave generation and active wave absorption for Navier-Stokes models application to OpenFOAM. *Coastal Engineering*, **Volume 71**, 102–118.

Higuera, P., Lara, L. and Losada, I. (2014). Three-dimensional interaction of waves and porous coastal structures using OpenFOAM. Part II: application. *Coastal Engineering*, **Volume 83**, 259–270.

Hossain, M. and Rodi, W. (1980). Mathematical modeling of vertical mixing in stratified channel flow. Second Symposium on Stratified Flows, Trondheim, Norway.

Jacobsen, N., Fuhrman, D. and Fredsøe, J. (2012). A wave generation toolbox for the open-source CFD library: OpenFOAM. *Int J Numer Meth Fluids*, **Volume 70 (9)**, 1073–1088.

Jacobsen, N.G. (2015). Mass conservation in computational morphodynamics: Uniform sediment and infinite availability. *International Journal for Numerical Methods in Fluids*, **78**(4), 233–256.

Jeschke, A., Pedersen, G.K., Vater, S. and Behrens, J. (2017). Depth-averaged non-hydrostatic extension for shallow water equations with quadratic vertical pressure profile: equivalence to boussinesq-type equations. *International Journal for Numerical Methods in Fluids*, **84**(10), 569–583. 10.1002/fld.4361.

Jiang, G. and Peng, D. (2000). Weighted ENO schemes for Hamilton Jacobi equations. *SIAM Journal of Scientific Computing*, **Volume 21**, 2126–2143.

Jiang, G. and Shu, C. (1996). Efficient implementation of weighted ENO schemes. *Journal of Computational Physics*, **Volume 126(1)**, 202–228.

Kamath, A., Fleit, G. and Bihs, H. (2019). Investigation of free surface turbulence damping in rans simulations for complex free surface flows. *Water*, **11**(3), 456.

Kamath, A., Sasikumar, A. and Bihs, H. (2018). Numerical study of wave interaction with a submerged porous breakwater in combination with a floating breakwater. *Coastal Engineering Proceedings*, **1**(36).

Li, B. and Fleming, C.A. (1997). A three dimensional multigrid model for fully nonlinear water waves. *Coastal Engineering*, **30**(3), 235 – 258. ISSN 0378-3839. https://doi.org/10.1016/S0378-3839(96)00046-4.

Madsen, P., Bingham, H. and Liu, H. (2002). A new Boussinesq method for fully nonlinear waves from shallow to deep water. *J Fluid Mech*, **Volume 462**, 1–30.

Madsen, P., Murray, R. and Sørensen, O. (1991). A new form of the Boussinesq equations with improved linear dispersion characteristics. *Coastal Engineering*, **Volume 15**, 371–388.

Martin, T., Kamath, A. and Bihs, H. (2018). Numerical simulation of interactions between water waves and a moored-floating breakwater. *Coastal Engineering Proceedings*, **1**(36).

Martin, T., Kamath, A. and Bihs, H. (2019). Modeling and simulation of moored-floating structures using the tension element method. *Journal of Offshore Mechanics and Arctic Engineering*, **142**(1). 10.1115/1.4044289.

Moreno Miquel, A., Kamath, A., Alagan Chella, M., Archetti, R. and Bihs, H. (2018). Analysis of different methods for wave generation and absorption in a cfd-based numerical wave tank. *Journal of Marine Science and Engineering*, **6 (2)**. 10.3390/jmse6020073.

Naot, D. and Rodi, W. (1982). Calculation of secondary currents in channel flow. *Journal of the Hydraulics Division, ASCE*, **Volume 108**, 948–968.

Osher, S. and Sethian, J. (1988). Fronts propagating with curvature-dependent speed: Algorithms based on Hamilton-Jacobi formulations. *Journal of Computational Physics*, **Volume 79**, 12–49.

Osher, S. and Sethian, J.A. (1988). Fronts propagating with curvature-dependent speed: Algorithms based on Hamilton-Jacobi formulations. *Journal of Computational Physics*, **79**, 12–49.

Pakozdi, C., Wang, W., Kamath, A. and Bihs, H. (2019). Definition of the vertical spacing of a sigma grid based on the constant trucation error. *Proceedings of the 10th National Conference on Computational Mechanics MekIT19, Trondheim, Norway.*

Paulsen, B., Bredmose, H. and Bingham, H. (2014). An efficient domain decomposition strategy for wave loads on surface piercing circular cylinders. *Coastal Engineering*, **Volume 86**, 57–76.

Peng, D., Merriman, B., Osher, S., Zhao, H. and Kang, M. (1999). A pde-based fast local level set method. *Journal of Computational Physics*, **155**.

Seiffert, B. and Ducrozet, G. (2018). Simulation of breaking waves using the high-order spectral method with laboratory experiments: wave-breaking energy dissipation. *Ocean Dynamics*, **Volume 68(1)**, 65–89.

Seiffert, B., Hayatdavoodi, M. and Ertekin, R. (2014). Experiments and computations of solitary-wave forces on a coastal-bridge deck. Part I: flat plate. *Coastal Engineering*, **Volume 88**, 194–209.

Shepard, D. (1968). A two-dimensional interpolation function for irregularly-spaced data. In: *Proceedings of the 1968 23rd ACM national conference*, 517–524.

Shu, C. and Osher, S. (1988). Efficient implementation of essentially non-oscillatory shock-capturing schemes. *Journal of Computational Physics*, **Volume 77(2)**, 439–471.

Stelling, G.S. and Duinmeijer, S.P.A. (2003). A staggered conservative scheme for every froude number in rapidly varied shallow water flows. *International Journal for Numerical Methods in Fluids*, **43**(12), 1329–1354. 10.1002/fld.537.

Sussman, M., Smereka, P. and Osher, S. (1994). A level set approach for computing solutions to incompressible two-phase flow. *Journal of Computational Physics*, **Volume 114**, 146–159.

Sussman, M., Smereka, P. and Osher, S. (1994). A level set approach for computing solutions to incompressible two-phase flow. *Journal of Computational Physics*, **114**(1), 146 – 159. ISSN 0021-9991. https://doi.org/10.1006/jcph.1994.1155.

SWASH developers (2017). SWASH User Manual version 4.01A.

Ting, F.C.K. and Kirby, J.T. (1995). Dynamics of surf-zone turbulence in a strong plunging breaker. *Coastal Engineering*, **24**, 177–204.

van der Vorst, H. (1992). BiCGStab: A fast and smoothly converging variant of Bi-CG for the solution of nonsymmetric linear systems. *SIAM Journal of Scientific Computing*, **Volume 13**, 631–644.

Wang, W., Bihs, H., Kamath, A. and Arntsen, Ø.A. (2018). Multi-directional irregular wave modelling with cfd. In: *Proceedings of the Fourth International Conference in Ocean Engineering (ICOE2018)*, 521–529. Springer Singapore.

Wang, W., Martin, T., Kamath, A. and Bihs, H. (2020). An improved depth-averaged non-hydrostatic shallow water model with quadratic pressure approximation. *International Journal for Numerical Methods in Fluids*, 10.1002/fld.4807.

Weller, H. (2008). A new approach to VOF-based interface capturing methods for incompressible and compressible flow. Technical Report OpenFOAM.

West, B., Brueckner, K., Janda, R., Milder, D. and Milton, R. (1987). A new numerical method for surface hydrodynamics. *Journal of Geophysical Research: Oceans*, **Volume 92(C11)**, 11803–11824.

Wilcox, D.C. (1988). Reassessment of the scale-determining equation for advanced turbulence models. *AIAA Journal*, **26**(11), 1299–1310. 10.2514/3.10041.

Yang, J. and Stern, F. (2013). Robust and Efficient Setup Procedure for Complex Triangulations in Immersed Boundary Simulations. *Journal of Fluids Engineering*, **Volume 135 (10)**, 101107.1–101107.11.

Zijlema, M. and Stelling, G. (2008). Efficient computation of surf zone waves using the nonlinear shallow water equations with non-hydrostatic pressure. *Coastal Engineering*, **55**(780–790).